RUHR-UNIVERSITÄT BOCHUM

Andrea Geppetti

Experimental and numerical investigations on the behaviour of tailings storage facilities under seismic loading

Bochum 2023

Heft 78

Schriftenreihe des Lehrstuhls für
Bodenmechanik, Grundbau und Umweltgeotechnik

Herausgeber: Torsten Wichtmann

ISSN 2699-1020

Andrea Geppetti Behaviour of tailings storage facilities under seismic loading

78

ISSN 2699-1020

Ruhr-Universität Bochum
Schriftenreihe Bodenmechanik, Grundbau und Umweltgeotechnik
Heft 78

Herausgeber:
Prof. Dr.-Ing. habil. Torsten Wichtmann
Ruhr-Universität Bochum
Fakultät für Bau- und Umweltingenieurwissenschaften
Lehrstuhl für Bodenmechanik, Grundbau und Umweltgeotechnik
44801 Bochum
Telefon: 0234/ 3226135
Telefax: 0234/ 3214236
Internet: www.bgu.ruhr-uni-bochum.de

ISSN 2699-1020

Department of Civil and Environmental Engineering of the University of Florence

Chair of Soil Mechanics, Foundation Engineering and Environmental Geotechnics of the Ruhr University of Bochum (RUB)

Ph.D. Dissertation in International Doctorate in Civil and Environmental Engineering

November 2023

Experimental and numerical investigations on the behaviour of tailings storage facilities under seismic loading

Advisors:

Prof. Ing. Claudia Madiai

Prof. Ing. Johann Facciorusso

Prof. Dr.-Ing. habil. Torsten Wichtmann

Dr.-Ing., As. Prof. Luis Felipe Prada-Sarmiento

By:

Andrea Geppetti

Coordinator Prof. Ing. Luca Solari

Preface of the editor

The doctoral thesis of Andrea Geppetti was prepared in the framework of a Cotutelle agreement between the University of Florence and Ruhr-Universität Bochum. The research was mainly done at the University of Florence, supervised by Prof. Claudia Madiai and Prof. Johann Facciorusso, but also involved long-term visits at Ruhr-Universität Bochum, where Dr. Felipe Prada supported the research.

The extraction of ores or other minerals in mining often involves milling processes, leading to large quantities of fine-grained waste materials called tailings. These tailings are usually deposited as water-rich slurries in special basins in the vicinity of the mines. As a result of the milling process the particles of the tailings are fine and angular, but the materials show almost no cohesion. The tailings are found in a rather loose state after consolidation. As an artificial material the mechanical behaviour of tailings may significantly differ from natural soils with similar grain size distribution curve. The basins containing the tailings are usually encompassed by dams constructed either with natural material excavated nearby or composed of coarser waste materials from the mines. The storage facility composed of the basin and the dam is often stepwise increased in height, using different construction methods like the down-stream or the up-stream methods. In the last decades numerous tailings dams failed, with the released fluidized masses of tailings causing major damage and loss of lives downstream. These failure cases highlight the need for a proper design, construction and maintenance of tailings storage facilities. In several cases failure of tailings dams was caused by seismic events. In his doctoral thesis Andrea Geppetti has developed a consistent methodology to evaluate the performance of tailings storage facilities under earthquake loading. It is based on dynamic finite element simulations using sophisticated constitutive models for soils with parameters calibrated from experiments on high-quality undisturbed samples. In order to take such samples from the tailings Andrea Geppetti has developed a simple and cost-effective method utilizing ground freezing. He has demonstrated the applicability of the developed methodology in a case study of a tailings storage facility of an abandoned mine in southern Tuscany. He was able to collect comprehensive information regarding the geometry and construction history of the facility, as well as on ground composition, groundwater conditions, geology and seismicity of the region. In two field campaigns he took disturbed and undisturbed samples from the basin containing the tailings and from the encompassing dam. On these samples he performed triaxial tests in the laboratories in Florence and Bochum, with a focus on the liquefaction susceptibility of the materials under undrained cyclic loading conditions. The test data served as basis for the calibration of four sophisticated constitutive models. Finite element models of the tailings storage facility were built with the open-source code OpenSees and subjected to different seismic signals being representative for possible earthquakes in that region, thereby also varying the constitutive model used for the tailings. The simulation results were analysed with respect to a possible soil liquefaction and displacements caused by the seismic event. The doctoral thesis of Andrea Geppetti may serve as a guideline for future evaluations of tailings storage facilities under seismic loading. Furthermore, the experimental results will be useful for researchers developing constitutive models for tailings. The proposed sampling method can be applied by other researchers and practical engineers, too.

Torsten Wichtmann

Acknowledgements

This doctoral thesis was accomplished at the Department of Civil and Environmental Engineering of the University of Florence and at the Chair of Soil Mechanics, Foundation Engineering and Environmental Geotechnics of the Ruhr University of Bochum (RUB). So first I must thank my supervisors from the Italian and from the German side who have always tried to understand my ideas, supported and advised. I also want to thank my colleagues both from the Italian and German side who obviously have become friends and sharers of this path that it would be impossible to face alone. A thank you goes to the people who are in a certain sense behind the scenes but who are fundamental. I am referring to the people who deal with administrative bureaucratic matters and who give a human face to what for me appears to be an impenetrable labyrinth of documents. Obviously, friends, family and relatives cannot be missing from this list. But a special thanks goes to my wife who has always been by my side and supported me.

Abstract

The development of human society is strongly linked to and dependent from extractive activities. The waste storage facilities from the latter, known as tailing dams, can pose significant risks to the environment and communities if not properly designed, operated, and maintained, as demonstrated by catastrophic consequences of several incidents occurred in the more or less recent past. In this doctoral dissertation, a comprehensive methodological approach, based on the integrated use of experimental activity, constitutive modelling and finite element numerical simulations, is proposed, with the aim of contributing to a better understanding of the behaviour of tailings dams under seismic conditions. A tailings dam located in the Metalliferous Hills National Park in southern Tuscany (Italy) is deeply analysed as a case study. In the first part of the thesis the main characteristics of these structures are outlined in terms of mining processes and origin of tailings, construction methodologies, facilities components, etc. The strong susceptibility of tailings dams to failure is demonstrated by means of statistical data. Through an extensive literature research based on the available international databases, the failure of a large number of tailings dams that occurred in the past has been considered and classified. Since seismic liquefaction is identified as one of the most important causes of failure of these structures, past cases of this failure type are presented and the fundamental concepts regarding this phenomenon are outlined. With reference to the case study, the materials constituting the tailings basin, the embankment and soil foundation, were characterized from a geotechnical point of view through classification tests (grain sizes, volume weights, index quantities, etc.) and by means of monotonic and cyclic triaxial tests. The outcomes of the testing activity on the investigated materials is reported. In this regard, an innovative relatively inexpensive methodology for collecting undisturbed samples of material at shallow depths by freezing with liquid nitrogen is described. The monotonic triaxial tests were conducted under drained and undrained conditions on samples reconstituted with the moist tamping method. The cyclic triaxial tests were performed under undrained conditions and stress control, on reconstituted and undisturbed samples. An extensive literature review of scientific papers dealing with the analysis of tailings dams with numerical methods is reported with reference to some main aspects: model size, mesh discretization, elements used, boundary and initial conditions, constitutive laws and applied loads. After framing the case study, and the surrounding area, from a historical, geological, hydrogeological and seismic point of view, the geotechnical model has been defined through the combination of the information gathered from the laboratory tests conducted and through the analysis of material from previous investigations. A brief description of the SANISAND, Pressure Dependent Multi Yield (PDMY), Pressure Independent Multi Yield (PDMY) and PM4Sand constitutive models used is given and the definition of the required input parameters of these constitutive models is reported. To characterize the geotechnical model, these parameters have been determined through the interpretation of some laboratory tests, from values recommended in the literature and through iterative trial and error procedures. The iterative and validation procedures consisted in comparing the results of the laboratory tests with those obtained from the simulations of these tests (element tests) with the finite element software OpenSees. The behavior of a cross section of the tailing dam structure in seismic conditions was studied through numerical analyses conducted with the OpenSees software. Choice of the dimensions of the model, the type and size of elements and the

boundary conditions is explained in detail. The stress state of the system before the seismic load was determined by simulating the construction of the structure through three successive phases. The seismic behaviour was evaluated by loading the structure with seven seismic signals spectrum compatible with the elastic response spectrum assigned by the Italian building regulations (NTC2018). The results in terms of effective stress decay, shear strains and displacements are discussed for all the assigned seismic signals, comparing results for the tailings basin material described by either the SANISAND or the PDMY constitutive models.

List of Symbols

AR	Aspect ratio	[-]
B	Skempton coefficient	[-]
B	Bulk modulus in PIMY and PDMY model	$[ML^{-1}T^{-2}]$
c	Soil cohesion	$[ML^{-1}T^{-2}]$
c_1	Plastic volumetric strain rate	[-]
c_2	Material damage factor	[-]
c_3	Overburden stress factor	[-]
C_B	Standard Penetration Test (SPT) diameter correction	[-]
C_{GD}	Shear modulus degradation factor	[-]
C_E	Hammer energy percentage	[-]
C_i	Circularity	[-]
C_N	Overburden correction factor	[-]
C_R	Standard Penetration Test (SPT) rod correction	[-]
$CRR_{M=7.5,\sigma=1\,[atm]}$	Cyclic resistance ratio for a 7.5 magnitude earthquake and an overburden stress of 1 atm	[-]
C_S	Standard Penetration Test (SPT) sampler correction	[-]
CSR	Cyclic stress ratio	[-]
C_{SR}	Stress ratio effects factor	[-]
c_u	Undrained cohesion	$[ML^{-1}T^{-2}]$
C_u	Uniformity coefficient	[%]
d	Dilatancy	[-]
D	Volumetric component of plastic strain direction tensor	[-]
d_1	Dilatation rate factor	[-]
d_2	Fabric damage factor	[-]
d_3	Overburden effect factor	[-]
d_{50}	Diameter of the grains referred to 50% of passing material	[L]
d_{10}	Diameter of the grains referred to 10% of passing material	[L]
d_{60}	Diameter of the grains referred to 60% of passing material	[L]
D_R	Soil relative density	[%]
$D_{R,cons}$	Relative density after consolidation	[-]
$D_{R,cs}$	Critical state relative density	[-]
$\boldsymbol{e}^e$	Deviatoric elastic strain tensor	[-]
E_m	Standard Penetration Test (SPT) hammer efficiency	[-]
e_{max}	Maximum void ratio	[-]
$e_{max,i}$	Maximum void ratio referred to the i-th test	[-]
e_{min}	Minimum void ratio	[-]

$\boldsymbol{e}^p$	Deviatoric plastic strain tensor	[-]
FC	Fines content	[%]
f_s	Piezocone Penetration Tests (CPTu) lateral friction resistance	[$ML^{-1}T^{-2}$]
G_S	Specific gravity	[-]
h	Element size	[-]
H	Plastic hardening modulus	[-]
h_n	Layer height in sample preparation by moist tamping according to undercompaction method	[L]
h_t	Total sample height	[L]
$\boldsymbol{I}$	Identity tensor	[-]
I_c	Piezocone Penetration Tests (CPTu) Soil Behavior Type index	[-]
IP	Plasticity index	[%]
J_2	Second deviatoric stress invariant	[-]
K	Bulk modulus	[$ML^{-1}T^{-2}$]
K_p	Plastic modulus of PM4Sand model	[-]
L	Loading index	[-]
l_1	Liquefaction-induced plastic shear strain factor	[-]
l_2	Liquefaction-induced plastic shear strain factor	[-]
M^b	Bounding stress ratio	[-]
M_{CS}	Critical state stress ratio	[-]
M_d	Dry mass	[M]
M^d	Dilatancy stress ratio	[-]
$M_{S,i}$	Mass of i-th layer for moist tamping	[M]
$M_{Smax,i}$	Mass of i-th weighing for maximum void ratio	[M]
$M_{Smax,5}$	Mass of fifth weighing for mininimum void ratio	[M]
n	Current layer number	[-]
N	Standard Penetration Test (SPT) average blow count	[-]
$(N_1)_{60cs}$	Corrected penetration resistance for equivalent clean sand	[-]
N_{SPT}	Standard Penetration Test (SPT) blow-count	[-]
n_t	Number of layers in sample preparation by moist tamping according to undercompaction method	[-]
NYS	Number of yield surfaces	[-]
$\boldsymbol{P}$	Direction of plastic deformations	[-]
p'	Average effective stress	[$ML^{-1}T^{-2}$]
$\boldsymbol{P'}$	Deviatoric component of plastic deformations	[-]
p_a	Atmospheric pressure	[$ML^{-1}T^{-2}$]
p'_{cons}	Consolidation average effective stress	[$ML^{-1}T^{-2}$]
q	Deviatoric stress	[$ML^{-1}T^{-2}$]

$\boldsymbol{Q}$	Outer normal to the yield surface tensor	[-]
$\boldsymbol{Q'}$	Deviatoric component of the outer normal to the yield surface tensor	[-]
q_c	Piezocone Penetration Tests (CPTu) tip resistance	$[ML^{-1}T^{-2}]$
q_S	Static shear stress	$[ML^{-1}T^{-2}]$
q_t	Piezocone Penetration Tests (CPTu) corrected cone resistance	$[ML^{-1}T^{-2}]$
r_u	Pore water pressure ratio	[-]
$\boldsymbol{R}$	Tensor of plastic strain direction	[-]
$\boldsymbol{R'}$	Deviatoric component of plastic strain direction tensor	[-]
S_u	Undrained shear strength	$[ML^{-1}T^{-2}]$
U_n	Undercompaction degree	[-]
U_{ni}	First layer undercompaction degree	[-]
U_{nt}	Last layer undercompaction degree	[-]
v	Specific volume	[-]
V_s	Shear wave velocity	$[LT^{-1}]$
V	Volume for max void ratio determination	$[L^3]$
$V_{S,i}$	Volume of the i-th layer for moist tamping	$[L^3]$
$V_{TOTmin,i}$	Total volume for i-th minimum void ratio	$[L^3]$
w_L	Liquid limit	[%]
z	Fabric-dilatancy internal variable	[-]

α	Slope of bisector of yield function of SANISAND model	[-]
γ_v	Unit weight	$[ML^{-2}T^{-2}]$
Γ	Specific volume for average effective stress equal to unity	[-]
γ_d	Dry unit weight	$[ML^{-2}T^{-2}]$
γ_d	Octahedral shear deformation	[-]
$\gamma_{max,r}$	Maximum octahedral shear strain	[-]
γ_s	Solid unit weight	$[ML^{-2}T^{-2}]$
γ_{sat}	Saturated unit weight	$[ML^{-2}T^{-2}]$
$\Delta(N_1)_{60cs}$	Fines content correction	[-]
Δu	Excess pore water pressure	$[ML^{-1}T^{-2}]$
ε_1	Component 1 of strain tensor	[-]
ε_2	Component 2 of strain tensor	[-]
ε_q	Deviatoric strain	[-]
ε_q^e	Elastic deviatoric strain	[-]
ε_q^p	Plastic deviatoric strain	[-]
ε_v	Volumetric strain	[-]
ε_v^e	Elastic volumetric strain	[-]
ε_v^p	Plastic volumetric strain	[-]
ζ	Effective stresses decay	[-]
η	Stress ratio	[-]

η_{PT}	Phase transformation stress ratio	[-]
θ	Lode angle	[-]
λ	Critical state line slope	[-]
$\boldsymbol{\mu}$	Translation direction deviatoric tensor	[-]
υ	Poisson's ratio	[-]
ξ_R	State parameter index	[%]
ρ_S	Soil particles density	[ML^{-3}]
$\rho_{S,i}$	Soil particles density of the i-th layer for moist tamping	[ML^{-3}]
ρ_w	Water density	[ML^{-3}]
σ'	Effective stress	[$ML^{-1}T^{-2}$]
σ'_1	Component 1 of effective stress tensor	[$ML^{-1}T^{-2}$]
σ'_3	Component 2 of effective stress tensor	[$ML^{-1}T^{-2}$]
σ'_{v0}	Vertical initial effective stress	[$ML^{-1}T^{-2}$]
τ	Shear stress	[$ML^{-1}T^{-2}$]
ϕ'	Effective friction angle	[°]
Ψ	State parameter	[-]

Contents

1. Introduction

1.1. Background

The development of human societies and mining activities are undeniably closely linked. A striking example is the so-called three-age system, according to which each prehistoric society went through three periods of development, which were: Stone age, Bronze age, and Iron age. According to this system, the progress of a society, before the advent of writing, could be measured by the raw materials which, being used in increasing quantities, required the development of mining practices. This classification system has limitations and does not consider many aspects that mark the development of a community, not contemplating features such as politics and economics; nevertheless, it gives an idea of how crucial mining is for progress. Valuable materials are almost never found isolated but are generally mixed with other materials that are not of interest and inevitably become waste. Over time, the ratio between valuable material and waste material has gradually diminished, making the worthless fraction no longer negligible. To cite an example, Calvo et al. (2016) studied the ore grade trend (ratio of valuable material to a ton of extracted material) of copper in numerous mines, observing that this decreased by 25% in ten years. This aspect, along with the exponential growth of the human population and the expanding need of raw materials deriving from the subsoil, has generated immeasurable quantities of waste in recent decades. If this waste material is obtained by crushing rocks and then deposited in the form of a slurry, it takes the name of tailings (Vick 1990). Originally, tailings were deposited in waterways close to the mines, while various other techniques were developed over time, including subaqueous dumping, disposal of dry or thickened tailings in impoundments or free-standing piles, and backfilling of underground mines or open pits (EPA 1994). Subaqueous disposal is a very bad practice for the environment and it is only allowed in a few countries. Thickening the tailings basically consists in removing excess water from the material, thereby maximizing its density and reducing the volume of the disposed material with consequent benefits for the ecosystem. The backfilling technique consists in reinserting the waste material into the cavities created to build mines or open pits. Although this method has the greatest environmental benefits, it is not always applicable due to the high cost of the temporary storage of the waste while the mine is still operating. However, today the most common method for storing tailings is to arrange them without any specific treatment in settling basins. When the orography of the territory makes it necessary, these basins are retained through soil embankments. These structures are called tailings dams or tailings storage facilities (TSF). There are testimonies of tailings dams that date back to 3000 BCE (Guimarães et al., 2022), but the first structure with the characteristics of a modern tailings dam was built in 1817 in Japan (Global Tailings Portal, 2023). From that moment on, tailings dams of increasingly larger dimensions were built more or less all over the world, and to this day they are the largest structures made by man. These dams have a huge impact on neighboring territories both during operating conditions and following their closure because they disfigure the landscape with their imposing dimensions, can cause pollution of the surrounding aquifers and, if not

adequately treated, can generate dust that can be dispersed for kilometers by the wind. However, the most worrying aspect of these structures is that they are extremely susceptible to collapse, with a failure rate two orders of magnitude higher than that of the best-known conventional water-retaining dams (ICOLD 2001). Except for minor cases, the rupture of these dams generally leads to the release of the retained materials that flow downstream as a wave constituted by a heavy fluid, with devastating and long-term economic, social, and environmental consequences. In recent years, there have been numerous catastrophes due to the collapse of tailings dams. To name just the disasters that have resulted in fatalities recorded in the last eight years: Hpakant (Kachin state, Myanmar) in 2020, Hpakant (Kachin state, Myanmar) in 2019, Brumadinho (Belo Horizonte, Minas Gerais, Brazil) in 2019, Satemu (Kachin state, Myanmar) in 2016, San Kat Kuu (Kachin state, Myanmar) in 2015, Fundao tailings dam Germano mine (Bento Rodrigues Mariana, Brazil) in 2015. For all these reasons, the opening of new mines often finds strong opposition by local communities, as currently is the case in Spain, for example, where a large deposit of rare earths has been discovered. As is well known, rare earths are fundamental for production in the high-tech field as well as for the manufacture of components being essential for ecological transition, such as batteries for electric cars. Currently, 95 percent of the rare earth supply comes from China and, therefore, the field discovered in Spain represents an enormous opportunity for the entire European community from both an environmental and socio-economic point of view. However, the Spanish authorities are unable to have these new mines opened mainly due to the opposition of the local communities who are frightened by the risks that the new tailings dams could pose to the territories concerned.

1.2. Scope and objectives

As mentioned in the opening paragraph, mining activities inevitably produce large quantities of waste materials. They have the consistency of a sludge, and are often stored in structures called tailings dams, or tailings storage facilities (TSF), which can be characterized by a high risk of failure. It is estimated that there are about 3500 active TSFs (Martin & Davies 2000) in the world, in addition to those already closed. These numbers give hints how many territories may be subject to the consequences of a failure of one of these structures, potentially bringing the risk to a global level. There are several causes leading to the collapse of these structures which will be analysed in detail in this thesis. Among them, seismic liquefaction is one of the most frequent causes for both morphological and geotechnical reasons. In general, the morphology is complex and characterized by numerous and steep slopes, and the material is saturated and exhibits the typical behaviour of intermediate non-cohesive contracting soils. These conditions can be particularly prone to trigger liquefaction phenomena. Therefore, in-depth analysis of liquefaction processes is fundamental in mitigating the risk of tailings dam failure and preventing the associated catastrophic consequences. The present thesis aims to investigate in detail the behaviour of tailings storage facilities with regards to seismic liquefaction. The phenomenon will be investigated both in general and by considering a case study situated in southern Tuscany (Italy). The results of the study of the behaviour of the Tuscan tailings dam could be extended

to numerous other TSFs with similar characteristics, therefore being of general interest.

1.3. Methodology

The behaviour of a tailings dam during a seismic event is extremely complicated to examine as it is governed by numerous factors of different nature. First, the geometry and stratigraphy of the site is generally complex. In the simplest cases, there is at least one embankment which retains a settling basin; in more complex cases, there are multiple embankments and complex buried morphologies that make the prediction of the behaviour of the structure highly uncertain. Usually, the area on which the structure is built is not treated in any way and, therefore, the morphological and mechanical characteristics of the foundation soils can significantly affect the stability of the system. Second, tailings are waste that derives from separation from valuable materials. In order to efficiently separate the valuable fraction from the valueless one, the material extracted from the mines must be crushed to dimensions smaller than a tenth of a millimeter. Consequently, tailings have particle diameters comparable to those of fine sands and silts. Resulting from mechanical crushing, the shape of the particles is mostly angular, differing from the rounded or subroundend shape that often found in particles deriving from natural degradation processes. Further elements that influence the behaviour of TSF are the presence and position of the water table, the hydraulic conditions, proximity to constructions, applied loads, etc. It is therefore evident that a global and correct understanding of the performance of a tailings storage facility is anything but simple.

With regards to the case study of the present thesis, several analyses were conducted keeping in mind all the aspects that characterize the structure. First, documents, test certificates, and reports of previous investigations carried out at the site were carefully examined. This made it possible to build a preliminary geotechnical model and to plan subsequent investigations to refine it. With the aid of a digital terrain model (DTM) of great precision, it was possible to identify the most critical morphological areas on which to focus attention. Based on the information gathered, it was therefore possible to plan various exploratory visits and survey campaigns, thereby broadening the knowledge of the structure. The survey campaigns also made it possible to take soil samples from both the settling basin and the dam embankments. Disturbed samples were taken from the settling basins and used to carry out soil classification tests and to make reconstituted samples on which drained and undrained monotonic triaxial tests and undrained cyclic triaxial tests were conducted. Undisturbed frozen samples were also taken from the settling basin using liquid nitrogen and they were tested under undrained cyclic triaxial conditions. Finally, disturbed samples were taken from the dam embankments. Only classification tests were carried out on these, as the coarse size of the material did not allow other types of tests. Also, Electron microscope (SEM) images were acquired from the material extracted from the settling basin. This provided qualitative and quantitative information regarding the shape and mineralogy of the grains.

To evaluate the behaviour of the structure subjected to seismic loads in terms of stresses, strains, accelerations, displacements, and pore water pressures, a numerical model was created and finite element analyses (FEA) were carried out. Different constitutive models were used to describe the mechanical behaviour of the different components of the facility. The constitutive models were calibrated on the results of the laboratory tests and the field investigations performed. Suitable conditions were imposed at the lateral boundaries of the model to simulate free field conditions and at the base of the model to simulate a transmitting base. The initial conditions were determined by simulating the construction of the structure in successive steps, in order to obtain a stress state as close as possible to the real one. This technique also provided a correct evolution of the "memory" parameters of the constitutive models. The seismic inputs were identified through tools supplied by the local authorities and with reference to the regulations in force. The seismic action was assigned to the outcropping bedrock and transferred to the basis of the model though a deconvolution procedure.

1.4. Dissertation outline

As already mentioned, the research topic of this thesis is the analysis of the behaviour of tailings storage facilities with respect to seismic liquefaction. Chapter 2 opens with a description of these facilities reporting the most important characteristics, such as the origin of the tailings and the difficulties in their storage, a description of tailings dams, construction methods and problems related to these structures, and the different types of failure. Then, a review of tailings dam failures is presented by compiling various databases with technical scientific reports and review articles. Furthermore, a possible cause of collapse for some of the events that are defined as unknown by the consulted sources is provided. To conclude Chapter 2, the concepts underlying the phenomenon of seismic liquefaction are briefly described.

Chapter 3 addresses the experimental activity and testing procedures carried out on the various materials involved. First, the procedures used to determine the main physical and index properties are described. Then, a technique developed in the context of this research for taking undisturbed frozen samples using liquid nitrogen is presented. At the end of the chapter, the triaxial equipment, the samples reconstitution method, and the tests performed are described.

Chapter 4 is dedicated to the fundamentals of numerical modelling of tailings dams, starting with a literature review of scientific articles dealing with the topic. The articles cited study tailings dams located more or less all over the world made with different construction techniques that derive from different types of mining cultivations subject to static or dynamic loads analysed with finite element methods in one, two, or three dimensions. The key aspects for the finite element analyses are presented, including boundary conditions, dimensions of the model, initial conditions, types of input, constitutive models, etc. At the end of the chapter, the different types of elements used for the numerical analyses and the calibration of the constitutive models are briefly described.

Chapter 5 is an overview of the case study analysed in this thesis from a historical, geological, hydrogeological, geotechnical, and seismic point of view. Also in this chapter, the procedure used to define the geotechnical model of the structure was described by combining the information obtained from the tests conducted for this thesis with the previous investigations carried out on the facility since 2007. Given their importance in geotechnical numerical analyses, Chapter 6 of this thesis is dedicated to the description and definition of the constitutive models used. Specifically, the different methods to derive the parameters of the different constitutive models adopted in the numerical analysis are depicted. The calibration of the parameters is carried out by comparing the results of the triaxial laboratory tests with the results obtained by simulating these tests with numerical analyses (element test). Chapter 7 describes the numerical model created for the case study, presents the analyses carried out, and provides comments on the results. Finally, chapter 8 is dedicated to the conclusions and comments raised from the work performed.

Bibliography

Calvo, G., Mudd, G., Valero, A., & Valero, A. (2016). Decreasing ore grades in global metallic mining: a theoretical issue or a global reality?. Resources, 5(4), 36.

Global Tailings Portal. (n.d.). Retrieved February 20, 2023, from https://tailing.grida.no/

Guimarães, R. N., Moreira, V. R., Cruz, J. R., Saliba, A. P., & Amaral, M. C. (2022). History of tailings dam failure: Impacts on access to safe water and influence on the legislative framework. Science of The Total Environment, 158536.

ICOLD.: Tailings Dams - Risk of Dangerous Occurrences, Lessons Learnt from Practical Experiences, Bulletin 121, (2001)

Martin, T. E., & Davies, M. P. (2022). Trends in the stewardship of tailings dams. In Tailings and Mine Waste 2000 (pp. 393-407). CRC Press.

US Environmental Protection Agency (EPA) (1994). Design and Evaluation of tailings Dams. Available at https://nepis.epa.gov

Vick, S. G. (1990). Planning, design, and analysis of tailings dams. BiTech Publishers Ltd.

2. Tailings storage facilities and failure mechanisms

Mining activity inevitably leads to the production and consequent management of waste. The problem of managing large quantities of waste began in the nineteenth century with the advent of the second industrial revolution, during which, with the introduction of new technologies, the material extracted from mines increased considerably. Since then, extraction processes have grown, and there are still numerous activities that require the opening of new waste storage sites. One example is the construction of a tailings dam in British Columbia, which, according to the project, will house 440 million tons of waste in 20 years (Klassen & Ngwenya 2015). As mentioned in the Introduction section, among the various existing methods for storing mining waste, the most common is to deposit them in basins, generally held by an embankment. This chapter is devoted to the examination of the characteristics of these complex structures and their failure mechanisms.

2.1. Tailings origin and characteristics

It is essential to know where and how tailings originate to better understand the mechanical behavior of these materials and how close it can be considered to that of non-plastic fine soils (intermediate soils). The main characteristics that tailings receive from the production processes, and which differentiate them from other types of soils, can be traced back to the shape, grain size and oxidative states generated by the flotation processes (Vick 1990; Kossoff et al. 2014). Tailings are the waste part of the ore extracted from a mine. All the ore extracted from the mine is brought to a plant called *mill building*, or simply *mill*. This plant contains numerous machines that crush the rock into small fractions and separate the various elements contained in the rock blocks. Generally, the first process undertaken is *crushing*. Toothed and rotary crushers break the rock up into diameters comparable to those of grains of sand. The product obtained from the crushing process is then introduced to machines called *mills* (hence the name of the plant). The mills are cylinders that contain steel spheres, which, by rotating, crumble the material mixed with water into smaller fractions. The slurry obtained is screened, and the larger fractions go back through the processes described above, while the finer fractions are subjected to a concentration procedure. The concentration procedure consists first of a *flotation process*, which, by means of specific chemical reagents, makes the elements of interest hydrophobic. The hydrophobic elements attach themselves to the air bubbles and form a froth on the surface of the water when the solution passes through tanks with bubbles. The material contained in the froth is collected, thickened, and sent to a *smelter*. The heavier material deposited on the bottom of the tanks during the flotation process is collected and passed back through other flotation processes with different chemicals to extract the different materials. All materials that are not sent to smelting become tailings and are sent to the tailings storage facility in most cases (as described in Chapter 1, in some cases different kinds of storage are used). The processes previously mentioned are general and quite common to most plants (Baba et al. 2012). However, there may be more particular procedures specific to a given extraction method or to a given technology.

From the sequence of the processes undertaken in a mill building (Fig. 2.1) tailings are generally made of angular or sub-angular particles, ranging in size between sand and clay (Kossoff et al. 2014). They are rich in minerals and products (because the processes are unable to totally remove the elements of interest), and often contain the chemical reagents used in the flotation process.

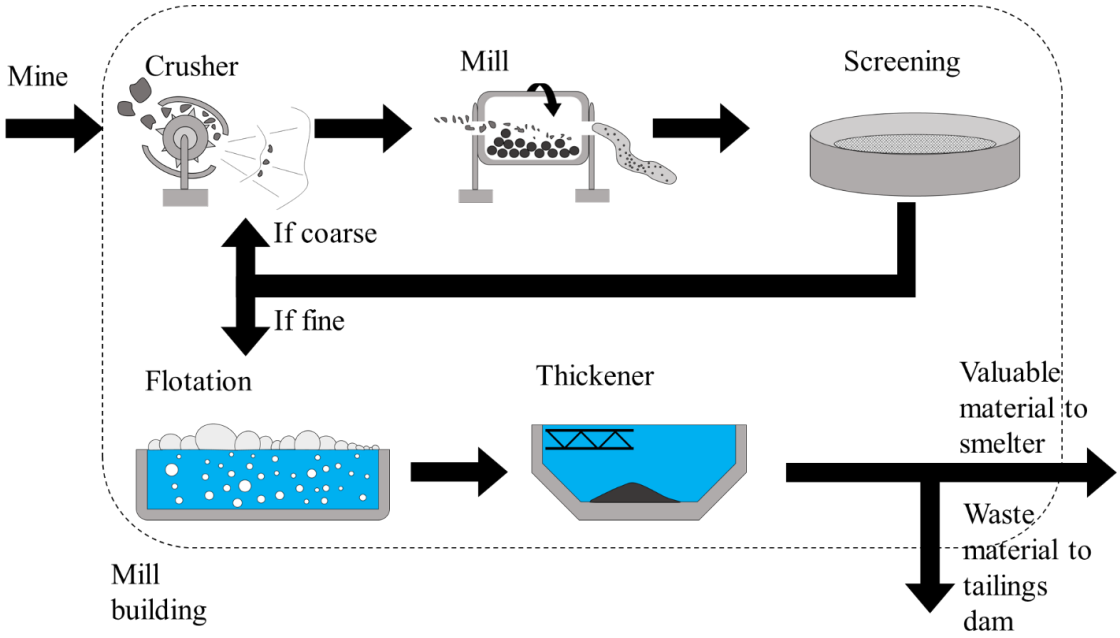

Figure 2.1: *Mill building processes.*

Tailings derive from soils or rocks located all over the planet, so it is difficult to generalize their characteristics, as they originate from different materials. Some studies have attributed tailings with unit weights ranging between 17-18.6 kN/m^3, specific gravity between 1.5-3.3 (Vick 1990; Sarsby 2000; Kossoff et al. 2014), maximum void ratios ranging between 0.72-1.32, and minimum void ratios between 0.52-0.68 (Pettibone & Kealy 1971; Mittal & Morgenstern 1975; Vick 1990). Obviously, the geotechnical characteristics of the tailings vary also (together with the processes of extraction, crushing, processing, etc.) according to the material of interest extracted from the mine (Villavicencio et al. 2011). For example, copper tailings have friction angles that range between 13-40 degrees (Wahler 1974; Volpe 1979; Shamsai et al. 2007; Villavicencio et al. 2011). Characteristics of several types of tailings are described in Table 2.1.

Table 2.1: *Specific gravity, liquid limit, plasticity index, friction angle and undrained shear strength of different types of tailings.*

Tailings	Specific Gravity [-]	Liquid limit [%]	Plasticity index [%]	Friction angle ϕ [°]	Undrained shear strength c_u [kPa]	Source
Coal	1.5-2.4	20-60	0-30	16-24	29-72	Wahler 1973; Busch et al. 1975; Backer et al. 1977; Vick 1990
Lead and Zinc	2.8-3.6			21	0	Soderberg et al. 1977; Vick 1990
Gold and Silver	2.6-3.1			28	0	Hamel & Gunderson 1973; Soderberg et al. 1977
Copper	2.6-3.0	0-30	0-11	13-24	0-96	Mittal & Morgenstern 1976; Volpe 1979
Taconite	3.0-3.4					Vick 1990
Bauxite	2.6-3.1	46	7-9	22	5	Vick 1990
Uranium	2.6-2.8					Vick 1990

The chemical composition of tailings depends on the processes used to extract the valuable materials, the mineralogy of the extraction site, and other manufacturing processes. Several studies have shown that the following elements are almost always present: silica, iron, aluminium, calcium, potassium, magnesium, manganese, sodium, phosphorus, thallium, and sulphur (Kossoff et al. 2014). In some sites, non-negligible quantities of harmful substances, such as arsenic and lead, are often found (David 2003; Hudson-Edwards et al. 2003; Rabinowitz 2005; Meck & Mapani 2006; Kossoff et al. 2014). From a mineralogical point of view, tailings are usually characterized by quartz, sodium potassium, calcium feldspar, sericite, chlorite, calcite, and dolomite (Lottermoser 2007; Rutley 2012; Kossoff et al. 2014). The mineralogy of tailings has an effect on the shear strength of these materials as demonstrated by Geremew & Yanful (2013) and Zhang et al. (2022) where triaxial tests are performed on samples with different clay mineral content.

2.2. Tailings storage

After processing in the mill, tailings are transported to the storage area. Tailings exhibit high densities, and are usually produced in large quantities; therefore, for economic and logistical reasons, the storage area must not be too far from the mill. Moreover, since a large amount of water is used during the extraction of the valuable materials, tailings have the consistency of a slurry. Transporting the slurry to the storage area through pipelines is convenient. Transport systems (pipes, pumps, valves, etc.) must be designed

accordingly with the specific properties of the transported materials, which are characterized by very high unit weight and are very abrasive. When tailings are stored in dam-supported basins, it is preferable to discharge the tailings into the settling pond from multiple points on the crest of the dam in order to obtain a more uniform distribution. Furthermore, in this way, the coarser and heavier particles will deposit near the dam, while the finer and lighter ones will float to the more central points of the basin, favouring filtration processes. The water that forms in the pond is often collected and reused in the mill. It is necessary to build retaining structures in advance, such as dams or embankments, to contain the impounded tailings. If these structures were built similarly to water retention dams, they would have to be raised to their final height before the discharge of the tailings and, similarly to some kinds of water retention dams, these TSFs are characterized by an impervious central nucleus, and coarser material on the banks (Fig. 2.2).

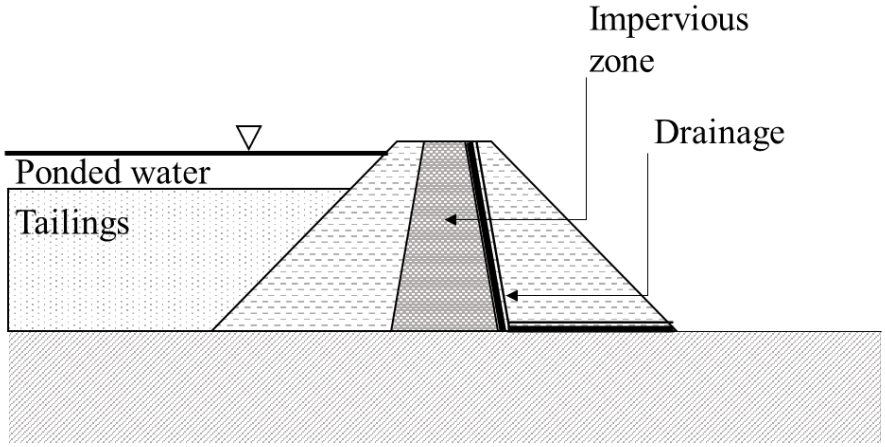

Figure 2.2: *Tailings storage facility with water retention type dam (reworked from Vick 1990).*

Although desirable from a structural point of view, this practice is not often used, mostly for economic reasons since the dam must be completed before the tailings discharge, resulting in a significant initial capital outlay. In addition, the material needed to build the structure must be purchased and transferred to the construction location. For these reasons, tailings storage facilities are commonly made with raised embankments. The building of a raised embankment is usually accomplished in stages. Initially, the so-called 'starter dike' is built, i.e., a bank of a few meters in height formed by materials found in the construction area. The starter dike generally allows the waste materials derived from the mill to be stored for a few years. Once a certain safety margin has been reached, a new bank is built from the crest of the starter dike to increase the height of the containment structure and allow to store additional waste materials. This phase is repeated until the final design height is reached. The embankments can be made with natural borrow soil or pit waste, or with tailings deposited hydraulically or sand tailings from cyclones. This construction method is the most economically advantageous for the stakeholders of the mine. Capital for the construction of the dam does not have to be used immediately, as in the case of a water retention dam. Moreover, by using the waste itself to construct the embankments, purchase and transport costs are eliminated. This construction method is

also very flexible, adapting to the production needs of the mine. There are three main types of raised embankment construction: upstream method, downstream method, and centerline method. They are described in the following paragraphs.

2.2.1. Upstream method

As for all other types of raised embankments, the first stage of the construction of a tailings dam with the upstream method involves the construction of a starter dike (Fig. 2.3), which is usually made with natural borrow material. From the crest of the starter dike, the tailings are discharged into the space upstream of the embankment, which becomes the settling pond. Once the deposited material reaches the crest of the starter dike, a new bank is constructed to raise the elevation of the retention complex (Fig. 2.3). In the area of the pond closest to the dam, a coarser fraction of material is formed due to segregation phenomena and special spigotting or cycloning techniques. This area of the settling basin is generally called the beach. Under regular operating conditions, the beach must not be submerged under settling water. The embankment built after the starter dike can be realized just on the beach, or partly on the beach and partly on the crest of the dike. Subsequent phases of the upstream method repeat as the previous phase each time the impoundment level reaches the top of the highest bank. The advantages of this method are simplicity and flexibility but, above all, low cost because of the less intensive need for machinery and personnel. On the other hand, this type of structure is somewhat fragile and would be better employed in a limited number of well-controlled cases. The factor that most influences the stability of tailings dams made with the upstream method is the position of the phreatic surface within the embankment. Furthermore, these structures are very susceptible to seismic liquefaction phenomena and therefore should not be located in areas with a high seismic risk (Dobry & Alvarez 1967; Castro & Troncoso 1989; Vick 1990; Prakash 1998; Psarropoulos 2005; Verdugo et al. 2012). In any case, to maintain a sufficient degree of safety in this type of structure, it is necessary to keep the beach as large as possible.

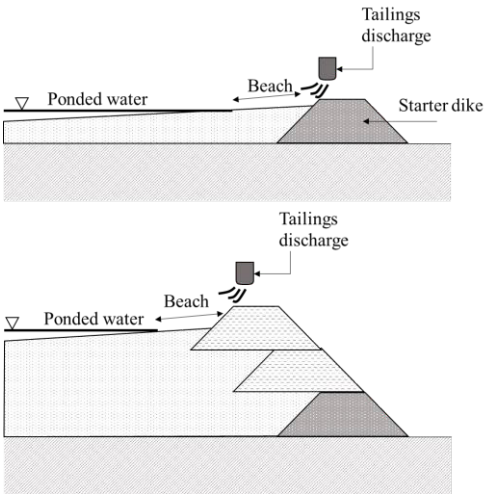

Figure 2.3: *Upstream method (reworked from Vick 1990).*

2.2.2. Downstream method

The downstream construction method also involves the construction of a starter dike made with borrow material. In this case, the subsequent embankments are built by placing them on the downstream slope of the previous embankment (Fig. 2.4). This method allows the planning of the installation of equipment, such as drainage or barriers, to be developed during the construction phases. These practices can avoid to maintain a beach and control the phreatic surfaces within the banks. Downstream dams can have equivalent characteristics to water retention dams. If well designed and well built, tailings dams realized with the downstream method can have a high resistance to liquefaction (Vick 1990). However, their planning and design is not as flexible as for dams built with the upstream method. In addition, since their construction requires much larger volumes of material, these dams are more expensive and rare than the upstream ones.

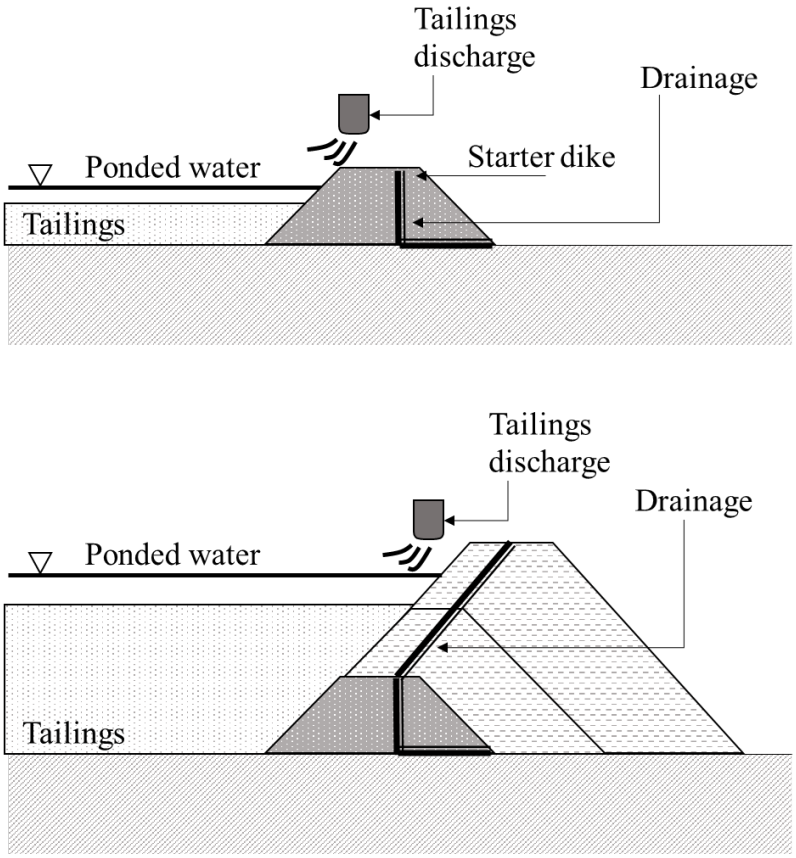

Figure 2.4: *Downstream method (reworked from Vick 1990).*

2.2.3. Centerline method

The centerline method is a combination of the upstream and downstream methods (Fig. 2.5). As in the previous cases, the first phase involves the construction of a starter dike. The subsequent embankments lay partly on the upstream beach (and/or on the crest of the previous embankment), and partly on the downstream slope of the previous embankment. Along with raising the embankments, drainages can be inserted to control the phreatic

surface within the banks. Even if the insertion of beaches is necessary for the support of parts of the embankments, these do not need to be as wide as in the case of the upstream method. Since the saturation line can be kept under control with drainage, and since the layers can be compacted during construction, the seismic resistance of structures realized by this method is quite good. The volumes of material required for construction are between those of the upstream and downstream methods. Another limitation of this construction method, as well as the downstream one, is that the raising of the dam also involves the downstream development of the structure. Therefore, it must be foreseen in the design phase that the development spaces are sufficient and free of obstacles.

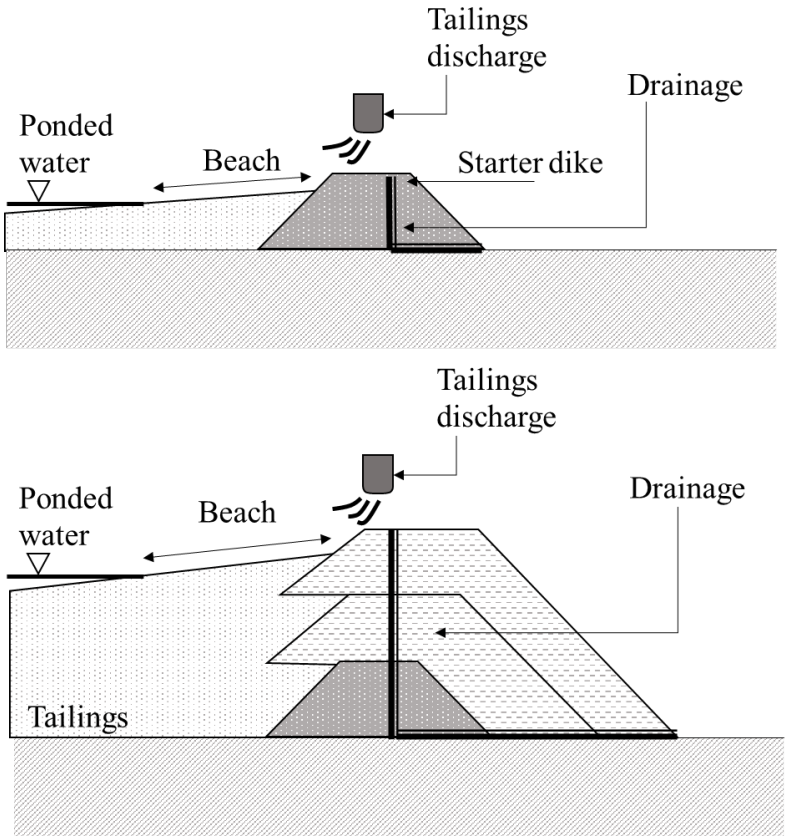

Figure 2.5: *Centerline method (reworked from Vick 1990).*

2.1. Failure mechanisms

In the context of embankments of dams or tailings dams, the term ‘failure’ can be used with different meanings. In the most general sense, it is used to describe the ’inability to achieve a defined performance threshold for a given function (or limit state)’ (Van et al. 2022); however, in some specific contexts, it can also be used to describe the physical collapse or disintegration of a significant part of a structure. The latter definition is used in this section to refer to the failure of a dam retaining tailings, resulting in flooding of the surrounding area, with sometimes catastrophic consequences. The causes of failure are numerous and vary in nature. Different failure mechanisms are described below, paying particular attention to seismic liquefaction. ICOLD 2001 (ICOLD, U. 2001) has classified tailings dams failure mechanisms into nine categories: slope instability (SI),

seepage (SE), foundation (FN), overtopping (OT), structural (ST), earthquake (EQ), mine subsidence (MS), erosion (ER), unknown (U). As tailings storage facilities are often bounded by one or more embankments, the instability of one of these can be a cause of failure. For the slope instability (SI) category, the onset of the movement prior to the instability occurs when, in a shear band, the shear stresses required to maintain equilibrium reach or exceed the available shearing resistance. This event can be triggered by an increase in strength demand (for instance, due to the application of excessive loading at the head of the slope), by a reduction in resistance capacity (for instance, due to a rise in groundwater level), or both. The latter condition occurs, for example, during seismic events. It should be noted, however, that earthquake-induced failure belongs to a different category (EQ). In addition to retaining solid material, tailings dams contain liquids forming the so-called decant pond. It is, therefore, evident that seepage (SE) is present and generally goes from the tailings basins towards the foot of the dam. Seepage in tailings dams can cause three types of problems (Klohn 1979; Clarkson & Williams 2021):

- Piping can occur when the hydraulic gradient (head loss per flow length) is sufficiently large to destabilize the soil particles.
- Slope instability, which can be caused by excess pore water pressures.
- Excessive fluid losses can be highly harmful if the highly contaminated fluids contained in the tailings dams are released into the environment.

Foundation (FN) soil-related factors contributing to the failure of a tailings dam are:

- Inadequate bearing capacity of the foundation soil.
- Permeability: if the foundation soil is almost impervious, conditions of short-term instability can occur. On the other hand, if the soil is highly permeable, the application of the load due to the construction of the TSF can cause relatively fast flows, which can lead to erosion processes.
- Compressibility: if the foundation soil is very compressible, the load transmitted by the structure can cause a lowering of the ground level with even significant differential settlements and failure.

Overtopping (OT) is characterized by a downstream surpass of the mass contained in the tailings pond over the dam crest. A prolonged and massive overtopping can cause external erosion phenomena on the land side of the embankment. Structural (ST) failure can be caused by the rupture of an element of the storage facility, such as a pipeline or drainage, leading to the instability of the dam or part of it. Earthquake (EQ) action has the potential to destabilize the structure by causing cracks, excessive displacements, or pore water pressure build up, potentially leading to soil liquefaction, slope instability and collapse. The induced phenomena depend on the earthquake magnitude and seismic motion conditions, as well as the characteristics of the embankments, tailings, and foundation soils. Mine subsidence (MS) refers to cases in which, for some reason, a cavity suddenly forms in the subsoil, such as a sinkhole, which can consequently affect the stability of the tailings dam. Localized or widespread external or internal erosive (ER) phenomena caused by flows that destabilize the particles of the granular material of which the structure is composed can also lead to the failure of the dam. External erosion refers to erosion at the surface of the land side slope of the embankment due to hydraulic loading. The loading may be due to a discontinuous overtopping or a continuous overflow of the

decant pond over the crest of the embankment, but also to other external forces such as wind, precipitation, etc.

2.3. Failure causes analysis

Information about tailings dam failures are collected in several main databases: ICOLD, WISE, World mine tailings failures-from 1915, and CSP2. Each of these databases has advantages and disadvantages, such as the type and amount of information provided for each disaster, the start date of records, the update of disasters over time, etc. It is not easy to collect all the necessary data in an organized way to draw quantitative and statistical conclusions. Some authors (Rico et al. 2008; Azam & Li 2010; Lyu et al. 2019; Clarkson & Williams 2021; Franks et al. 2021; Piciullo 2022; Stark 2022) have analysed numerous data to obtain information about the type and cause of failures, historical periods in which failures occurred more frequently, geographical areas in which a greater number of disasters occurred or number of collapses in relation to the construction methodology, Rico et al. (2008) compared the number of accidents recorded worldwide and in Europe. They identified different failure mechanisms and causes: foundation instability, slope sliding, overtopping/overflow, mine subsidence, unusual rain fall, snow melt, piping/seepage, seismic liquefaction, structural, unknown, and management operation. According to their analyses, both on a worldwide and European scale, most failures have occurred as a result of meteorological events, namely unusual rain fall and snow melt. The second cause of collapse is the poor management of the facility, particularly poor maintenance of the beach and drainage systems, a too rapid raising of the dam, and the presence of heavy machinery on unstable areas. Finally, the authors point out that, in Europe, no cases of failure due to seismic liquefaction are reported, while worldwide this cause of collapse is encountered in around 14% of all failure cases. An article by Azam & Li (2010) also shows that the main causes of failure are meteorological events and shortcomings in management, and that these have been increasing in recent years. Lyu et al. (2019) analysed five causes of failure: seepage, foundation instability, overtopping, earthquake effects, and others (mine subsidence, structural, external erosion, and slope instability). From their analyses, it emerged that, after “other” (72 cases), the highest number of failures occurred due to seepage (66 cases), followed by overtopping (64 cases), foundation failure (53 cases) and earthquake (52 cases), out of a total of 306 cases analysed. In a study by Piciullo et al. (2022), the classification system for failure cases proposed by ICOLD (2001) was used. From their results, the first cause of failure is overtopping (OT 23%), followed by reasons related to foundations (FN 19%), and slope instability (SI 16%). Also, according to the works by Picullo et al. (2022) and Rico et al. (2008), the percentage of failures due to seismic liquefaction stands at 14%, indicating that there have been no accidents triggered by this process in the last 14 years. A study by Stark et al. 2022 shows that, out of a total of 325 cases investigated, the three most frequent causes of failure are: overtopping (54 cases), earthquake (53 cases), and slope instability (50 cases). From an examination of all the studies cited above, referring to cases all over the world, it is possible to deduce that the most frequent causes of collapse are external meteorological phenomena, poor maintenance, and seismic events, with comparable percentages. From the works of Rico et al. (2008), Lyu et al. (2019), and Piciullo et al. (2011), it can be inferred that upstream dams are the most susceptible to

failure, followed by those built with the downstream method and, finally, by the centerline method.

2.4. Identification of failure causes classified as unknown

Despite the constantly growing attention of the scientific community, mass media and society on TSF failures, numerous causes for collapse are still classified as unknown today. This is due to various factors, including that many accidents, especially in the past, were considered minor and were not disclosed outside the company that managed the mining plant. However, there is also the suspicion that the mining companies do not report many collapses due to the bad publicity that would be created and the legal consequences that could arise (Davies 2002; Kossoff et al. 2014). In this context, in-depth work was performed to investigate numerous sources of information, including newspaper articles, government inquiry reports, technical documents of the companies, seminars handouts and others, with the aim to identify the collapse causes for some events that in the databases have been classified as unknown. The analysis allowed to identify 11 causes of collapse out of 33 cases classified as unknown.

On December 18, 1981, the Ages impoundment facility in Kentucky, United States, collapsed, releasing approximately 3540 cubic meters of waste into the environment, and killing one person. The cause of this event is classified as unknown. In the paper proposing regulations for the storage of coal mining waste disposal, Fitzgerald (1984), mention that failure was caused by a "large quantity of water trapped within the pile". In the notes of the same document, the definition of refuse pile is given as "deposit of coal mine waste which may contain a mixture of coal, shale, claystone, siltstone, limestone, and related materials that are excavated during mining operations or separated from mined coal and disposed of on the surface as waste by-products of either coal mining or preparation operations". From further analysis of the document, it is possible to deduce that there was no adequate plan for designing and maintaining these piles in the collapsed TSF. Therefore, referring to the failure causes proposed by Rico et al. (2008), this collapse can be ascribed to 'management operation'. In 1990 in Ontario, Canada, the Matachewan Mines tailings dam breaching caused severe environmental damage. A local report shows that the cause of this failure is due to overtopping. In 1994, a breach of about 50 m formed on the dike of an inactive pond of the Payne Creek Phosphate Mine in Florida, United States. A report by the US Environmental Protection Agency (EPA) (1997) suggested that a structural weakening of the containment dam caused the collapse. In 1996 in Bolivia, the El Porco tailings dam spilt waste, including toxic elements such as arsenic and lead, into the Pilaya and Pilcomayo river basins. Macklin et al. (1996) attributed the cause of the failure to an important increment in the water influx received by the structure due to rainy events and snow melt. In 2003, the spill of 1.2 million cubic meters of toxic sludge from Brazil's Mineracao Rio Pomba Cataguases plant caused severe environmental damage in the Pomba and Paraíba do Sul rivers. According to Almeida (2015), the poor maintenance of the dam triggered the collapse. The failure of the Partizansk tailings dam in 2004 in Russia could also be attributed to the poor maintenance of the plant (Robinson 2004). In 2008, the ash pond at the Kingston Fossil Plant in Tennessee, USA, broke, spilling about 4.2 million cubic meters of coal ash into the Emory

River. In this case, the cause that triggered the accident lies in foundation problems and excessive dike raising (Moore 2009). In 2011, the Bloom Lake facility in Canada released the equivalent of 20 Olympic-sized swimming pools of waste into the environment. In this case, it appears that the accident occurred due to a design error in the drainage system (La Presse 2012). In 2013, the Obed Dam in Canada failed due to overtopping, releasing approximately 808000 cubic meters of sludge into the environment (Alberta Energy Regulator 2013). In 2017 there was a partial breach of the Tonglvshan Mine tailings pond in the Hubei Province, China, which caused the death of two people. This collapse occurred because illegal mining activities were conducted at the foot of the dam. These activities led to the formation of cavities in the embankment which brought of a part of the structure Mir (2018). In 2017, in South Africa, a V-shaped break formed on the Hernic PGM Project Dam without significant damage. Overtopping was the cause of this accident (Strachan & Robertson 2018).

Table 2.2. summarizes the information about the 11 cases described above, for which the causes of collapse were identified as a part of this PhD research work.

Table 2.2: *Failures originally classified as unknown.*

Year	Name	Country	Ore	Flow Volume [m^3]	Failure cause
1981	Ages	United States	Coal	3540	Management operation
1990	Matachewan	Canada		190000	Overtopping
1994	Payne Creek	United States	Phosphorus	6800000	Structural issue
1996	El Porco	Bolivia	Lead Zinc	1200000	Meteorological
2003	Mineracao Rio Pomba Cataguases	Brazil			Management operation
2004	Partizansk	Russia	Coal	16000	Management operation
2008	Kingston fossil plant	United States	Coal	1200000	Foundation and excessive dike raising
2011	Bloom Lake	Canada	Iron	200000	Structural issue
2013	Obed	Canada	Coal	670000	Overtopping
2017	Tonglvshan Mine	China	Copper gold silver iron	200000	Illegal mining activities
2017	Hernic PGM Project	South Africa	Chrome		Overtopping

2.5. Liquefaction phenomena

Among the collapse mechanisms described by the ICOLD 2001 classification system, no explicit reference is made to seismic liquefaction, but the general case of earthquake collapse (EQ) is cited. However, as reported in the previous section, this cause of collapse

is quite frequent. Moreover, it can produce devastating failures since it is related to a brittle behaviour of the structure. Thus, being sudden, it does not allow to intervene in time to prevent failure. Therefore, it is crucial to pay attention to and investigate this type of process to predict and possibly prevent its catastrophic consequences. Since the primary goal of this study is to analyse the behaviour of tailings dams undergoing seismic liquefaction, it is helpful to briefly recall some well-known fundamental issues here, with reference to the terminology that will be used in the following chapters.

A loose granular soil is characterized by a high percentage of voids and it will tend to reduce in volume if subjected to monotonic shear stress under drained conditions. During the application of the shear force, the soil particles will undergo roto-translating movements on each other, filling up the voids. This behaviour, typical for loose soils, is called “contractive”. On the contrary, if a dense granular soil specimen is subjected to monotonic shear stress under drained conditions, an increase in volume is expected. In this case, the particles that initially are in close contact with each other, tend to separate when subjected to a shearing action. This behaviour, typical of dense soils, is defined as “dilatant”. These behaviours are directly linked to the "state" of the material in relation to a critical (or steady) state for a given void ratio e and confining pressure p'. The critical state of a soil is reached when it deforms at constant confining pressure, shear resistance and volumetric strain. To illustrate these behaviours it referred to Figure 2.6 in which the path of a monotonic undrained (constant-volume) shear test is represented for a dense and a loose sample. If in the initial "state" for a given mean effective stress p'_0 the sample is characterized by a void ratio e_{0L} greater than that on the critical state line e_{0CS}, the material is defined as loose and its behaviour will be “contractive”. In this case, if the sample was subjected to a shear stress under drained conditions it would decrease in volume until it reached the critical state line at e_{0CS}, where, by definition, the volume (and therefore the void ratio) remains constant. Accordingly, under undrained conditions, the pore water pressure would increase with a consequent decrease in mean effective stress until the critical state line is reached. If, instead, in the initial "state" the sample is characterized, with reference to the same mean effective stress p'_0, by a void ratio e_{0D} smaller than that of the critical state, the behaviour will be “dilatant”, with an increase in volume under drained conditions (increase in void ratio up to e_{0CS}) or a decrease in pore pressure and consequent increase in mean effective stress p' under undrained conditions until the critical state is reached.

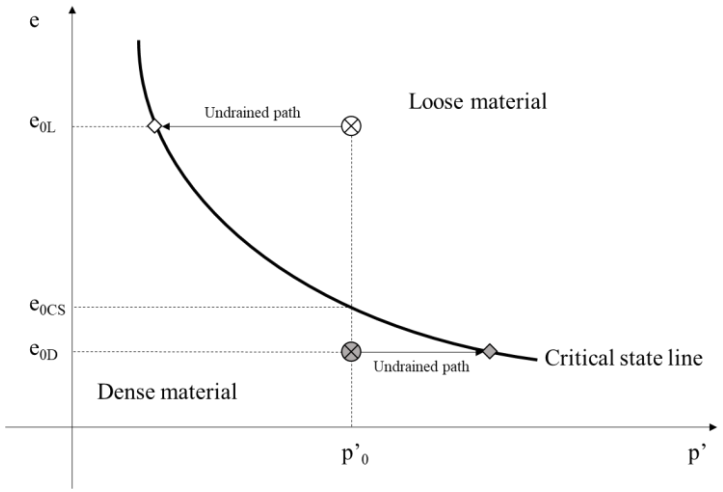

Figure 2.6: *Paths finally reaching the critical state line for a dense and a loose material under undrained monotonic shearing conditions (reworked from Crespellani & Facciorusso 2010).*

Analogously, if a loose saturated non-cohesive soil is subjected to a cyclic shear stress under undrained conditions, such as those occurring under seismic conditions, it will tend to contract. However, the contraction is prevented by undrained conditions and, consequently, the pore water pressures will increase. According to the principle of effective stresses ($\sigma' = \sigma - u$), if the total stresses σ are constant, an increase in pore water pressure u leads to a decrease in effective stresses σ'.

In turn, according to the Mohr-Coulomb failure criterion, a reduction in effective normal stresses on a potential failure surface leads to a reduction in shear strength τ, described by:

$$\tau = \sigma' \tan \phi' \tag{2.1}$$

where ϕ' is the effective friction angle.
If the effective stresses become zero, then the soil completely loses its shearing resistance, and the compound behaves like a suspension of water and solid particles. This collapsed condition is called “liquefaction”. On the other hand, when a dense soil is subjected to a cyclic shear stress under undrained conditions, such as those occurring under seismic conditions, the behaviour is different. Pore water pressures fluctuate widely around an average value and grow very slowly. As a result of these oscillations, when pore water pressures decrease, the effective stresses increase, and therefore, a temporary strength recovery occurs. As the load cycles progress, a process of accumulation of both pore water pressure and irreversible deformations takes place, leading to a decay of strength and, in this case, the failure is related to exceeding an admissible deformation threshold. This type of failure is called “cyclic mobility”.

Figure 2.6 shows the paths of five samples with the same initial void ratio but consolidated at different stresses. Soil samples A and B are below the critical state line in the e-p’ space and therefore their behaviour is “dilatant”. On the other hand, the initial states of specimens C, D and E are above located the critical state line and therefore their behaviour is “contractive”. Observing the q-p' plane in Figure 2.6 (where q is the deviatoric stress) it is possible to note that, since all the samples start from an initial state characterized by the same void ratio e_0, their effective stress paths converge at the same point on the critical state line (which is represented by a line in the q-p’ plane). However, the pathways are very different between dilatant and contractive samples. In fact, the paths of samples A and B show a continuous increase in the deviatoric stress until reaching the critical state line, while samples C, D and E are characterized by paths in which after an initial increase at a certain point the deviatoric stress shows a decay until reaching of the critical state. Connecting the points from which the decay of the deviatoric stress begins, it is possible to obtain the so-called Flow Liquefaction Surface. This surface denotes the liquefaction trigger point or a boundary between stable and unstable behaviour. Samples C, D and E can liquefy only if the stress path exceeds the critical state point, which is why the two regions in figure 2.6 in the q-p' plane are denoted “Flow

liquefaction Susceptible" and "Cyclic Mobility Susceptible". This condition occurs whether the shear stresses are monotonic or cyclic (Vaid & Chern 1983).

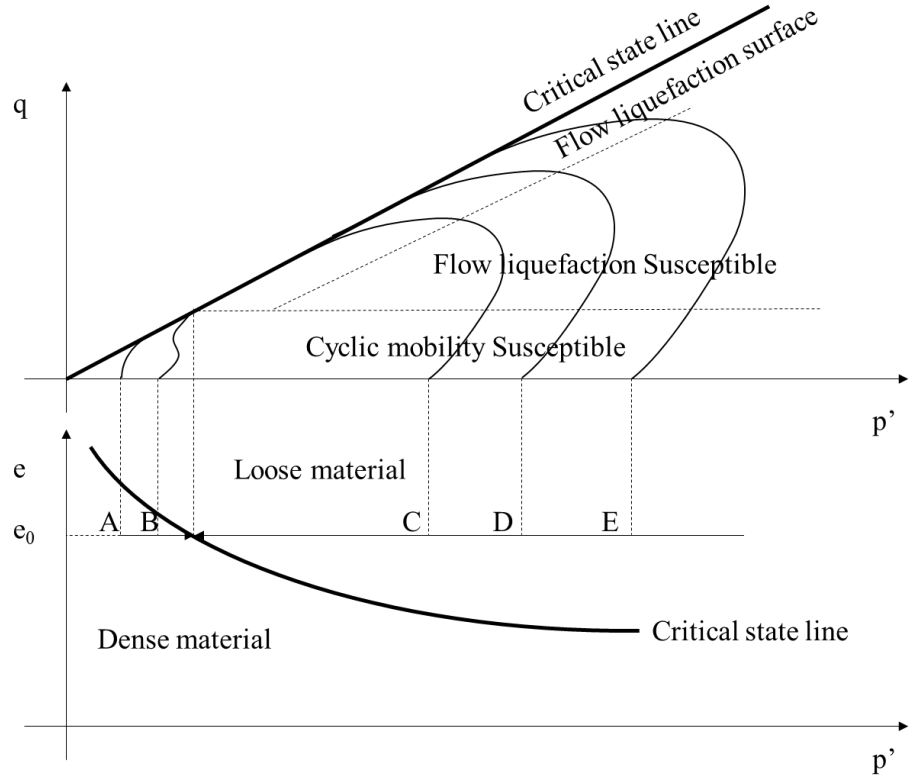

Figure 2.6: *Effective stress paths of five specimens consolidated at different pressures and identification of the Flow Liquefaction Surface (reworked from Crespellani & Facciorusso 2010).*

Consequently, in a given soil, the tendency to generate excess pore water pressure (i.e. contractive or dilatant behaviour) is influenced not only by the density but also by the initial stress conditions. In situ, the shear stresses required for static equilibrium (static shear stresses), also known as 'driving stresses' (as those in bank slopes or foundation soil under tailings dams), are fundamental for the occurrence of two different types of processes under undrained cyclic loading: flow liquefaction and cyclic mobility. Flow liquefaction can occur in potentially liquefiable soils when the static shear stress q_S is greater than the undrained shear strength S_u of the soil. In the opposite case, when q_S is smaller than S_u, the material behaviour is rather stable, and collapse occurs with rather high mean effective stress. This type of collapse can be traced back to cyclic mobility. A particular case of cyclic mobility is known as 'level ground liquefaction' which occurs when static driving stresses are absent and very high excess pore pressure is attained. In some cases, this phenomenon produces "spectacular" manifestations such as surface bubbling or jets of water and sand.

At the microelement scale, for discrete materials in which the forces transmitted between the particles are frictional, liquefaction is a process governed, by the principle of effective stresses and dilatancy. To better understand the mechanism referred to Figure 2.7 which represents a simple experiment in which water and a non-cohesive granular material are

present inside a container. The granular material is deposited on a scale plate placed inside the container which therefore measures only the mass of the granular material and therefore the effective stresses. A pressure gauge connected to the container allows to measure the pressure of the water in the container. An external balance measures the mass of the entire system (and therefore the total stresses) which, being closed, remains constant during the experiment. The granular material in the tank must be loose so that it exhibits a contractive behaviour. Prior to liquefaction (Figure 2.7 a) the particles although loose are in contact to each other and therefore the scale in the container measures a certain pressure. During liquefaction (Figure 2.7 b) the particles are lose and float in the water. Therefore, the scale in the container doesn't register any pressure while the water pressure has increased reaching the total pressure value. After liquefaction and reconsolidation (Figure 2.7 c) the water pressure has returned to its initial value and the granular particles have got back in contact restoring the initial effective pressure. After liquefaction the particles compact resulting in a denser state with respect to the state before liquefaction.

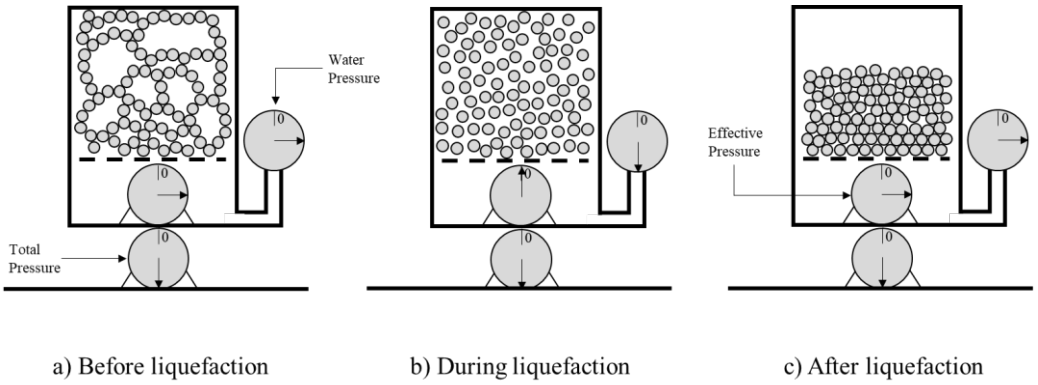

Figure 2.7: *Scheme of the mechanism of cyclic liquefaction (reworked from Ishihara 1985).*

It is evident that during a seismic event a soil exhibits significant deformations and the shear strains exceed the so-called volumetric threshold γ_{tv} for which the soil behaviour is markedly non-linear and, in undrained conditions, an accumulation of pore water pressures starts (Vucetic & Dobry 1988). Based on the above considerations, the triggering of flow liquefaction can occur under specific conditions which are: contractive behaviour; exceeding the volumetric shear strain; number of loading cycles sufficient to achieve the reduction of the effective pressures and, consequently, the resistance below the value required for static equilibrium; partial or complete alternation of cyclic loads; stress paths with maximum deviatoric stresses surpassing the undrained shear strength (Crespellani & Facciorusso 2010).

2.6. Seismic liquefaction failure case history

The first reported failure of a tailings dam by seismic liquefaction is the Barahona disaster, which occurred in Chile in 1928 following the 1928 Talca earthquake. Troncoso et al. (1993) attributed this failure to the dam's construction with the upstream method, which allowed the impoundment slimes to seep through the dikes. These pockets of slimes, which had not enough time to consolidate, represented a substantial weakening of

the whole structure during cyclic loading under undrained conditions. During the earthquake, the liquefaction of some areas inside the impoundment increased the driving forces, while the shear strength decreased to a minimum residual value, and the safety factor became less than one with the consequent collapse of the system. The dam collapse destroyed urban and rural settlements and crops and killed 54 people. In 1965 in Chile, following an earthquake of magnitude 7.5, 9 tailings dams failed due to seismic liquefaction. Each failure caused significant destruction to the affected territories, but the collapse of the new and old El Cobre dams caused the most devastating damage. This dam was composed of uncompacted sands with an outer bank slope of approximately 35 degrees. Following the rupture of the embankment, about 2,400,000 tons of tailings flowed downstream for about 12 km, destroying the village of El Cobre and killing 200 people (Dobry & Alvarez 1967).

In 1978 the Izu-Ohshima-Kinkai earthquake with magnitude 7 caused the collapse of two tailings dams at the Mochikoshi gold mine. The two dams, called Dike No. 1 and Dike No. 2, failed in sequence. One dam collapsed practically immediately after the main shock, while the other failed the day after when no ground movements caused by aftershocks were recorded. Okusa & Maikuma (1980) attributed the failure of Dike No. 1 to the pressure on the dam triggered by the liquefaction at a depth of 6-8 m of the tailings contained in the settling pond. Regarding the failure of Dike No.2, which collapsed about 24 hours after the main shock, Ishihara (1984) explained that following the earthquake, the soil in the pond liquefied, but not the material forming the embankment. However, the increment in pore water pressure exerted by the liquefied tailings created a seepage imbalance in the underlying deposits. In the hours following the earthquake, this process led to an increase in the phreatic level within the embankment with a consequent reduction of the safety factor until collapse was observed.

On February 27, 2010, an earthquake of magnitude 8.8 hit Chile offshore of the Maule Region. This earthquake was the sixth most powerful earthquake recorded since 1900 up to that date. The consequences of this earthquake were devastating and the failure of two tailings dams due to liquefaction was among the numerous catastrophic events. The Las Palmas dam was closed in 1997 and covered by a layer of clayey soils. Its collapse killed four people. This structure is located near the city of Pencahue at a distance of 133 km from the earthquake's epicentre. A layer of the dike with a high degree of saturation, which was not identified until after the collapse, liquified during the earthquake (Villavicencio 2014). The same earthquake caused the collapse of the Adosado dam, 271 km from the epicentre. In this case, the embankment had been built with the downstream method with a poor compaction degree. A high degree of saturation was identified in the dike, probably due to an inadequate beach extension and also due to a sprinkler system that sprayed water on the plant to prevent dust buildup. Following this discovery, measures were taken to lower the water table. This was not enough to prevent the structure from collapsing; however, it is believed that the consequences could have been much more serious if they had not been taken (Villavicencio 2014).

One of the best-known failures that happened in recent years is that of Fundao's (Brazil) Tailings Dam in 2015. Following the disaster, a commission of experts was set up to determine the cause of the failure. The commission concluded that flow liquefaction was triggered by an extrusion of slimes during the construction of the embankment. This extrusion or lateral spreading of the slimes involved a change in the stress state of the

system with a loss of confinement. However, the commission also concluded that a small earthquake that occurred shortly before the collapse accelerated the pore water pressure build-up process that triggered the liquefaction (Morgenstern et al. 2016). Sadrekarim et al. (2020) attributed the cause of the collapse exclusively to static liquefaction; however, the doubt remains as a shock was recorded shortly before the event, albeit small, and testimonies of operators present on the site speak of having warned of the shockwaves.

The cases described in the previous pargraphs are the most important and best described cases of failure by the scientific and technical literature. A joint analysis of various databases articles and reports emerged that the number of failures of tailings storage facilities due to seismic liquefaction is 25 out of 202 (total number of failures) more than 8 %. They are listed in Table 2.3, while Figure 2.8 shows the number and countries in which accidents due to seismic liquefaction have occurred.

Table 2.3: *Failures caused by seismic liquefaction.*

Year	Name	Country	Construction method	Ore	Flow Volume [m^3]
2015	Germano mine	Brazil	Upstream	iron	32000000
2010	Las Palmas	Chile	Downstream		170000
2010	Adosado	Chile	Downstream		
1997	Almendro	Chile	Upstream		
1997	Algarrobo	Chile	Upstream	iron	
1997	Maitén	Chile	Upstream		
1997	Planta La	Chile	Upstream and centerline		60000
1996	Amatista, Nazca	Peru	Upstream		300000
1985	Veta de Agua No.1	Chile	Upstream and centerline	copper	280000
1985	Cerro Negro No.4	Chile	Upstream and centerline	copper	500000
1981	Veta del Agua No. 2	Chile	Upstream		
1978	Mochikoshi Dike No.1	Japan	Upstream	gold	80000
1979	Mochikoshi Dike No.2	Japan	Upstream	gold	
1968	Hokkaido	Japan	Upstream	lead and zinc	90000
1965	El Cobre New Dam	Chile	Upstream	copper	350000
1965	El Cobre Old Dam	Chile	Upstream	copper	1900000
1965	La Patagua New Dam	Chile	Upstream	copper	35000
1965	Cerro Negro No. 3	Chile	Upstream	copper	85000

Year	Name	Country	Construction method	Ore	Flow Volume [m^3]
1965	Bellavista	Chile	Upstream	copper	70000
1965	Los Maquis 3	Chile	Upstream	copper	21000
1965	El Sauce 1	Chile	Upstream		
1965	Ramayana	Chile	Upstream	copper	156
1965	Hierro Viejo	Chile	Upstream	copper	800
1962	Almivirca	Peru	Upstream	copper, silver, lead and zinc	
1928	Barahona	Chile	Upstream	copper	2800000

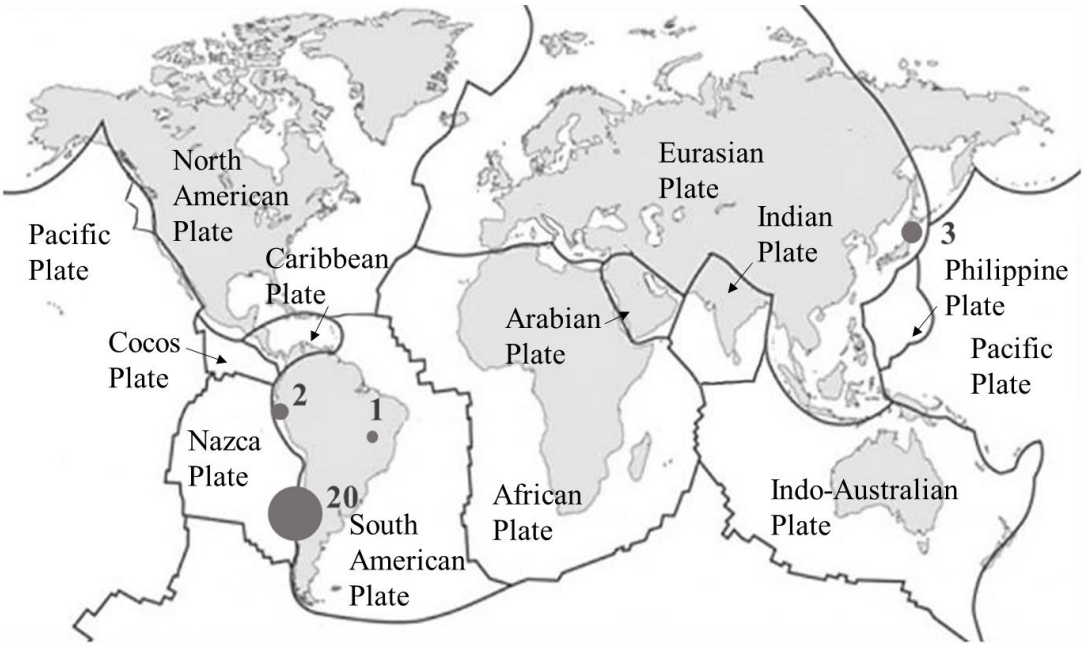

Figure 2.8: *Number of failures of tailings storages facilities caused by seismic liquefaction in the world*.

From the data in Table 2.3 and Figure 2.8, it is evident that Chile is the country most affected by the collapse of tailings dams due to seismic liquefaction, where 19 cases out of the 25 reported occurred. This is probably due to the fact that Chile is a highly seismic territory with an important mining industry. Almost all of the collapses (19 out of 25) occurred in structures built with the upstream method and in 3 cases in structures built with a hybrid technique between the upstream and the centerline methods. In Figure 2.9 is represented an histogram with the number of seismic liquefaction failures for construction types in the four countries where they occurred.

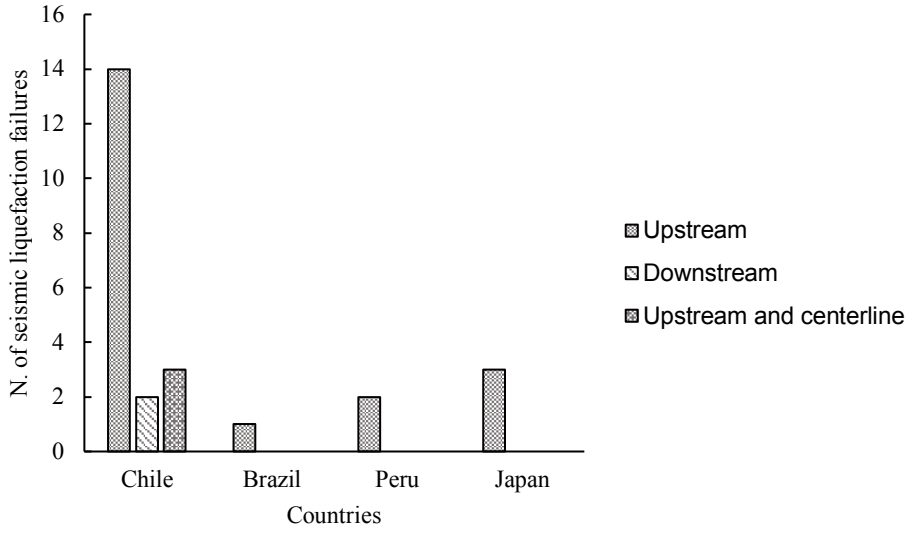

Figure 2.9: *Histogram representing the failure due to seismic liquefaction for different construction types in the different countries where they occurred.*

2.7. Methods to reduce risks and consequences induced by liquefaction

One of the main purposes of a designer or manager of tailings storage facilities is to reduce as much as possible (always aware that it is impossible to completely eliminate the risk) the possibility of failure of the structure. In this section, special attention has been paid to the risk of failure due to liquefaction. As suggested by several authors (Klohn 1979; Vick 1990; Adams et al. 2017; Rodríguez et al. 2021; Araruna et al. 2022; Boschi et al. 2022), the most direct way to mitigate liquefaction risk in a tailings dam is to minimize the presence of water in the materials. Rodríguez et al. (2021) have stated that the risk of liquefaction in tailings occurs for saturation levels greater than or equal to 80%, and that it is necessary to keep the saturation below this threshold. In a tailings facility, the presence of water can derive from the tailing pond, water used to transport the material in the construction processes (cyclone water or spigotted water), water that escapes during the consolidation of the materials, rainwater, and the possible presence of groundwater (Klohn 1979). One of the most effective systems for keeping seepage under control in the dam body is to move the tailing pond as far away as possible from the embankment by increasing the length of the beach. This can be arranged in the design phase by attributing adequate dimensions to the various components of the structure. However, this method requires that large storage volumes are not used, resulting in a loss of efficiency of the plant and an increase in management costs. Removal of water via drains and filters or pumping systems is often preferred. Drainage systems generally consist of appropriately sized pipes that are able to collect and transport water away from liquefaction risk areas. These pipes must be made with appropriate materials capable of resisting the geostatic loads of the basin and the embankment and flexible enough to withstand deformation caused by the consolidation of the materials. Filter pipes, which are pipes filled with coarse material, are often used. This economical technique provides an increase in the resistance of the pipes. However, attention must be paid to the sizing of the void spaces left by the fill material, which could clog and inhibit water flow. The design of drainage systems in tailings dams is more complex than that for hydraulic retention dams, as it

must also take into account the growing phases of the embankment over time, which can last several years. Rodríguez et al. (2021) recommended providing two drainage systems: one dedicated to the removal of basin water and another for the foundation layers. Another important aspect is surface water runoff. In fact, an adequate surface water disposal system quickly removes rainwater, which therefore does not have time to infiltrate the materials, which would increase the degree of saturation. Following the closure of the structure, it is advisable to provide an adequate capping system. This measure also reduces the infiltration of surface water. In general, capping is achieved by laying a layer of impervious soil over the basin area. If the PH of the soil is not lower than 5.5, the basin area can be reforested (Rodríguez et al. 2021). Vegetation "captures" a significant part of the rainwater through the foliage, reducing infiltration. Another way to reduce the water in the pores is to replace it with other materials through grouting processes. Boschi et al. (2022) proposed an innovative grouting technique with colloidal siliceous materials demonstrating the effectiveness of this technique through numerical simulations. Another innovative technique for reducing the degree of saturation of tailings has been proposed by Araruna et al. (2022) through electrokinetic dewatering. This technique was tested on samples of material from the Germano Mining Complex (Brazil), with promising results according to the authors.

In addition to the aforementioned "direct" solutions to mitigate liquefaction risk, there are "indirect" solutions that contribute to safety and prevention plans that can be decisive in situations of danger. If the morphological conditions in which the structure is located allow it, the territories located downstream of the tailings dam could be protected through the creation of a second containment structure that prevents the flow from advancing. This solution involves the loss of large spaces otherwise usable by the mining company and is generally implemented by governments to protect populations that could be affected by the collapse of the dam. Nowadays, with the development of new technologies, it is possible to control and monitor the situation of a given structure in real time both during the construction phase and following closure. In particular, during the construction phase, it is important to monitor the deposition rate and consistency of the materials in order to check that they are in line with what is foreseen by the project and the regulations. Piezometers, inclinometers, and pressure gauges, especially if connected to a continuous monitoring system, are fundamental tools for controlling the groundwater level, deep movements, and changes in water pressure in drainage systems. Another fundamental tool for the correct monitoring of a tailings dam are seismic sensors. These sensors are useful because they can give an early warning if a seismic shock is recorded that can cause the collapse of the structure, but they can also detect waves caused by explosions in the nearby mine. Surface movements of the facility can be monitored through LiDAR, InSAR, and total station automation systems. LiDAR is a system that uses laser scanners to map surfaces. Through the comparison of mappings recorded at different times it is possible to measure any movements. InSAR is capable of making subcentimeter measurements from a satellite. Total station automation surveys measure the position of targets placed on the body of the dam via one or more total stations over time. The comparison of the information obtained through LiDAR, InSAR, and total automation systems accurately controls the presence of total or differential movements of the structure.

2.8. Chapter conclusions

From the topics covered in this chapter it is already possible to draw conclusions about tailings dams. They are structures created to contain waste deriving from mining processes which in the majority of cases are made exclusively with earthy materials or materials deriving from mining processes. The tailings are particular materials that differ from soils of natural origin in terms of shape, mineralogy, composition and mechanical behaviour. The containment structure itself (which should guarantee the safety of the plant in relation to the surrounding territories) is made with these waste materials. That they are structures particularly susceptible to failure and a very frequent cause of collapse is attributable to seismic liquefaction phenomena. Dam structures built using the upstream method are the most susceptible to seismic liquefaction failure. Therefore, the topic of seismic liquefaction in upstream tailings dams is of primary importance for the safety and prevention linked to these facilities.

Bibliography

Adams, A., Friedman, D., Brouwer, K., & Davidson, S. (2017, July). Tailings impoundment stabilization to mitigate mudrush risk. In Proceedings of the 85th Annual Meeting of the International Commission on Large Dams (ICOLD).

Alberta Energy Regulator (aer). (2013). Investigation Summary Report 2013-006: Coal Valley Resources

Almeida B. (2015, November 6). Em Cataguases, barragem rompida foi desativada após acidente em 2003. Zona Da Mata. https://g1.globo.com/mg/zona-da-mata/noticia/2015/11/em-cataguases-barragem-rompida-foi-desativada-apos-acidente-em-2003.html

Araruna Jr, J. T., Sanchez, R. M., Qi, X., Wang, H., Liu, S., de Souza, R. F. M., & Manhães, P. M. B. (2022). A Promising Approach to Mitigate Risks on the Existing Tailings Dams in Brazil. Bulletin of Environmental Contamination and Toxicology, 109(1), 44-50.

Azam, S., & Li, Q. (2010). Tailings dam failures: a review of the last one hundred years. Geotechnical news, 28(4), 50-54.

Baba, A. A., Ayinla, K. I., Adekola, F. A., Ghosh, M. K., Ayanda, O. S., Bale, R. B., … & Pradhan, S. R. (2012). A review on novel techniques for chalcopyrite ore processing. International journal of mining engineering and mineral processing.

Backer, R. R., Busch, R. A., & Atkins, L. A. (1977). Physical properties of western coal waste materials (Vol. 8216). Department of the Interior, Bureau of Mines.

Boschi, K., Arroyo Alvarez de Toledo, M., Burbano Barzallo, D. A., & Spagnoli, G. (2022). Permeation grouting of an upstream tailing dam: a feasibility study. In Tailings and Mine Waste'22: Proceedings of the 26th International Conference on Tailings and Mine Waste (pp. 59-70). University of British Columbia (UBC).

Busch, R. A. (1975). Physical property data on fine coal refuse (Vol. 8062). US Department of the Interior, Bureau of Mines.

Castro, G., & Troncoso, J. (1989, August). Effects of 1985 Chilean earthquake on three tailings dams. In 5th Chilean Conference on Seismology and Earthquake Engineering, Santiago, Chile.

Clarkson, L., & Williams, D. (2021). An overview of conventional tailings dam geotechnical failure mechanisms. Mining, Metallurgy & Exploration, 38(3), 1305-1328.

Crespellani, T., & Facciorusso, J. (2010). Dinamica dei terreni per le applicazioni sismiche. Dario Flaccovio Editore.

David, C. P. (2003). Heavy metal concentrations in growth bands of corals: a record of mine tailings input through time (Marinduque Island, Philippines). Marine Pollution Bulletin, 46(2), 187-196.

Davies, M. P. (2002). Tailings impoundment failures are geotechnical engineers listening? GEOTECHNICAL NEWS-VANCOUVER-, 20(3), 31-36.

Dobry, R., & Alvarez, L. (1967). Seismic failures of Chilean tailings dams. Journal of the Soil Mechanics and Foundations Division, 93(6), 237-260.

FitzGerald, T. J. (1984). Federal Regulation of Coal Mine Waste Disposal: A Blueprint for Disaster. West Virginia Law Review, 86(3), 14.

Franks, D. M., Stringer, M., Torres-Cruz, L. A., Baker, E., Valenta, R., Thygesen, K., ... & Barrie, S. (2021). Tailings facility disclosures reveal stability risks. Scientific reports, 11(1), 5353.

Geremew, A. M., & Yanful, E. K. (2013). Dynamic properties and influence of clay mineralogy types on the cyclic strength of mine tailings. International Journal of Geomechanics, 13(4), 441-453.

Hamel, J. V., & Gunderson, J. W. (1973). Shear strength of Homestake slimes tailings. Journal of the Soil Mechanics and Foundations Division, 99(5), 427-432.

Hudson-Edwards, K. A., Macklin, M. G., Jamieson, H. E., Brewer, P. A., Coulthard, T. J., Howard, A. J., & Turner, J. N. (2003). The impact of tailings dam spills and clean-up operations on sediment and water quality in river systems: the Ríos Agrio–Guadiamar, Aznalcóllar, Spain. Applied Geochemistry, 18(2), 221-239.

ICOLD, U. (2001). Tailings dams–risk of dangerous occurrences, lessons learnt from practical experiences (bulletin 121). Commission Internationale des Grands Barrages, Paris, 155.

Ishihara, K. (1984). Post-earthquake failure of a tailings dam due to liquefaction of pond deposit.

Ishihara, K. (1985). Stability of natural deposits during earthquakes. In Proceedings of the 11th international conference on soil mechanics and foundation engineering. AA Balkema Publishers.

Klassen, C. & Ngwenya, E. (2015). Environmental Assessment Certificate Application / Environmental Impact Statement for a Comprehensive Study. Norwest Corporation

Klohn, E. J. (1979, May). Seepage control for tailings dams. In Proceedings, First International Conference on Mine Drainage, Miller Freeman Publications, San Francisco, CA.

Klohn, E. J. (1979, May). Seepage control for tailings dams. In Proceedings, First International Conference on Mine Drainage, Miller Freeman Publications, San Francisco, CA.

Kossoff, D., Dubbin, W. E., Alfredsson, M., Edwards, S. J., Macklin, M. G., & Hudson-Edwards, K. A. (2014). Mine tailings dams: Characteristics, failure, environmental impacts, and remediation. Applied Geochemistry, 51, 229-245.

Lottermoser, B. (2007). Mine wastes (pp. 43-118). Springer-Verlag Berlin Heidelberg.

Lyu, Z., Chai, J., Xu, Z., Qin, Y., & Cao, J. (2019). A comprehensive review on reasons for tailings dam failures based on case history. Advances in Civil Engineering, 2019, 1-18.

Macklin, M. G., Payne, I., Preston, D., & Sedgwick, C. (1996). Review of the Porco mine tailings dam burst and associated mining waste problems, Pilcomayo basin, Bolivia. Report to the UK Overseas Development Agency, 33.

Meck, M., Love, D., & Mapani, B. (2006). Zimbabwean mine dumps and their impacts on river water quality–a reconnaissance study. Physics and Chemistry of the Earth, Parts A/B/C, 31(15-16), 797-803.

Mine de fer du lac Bloom : déversements à répétition. (2012, September 22). La Presse. https ://www.lapresse.ca/environnement/pollution/201209/22/01-4576586-mine-de-fer-du-lac-bloom-deversements-a-repetition.php

Mir, F. (2018). China Daye racks up 45.2M yuan loss from Tonglvshan mine dam failure. S&P Global Homepage | S&P Global. https://www.spglobal.com/marketintelligence/en/newsinsights/trending/jp1y9bqovwmxltbbmztxgg2

Mittal, H. K., & Morgenstern, N. R. (1975). Parameters for the design of tailings dams. Canadian Geotechnical Journal, 12(2), 235-261.

Mittal, H. K., & Morgenstern, N. R. (1976). Seepage control in tailings dams. Canadian Geotechnical Journal, 13(3), 277-293.

Mogami, T. (1953). The behavior of sand during vibration. In Proc. 3rd ICSMFE (Vol. 1, pp. 152-155).

Moore R. W. (2009). Review of the Kingston fossil plant ash spill root cause study and observations about ash management. Inspection Report. Tennessee Valley Authority Office of the Inspector General

Morgenstern, N. R., Vick, S. G., Viotti, C. B., & Watts, B. D. (2016). Fundão tailings dam review panel report on the immediate causes of the failure of the Fundão dam. Cleary Gottlieb Steen & Hamilton LLP, New York.

Okusa, S., Anma, S., & Maikuma, H. (1980, September). Liquefaction of mine tailings in the 1978 Izu-Ohshima-Kinkai earthquake, central Japan. In Proceedings of the 7th World Conference on Earthquake Engineering, Istanbul, Turkey (pp. 8-13).

Pettibone, H. C., & Kealy, C. D. (1971). Engineering properties of mine tailings. Journal of the Soil Mechanics and Foundations Division, 97(9), 1207-1225.

Piciullo, L., Storrøsten, E. B., Liu, Z., Nadim, F., & Lacasse, S. (2022). A new look at the statistics of tailings dam failures. Engineering Geology, 303, 106657.

Prakash, S. (1998). Liquefaction of silts and silt-clay mixtures. Geotech. Engrg. And Soil Dynamics III, Geotech. Special Publication (75), ASCE, 1, 385-397.

Psarropoulos, P. N., Tsompanakis, Y., Karabatsos, Y., Xiroudakis, G., & Sarris, E. (2005, September). Stability of tailings dams–Part II: dynamic loading. In International Workshop in Geoenvironment and Geotechnics (pp. 37-44).

Rabinowitz, M. B. (2005). Lead isotopes in soils near five historic American lead smelters and refineries. Science of the Total Environment, 346(1-3), 138-148.

Rico, M., Benito, G., Salgueiro, A. R., Díez-Herrero, A., & Pereira, H. G. (2008). Reported tailings dam failures: a review of the European incidents in the worldwide context. Journal of hazardous materials, 152(2), 846-852.

Robinson, P. (2004). Partizansk coal ash dam break and spill observation. Southwest Research and Information Center.

Rodríguez, R., Munoz-Moreno, A., Caparrós, A. V., Garcia-Garcia, C., Brime-Barrios, A., Arranz-González, J. C., ... & Alcolea, A. (2021). How to prevent flow failures in tailings dams. Mine Water Environ, 40(1), 83-112.

Rutley, F. (2012). Rutley's elements of mineralogy. Springer Science & Business Media.

Sadrekarimi, A., & Riveros, G. A. (2020). Static liquefaction analysis of the Fundão dam failure. Geotechnical and Geological Engineering, 38, 6431-6446.

Sarsby, R. W. (2000). Environmental geotechnics. Thomas Telford.

Seed, H. B. (1982). Ground motions and soil liquefaction during earthquakes. Earthquake engineering research insititue.

Shamsai, A., Pak, A., Bateni, S. M., & Ayatollahi, S. A. H. (2007). Geotechnical characteristics of copper mine tailings: a case study. Geotechnical and geological engineering, 25, 591-602.

Soderberg, R. L., & Busch, R. A. (1977). Design guide for metal and nonmetal tailings disposal (Vol. 8755). Department of the Interior, Bureau of Mines.

Stark, T. D., Moya, L., & Lin, J. (2022). Rates and Causes of Tailings Dam Failures. Advances in Civil Engineering, 2022.

Strachan, C., & Robertson, J., C. (2018). Tailings facility performance 2017 and 2018. Tailings & Mine Waste 2018.

Tailings dam safety. WISE Uranium Project – Tailings Dam Safety. (n.d.). Retrieved March 23, 2023, from https://www.wise-uranium.org/indexm.html

Troncoso, J. H., Vergara, A., & Avendaño, A. (1993, June). The seismic failure of Barahona tailings dam. In 3rd International Conference on Case Histories in Geotechnical Engineering (pp. 1473-1479).

TSF failures from 1915. CSP2. (n.d.). Retrieved March 23, 2023, from http://www.csp2.org/tsf-failures-from-1915

US Environmental Protection Agency (EPA) (1997). US Environmental Protection Agency, Office of Solid Waste (62 summaries illustrating recent mining and mineral processing damage cases in a variety of mineral commodity sectors and states, including several tailings dam failures). Washington DC.

Vaid, Y. P., & Chern, J. C. (1983). Effect of static shear on resistance to liquefaction. Soils and foundations, 23(1), 47-60.

Van, M.A., Rosenbrand, E., Tourment, R., Smith, P. and Zwanenburg, C. (2022, February) Failure paths for levees. International Society of Soil mechanics and Geotechnical Engineering (ISSMGE) – Technical Committee TC201 'Geotechnical aspects of dikes and levees',. https://doi.org/10.53243/R0006

Verdugo, R., Sitar, N., Frost, J. D., Bray, J. D., Candia, G., Eldridge, T., … & Urzua, A. (2012). Seismic performance of earth structures during the February 2010 Maule, Chile, earthquake: dams, levees, tailings dams, and retaining walls. Earthquake Spectra, 28(1_suppl1), 75-96.

Vick, S. G. (1990). Planning, design, and analysis of tailings dams. BiTech Publishers Ltd..

Villavicencio, A. G., Breul, P., Bacconnet, C., Boissier, D., & Espinace, A. R. (2011). Estimation of the variability of tailings dams properties in order to perform probabilistic assessment. Geotechnical and Geological engineering, 29, 1073-1084.

Villavicencio, G., Espinace, R., Palma, J., Fourie, A., & Valenzuela, P. (2014). Failures of sand tailings dams in a highly seismic country. Canadian geotechnical journal, 51(4), 449-464.

Volpe, R. (1979). Physical and engineering properties of copper tailings, Current geotechnical practice in mine waste disposal, ASCE, 242–260.

Vucetic, M., & Dobry, R. (1988). Cyclic triaxial strain-controlled testing of liquefiable sands. In Advanced triaxial testing of soil and rock. ASTM International.

Wahler (WA) & Associates. (1973). Analysis of Coal Refuse Dam Failure: Middle Fork Buffalo Creek, Saunders, West Virginia (Vol. 2).

Wahler WA, and Assoc. (1974) Evaluation of mill tailings disposal practices and potential dam stability problems in Southwestern United States. U.S. Bureau of Mines, OFR50(1)-75–OFR50(5)-75.

World mine tailings failures-from 1915. World Mine Tailings Failuresfrom 1915. (n.d.). Retrieved March 23, 2023, from https://worldminetailingsfailures.org/

Zhang, C., Pan, Z., Yin, H., Ma, C., Ma, L., & Li, X. (2022). Influence of clay mineral content on mechanical properties and microfabric of tailings. Scientific Reports, 12(1), 10700.

3. Experimental investigations: tested materials, testing devices, procedures and results

In order to analyze the seismic behavior of the case study, which consists of a tailings dam built with the upstream method located in southern Tuscany (Italy), it was necessary to examine in detail the static and dynamic geotechnical characteristics of the material stored within the basin and of those constituting the bank and the subsoil of the area covered by the facility. For this purpose, various laboratory tests were performed at the geotechnical laboratory of the University of Florence and at the geotechnical laboratory of the Ruhr-Universität Bochum on soil samples collected from the investigation site. This chapter describes the materials investigated, the techniques for collecting the soil samples, the methods used, as well as the purposes and objectives pursued for the various tests performed. Furthermore, the results of various tests are presented. Two types of materials are analyzed: those being stored inside the settling basin and constituting the retention dam. Samples belonging to the foundation soils could not be taken and analyzed; therefore, reference was made to existing data for their characterization. Regarding the material from the settling basin, pictures were taken with an electron scanning microscope to obtain information regarding the shape aspects and mineralogy of the particles. Furthermore, characterization tests were performed, such as granulometric analyses and index tests. In addition, the maximum and minimum void ratios and specific gravity were determined. Monotonic and cyclic triaxial tests were performed on reconstituted and undisturbed samples to study the soil behavior in static and dynamic loading conditions. The undisturbed samples were obtained with a special sampling technique based on the use of liquid nitrogen, which will be described in this chapter. Regarding the soils constituting the embankment, it was possible to accomplish only granulometric analyses due to the abundant presence of coarse material consisting of gravel and pebbles that prevented to perform other types of tests.

3.1. Tested materials

The tailings stored in a facility can be very heterogeneous due to their origin, treatment processes, deposition techniques, segregation, etc. These factors, which can greatly influence the behavior of the structure, often make it difficult to characterize the materials and define the geotechnical model of the whole complex. As will be further explained in Chapters 5 and 6, for the purpose of modelling the case study, in the present case it is possible to refer to three lithological units, which are defined as: settling basin materials (SBM), embankment materials (ENM), and foundation materials (FNM). Soil samples were collected from SBM and ENM units in two different survey campaigns carried out in 2021 and 2022. Due to economic, logistical, and site management problems, it was possible to carry out sampling only at a superficial level (0.7-1 m depth) by means of a manual equipment. The management of the area is assigned to a private company and is not accessible to the public without specific authorizations. Moreover, for safety reasons, there must always be company

employees present during site operations. Furthermore, the area is quite inaccessible and very difficult to reach by vehicles such as cars and service trucks; therefore, it was often necessary to carry the equipment on foot for long distances. For all these reasons, it was necessary to minimize the number of trips and time spent on site, and to plan the procedures and phases in detail, in order to obtain the desired number of samples and information. Without the aid of mechanical means, such as a core drilling machine, it was not possible to collect soil samples from the foundation material (FNM), because they are located at an average depth of about 35 m below ground level. The characterization of these materials was performed through the analysis of previous investigations (see Chapter 5).

In previous surveys, various field tests were carried out such as Standard Penetration Tests (SPT), Cone Penetration Tests (CPT), Down Hole Tests and Seismic refraction tests. Additionally, boreholes were drilled, and more or less disturbed samples were taken for subsequent characterization tests (grain sizes, Atterberg limits, etc.) and tests on their mechanical behavior (direct shear tests). As explained in detail in Chapter 5, these tests were carried out to cover a large area of the basin and dam and various depths. The comparison of the results obtained from the 2021 and 2022 investigation campaigns, in which only superficial samples were taken, with those of previous campaigns (in which larger areas and depths were investigated) allowed to conclude that the characteristics of the materials of the basin and the dam are rather homogeneous and therefore the hypothesis of modeling them as homogeneous materials is acceptable. Furthermore, as explained in Chapter 6, the definition of the input parameters and the calibration of the constitutive models employed in the numerical analyzes are based on sophisticated laboratory tests carried out specifically for this thesis work. These tests were performed on samples collected in the 2021 and 2022 campaigns. Consequently, it was deemed that the analyzes would yield more realistic results by modeling the materials as homogeneous with well-defined characteristics.

However, it should be noted that despite the investigations carried out in this thesis work and previous investigation campaigns, there are uncertainties regarding the actual homogeneity of the materials within the basin and the dam. In fact, the volumes involved are of considerable size and therefore it would be necessary to carry out further investigations to adequately characterize the structure. Geophysical investigations could be useful to identify any volumes of inhomogeneity which could be characterized with specific tests. To date, only two seismic refraction tests have been carried out, the results of which have essentially made it possible to identify the depth of the bedrock (Chapter 5). A geostatistical analysis would also be very useful to characterize the materials in detail. However, to obtain a reliable result, these analyzes would need to be based on a substantial dataset obtained from a large number of samples as shown by the information in Table 3.1. Furthermore, this type of investigation is typically undertaken within the framework of a detailed planned investigative campaign in which the location and depth of additional surveys is defined through the analysis of big amounts of information.

Table 3.1: *Number of boreholes and samples collected in papers dealing with geo-statistics.*

Work	No. of boreholes	No. of samples
Tripodi et al. (2019)	37	84
Soto et al. (2022)	165	1201
Lemos et al. (2023)		1586
Karacan et al (2023)		172
González-Díaz et al. (2023)	32	755
Blannin et al. (2023)	78	176

In this particular case, it was not feasible to acquire the extensive and detailed dataset required for a geostatistical investigation.

During the 2021 survey campaign, several samples were taken from two locations in the basin and others from two locations on the embankment. The choice of these locations was made based on the information gathered from previous surveys and considered particularly representative of the plant. During this investigation campaign, a technique was also developed for taking undisturbed samples by freezing with liquid nitrogen, as described in Section 3.2. The 2022 investigative campaign was aimed at collecting undisturbed samples of the settling basin material (SBM). The settling basin material derives from the processes performed inside the mill (as described in Section 2.1) and it is the one investigated in greatest detail in the present study (Figure 3.1).

Figure 3.1: *Sample of settling basin material (SBM).*

The embankment retaining the settling basin was built with the material extracted from the mine and considered less valuable. This material was only subjected to a coarse crushing process and used for the construction of the dam. A visual analysis of the embankment material (ENM) sample shown in Figure 3.2 points to the presence of an abundant coarse fraction.

Figure 3.2: *Sample of embankment material (ENM).*

3.1.1. Electronic microscope and chemical investigation

Grain shape is one of the main factors influencing the behavior of a granular soil (Krumbein 1941; Santamarina & Cho 2004; Wichtmann 2016; Zięba 2017; Sun et al. 2019). For this reason, electron microscope images of the material from the settling basin were acquired.

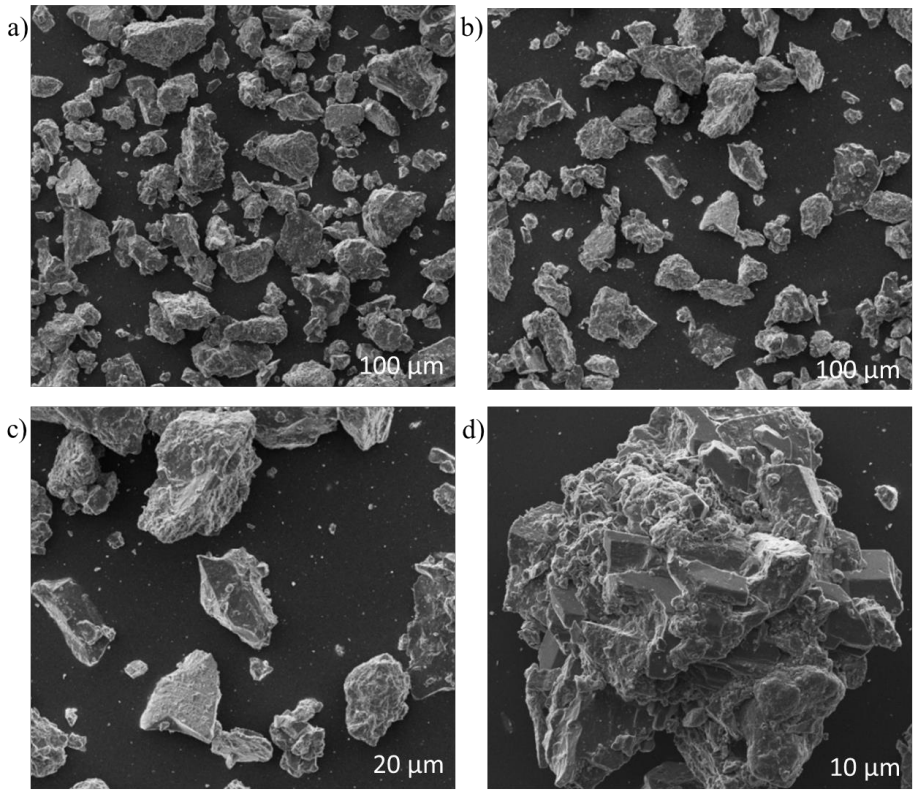

Figure 3.3: *Electron scanning microscope (SEM) images of settling basin material (SBM).*

Observing the images of Figure 3.3, it is evident that the material from the settling basin derives from a crushing process. The particles appear mostly elongated with angular edges. From the 10 µm scale image (Fig. 3.3 d) it can be seen that minerals are present on the surface of the particles due to the presence of euhedral crystals. Images at 100 µm scale (Fig. 3.3 a and b) were analyzed with Image J (Schneider et al. 2012) software to extract information regarding particle shape. In particular, the information obtained with this procedure is the aspect ratio AR, i.e. the ratio between the major and minor diameter of the particle and the circularity C_i, i.e. the ratio between the particle area and that of a circle having the same perimeter as the particle. AR and C_i were determined using the procedure used proposed by Cox et al. (2009) and described in Wichtmann (2016) which as a first step involves converting the SEM pictures (Fig. 3.3 a and b) into black and white images, as shown in Figure 3.4.

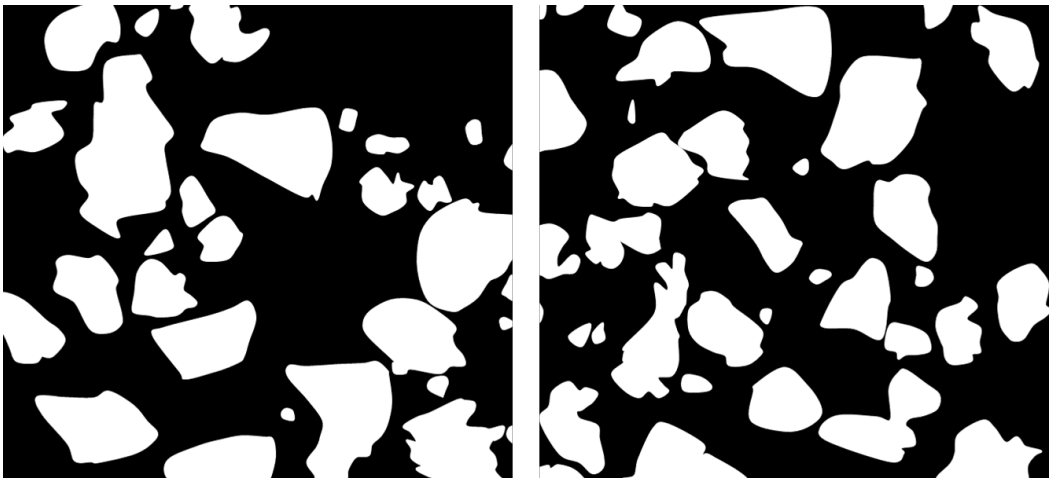

Figure 3.4: *Converting the images of Figure 3.3 a and b to black and white.*

When converting images to black and white, unrelated particles (e.g., dust or filaments) as well as overlapping grains must be excluded.

From the analyses performed, an aspect ratio AR equal to 1.77 and a circularity C_i equal to 0.67 were determined for Fig. 3.4 a), while for Fig. 3.4 b) an aspect ratio AR equal to 1.55 and a circularity C_i equal to 0.74 were obtained. An important limitation of this analysis is that, since it is conducted on an image, remain the two-dimensional. Thanks to the advent of new technologies such as 3D laser scanner, stereophotography and structured light techniques, numerous procedures are being developed for analyzing the shape and size of soil particles considering three-dimensional models (Cavarretta et al. 2009; Fonseca et al. 2012; Yan & Su 2018; Maroof et al. 2020; Zheng et al. 2020). These techniques allow to obtain information that 2D image analysis is not able to provide such as solidity, intercept sphericity, volume sphericity or sphere ratio sphericity, etc (Zheng et al. 2020). In future, it would be very useful to apply these procedures on the materials examined in this thesis in order to evaluate also these quantities. From a chemical point of view, analysis conducted on the materials of the settling basin revealed the presence of the following elements: silicon, magnesium, potassium, calcium, and iron, in accordance with what is stated in Section 2.3.

3.1.2. Grain size distribution

Grain size distribution analysis was performed on three samples collected from the settling pond and on three samples taken from the embankment. In Chapter 6, the results obtained are compared with those already available from previous survey campaigns. The granulometric analyses were performed by sieving for diameters larger than 0.075 mm and by sedimentation for smaller diameters. Figure 3.5 shows the pictures of the graduated burettes containing the settling basin material (SBM) during the sedimentation process immediately after shaking the solution (Fig. 3.5 a), after 3 minutes and 40 seconds after shaking (Fig. 3.5 b), and after 42 minutes after shaking (Fig. 3.5 c). A rather large settling velocity of the basin material is noted especially if compared to that of the embankment material (ENM) as shown in Figure

3.5 c after 6 hours and 20 minutes from shaking. A possible explanation for this phenomenon is that the tailings have undergone numerous densification processes before being deposited in the tailing pond and therefore are lacking the fractions that usually remain in suspension, while the dam materials have not undergone these processes.

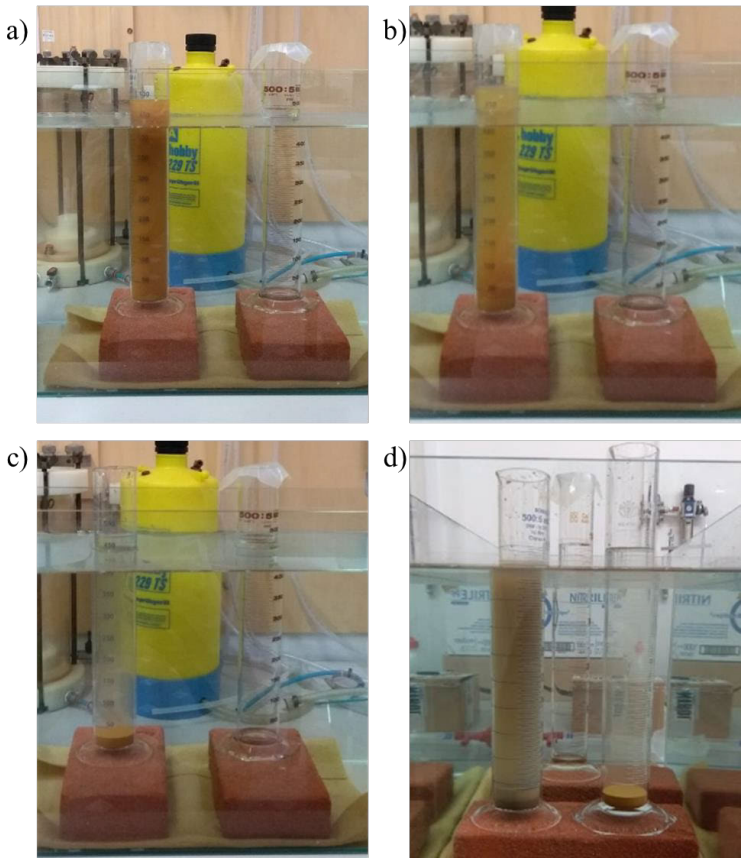

Figure 3.5: *Settling of basin material a) after shaking, b) 3'40'' after shaking, c) 42' after shaking, d) comparison between settling of basin (right) and embankment (left) material after $6^h20'$.*

Settling basin material (SBM)

The granulometric analyses of the material from the settling basin (SBM) were performed on three disturbed samples collected (C1_GRN_SBM_21, C2_GRN_SBM_21, and C3_GRN_SBM_21) during the 2021 survey campaign. From the results in Figure 3.6, it can be deduced that the three analyzed samples have similar grain size distribution curves.

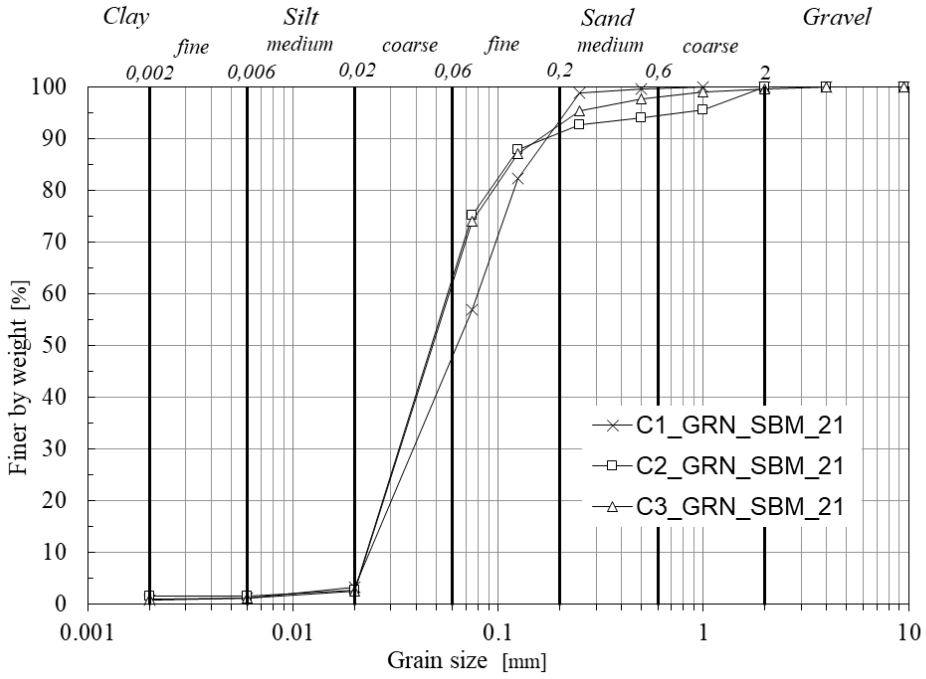

Figure 3.6: *Grain size distribution of settling basin material (SBM) samples.*

The fine content FC defined as the percentage of material with a diameter smaller than 0.063 mm is about 45% for sample C1_GRN_SBM_21, 59% for sample C2_GRN_SBM_21, and 58% for sample C3_GRN_SBM_21. The diameter of the grains referred to 50% of passing material (d_{50}) is equal to 0.068 mm for sample C1_GRN_SBM_21, 0.056 and 0.057 mm for C2_GRN_SBM_21 and C3_GRN_SBM_21 samples respectively. The value of the uniformity coefficient C_u, defined as the ratio between d_{60} and d_{10}, is 3.02 for sample C1_GRN_SBM_21, and 2.49 for both C2_GRN_SBM_21 and C3_GRN_SBM_21 samples. The characteristics described above are summarized in Table 3.2.

Table 3.2: *Index properties of settling basin material (SBM) samples.*

Sample	FC [%]	d_{50} [mm]	d_{10} [mm]	d_{60} [mm]	C_u [-]
C1_GRN_SBM_21	45	0.068	0.027	0.081	3.02
C2_GRN_SBM_21	59	0.056	0.026	0.063	2.49
C3_GRN_SBM_21	58	0.057	0.026	0.064	2.49

For sample C1_GRN_SBM_21, the Atterberg limits were also determined. The results obtained point out that the material is not plastic, with the plasticity index being 1%. However, it should be noted that the determination of the plastic limit was very difficult as the soil flaked during processing (Figure 3.7). Therefore, it was decided not to proceed with the determination of the Atterberg limits for the other two samples.

Figure 3.7: *Atterberg limits determination.*

Embankment material (ENM)

Granulometric analyses were also performed on three samples of the material from the embankment (C1_GRN_ ENM _21, C2_GRN_ ENM _21, and C3_GRN_ ENM _21) which were collected during the 2021 survey campaign. Figure 3.8 shows the grain size distributions of the embankment material (ENM) samples. As can be noted from Figure 3.8, the three grain size distribution curves are quite different and reveal the presence of a gravel content of more than approximately 50%.

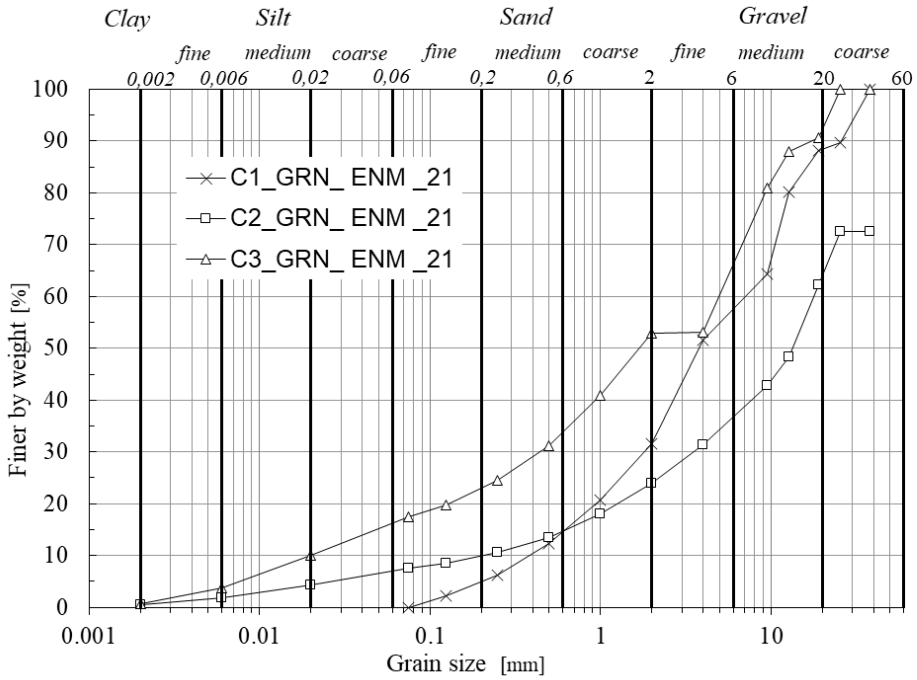

Figure 3.8: *Grain size distribution of embankment material (ENM) samples.*

The fine content FC is 0% for sample C1_GRN_ENM_21, 7% for sample C2_GRN_ ENM _21, and 16% for sample C3_GRN_ ENM _21. The diameter of the grains referred to 50% of passing material (d_{50}) is equal to 3.845 mm for sample C1_GRN_ ENM _21, 13.485 mm for sample C2_GRN_ ENM _21 and 1.757 mm for sample C3_GRN_ ENM _21. The uniformity coefficient C_u for all three samples is greater than 15. The characteristics described above are summarized in Table 3.3.

Table 3.3: *Index properties of embankment material (ENM) samples.*

Sample	FC [%]	d_{50} [mm]	d_{10} [mm]	d_{60} [mm]	C_u [-]
C1_GRN_ ENM _21	0	3.845	0.405	7.621	>15
C2_GRN_ ENM _21	7	13.485	0.213	18.049	>15
C3_GRN_ ENM _21	16	1.757	0.020	5.369	>15

3.1.3. Soil specific density

The soil specific density was determined only for the basin material, as it was impossible to measure it, with the available equipment, for the embankment materials due to the very high content of gravel. The procedure used is the one indicated in the CNR-UNI 10010 (UNI 1964) standard. The test consists in inserting a known mass M_d of dried material into a pycnometer and then adding distilled water until the pycnometer is half full. The solution thus obtained must rest at room temperature for one hour. Subsequently, the air dissolved in the solution is eliminated by boiling. When the mixture has cooled, more de-aerated distilled water is added until the pycnometer is full. Then the pycnometer with its content is weighed and the mass M_1 is found. The pycnometer is then carefully emptied, filled with de-aerated distilled water, and weighed again in order to find the mass M_2. The specific density of the soil is therefore calculated by:

$$\rho_S = \frac{M_d}{M_d + M_2 - M_1}\rho_w \tag{3.1}$$

where ρ_w is the specific density of water. Following the procedure, the specific density of the material was determined as 2.8 kg/cm^3. The case study tailings derive from the extraction of copper, lead and zinc; therefore, the specific density value determined for the analyzed material is similar to those reported in literature for tailings resulting from extraction of these metals.

3.1.4. Maximum and minimum void ratio

Maximum and minimum void ratios were determined only for the settling basin material since the larger particles of the embankment material are not compatible with the standard used equipment, which has a diameter of about 7 cm. The procedure applied was the one indicated by the German DIN_18126 (DIN 18126 1996) standards and the tests were performed in part at the geotechnical laboratory of Ruhr-Universität

Bochum, and in part at the geotechnical laboratory of the University of Florence. The procedure for minimum void ratio consists in depositing the material, previously dried, in a cylindrical container of defined dimensions with a standardized funnel. The funnel is lifted in the center of the container (Fig. 3.9 a), preventing the formation of a gap between the outflowing soil and the current soil surface in the cylinder. After filling the cylinder and leveling the surface, the material contained in the cylinder is then weighed to obtain the mass of the solid phase $M_{Smax,i}$ (Fig. 3.9 b). With the known volume of the cylinder V the minimum dry density $\rho_{dmin,i} = {M_{Smax,i}}/{V}$ is calculated. The maximum void ratio is obtained from $e_{max,i} = {\rho_S}/{\rho_{dmin,i}} - 1$. This test is repeated five times, obtaining five values of the maximum void ratio.

The average value of the 5 maximum void ratios is assumed as the maximum void ratio of the material. The procedure for determining the minimum void ratio starts from the last weighed mass $M_{Smax,5}$ used for determining the maximum void ratio, which is divided into five parts. Then, the five sub masses are weighed and poured one at a time into a metal cylinder (Fig. 3.9 c). Each time a mass is poured, before pouring the next one, it is covered with a metal weight of standardized dimensions and the edges of the cylinder are struck with a special Y-shaped tool 30 times in about 10 seconds to densify the material (Fig. 3.9 d). Once the procedure is repeated for all layers, the sag undergone by the metal disc is measured with a caliper (Fig. 3.9 e) and, in this way, it is possible to obtain the total volume $V_{TOTmin,i}$ occupied by the densified soil. Since the mass $M_{Smax,5}$ and density ρ_S of the material are known, it is possible to determine the i-th minimum void ratio $e_{min,i}$. In this case, the procedure is repeated three times and the average of the minimum void ratios represents the three e_{min} values of the test. It should be noted that according to the DIN standard the test on the minimum void ratio is done with water in the cylinder. However considering the high fines content of the studied basin material it was decided to let away the water and perform the test under dry conditions.

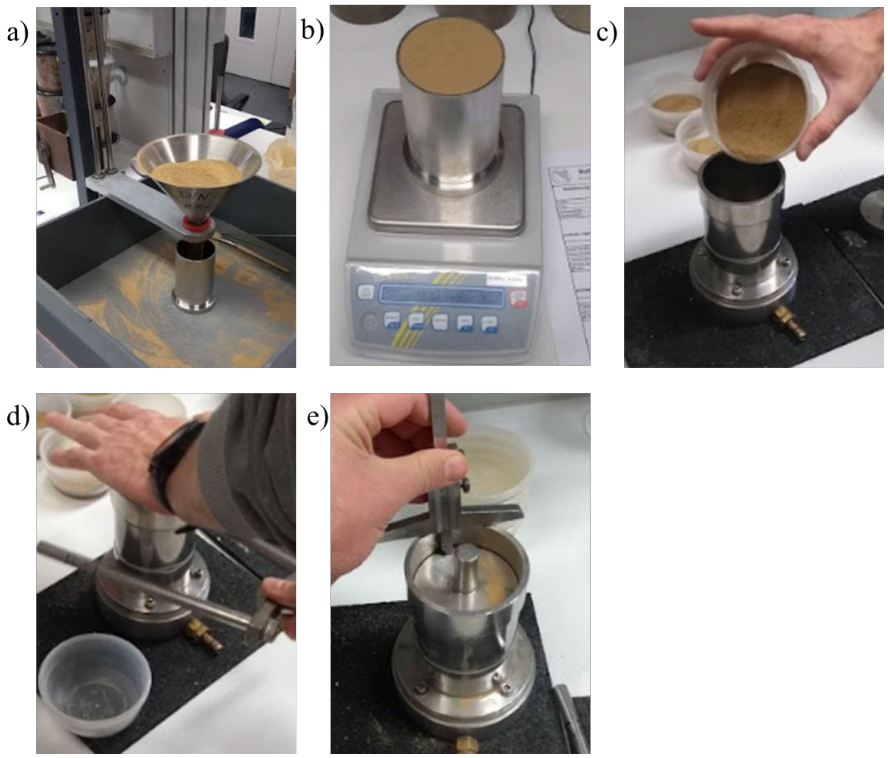

Figure 3.9: *Procedure for determining the maximum and minimum voids ratio: a) pouring of the material with a funnel into a cylinder, b) weighing the filled cylinder to determine the maximum void ratio, c) pouring one fifth of the last mass used in determining the maximum void ratio into the cylinder, d) densifying the sample be means of repeated shots applied with the Y-shaped instrument, e) measuring the sag of the metal disc using a caliper. (pictures taken at the geotechnical laboratory of Ruhr-Universität Bochum)*

Following the procedures described above, five tests were performed to determine the maximum and minimum void ratios and the average of the results obtained was taken as the reference values as shown in Table 3.4.

Table 3.4: *Maximum and minimum void ratios*

Test	e_{max} [-]	e_{min} [-]
C1_VOID_SBM_21	1.383	0.714
C2_VOID_SBM_21	1.373	0.713
C3_VOID_SBM_21	1.384	0.718
C4_VOID_SBM_21	1.385	0.746
C5_VOID_SBM_21	1.394	0.746
Average	1.384	0.727

3.2. Frozen undisturbed sample collection

It is well known that the collection of high-quality undisturbed samples of non-cohesive soils (such as tailings) is extremely difficult. Over the years, various techniques have been proposed to extract samples of non-cohesive soil, such as special multi-sleeve samplers or through the use of special gels. In the context of this work,

the samples of tailings from the settling basin were collected by freezing soil with liquid nitrogen. Liquid nitrogen is a liquid with a boiling point of -196 degrees Celsius. It is used in many fields and applications to cool and/or keep cold various products. As part of this research, it was chosen to use liquid nitrogen because it has been shown to be the most efficient liquid to cool the soil, and also because, being the most common element in the atmosphere, it is environmentally friendly and quite cheap. The following subsection describe the method devised to collect undisturbed samples by referring to a literature search of methods using liquid nitrogen that were developed in the past.

3.2.1. Literature review on sample collection by means of liquid nitrogen methods

The first ground freezing campaign to extract undisturbed soil samples was performed by Horslev in the 1940s at the Fort Peck Dam in Montana, United States. The procedure devised by Horslev involved cooling a volume of soil through the circulation of a refrigerant liquid in seven tubes arranged as a ring. Once the soil had reached the frozen phase, the samples were extracted by means of a 914 mm diameter core barrel (Horslev, 1949). Between the 1970s and 1990s, Japanese research groups devoted their attention to the study and development of these techniques (Yoshimi et al. 1978; 1984 and 1989). In this period, techniques were tested that had some characteristics in common: the installation of a single pipe in which to make the coolant flow and the withdrawal of a large volume of soil. They differed in the type of coolant, depth of freezing, and type of collection of the frozen bulb, which could be extracted with a crane or with a core barrel. Significant quantities of liquid hydrogen (5000 kg) and time (40 hours) were required to freeze the soil (Yoshimi et al. 1984). A relatively less expensive and onerous methodology in terms of time and equipment was proposed by Konrad (1990). He was able to sample a sand cylinder of 26 cm in diameter in 4 hours using a rectangular section rod inside which refrigerated ethanol circulated (Konrad 1990). The development and analysis of different methodologies, including freezing, to obtain high quality soil samples was one of the main objectives of the project "Canadian Liquefaction Experiment" (CANLEX) (Wride et al. 2000). The procedure used by the CANLEX project researchers involved cooling the soil around a tube in which liquid nitrogen circulated until it reached a volume of frozen material of about 2 m in diameter and with a height that could vary between 4 and 10 m, depending on the characteristics of the site. Once the freezing phase was done, the samples were taken by coring placed about 0.6 m from the freezer tube. In the paper, the authors report the costs related to these sampling techniques, which were around 50,000 Canadian dollars per survey (referring to the year 2000), which corresponds to approximately 34,300 € (current currency). In the early 2000s, samples of frozen soil were collected at Gioia Tauro, Calabria, Italy (Ghionna & Porcino 2001). A technique similar to those proposed by Japanese researchers, in which samples extracted from large volumes of frozen soil was used. Subsequently, in northern Tuscany (Italy), a procedure more similar to that described in the CANLEX project was used, freezing the area of soil to be investigated and then taking samples at regular depths by means of three boreholes arranged about 1 m from the freezing hole (Lo Presti et al. 2006).

In 2018, a group of South Korean researchers devised a ground freezing technique by means of two freezer tubes placed at a distance of about 1.5 m, which was able to freeze a large volume of soil of 4 m in diameter (Kim et al. 2018). The volume of frozen material was then evaluated by electrical tomography without taking samples.

3.2.2. Developed method

The previous subsection briefly describes the techniques for collecting undisturbed samples of non-cohesive soil by freezing proposed by various authors over the years. Although these techniques make it possible to reach relatively large depths and to obtain high quality samples, at the same time, they involve the use of massive resources in terms of time, personnel, materials, and machinery. The deployment of such huge resources was incompatible with the present project for economic and time reasons, and available means. To collect undisturbed samples with a technique compatible with the available resources, reference was made to Wichtmann et al. (2019) in the context of lignite opencast mine recultivation. Such mines have been dug in the last centuries in various regions of Germany to extract coal and there is currently a plan to convert the cavities left by some of these now inactive pits into lakes. The lakes will be enclosed by embankments made with the waste material deriving from the excavation activities of the pits. In order to study the liquefaction behavior of these materials, Wichtmann et al. (2019) devised a method to collect undisturbed samples of material for laboratory testing. The developed technique involved forming blocks of frozen soil at the base of excavations of about 2 m depth by slowly pouring liquid nitrogen directly onto the ground from the tap of a tank. From the blocks, which were kept frozen during transportation and storage in the laboratory, it was possible to obtain several samples with a diameter and height of 10 cm for triaxial tests through extrusion and cutting procedures performed in controlled temperature rooms. In the present case it was not possible to proceed with the formation of frozen blocks because the freezer available for storing the samples was not large enough to accommodate blocks of that size, and because there were no controlled temperature rooms in which to carry out the extrusion. Therefore, the procedure had to foresee some differences from the one proposed by Wichtmann et al. (2019) and was optimized through tests initially conducted in a purpose-built test field and in two subsequent investigation campaigns conducted at the case study tailings dam.

Test field trials

To simulate the working conditions at the study site, an excavation of approximately 1.5 m in depth was realized and various simulations of sampling undisturbed specimens were carried out to refine the technique. Since the excavated soil was basically cohesive, loose river sand was poured onto the bottom of the excavation to form a layer of a few dozen centimeters. Then, metal samplers were inserted into the layer of sand and liquid nitrogen was poured into the excavation bottom. Once the freezing phase was completed, the samplers were extracted from the sand, carried in coolers to the geotechnical laboratory of the University of Florence and stored in freezer. Two types of samplers were used, one called whole, and one called split (Fig. 3.10). The triaxial equipment at the Geotechnical laboratory of the University of

Florence involves the use of cylindrical specimens with a diameter of about 5 cm (2 inches) and a height of about 10 cm. Therefore, the samplers were designed to have a diameter the same as that of the specimen to be tested in triaxial apparatus and to be high enough to avoid disturbance phenomena at the ends of the sample.

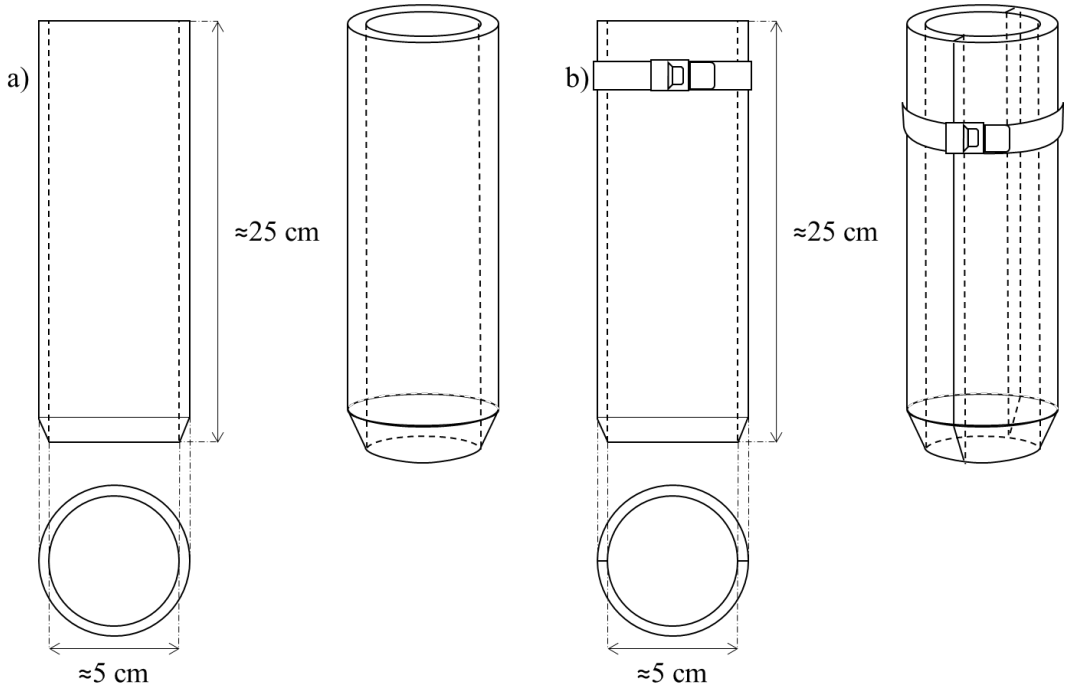

Figure 3.10: *Samplers: a) whole, b) split.*

The samplers were obtained by cutting a long steel tube into punches of about 25 cm each and the edges on the driving side were flared with the dual purpose of minimizing the disturbance to the ground and to facilitate driving (Fig. 3.11). A number of samplers were split in half for the purpose of examining whether this modification would make it easier to extract the soil specimen. Various extraction tests of the specimens from the punches were carried out (Fig. 3.11 a) and images of the samples extracted were acquired with a special thermal imaging camera to verify the effective freezing. Through the acquired images, it was possible to verify that the temperature of the samples was around minus 40 degrees Celsius (Fig. 3.11 b).

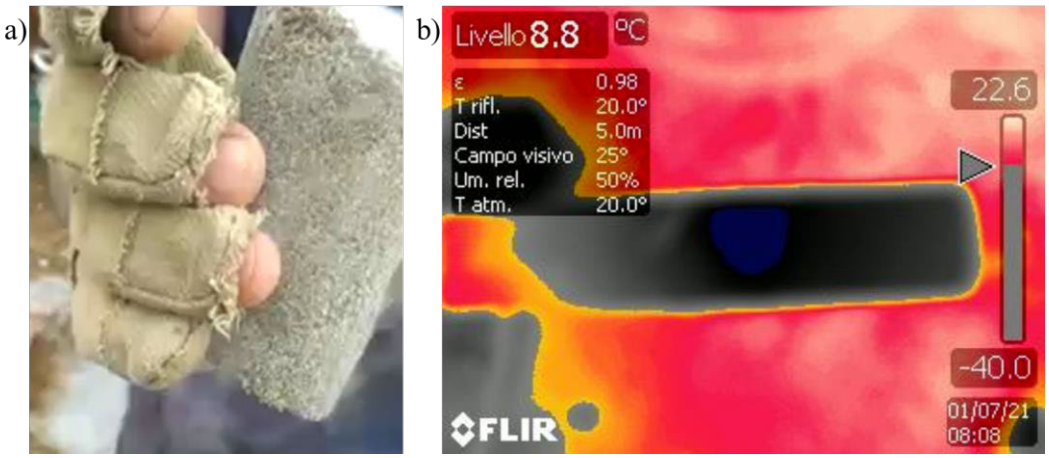

Figure 3.11: *Freezing tests: a) frozen specimen just extracted from the ground, b) thermal image of the frozen sample.*

From Figure 3.11 a it is possible to deduce that the sample held in the hand by the operator was solid while the sand before freezing was completely loose.

2021 investigation campaign

The 2021 investigation campaign required three days of work on the case study site. Two days were needed to carry out the 4 excavations (two on the embankment and two in the basin) called S1_ENM_21 and S2_ENM_21 on the embankment, S3_SBM_21 and S4_SBM_21 in the basin (Fig. 3.12).

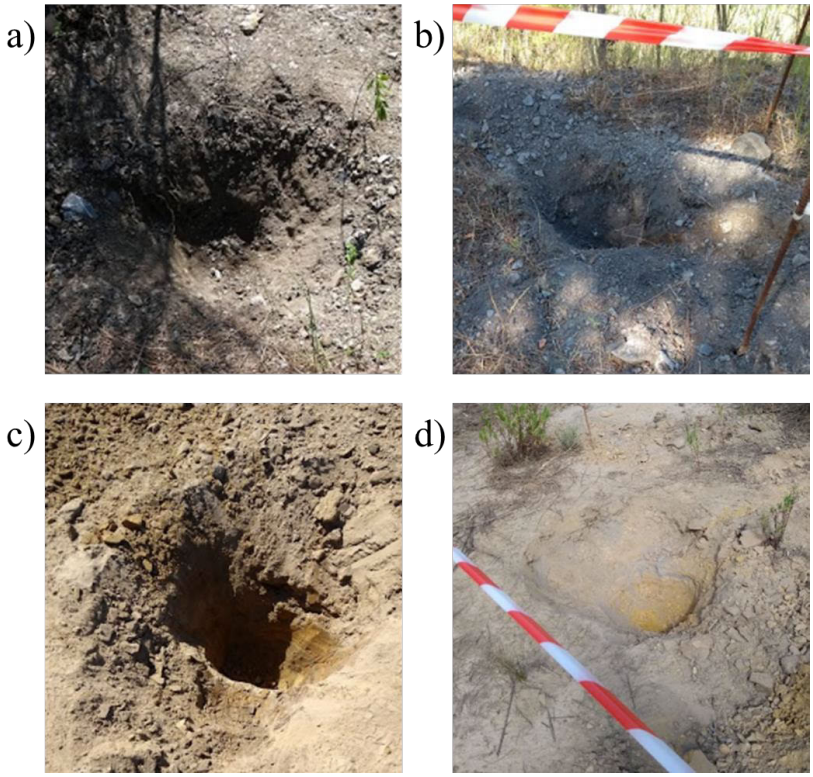

Figure 3.12: *2021 campaign excavations: a) S1_ENM_21, b) S2_ENM_21, c) S3_SBM_21, d) S4_SBM_21.*

The excavations, which had a diameter of about 40 cm and a depth of about 60 cm each, were carried out by hand to limit soil disturbance as much as possible. A visual evaluation of the embankment material allowed to conclude that the high presence of coarse material (with diameters up to 5 cm) would have made it impossible to carry out triaxial tests; therefore, from excavations S1_ENM_21 and S2_ENM_21 only disturbed samples were taken. Instead, in the bottom of each of the excavations S3_SBM_21 and S4_SBM_21, a split and a whole sampler were driven into the ground (Fig. 3.13) and about 17.5 liters of liquid nitrogen were poured in to each excavation (Fig. 3.14).

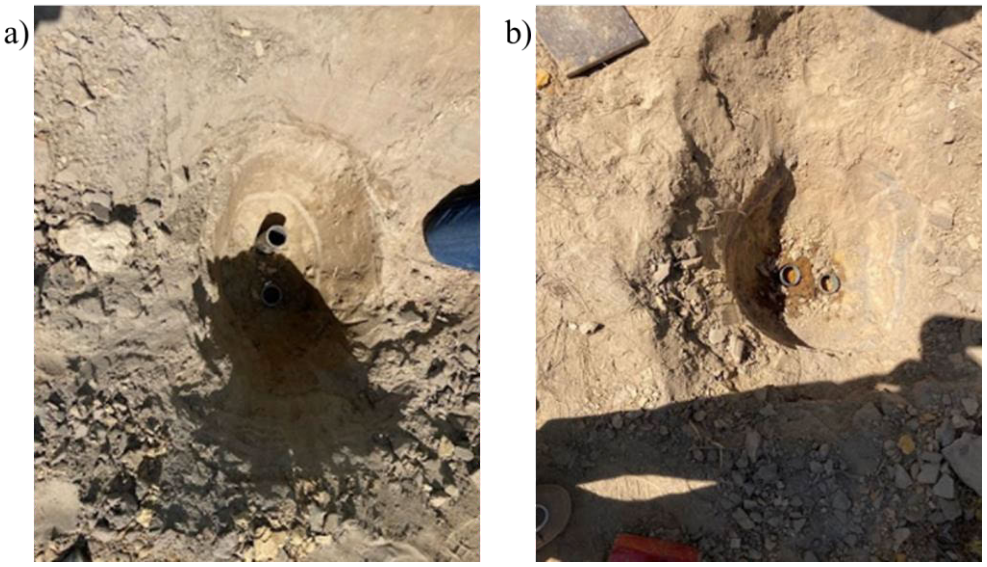

Figure 3.13: *Samplers in the excavations: a) S3_ENM_21, b) S4_ENM_21.*

Figure 3.14: *Pouring of liquid nitrogen into S3_ENM_21.*

Once the freezing process, which took about 15 minutes, was completed, the samples were extracted (Figure 3.15) and placed inside a thermally insulated container containing a few kg of dry ice which allowed them to be transported perfectly frozen to the Geotechnical laboratory of the University of Florence.

Figure 3.15: *Extracting samplers from S3_SBM_21.*

In conclusion, with the described procedure it was possible to obtain 4 undisturbed samples using 35 l of liquid nitrogen and a few hours of work. Extracting samples from the whole samplers proved to be extremely difficult in this case compared to that of the field test. A possible explanation is that, in the case of the preliminary field test, the samplers had been inserted in a layer of sand that had recently been poured and was therefore extremely loose in comparison with the material taken the tailings dam. On the other hand, extraction of samples from split-type mold was rather easy; therefore, also in order to limit the sample disturbance, it was decided to use only this type of sampler in subsequent campaigns.

2022 investigation campaign

In 2022, a second survey campaign was carried out in the case study site, with the skills and knowledge gained from previous experiences, it was possible to take 8 undisturbed samples to be subjected to triaxial tests. Compared to the previous campaigns, changes were made to the procedure. In particular, only split-type samplers were used and a tank equipped with a tap was applied to pour the liquid nitrogen more slowly into the excavation pit in order to induce less disturbance to the ground. Furthermore, after the punches were inserted, the ground around them was dug for

about 3/4 of their height to facilitate their extraction following freezing. It had been planned to exploit the S4_SBM_21 excavation again to carry out the extraction, however, in the previous days the site had been hit by violent storms which flooded the excavation. It was therefore necessary to realize a new excavation called S4_SBM_22, which had a rectangular plan with sides of about 70 x 140 cm and a depth of about 70 cm (Fig. 3.16 a).

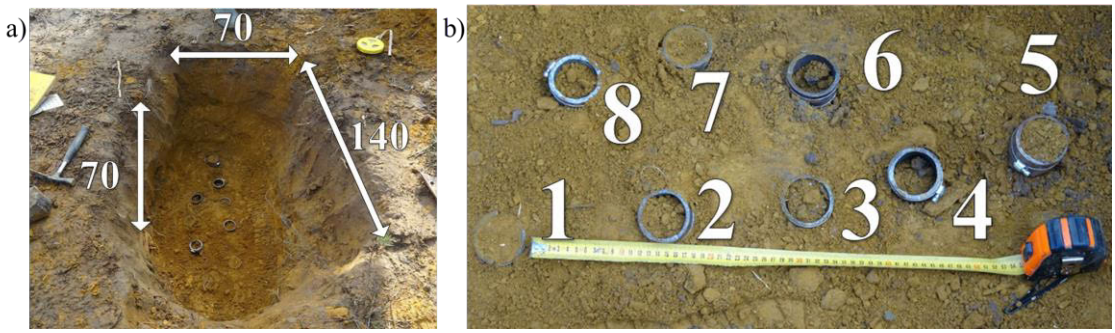

Figure 3.16: *S4_SBM_22 excavation: a) dimensions, b) samples.*

After the excavation was realized, the eight samplers were inserted into the ground and subsequently the ground was dug around for about 3/4 of their height (Fig. 3.17 a). Then the liquid nitrogen was poured into the tank fitted with a tap (Fig. 3.17 b).

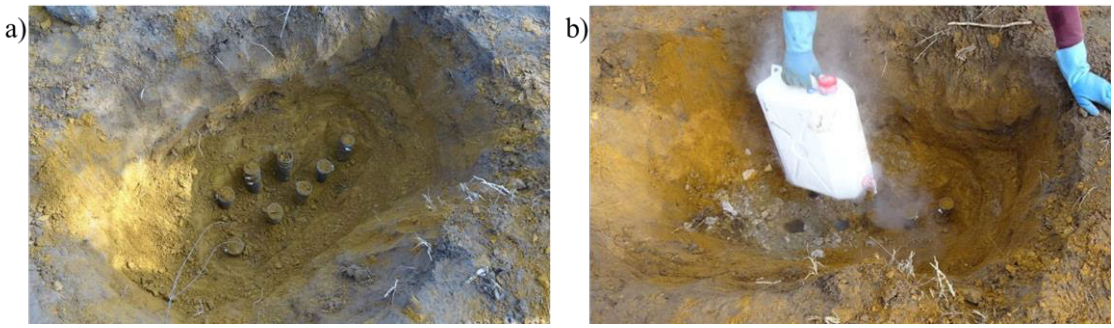

Figure 3.17: *S4_SBM_22 excavation: a) samplers protruding 3/4h from the ground b) pouring of the liquid nitrogen by means of a tank with a tap.*

The subsequent phases are equivalent to those described previously. The phases described above are sketched in Figure 3.18.

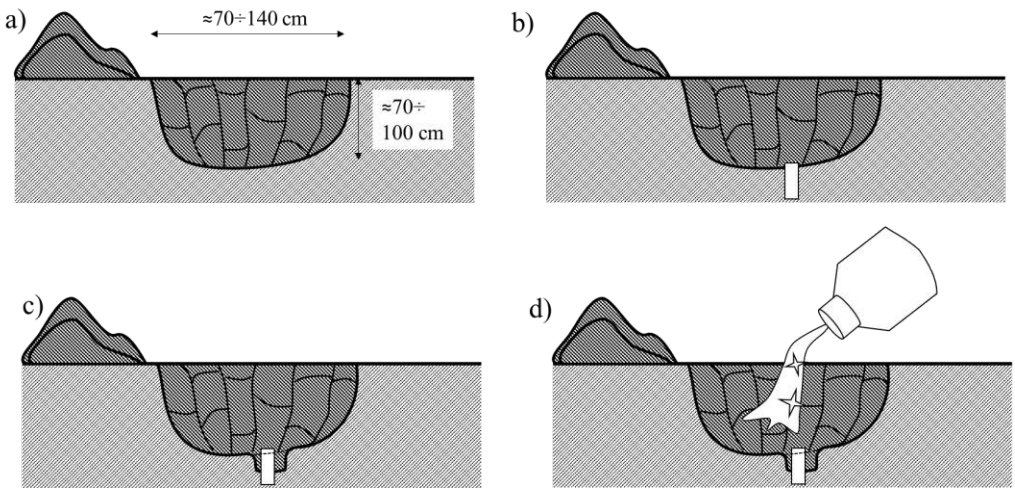

Figure 3.18: *Undisturbed sampling method phases: a) excavation, b) sampler insertion in the bottom of the excavation, c) excavation around the samplers along 3/4 of their height, c) pouring liquid nitrogen into the excavation.*

3.3. Triaxial tests

Several triaxial tests were performed to study the behavior of the material collected in the settling basin. The tests were conducted at the geotechnical laboratory of the University of Florence and at the geotechnical laboratory of the Ruhr-Universität Bochum. Monotonic drained and undrained triaxial tests and cyclic undrained triaxial tests were carried out both on reconstituted and undisturbed samples. It was not possible to perform tests on undisturbed samples in Bochum due to the difficulties associated with transporting the frozen material. This section describes the triaxial equipment of both Florence and Bochum laboratories. Then the techniques for preparing the reconstituted specimens in the two laboratories are described. Furthermore, the method for preparing the undisturbed specimens is presented. Finally, the test procedures and the results obtained are described.

3.3.1. Triaxial devices

Florence triaxial device

The triaxial device available at the geotechnical laboratory at the University of Florence is shown in Figure 3.19. The main components of the equipment are: the water supply tank, the bladders, the volume-meter, a Linear Variable Differential Transformer (LVDT), two control units, the frame with the electric servo-assisted actuator, the cell base, the cell, the compressed air reserve and the control PC. The tank containing distilled and de-aerated water is placed approximately 1.5 m above the cell and supplies water to the entire system. Bladders are devices in which a very resistant rubber ball is inserted into a plexiglas cell filled with water. The rubber ball is connected with a pneumatic system to the compressed air supply. Through solenoid valves controlled by the control units, the compressed air is used to inflate or deflate the rubber balls. As they inflate, the rubber balls increase the pressure of the water contained inside the plexiglas cell. So, bladders are devices that convert air pressure

into water pressure. One of the bladders controls the cell pressure while the other one controls the back pressure. The volume-meter is a device which allows to measure the variation of the volume of water contained in the sample during the saturation phase and in drained tests. The LVDT is connected to the cell piston and measures its axial displacements. The frame contains the cell and through the servo-assisted actuator allows to apply the axial load to the specimen. At the base of the cell there are some taps which allow to adduct the cell water and increase its pressure, to measure the pore pressure and to apply the back pressure. A plexiglas cell contains the sample and is fixed to the base by means of steel bolts. In the upper part of the cell there is the load piston which transfers the axial load to the specimen, and which is connected to the frame actuator. The load cell is positioned on the piston outside the cell containing the specimen. The compressed air reserve is a steel tank able to contain the high-pressure air produced by the compressor. This device has the task of equalizing the pressures produced by the compressor. From the PC through specialized software, it is possible to set the specimen data, the test phases, and the device settings. A scheme of the device is presented in Figure 3.20.

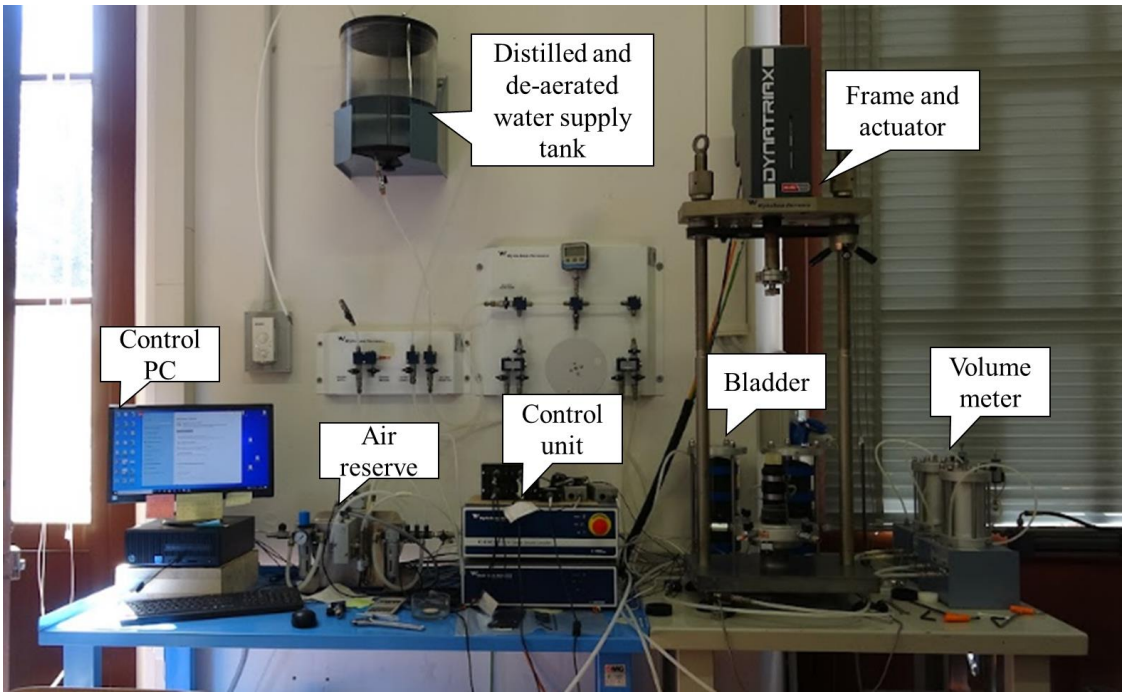

Figure 3.19: *Main components of the triaxial device at the geotechnical laboratory of the University of Florence.*

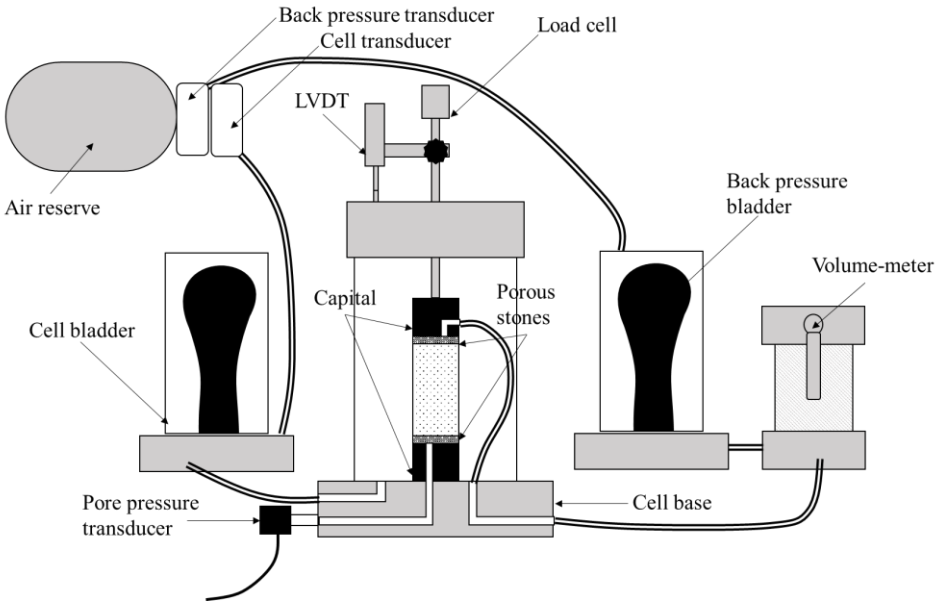

Figure 3.20: *Scheme of the triaxial device of the geotechnical laboratory of the University of Florence.*

Bochum triaxial device

The triaxial device used to the geotechnical laboratory of the Ruhr-Universität Bochum has been described in detail by Sarkar et al. (2022) and is represented in Figure 3.21. The main components of the equipment are: the water supply tank, a Volume Pressure Controller (VPC), a Linear Variable Differential Transformer (LVDT), the frame with the electric servo-assisted actuator, the cell base, the cell, and the control PC. The substantial differences of this device compared to the Florence one are: the dimensions (this device allows to test larger samples), the measurement of the vertical load inside the pressure cell and the absence of the bladders, and the characteristic parameter of the signal transmitted to the piston. In Florence sinusoidal cycles of constant deviatoric stress amplitudes were applied with a constant frequency.

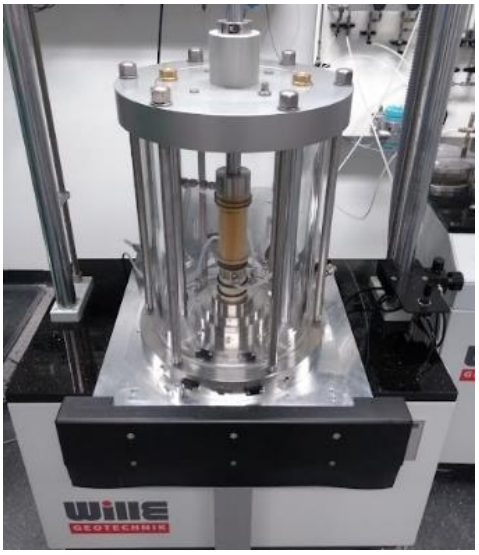

Figure 3.21: *Cell of the triaxial device used at the geotechnical laboratory of the Ruhr-Universität Bochum.*

3.3.2. Sample and test preparation

Reconstituted sample and test preparation at Florence

At the Florence laboratory, the reconstituted soil samples were prepared with the moist tamping method as described in Ciardi & Madiai (2022). The specimens were realized directly on the pedistal of the base of the cell. The first step was to place a disc of filter paper and a porous stone on the base pedistal and then the latex membrane which was fixed with two O-rings. At this point a split-mold was mounted and fixed. With the split-mold the membrane was tensioned through two holes at which vacuum was applied (Fig 3.22). The moist tamping method involved forming the specimens in 5 layers of equal height. In the present case each layer had a height of 2 cm. Undercompaction was taken into account by applying the target relative density to the central layer, a relative density reduced by one percentage point to each of the lower layers, and a relative density increased by one percentage point to each of the upper ones. Once the target relative density $D_{r,3}$ of the central layer had been established, it was possible to calculate the initial void ratio of each layer (Fig. 3.22) as:

$$e_{0,i} = \begin{cases} e_{max} - (D_{r,3} + 1)(e_{max} - e_{min}) \rightarrow i > 3 \\ e_{max} - (D_{r,3})(e_{max} - e_{min}) \rightarrow i = 3 \\ e_{max} - (D_{r,3} - 1)(e_{max} - e_{min}) \rightarrow i < 3 \end{cases} \quad (3.2)$$

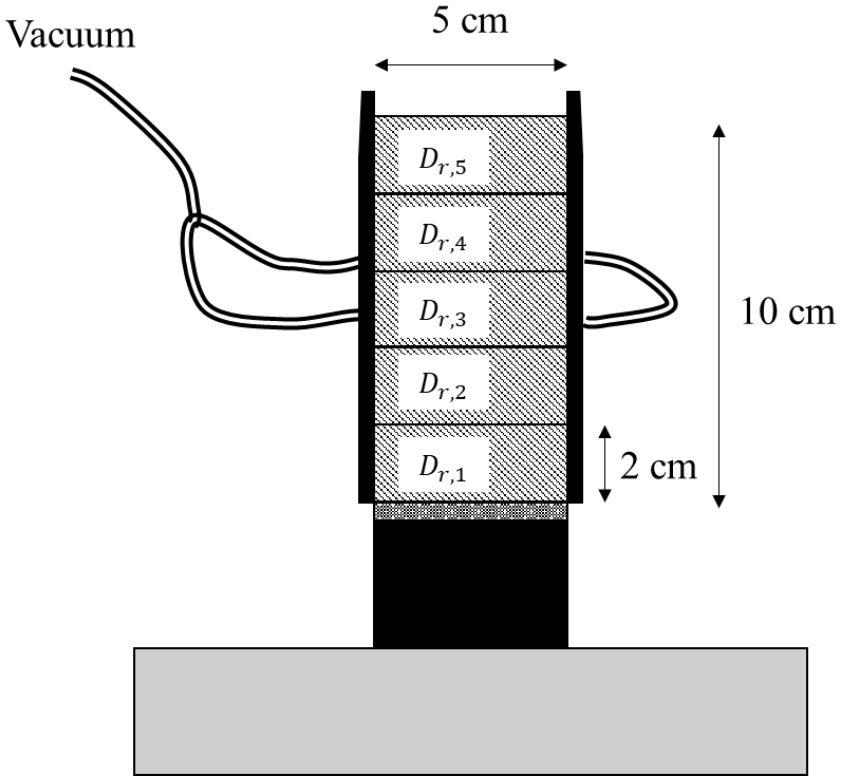

Figure 3.22: *Moist tamping layers.*

Since the total volume of each layer (one fifth of the volume of the split-mold) and the initial void ratio were known, it was possible to obtain the volume of the solid phase for each layer as:

$$V_{S,i} = \frac{\left(\frac{V}{5}\right)}{e_{0,i} + 1} \tag{3.3}$$

With the volume of the solid phase and the grain density $\rho_{S,i}$ the dry mass of each layer $\rho_{S,i} = M_{S,i}V_{S,i}$ could be calculated. The dry mass of each layer was wetted to reach the desired water content. Once all the material of the layer had been poured into the split-mold, this was gently compacted with a pestle to reach a uniform height of 2 cm. Having placed all the layers and having reached a height of about 10 cm, the verticality of the specimen was checked with a level and then a disc of filter paper, a porous stone and finally the upper cap were placed in this order (Fig. 3.23). To stabilize once the split-mold was removed a vacuum of approximately 30 kPa was applied which was gradually removed as the cell pressure was applied.

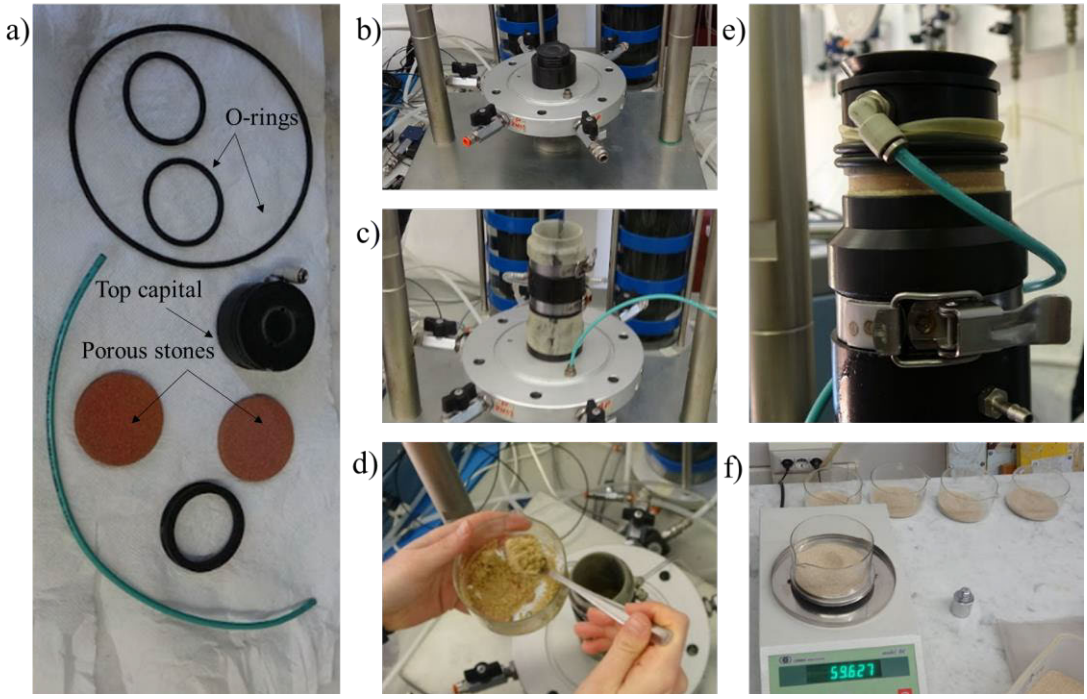

Figure 3.23: *Moist tamping phases: a) components of the triaxial device, b) base pedestal, c) split-mold and membrane, d) pouring the mixture in the split mold, e) top cap, f) weighing of samples. (Pictures taken at the geotechnical laboratory of the University of Florence, Italy).*

Once the specimen was prepared, the cell was assembled on the base and filled with water. Then the specimen was flushed with carbon dioxide CO_2 for about half an hour in order to replace the air trapped in the pores by this gas (which dissolves better in water). After that the specimen was flushed with distilled and de-aerated water in the course of the saturation process. After the application of the back pressure the sample was kept under this pressure for about 24 hours. A sufficient saturation was considered obtained for values of Skempton's B equal or greater to 0.95. Subsequently, the

specimen was subjected to isotropic consolidation. The next phase differed according to whether the test conducted was drained monotonic, undrained monotonic, or cyclic. In the case of cyclic tests, a sinusoidal load with a frequency of 0.01 Hz was applied.

Reconstituted sample and test preparation at Bochum

Also, at the Bochum laboratory the reconstituted samples were prepared on the pedestal of the lower base of the triaxial cell. The base pedestal is equipped with a 1 cm diameter porous stone (Fig. 3.24 a). The surface of the base pedestal was covered with a thin film of lubricant and a latex disk was placed on top (Fig 3.24 a). A small disc of filter paper was placed on top of the porous stone. Subsequently, the split mold was mounted which tensioned the membrane. The moist tamping method used derives from the one proposed by Ladd (1978). This method is applies the concept of undercompaction, assuming that during the formation of the sample by layers, the lower layers will undergo a further compaction by the compaction of the upper layers. Therefore to obtain a uniform density distribution in the sample it is necessary to compact the lower layers with a smaller density than the upper ones. The degree of undercompaction decreases with the height of the specimen and is generally set equal to zero for the last layer while for the first layer it generally ranges between zero (for very dense samples) to 15% (for loose samples). With the degrees of undercompaction of the first and last layer, it is possible to define it for the intermediate layers as:

$$U_n = U_{ni} - \left[\frac{(U_{ni} - U_{nt})}{n_t - 1}(n-1)\right] \tag{3.4}$$

Where U_{ni} is the first layer undercompaction percent, U_{nt} is the last layer undercompaction percent, n_t is the last layer number and n is the current layer number. Once the degree of undercompaction of the layer has been determined, it is possible to determine the height of the sample up to the top of this layer as:

$$h_n = \frac{h_t}{n_t}\left[(n-1) + \left(1 + \frac{U_n}{100}\right)\right] \tag{3.5}$$

Therein h_t is the total height of the sample. The dry mass for each layer was determined using the specific density of the soil and considering the chosen relative density of the specimen. Then, the dry mass was wetted and mixed with the amount of water necessary to reach the chosen water content. The sample was then divided into 5 parts of equal weight. The soil of the individual layers was placed in the mold and compacted, with a special pestle A ring fixed to the rod of the tamper in a certain height, which was controlled by a caliper, guaranteed that the layer was compacted to a height according to Eq. (3.5) (Figure 3.24). Once the total height of the specimen is reached, verticality was checked with a level and the top cap was positioned (Figure 3.24 d).

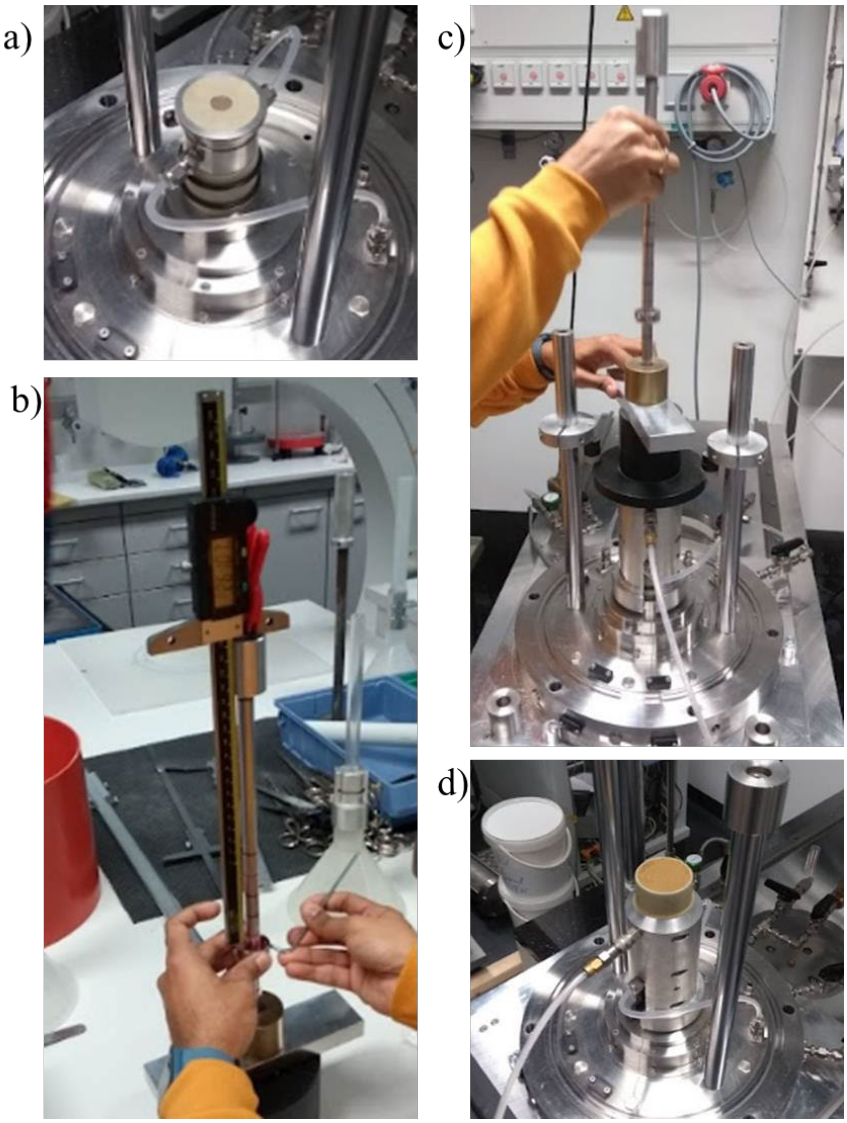

Figure 3.24: *Moist tamping phases: a) porous stone with membrane, b) ositioning of the ring defining the height of the compacted soil layer, c) sample tamping, d) finished sample. (Pictures taken at the geotechnical laboratory of the Ruhr-Universität Bochum, Bochum, Germany).*

The reconstituted specimens were flushed first with carbon dioxide CO_2 and then with distilled and de-aerated water. Subsequently, they were subjected to a back pressure and let rest for about 24 hours. The degree of saturation was checked by the B-value test. A sufficient saturation was considered achieved for a B coefficient equal or greater than 0.95. The saturation phase was followed by isotropic consolidation. During the loading phase the cyclic load was applied in a triangular shape.

Undisturbed sample and test preparation at Florence

As previously mentioned, the tests on undisturbed samples were performed only at the Florence geotechnical laboratory as the transport of the frozen samples to Bochum was not feasible. Eight undisturbed frozen specimens had been collected from the case study site in the 2022 sampling campaign and stored in a dedicated freezer until used. The first step in preparing the samples to be tested was the extraction from the split sampler. This procedure is extremely delicate and must be performed with extreme care to avoid specimen disturbances (Fig. 3.25).

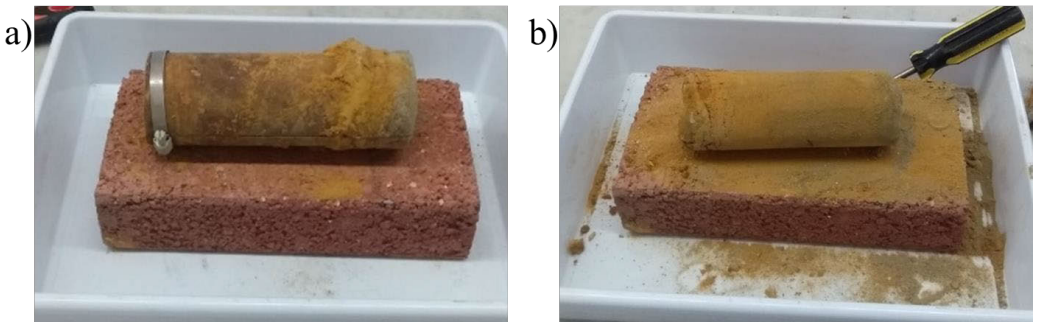

Figure 3.25: *Undisturbed sample: a) inside the split sampler, b) after removal* of the split sampler.

However, despite the great care taken, in four cases the extraction of the specimens from the sampler caused their breakage and consequently the impossibility of testing them. In cases where the extraction from the sampler was successful, the sample, about 20 cm long, was placed in a split-mold of 10 cm (Fig. 3.26) length and the excess ends were sawn off. For the first attempts a wire saw was used as shown in the Figure 3.27 a. However, it was immediately evident that this tool was not suitable because its teeths were too small and were not able to effectively remove the material; moreover, the considerable flexibility of the blade did not allow to achieve precise cuts. It was therefore decided to use a wood saw with a rigid blade which made it possible to obtain effective and precise cuts (Fig. 3.27 b).

Figure 3.26: *Undisturbed sample inside 10 cm split mold.*

Figure 3.27: *Saws used to cut undisturbed samples: a) wire saw, b) wood saw.*

Subsequently, the bases of the specimens were further processed to obtain flat and orthogonal surfaces using a spatula and a file (Fig. 3.28).

Figure 3.28: *Spatula and file.*

Once a specimen of the desired size was prepared, it was placed on the pedestal of the base of the cell (Fig. 3.29) and was then inserted into the membrane.

Figure 3.29: *Undisturbed sample on the base capital.*

The subsequent phases are completely similar to those described for the case of reconstitued specimens with the difference that the saturation phase was preceded by a thawing phase. For the latter, the method proposed by Ghionna & Porcino (2006) and by Wichtmann et al. (2019) was followed. This method consists in leaving the sample to thaw in the cell with a small confining pressure for about 24 h (present case 10 kPa) and controlling volume variations. No appreciable volume variations were found for all the tested samples.

3.3.3. Triaxial tests results

Monotonic triaxial tests

Four monotonic triaxial tests (01_TXMD_22, 02_TXMD_22, 03_TXMD_22, drained and 04_TXMU_22 undrained) were performed at the geotechnical laboratory of the University of Florence. The samples used for these tests were reconstituted with the procedures described in the paragraph 3.3.2. The main characteristics of the tests performed are summarized in table 3.5.

Table 3.5: *Monotonic triaxial tests.*

Sample	Test type	$p'_{cons.}$ [kPa]	$D_{rcons.}$ [%]	w [%]
01_TXMD_22	Drained	100	20.4	5
02_TXMD_22	Drained	200	24.8	5
03_TXMD_22	Drained	50	27.5	5
04_TXMU_22	Undrained	100	29.1	5

In Table 3.5, p'_{cons} is the consolidation average effective stress, $D_{rcons.}$ is the relative density after consolidation and w is the water content of the sample during preparation. The specimens denominated 01_TXMD_22, 02_TXMD_22, 03_TXMD_22 and 04_TXMU_22 were reconstituted with an initial relative density D_{rcons} smaller or equal to 30% (corresponding to a loose state). It was not possible to realize samples with the exact same initial relative density as it was very difficult to assign them the same initial volume.

Figure 3.30 shows the trend of the deviatoric stress $q = \sigma_1 - \sigma_3$ and volumetric strain with respect to the axial strain ε_1 for all four tests performed. These trends agree with those reported in previous studies with drained and undrained monotonic triaxial tests on tailings with loose initial state (Riemer et al. 2008; Bedin et al. 2012; Schnaid et al. 2013 Bhanbhro 2017; Reid et al. 2022: Vergaray et al. 2023).

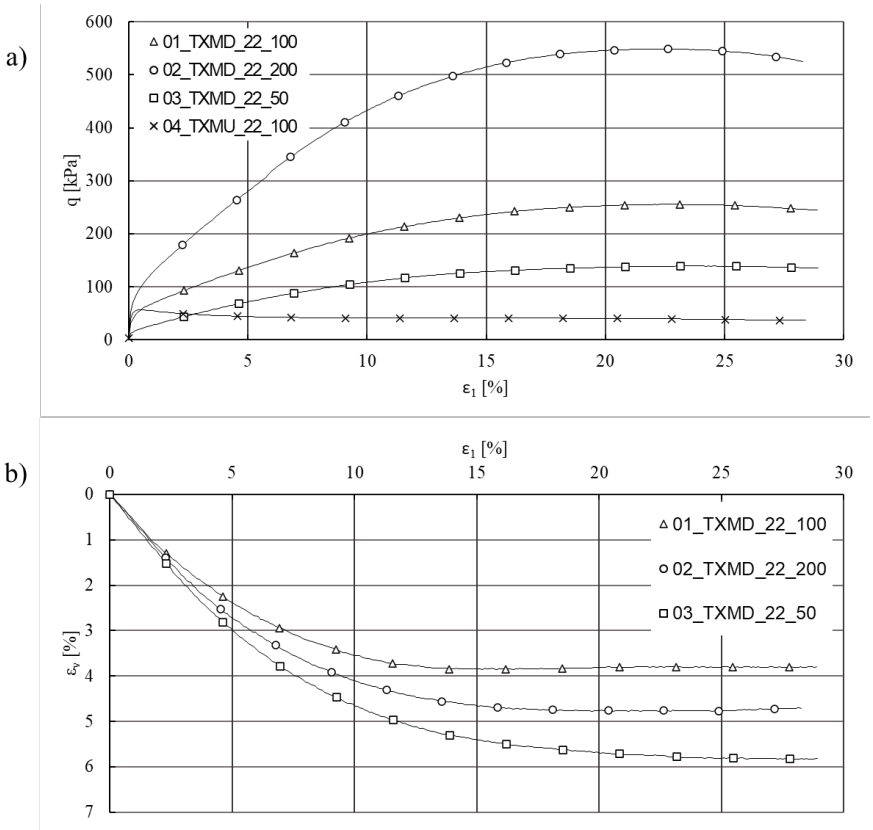

Figure 3.30: *Results of monotonic triaxial tests: a) deviatoric stress vs. axial strain, b) volumetric strain (compaction positive) vs. axial strain.*

Figure 3.31 shows the stress paths of four tests in a diagram with deviatoric stress q versus mean effective stress $p' = {(\sigma_1' + 2\sigma_2')}/{3}$. The effective stress paths of both the drained and the undrained tests end on the line inclined by M_{CS}=1.459. The effective stress path of the undrained test reflects the contractive tendency (excess pore water pressure build-up), which was already observed in the drained tests (Figure 3.30 b).

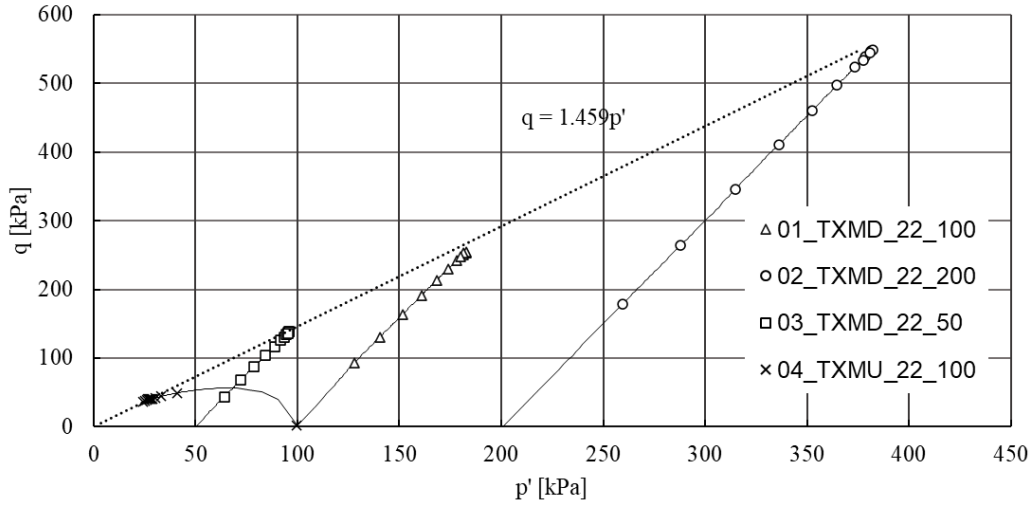

Figure 3.31: *Effective stress paths in drained and undrained monotonic triaxial tests.*

Figure 3.32 shows the trends of the specific volume $v = 1 + e$ with respect to the mean effective stress. The observed contractant trends in the drained and undrained tests agree with what was stated in Schnaid (2013), Da Fonseca (2021) and Reid (2022).

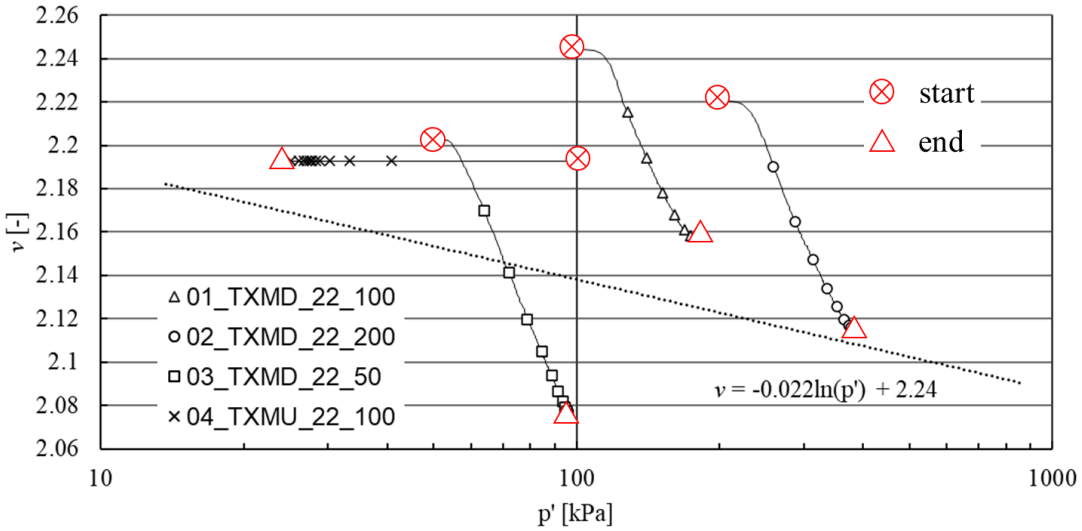

Figure 3.32: *Development of specific volume vs.. mean effective stress in the drained and undrained monotonic triaxial tests.*

In the log-linear diagram in Figure 3.32 the final points of the paths measured in the drained and the undrained tests, although showing some scatter, have been approximated by a linear relationship, representing the critical state line (CSL). The

parameters of the equation are given in Figure 3.32. The value of the specific volume Γ for the unit average effective stress is equal to 2.24 and that of the slope λ of the CSL is 0.022. These values do not differ much from those presented in some other works in which monotonic triaxial tests on tailings were carried out (Riemer et al. 2008; Schnaid et al. 2013; Reid et al. 2022).

Cyclic triaxial tests

Eight stress-controlled undrained cyclic triaxial tests were performed. The tests named 01_TXC_RE_22, 02_TXC_RE_22, 03_TXC_RE_22 and 04_TXC_RE_22 were done on reconstituted samples in the geotechnical laboratory at University of Florence. The tests 05_TXC_RE_22_B was performed on a reconstituted sample at the geotechnical laboratory at Ruhr-Universität Bochum. The tests named 06_TXC_UN_22, 07_TXC_UN_22 and 08_TXC_UN_22 were performed on undisturbed samples at Florence. The characteristics of all tests performed are summarized in Table 3.6. Therein p'_{cons} is the mean effective consolidation stress, q_i the initial (average) deviatoric stress, $CSR = {q_{ampl}}/{2p'_{cons}}$ the cyclic stress ratio, N the number of cycles to failure, D_{rcons} the relative density after consolidation and w the water content during sample preparation. In all tests similar mean effective consolidation stresses of about 100 kPa were chosen. The reconstituted samples were prepared with relative densities between 26% and 37% (i.e. all in the loose range) and subjected to a cyclic loading with different CSR values between 0.10 and 0.19. Of the eight undisturbed samples collected at the tailings dam it was possible to perform the triaxial tests on only three as four broke during the preparation and another sample broke during the consolidation phase of a test the membrane encompassing the sample showed leakage.

Table 3.6: *Cyclic triaxial tests.*

Sample	$p'_{cons.}$ [kPa]	q_i [kPa]	CSR [-]	N [-]	$D_{rcons.}$ [%]	w [%]
01_TXC_RE_22	100	30	0.15	15	37	5
02_TXC_RE_22	97	35.9	0.19	7	26	5
03_TXC_RE_22	98.5	26	0.13	33	30	5
04_TXC_RE_22	98.3	20.75	0.11	83	27	5
05_TXC_RE_22_B	99	19.61	0.10	31	36	5
06_TXC_UN_22	97	35	0.18	21	41	24
07_TXC_UN_22	96	39	0.20	27	69	-
08_TXC_UN_22	99	31	0.16	170	79	21

The results of the tests are shown in Figures 3.33÷3.40 in terms of the effective stress paths, deviatoric stress versus axial strain and of pore water pressure ratio and axial strain versus the number of cycles. The pore water pressure ratio is defined as:

$$r_u = \frac{\Delta u}{p'_{cons}} \tag{3.6}$$

where Δu is the excess pore water pressure and p'_{cons} is the consolidation mean effective stress that is equal to the mean effective stress at the beginning of the cyclic loading phase. Specimens were considered failed if a value of the pore water pressure ratio greater or equal to 0.95 was reached or if axial strain became greater or equal to 5%.

The result of test 01_TXC_RE_22 with D_{rcons}= 37% and CSR= 0.15 are shown in Figure 3.33. It can be seen that the pore water pressure ratio reaches unity (i.e. a state of liquefaction) at the fifteenth cycle accompanied by a considerable increase in axial strains, particularly in extension. The effective stress path reveals that a state with zero effective stress ($p' = q = 0$) is approximately reached.

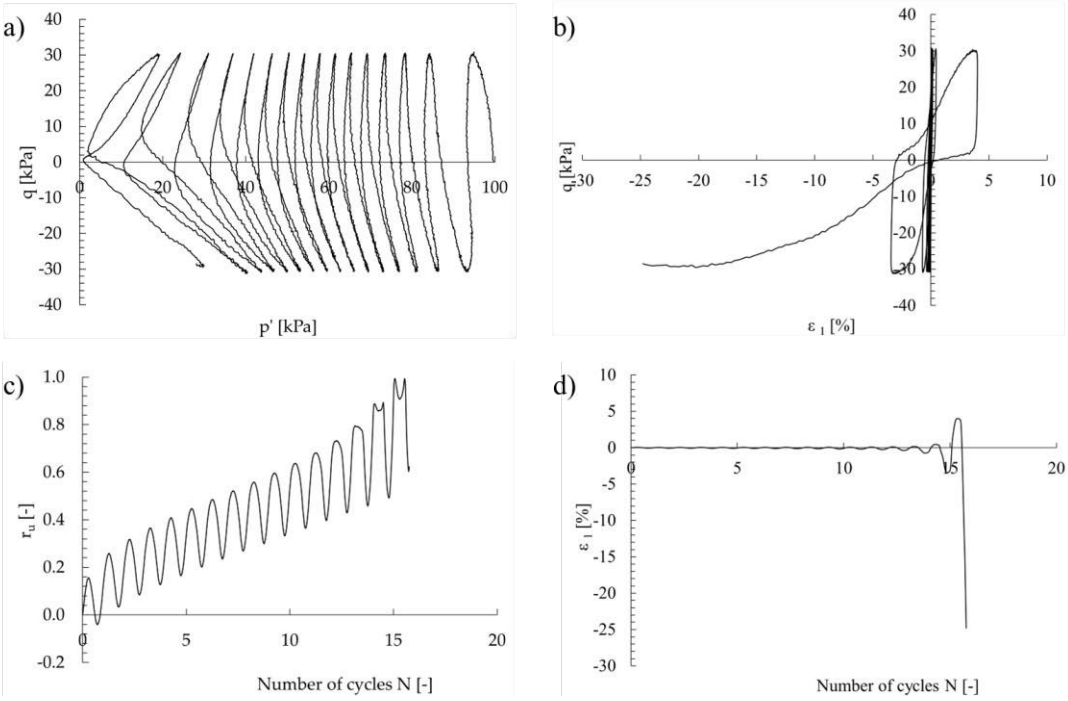

Figure 3.33: *Test 01_TXC_RE_22: a) effective stress paths, b) deviatoric stress vs. axial strain, c) pore water pressure ratio vs. number of cycles, d) axial strain vs. number of cycles.*

The results of test 02_TXC_RE_22 with D_{rcons}= 26 % and the highest cyclic stress ratio of the current test series CSR = 0.19 are presented in Figure 3.34. In this case, failure is reached due to large strains after 7 cycles when the pore water pressure ratio has not yet reached unity.

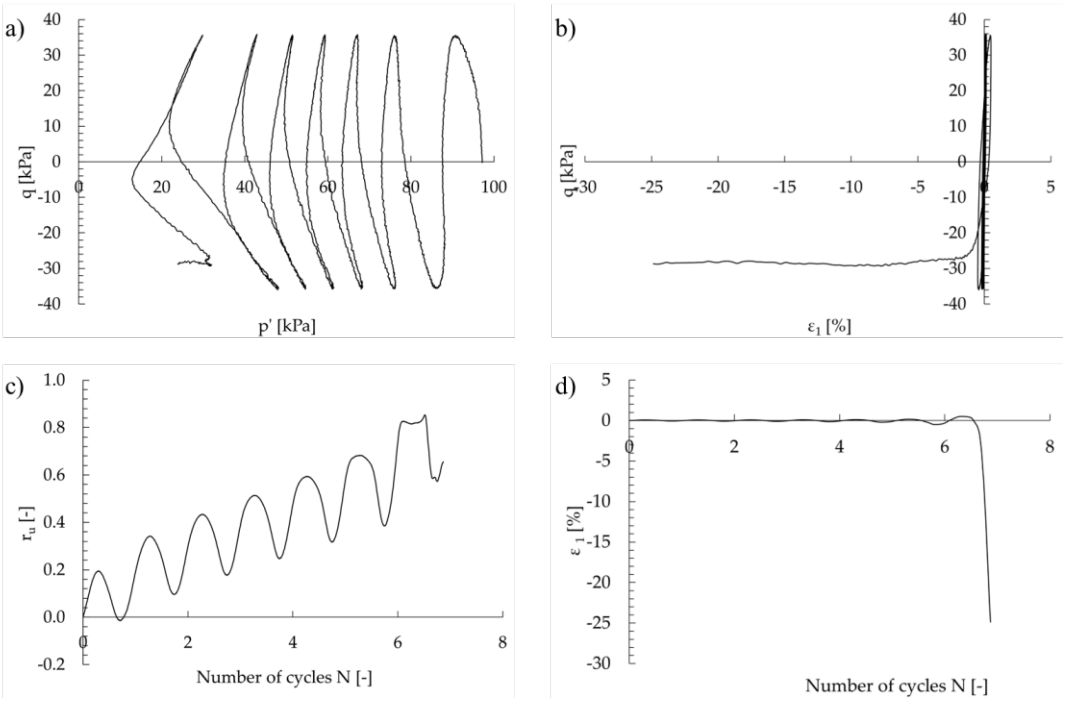

Figure 3.34: *Test 02_TXC_RE_22: a) effective stress paths, b) deviatoric stress vs. axial strain, c) pore water pressure ratio vs. number of cycles, d) axial strain vs. number of cycles.*

The results of test 03_TXC_RE_22 with D_{rcons}= 30 % and the highest cyclic stress ratio of the current test series CSR = 0.13 are given in Figure 3.35. In this case, the failure occurred when the pore water pressure ratio reached unity, resulting in a sudden increase in axial deformations.

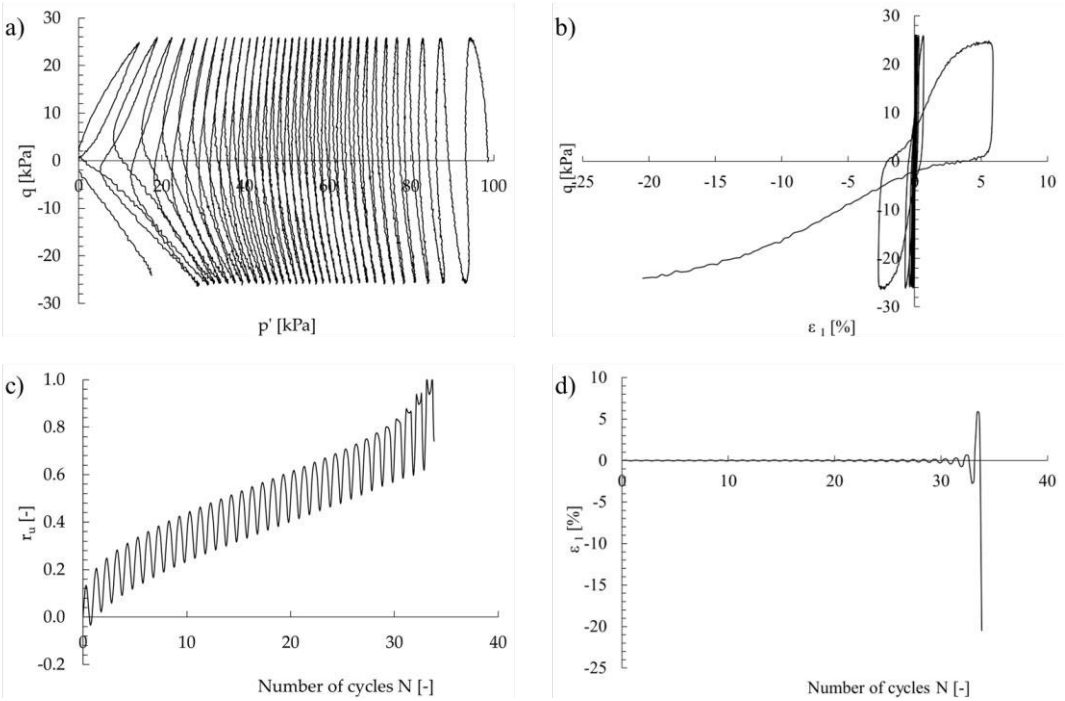

Figure 3.35: *Test 03_TXC_RE_22: a) effective stress paths, b) deviatoric stress vs. axial strain, c) pore water pressure ratio vs. number of cycles, d) axial strain vs. number of cycles.*

The results of test 04_TXC_RE_22 with D_{rcons}= 27 % and the highest cyclic stress ratio of the current test series CSR = 0.11 are shown in Figure 3.36. Also in this case, the specimen failed due to liquefaction after 83 cycles, accompanied by large axial extension strains.

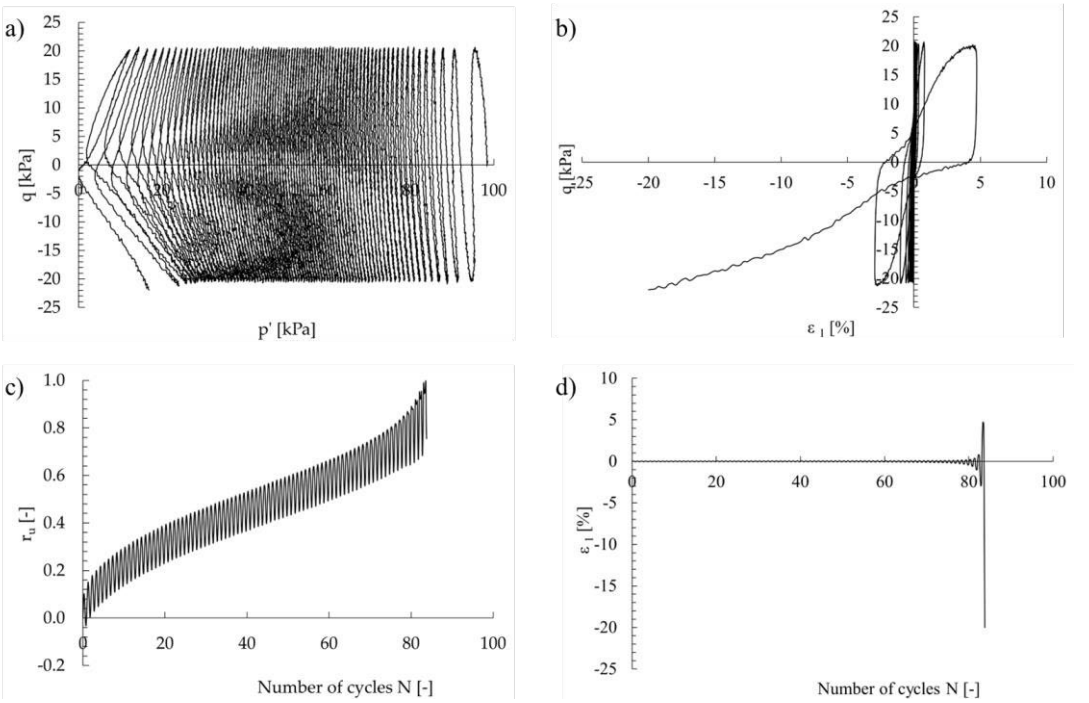

Figure 3.36: *Test 04_TXC_RE_22: a) effective stress paths, b) deviatoric stress vs. axial strain, c) pore water pressure ratio vs. number of cycles, d) axial strain vs. number of cycles.*

The results of test 05_TXC_RE_22_B D_{rcons}= 36 % and the lowest cyclic stress ratio of the current test series CSR = 0.10 performed in Bochum are shown in Figure 3.37. Also, in this case a value of the pore water pressure ratio equal to one was reached. It is interesting to note that the strains gradually increased on both the compression and the extension side as the cyclic loading progressed.

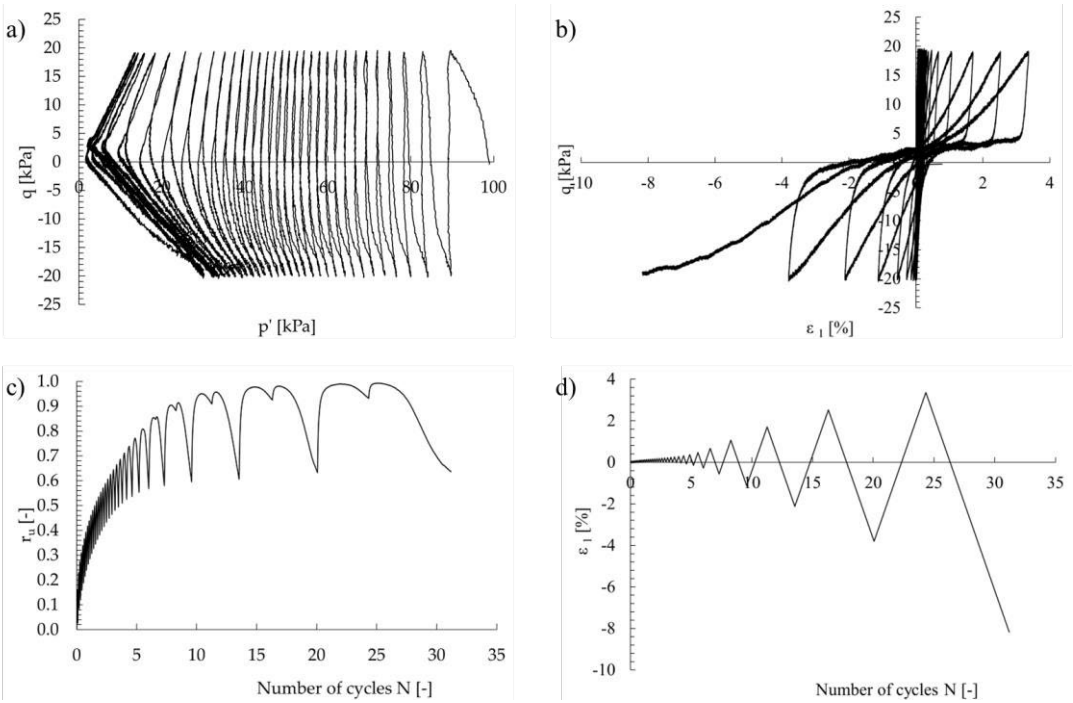

Figure 3.37: *Test 05_TXC_RE_22_B: a) effective stress paths, b) deviatoric stress vs. axial strain, c) pore water pressure ratio vs. number of cycles, d) axial strain vs. number of cycles.*

The results of test 06_TXC_UN_22 D_{rcons}= 41 % and the highest cyclic stress ratio of the current test series CSR = 0.18 performed on an undisturbed sample are shown in Figure 3.38. It is interesting to note that the pore water pressure increases with a different shape compared to the case of reconstituted samples, with a decreasing rate close to failure. At failure large axial strains in extension developed, similar to the reconstituted samples.

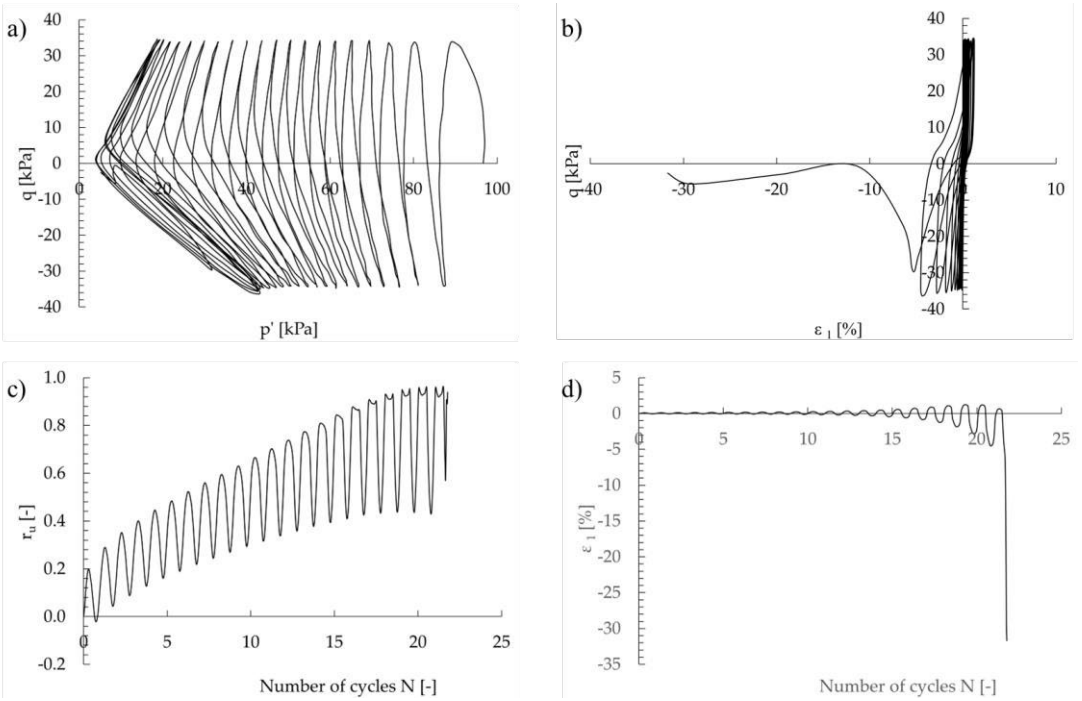

Figure 3.38: *Test 06_TXC_UN_22: a) effective stress paths, b) deviatoric stress vs. axial strain, c) pore water pressure ratio vs. number of cycles, d) axial strain vs. number of cycles.*

The results of test 07_TXC_UN_22 D_{rcons}= 69 % and the highest cyclic stress ratio of the current test series CSR = 0.20 performed on an undisturbed sample are shown in Figure 3.39. In this case it is interesting to note the gradual increase of the axial strains on both the compression and the extension side. Furthermore, the effective stress paths show a butterfly shape, which is typical for medium dense to dense samples of granular materials. The results of this test mainly differ from the previous ones due to the larger relative density of the sample.

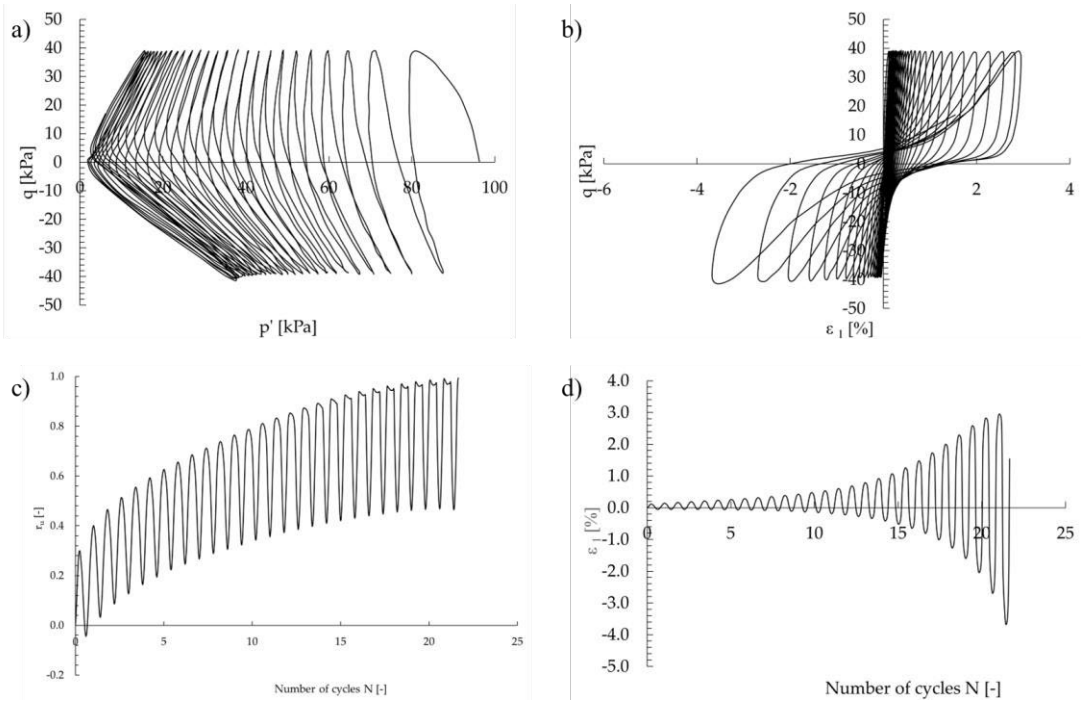

Figure 3.39: *Test 07_TXC_UN_22: a) effective stress paths, b) deviatoric stress vs. axial strain, c) pore water pressure ratio vs. number of cycles, d) axial strain vs. number of cycles.*

The results of test 08_TXC_UN_22 D_{rcons}= 79 % and the highest cyclic stress ratio of the current test series CSR = 0.16 performed on an undisturbed sample are shown in Figure 3.40. This sample failed after 170 cycles. The larger number of applicable cycles corresponds well to the high relative density compared to the other samples.

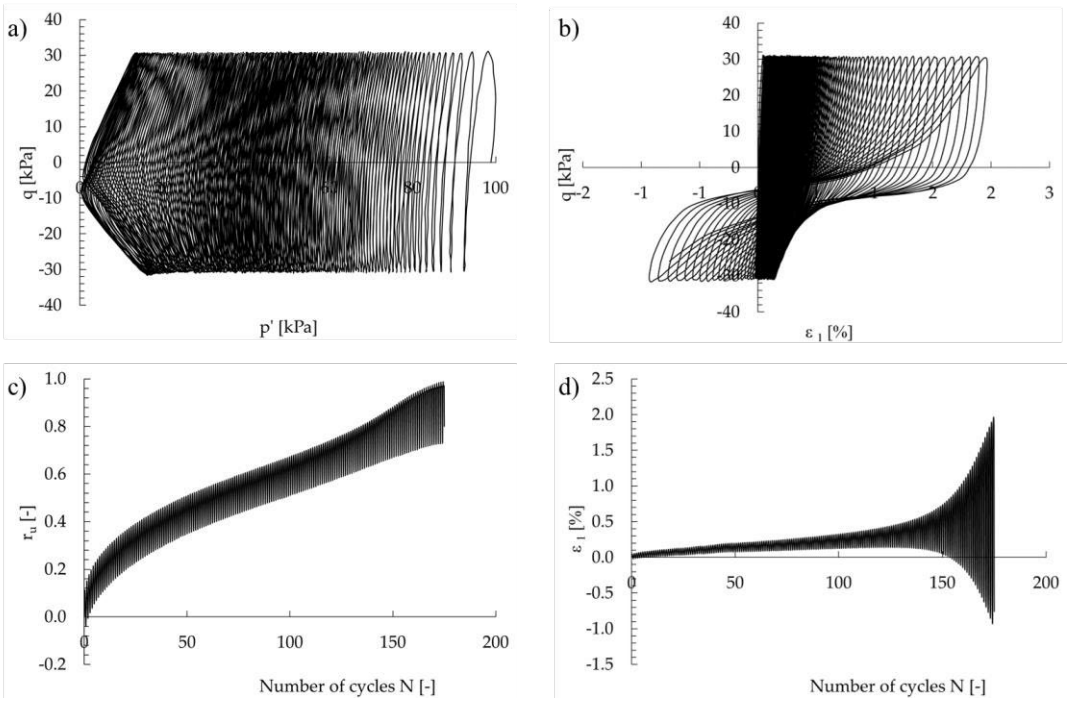

Figure 3.40: *Test 08_TXC_UN_22: a) effective stress paths, b) deviatoric stress vs. axial strain, c) pore water pressure ratio vs. number of cycles, d) axial strain vs. number of cycles.*

In Figure 3.41 the Cyclic Stress Ratio is plotted versus the number of cycles at failure. The diagram contains the data of all tests.

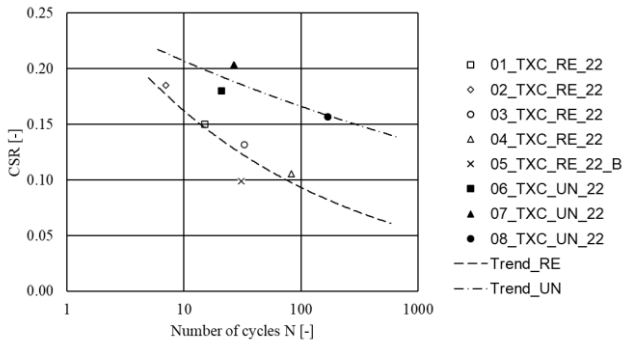

Figure 4.41: *Cyclic Stress Ratio (CSR). vs. number of cycles at failure.*

In Figure 3.41 two different almost parallel trends have been identified, one for the reconstituted specimens (Trend_Re) and one for the undisturbed specimens (Trend_UN). It is evident that the undisturbed samples show a higher, denoting a greater resistance against undrained cyclic loading compared to the reconstituted ones, which may be partly due to the higher relative density of the undisturbed samples. The reconstituted sample tested in Bochum showed a slightly lower liquefaction resistance than those tested in Florence. The reasons for these differences are unclear so far. The results, in terms of CSR and number of cycles, obtained are comparable to those shown by other authors obtained from cyclic tests on tailings (Ishihara et al. 1980; Ishihara et al. 1981; Garga & McKay 1984; Riemer et al. 2008; Liu et al. 2012; Bhanbhro 2017; Vergaray et al. 2023).

Bibliography

Bedin, J., Schnaid, F., Da Fonseca, A. V., & Costa Filho, L. D. M. (2012). Gold tailings liquefaction under critical state soil mechanics. Géotechnique, 62(3), 263-267.

Bhanbhro, R. (2017). Mechanical Behavior of Tailings: Laboratory Tests from a Swedish Tailings Dam (Doctoral dissertation, Luleå University of Technology).

Blannin, R., Frenzel, M., Tolosana-Delgado, R., Büttner, P., & Gutzmer, J. (2023). 3D geostatistical modelling of a tailings storage facility: Resource potential and environmental implications. Ore Geology Reviews, 105337.

Cavarretta, I., O'Sullivan, C., & Coop, M. R. (2009, June). Applying 2D shape analysis techniques to granular materials with 3D particle geometries. In AIP Conference Proceedings (Vol. 1145, No. 1, pp. 833-836). American Institute of Physics.

Ciardi, G., & Madiai, C. (2022). Effects of initial static shear stress on cyclic behaviour of sand stabilised with colloidal silica. Acta Geotechnica, 1-21.

Cox, B. R., Stokoe, K. H., & Rathje, E. M. (2009). An in situ test method for evaluating the coupled pore pressure generation and nonlinear shear modulus behavior of liquefiable soils. Geotechnical Testing Journal, 32(1), 11-21.

Da Fonseca, A. V., Cordeiro, D., & Molina-Gómez, F. (2021). Recommended procedures to assess critical state locus from triaxial tests in cohesionless remoulded samples. Geotechnics, 1(1), 95-127.

DIN 18126. (1996). Baugrund, Untersuchung von Bodenproben. Bestimmung der Dichte nichtbindiger Böden bei lockerster und dichtester Lagerung (in German).

Ente nazionale Italiano di unificazione (UNI). (1964). peso specifico reale di una terra (CNR-UNI 10010). Unificazione italiana.

Fonseca, J., O'Sullivan, C., Coop, M. R., & Lee, P. D. (2012). Non-invasive characterization of particle morphology of natural sands. Soils and Foundations, 52(4), 712-722.

Garga, V. K., & McKay, L. D. (1984). Cyclic triaxial strength of mine tailings. Journal of Geotechnical Engineering, 110(8), 1091-1105.

Ghionna, V. N., & Porcino, D. (2006). Liquefaction resistance of undisturbed and reconstituted samples of a natural coarse sand from undrained cyclic triaxial tests. Journal of Geotechnical and Geoenvironmental Engineering, 132(2), 194-202.

González-Díaz, E., García, S., Soto, F., Navarro, F., Townley, B., & Caraballo, M. A. (2022). Geochemical, mineralogical and geostatistical modelling of an IOCG tailings deposit (El Buitre, Chile): Implications for environmental safety and economic potential. Journal of Geochemical Exploration, 239, 106997.

Hvorslev, J. M. (1949). Subsurface Exploration and Sampling of Soils for Civil Engineering Purposes. Vicksburg: Waterways Experiment Station.

Ishihara, K., Troncoso, J., Kawase, Y., & Takahashi, Y. (1980). Cyclic strength characteristics of tailings materials. Soils and Foundations, 20(4), 127-142.

Ishihara, K., Yasuda, S., & Yokota, K. (1981, April). Cyclic strength of undisturbed mine tailings. In Proceedings of the International Conference on Recent Advances in Geotechnical Earthquake Engineering and Soil Dynamics, St. Louis, Mo (Vol. 26, pp. 53-58).

Kim, Y., Hwang, B., & Cho, W. (2018). Development of ground freezing system for undisturbed sampling of granular soils. Advances in Civil Engineering, 2018, 1-13.

Konrad, J. M. (1990). Sampling of saturated and unsaturated sands by freezing. Geotechnical Testing Journal, 13(2), 88-96.

Krumbein, W. C. (1941). Measurement and geological significance of shape and roundness of sedimentary particles. Journal of Sedimentary Research, 11(2), 64-72.

Ladd, R. S. (1978). Preparing test specimens using undercompaction. ASTM geotechnical testing journal, 1(1).

Lemos, M., Valente, T., Reis, P. M., Fonseca, R., Pantaleão, J. P., Guabiroba, F., … & Delbem, I. (2023). Geochemistry and mineralogy of auriferous tailings deposits and their potential for reuse in Nova Lima Region, Brazil. Scientific Reports, 13(1), 4339.

Liu, H. M., Yang, C. H., Zhang, C., & Mao, H. J. (2012). Study on static and dynamic strength characteristics of tailings silty sand and its engineering application. Safety science, 50(4), 828-834.

Maroof, M. A., Mahboubi, A., Noorzad, A., & Safi, Y. (2020). A new approach to particle shape classification of granular materials. Transportation Geotechnics, 22, 100296.

Presti, D. C. L., Pallara, O., Froio, F., Rinolfi, A., & Jamiolkowski, M. (2006). Stress-strain-strength behaviour of undisturbed and reconstituted gravelly soil samples. Rivista Italiana Di Geotecnica, 40(1), 9-27.

Reid, D., Fanni, R., & Fourie, A. (2022). Effect of tamping conditions on the shear strength of tailings. International Journal of Geomechanics, 22(3), 04021288.

Riemer, M., Moriwaki, Y., & Obermeyer, J. (2008). Effect of high confining stresses on static and cyclic strengths of mine tailing materials. In Geotechnical earthquake engineering and soil dynamics IV (pp. 1-10).

Santamarina, J. C., & Cho, G. C. (2004). Soil behaviour: The role of particle shape. In Advances in geotechnical engineering: The Skempton conference: Proceedings of a three day conference on advances in geotechnical engineering, organised by the Institution of Civil Engineers and held at the Royal Geographical Society, London, UK, on 29–31 March 2004 (pp. 604-617). Thomas Telford Publishing.

Sarkar, D., Koch, F., Goudarzy, M., & Wichtmann, T. (2022). The influence of various end restraints and grain shape on the cyclic undrained behaviour of granular materials. International Journal of Geotechnical Engineering, 1-17.

Schnaid, F., Bedin, J., Viana da Fonseca, A. J. P., & de Moura Costa Filho, L. (2013). Stiffness and strength governing the static liquefaction of tailings. Journal of Geotechnical and Geoenvironmental Engineering, 139(12), 2136-2144.

Schneider, C. A., Rasband, W. S., & Eliceiri, K. W. (2012). NIH Image to ImageJ: 25 years of image analysis. Nature Methods, 9(7), 671–675. doi:10.1038/nmeth.2089

Soto, F., Navarro, F., Díaz, G., Emery, X., Parviainen, A., & Egaña, Á. (2022). Transitive kriging for modeling tailings deposits: A case study in southwest Finland. Journal of Cleaner Production, 374, 133857.

Sun, Q., Zheng, J., Coop, M. R., & Altuhafi, F. N. (2019). Minimum image quality for reliable optical characterizations of soil particle shapes. Computers and Geotechnics, 114, 103110.

Tripodi, E. E. M., Rueda, J. A. G., Céspedes, C. A., Vega, J. D., & Gómez, C. C. (2019). Characterization and geostatistical modelling of contaminants and added value metals from an abandoned Cu–Au tailing dam in Taltal (Chile). Journal of South American Earth Sciences, 93, 183-202.

Vergaray, L., Macedo, J., & Arnold, C. (2023). Static and Cyclic Liquefaction of Copper Mine Tailings. Journal of Geotechnical and Geoenvironmental Engineering, 149(5), 04023021.

Wichtmann, T. (2016). Soil behaviour under cyclic loading-experimental observations, constitutive description and applications. Th. Triantafyllidis.

Wichtmann, T., Steller, K., Triantafyllidis, T., Back, M., & Dahmen, D. (2019). An experimental parametric study on the liquefaction resistance of sands in spreader dumps of lignite opencast mines. Soil Dynamics and Earthquake Engineering, 122, 290-309.

Wride, C. E., Hofmann, B. A., Sego, D. C., Plewes, H. D., Konrad, J. M., Biggar, K. W., ... & Monahan, P. A. (2000). Ground sampling program at the CANLEX test sites. Canadian geotechnical journal, 37(3), 530-542.

Yan, W. M., & Su, D. (2018). Inferring 3D particle size and shape characteristics from projected 2D images: Lessons learned from ellipsoids. Computers and Geotechnics, 104, 281-287.

Yoshimi, Y., Hatanaka, M., Oh-Oka, H. (1978). Undisturbed Sampling of Saturated Sands by Freezing. Soils and Foundation, 59-73.

Yoshimi, Y., Tokimatsu, K., & Hosaka, Y. (1989). Evaluation of liquefaction resistance of clean sands based on high-quality undisturbed samples. Soils and Foundations, 29(1), 93-104.

Yoshimi, Y., Tokimatsu, K., Kaneko, O., & Makihara, Y. (1984). Undrained cyclic shear strength of a dense Niigata sand. Soils and Foundations, 24(4), 131-145.

Zheng, J., Sun, Q., Zheng, H., Wei, D., Li, Z., & Gao, L. (2020). Three-dimensional particle shape characterizations from half particle geometries. Powder Technology, 367, 122-132.

Zięba, Z. (2017). Influence of soil particle shape on saturated hydraulic conductivity. Journal of Hydrology and Hydromechanics, 65(1), 80-87.

4. Numerical modeling of Tailings Storage Facilities (TSF)

A comprehensive study on the behavior of a tailings dam during and after a seismic event should provide results in terms of displacement, load, strain, stress, acceleration, and pore pressure trends. To date, the only way to obtain all these results is to perform a numerical finite element (or difference) analysis. These analyses are not always recommended (not only for the study of tailings dams, but more generally in the geotechnical field) due to their complexity, as they require a lot of time for the creation of the model and the analyses, the in-depth knowledge of numerical, mechanical, and geotechnical aspects needed by the operator, and for the numerous parameters required, which often implicate specialized tests (Zdravković 1999; Lees 2013). Conversely, other methods, such as the limit equilibrium method, although generally simpler, provide limited information, such as the safety factor FS, when analyzing the stability of a structure. In this chapter, these aspects are addressed with reference to a selection of tailings dam modeling cases from the literature. In Table 4.1, some information concerning the selected case studies are summarized: type and location of the facility (when reported), the construction method, the number of dimensions of the analysis, the used software, if the analysis is conducted with the finite element or difference method and the constitutive models. It should be noted that Machaček's et al. (2018) work is aimed at the analysis of a dump in the Rhenish mining area. and not strictly a tailings dam. However, it was decided to include this paper as well, as it deals with a structure with characteristics similar to those of a tailings storage facility and for the high quality of the work.

Table 4.1: *Scientific documents analyzed and main information about the reported case studies.*

No.	Year	Authors	SAC	D	Sft.	AT	Liq C.M.	Non liq. C.M.	Ele.Type
1	1990	Vick (1990)	Se.	2D		FEM			Quad.
2	2007	Liu et al. (2007)	St. & Se.	2D		FEM			
3	2008	Psarropoulos & Tsompanakis (2008)	St. & Se.	2D	Plaxis	FEM		Mohr-Coulomb	6 n. tri.
4	2009	Chakraborty & Choudhury (2009)	St. & Se.	3D	Flac 3D	FDM		Mohr-Coulomb	
5	n. d.	Nejad et al. (n. d.)	Se.	2D	Flac	FDM	Finn-Byrne	Mohr-Coulomb	Quad.
6	2010	Liang & Elias (2010, November)	Se.	2D	Plaxis	FEM		Mohr-Coulomb	15 n. tri.
7	2011	Chakraborty & Choudhury (2011)	St. & Se.	2D	Flac 3D	FDM	Finn-Byrne	Mohr-Coulomb	Quad.

No.	Year	Authors	SAC	D	Sft.	AT	Liq C.M.	Non liq. C.M.	Ele.Type
8	2011	Meisheng & Laigui (2011, April)	Se.	2D			Finn-Byrne	Mohr-Coulomb	Tri.
9	2011	Wang et al. (2011)	Se.	2D	Flac	FDM	Finn-Byrne	Mohr-Coulomb	Quad.
10	2013	Skau et al. (2013)	St.	2D	Plaxis	FEM		Hardening soil model	Tri.
11	2014	Ishihara et al. (2015)	Se.	2D					Quad.
12	2015	Barrero et al. (2015)	Se.	2D	Flac	FDM	SANISAND	Mohr-Coulomb	Quad.
13	2015	Xu et al. (2015)	Se.	2D	QUAKE/W	FEM	linear equivalent		
14	2016	Morgenstern et al. (2016)	St. & Se.	2D and 3D	Flac & Flac 3D	FDM	NorSand	Mohr-Coulomb and CHSoil	
15	2017	Świdziński (2016)	Se.	1D			C/L model		
16	2017	James & Aubertin (2017)	Se.	1D	Flac	FDM	UBCSAND		
17	2017	Zardari et al. (2017)	Se.	2D	Plaxis	FEM	UBCSAND	Mohr-Coulomb	15 n. tri.
18	2018	Machaček et al. (2018)	Se.	2D	Abaqus	FEM	hypoplastic	ISA-Clay	6 n. tri. & 8 n. Quad.
19	2018	Naeini & Akhtarpour (2018)	Se.	2D	SIGMA/W - QUAKE/W	FEM	linear equivalent	Mohr-Coulomb	7 n. tri. & 9 n. Quad.
20	2019	Hegde & Das (2019)	Se.	2D	RS^2	FEM		Mohr-Coulomb	6 n. tri.
21	2019	Vargas (2019, November)	Se.	2D	QUAKE/W	FEM	linear equivalent		Quad.
22	2020	Sottile et al. (2020)	St.	2D	Plaxis	FEM	(HSS)	Mohr-Coulomb	15 n. tri.
23	2021	Do et al. (2021)	St.	2D	Plaxis	FEM	UBCSAND	Mohr-Coulomb	15 n. tri.
24	2022	Ledesma et al. (2022)	St.	2D	Plaxis	FEM	Modified Pastor-Zienkie		15 n. tri.

No.	Year	Authors	SAC	D	Sft.	AT	Liq C.M.	Non liq. C.M.	Ele.Type
							wicz model		

* SAC: Stability analysis conditions: St. static; Se. seismic; D: Dimensions; Stf.: Software; AT: Type of analysis: Liq. C.M: Constitutive model for liquefiable materials; Non liq. C.M.: Constitutive model for non-liquefiable materials; Ele. Type: Element type; (Cntl. Centerline; Quad.: Quadrilateral; 6 n. tri.: six node triangular; 15 n. tri.: fifteen node triangular; Tri.: triangular; 6 n. tri. & 8 n. Quad: six node triangular and eight node quadrangular; 6 n. tri. & 9 n. Quad.: six node triangular and nine node quadrangular).

Table 4.1 also shows that Plaxis (Psarropoulos & Tsompanakis 2008; Liang & Elias 2010; Skau et al. 2013; Zardari et al. 2017; Sottile et al. 2020; Do et al. 2021; Ledesma et al. 2022) and Flac (Chakraborty & Choudhury 2009; Nejad et al. (n. d.); Chakraborty & Choudhury 2011; Wang et al. 2011; Barrero et al. 2015; Morgenstern et al. 2016; James & Aubertin 2017 et al.) are the most utilized softwares.

Table 4.2 shows for each article analyzed the ore type deposited in the tailings dam and the sources from which the geotechnical characteristics used to model the structures were obtained.

Table 4.2: *Tailings storage facility name and location, construction type, ore type and sources of the geotechnical parameters.*

No.	Authors	TSF/location	Construction Type	Ore type	Geotechnical characteristics origin
1	Vick (1990)	Typical tailings dams	Centerline	Not specified	Not specified
2	Liu et al. (2007)	Baizhishan - China	Upstream	Steel and iron	Laboratory tests
3	Psarropoulos & Tsompanakis (2008)	Typical tailings dams	Upstream Downstream Centerline	Not specified	Literature
4	Chakraborty & Choudhury (2009)	Typical tailings dams	Water retention type	Not specified	Not specified
5	Nejad et al. (n. d.)	Bobadil - Tasmania	Upstream	Zinc, lead and silver	Field tests, laboratory tests, literature, correlations and experience
6	Liang & Elias (2010, November)	Australia	Upstream Downstream	Not specified	Not specified
7	Chakraborty & Choudhury (2011)	India	Downstream	Not specified	Not specified
8	Meisheng & Laigui (2011, April)	China	Upstream	Not specified	Not specified

No.	Authors	TSF/location	Construction Type	Ore type	Geotechnical characteristics origin
9	Wang et al. (2011)	Xiangyun - China	Upstream	Phosphogypsum	Laboratory tests
10	Skau et al. (2013)	Żelazny Most - Poland	Upstream	Copper	Laboratory tests
11	Ishihara et al. (2015)	1)Takasegamori 2)Kayakari-Japan	Upstream	Gold and silver	Field tests and laboratory tests
12	Barrero et al. (2015)			Not specified	Not specified
13	Xu et al. (2015)	Lingshan - China	Upstream	Gold	Field tests and laboratory tests
14	Morgenstern et al. (2016)	Fundão - Brazil	Upstream	Iron	Field tests and laboratory tests
15	Świdziński (2016)	Żelazny Most - Poland	Upstream	Copper	Laboratory tests
16	James & Aubertin (2017)	Canada		Iron	Laboratory tests
17	Zardari et al. (2017)	Aitik - Sweden	Upstream	Copper	Field tests and, laboratory tests and literature
18	Machaček et al. (2018)	Germany		Lignite	Field tests and laboratory tests
19	Naeini & Akhtarpour (2018)	Sungun - Iran	Centerline	Copper	Field tests and laboratory tests
20	Hegde & Das (2019)	India	Upstream	Not specified	Not specified
21	Vargas (2019, November)	Mexico	Upstream	Not specified	Field tests and laboratory tests
22	Sottile et al. (2020)	Typical tailings dams	Upstream	Not specified	Laboratory tests
23	Do et al. (2021)	Typical tailings dams	Upstream	Not specified	Literature
24	Ledesma et al. (2022)	Fundão - Brazil	Upstream	Iron	Literature

From Table 4.1 it is possible to observe that the upstream type is the most studied type of structure (17 cases) (Liu et al. 2007; Psarropoulos & Tsompanakis 2008 Liang & Elias 2010; Nejad et al. (n. d.); Meisheng & Laigui 2011; Wang et al. 2011; Skau et al. 2013; Ishihara et al. 2015; Xu et al. 2015; Morgenstern et al. 2016; Świdziński 2016; Zardari et al. 2017; Hegde & Das 2019; Vargas 2019; Sottile et al. 2020; Do et al. 2021; Ledesma et al. 2022), denoting the greater attention to this type of construction method. Table 4.2 summarizes some geotechnical parameters that could be deduced from the analysis of the various articles. In particular these are: effective cohesion c', undrained shear strength c_u, effective friction angle φ', specific unit weight γ, permeability k, Poisson's ratio ν, initial shear modulus G_{max}, porosity n and small strain elastic modulus E. The numbers in the first column refer to the identification number of the articles shown in Tables 4.1 and 4.2.

Table 4.3: *Geotechnical parameters deduced from scientific documents*

No.	Par.	Bdr	Bbt-Fnd	Starter Dike	Cmt	Tailings - slimes	Cly-Md	Rckf-St	Drain layer	Alv	L.S	Last	Sot.
2	c'[kPa]					0	25						
3	c'[kPa]					5	40						
4	c'[kPa]		31.25		14.7	14.7							
5	c'[kPa]		1	1									
6	c'[kPa]		0		0	0	0	0					
7	c'[kPa]	300	70	0	15.2	12	80	70	0				
8	c'[kPa]			0.5	1.8-2-2.5	1-1.2	18						
9	c'[kPa]	11		20		6							
12	c'[kPa]	0	0			0		0		0	0		
17	c'[kPa]			1	13	10	1	1	1				6
19	c'[kPa]		10	0		0	15	0					
21	c'[kPa]			5	2	2		21					
22	c' [kPa]		1			1		5					
23	c'[kPa]		1	1				1					
24	c'[kPa]				5								
2	φ'[°]					36	28.4						
3	φ'[°]					5	25						
4	φ'[°]		28		15.2	12							
5	φ'[°]		40	39	0	0	0						
6	φ'[°]		40		30	20	35	38					
7	φ'[°]	35	20	42	14.7	14.7	17	20	32				
8	φ'[°]			38	32-33-35	31-35	17						
9	φ'[°]	22		28		23							
10	φ'[°]		35			35							
12	φ'[°]	40	40	34		33	34	34		35	28		
16	φ'[°]		33.5			36.6							
17	φ'[°]			35	26	22	37	42	32				18
18	φ'[°]				33.1	35.6							
19	φ'[°]		25	45		35	32						
21	φ'[°]			42	30	30	30	23					
22	φ'[°]		40			35		33					
23	φ'[°]		37	35				42					
24	φ'[°]				30								
2	γ [kN/m^3]					21.97	19.12						

No.	Par.	Bdr	Bbt-Fnd	Starter Dike	Cmt	Tailings - slimes	Cly-Md	Rckf-St	Drain layer	Alv	L.S	Last	Sot.
3	γ [kN/m^3]		18.3			24	18						
4	γ [kN/m^3]				19	19							
6	γ [kN/m^3]		22		18	17	17	18					
7	γ [kN/m^3]	20	19	20	19	19	19	19	20				
8	γ [kN/m^3]			19.13	18.37	17.02	17.65						
9	γ [kN/m^3]	16.18		16.67		11.28							
10	γ [kN/m^3]		20.7			21							
12	γ [kN/m^3]	20	25.6	15.8		19.9	15.8	15.8		16	14.4		
15	γ [kN/m^3]					15.88							
16	γ [kN/m^3]	25.49	13.72			23.24							
17	γ [kN/m^3]			22	19	18	22	20	20			19	18
19	γ [kN/m^3]		20.7			19.2	19.7	19.4					
20	γ [kN/m^3]				20.7	20							
21	γ [kN/m^3]	24	22	21				16.4					
23	γ [kN/m^3]		22	22				20					
24	γ [kN/m^3]				22								
2	k [m/s]					5.9E-06	6.8E-08						
4	k [m/s]		1.00E-08		1.00E-08	1.00E-08							
5	k [m/s]		5.00E-07		4.00E-07	5.00E-07	5.00E-08	1.00E-04					
7	k [m/s]	1.00E-09	1.50E-09	1.00E-02	1.00E-08	1.00E-08	1.00E-09	1.50E-09	1.00E-04				
8	k [m/s]			4.00E-03	2.00E-05	2.00E-05	1.80E-08						
9	k [m/s]	1.00E-08		2.00E-08		3.00E-07							
10	k [m/s]	2.00E-10	2.00E-07			1.20E-07							
17	k_x [m/s]			1.00E-07	1.00E-06	1.00E-07	5.00E-08	1.00E-01	1.00E-03			5.00E-07	5.00E-07
17	k_y [m/s]			5.00E-08	1.00E-07	1.00E-08	5.00E-08	1.00E-01	1.00E-03			5.00E-08	5.00E-07
19	k_y [m/s]		6.00E-06	1.60E-03		1.4 E-7 to 8.7 E-10	6.80E-09	4.90E-06					
21	k [m/s]	5.90E-08	1.00E-07	1.00E-06	f(z)	f(z)	f(z)	1.00E-08					
23	k [m/s]		4.98E-08	1.00E-07				1.00E-01					

No.	Par.	Bdr	Bbt-Fnd	Starter Dike	Cmt	Tailings - slimes	Cly-Md	Rckf-St	Drain layer	Alv	L.S	Last	Sot.
23	k [m/s]		1.00E-08	4.98E-08				1.00E-01					
2	ν [-]					0.30	0.33						
4	ν [-]		0.20		0.35	0.35							
5	ν [-]	0.4	0.33	0.33	0.45	0.45	0.45	0.26					
7	ν [-]	0.35	0.49	0.33	0.35	0.35	0.49	0.49	0.33				
8	ν [-]			0.25	0.3-0.35	0.3-0.35	0.38						
12	ν [-]	0.31	0.26	0.33		0.27	0.33	0.33		0.26	0.33		
16	ν [-]	0.2											
18	ν [-]				0.36	0.36							
19	ν [-]		0.3	0.23		0.3	0.3	0.28					
20	ν [-]				0.29	0.29							
21	ν [-]	0.25	0.3	0.28	0.33	0.33		0.3					
24	ν [-]				0.2								
4	G_{max} [Mpa]		217.35		53.65	45.64							
5	G_{max} [Mpa]	1350											
7	G_{max} [Mpa]	2000	15	40.5	95.4	45.6	24	15	40.5				
21	G_{max} [Mpa]	1198.777	330.275	342.508	260.958	65.24		104.485					
22	G_{max} [Mpa]				50								
4	n [-]				0.25	0.25	0.3						
9	n [-]	0.3		0.4		0.3							
16	n [-]	0.02	0.45			0.39							
3	E [MPa]	35500	764			3	8	4					
6	E [MPa]		100		10	3	20	50					
8	E [MPa]			120	43	16.74	10						
16	E [MPa]	20000				3	8						
17	E [MPa]			20	8.8	9.3	20	400	20				9.8
19	E [MPa]			50		7	20						
20	E [MPa]				25.7	12.8							
21	E [MPa]	4000	2000		18	5 -10		26.76					
23	E [MPa]		20	20				40					

* Par.: geotechnical parameter; Bdr: Bedrock; Bbt-Fnd: Layer beetwen bedrock and tailings-foundation; Cmt: Compacted tailings; Cly-Md: Clay-moraine dikes; Rckf-St: Rockfill - sand tailings; Alv: Alluvial; L.S: liquefiable sands; Last: Layered sand tailings; Sot: Soft sand tailings

From the analysis of Table 4.3 it is possible to deduce that the materials defined as tailings are generally attributed rather low cohesion values which do not exceed 5 kPa with the exception of Chakraborty & Choudhury (2009) and Zardari (2017) where values of 14.7 and 13 kPa are respectively assigned. As regards the values attributed to the friction angle, these are between 12 and 36 degrees with the particular case of Nejad (n.d.) in which a null value is assigned. The specific unit weights γ lie between 17 and 23 kN/m^3 with the exception of Wang (2011) which assigns a specific unit weight of 11.28 kN/m^3. Permeability k has orders of magnitude ranging from 10^{-6} to 10^{-8} m/s. For both the shear modulus G_{max} and the elastic modulus E quite different values for the various articles. Figure 4.1 shows the comparison between some geotechnical characteristics (cohesion, friction angle and specific unit weight) based on the ore type.

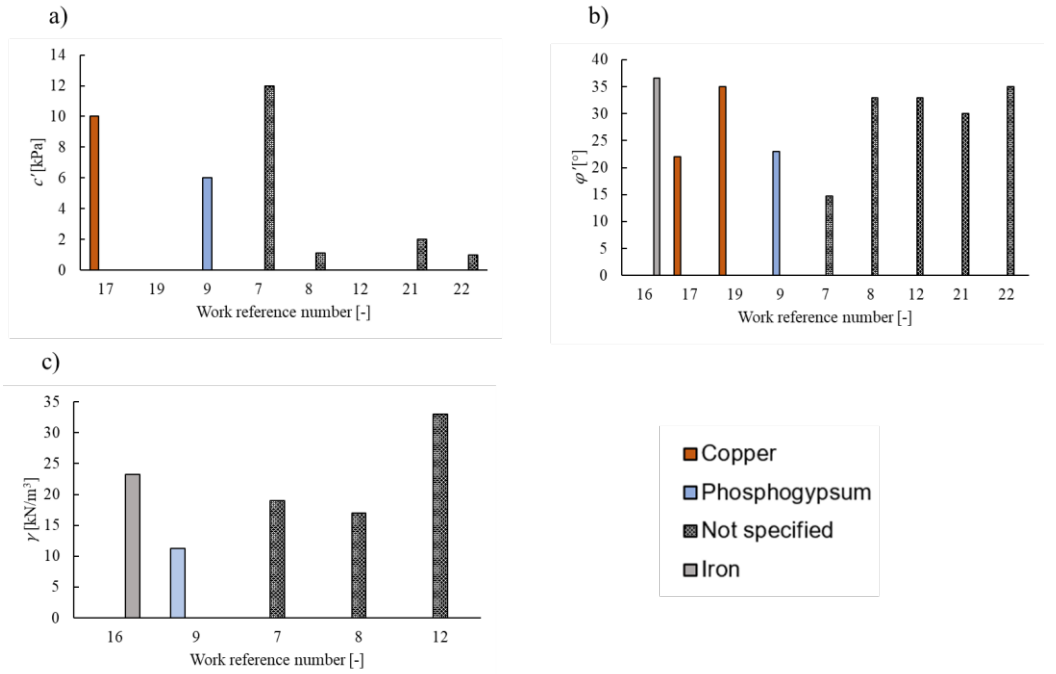

Figure 4.1: *Comparison of the geotechnical parameters a) cohesion, b) effective friction angle and c) specific unit weight, reported in Table 4.3 for different ore type.*

Given the limited amount of data from Figure 4.1, it is not possible to derive correlations between the geotechnical characteristics and the ore type. It would therefore be necessary to enrich the available data with information obtained from different types of scientific articles (which do not deal with numerical modeling but with other aspects concerning TSF) in order to be able to obtain useful information on these materials, which is beyond the scope of the present research.

Geometry, mesh and type of elements, boundary conditions, initial conditions, load definition, and constitutive models are the main key points required to define a finite element model. In the following paragraphs they are briefly described, discussed and compared for the selected cases listed in Table 4.1 where it was possible to distinguish them precisely.

Geometry

The modeling of tailings dams is formally linked to morphological aspects; therefore, the one-dimensional analysis of these structures is not very significant, although some authors have performed this kind of analysis. 2D plane strain models are generally conducted on a vertical section of the structure. Normal and shear deformations, as well as shear stresses, can only occur in the plane. The only non-zero stresses in the out-of-plane direction are the normal ones. A 3D model certainly describes more precisely the structure; however, it requires knowledge of aspects that are often unknown and considerably burdens the work and analysis. Of 24 documents dealing with the numerical modeling of tailings dams analyzed, 21 (Vick 1990; Liu et al. 2007; Psarropoulos & Tsompanakis 2008; Nejad et al. (n. d.); Liang & Elias 2010; Chakraborty & Choudhury 2011; Meisheng & Laigui 2011; Wang et al. 2011; Skau et al. 2013; Ishihara et al. 2015; Barrero et al. 2015; Xu et al. 2015; Zardari et al. 2017; Machaček et al. 2018; Naeini & Akhtarpour 2018; Hegde & Das 2019; Vargas 2019; Sottile et al. 2020; Do et al. 2021; Ledesma et al. 2022) describe the problem with a 2D model, 2 with a 1D model (Świdziński 2016; James & Aubertin 2017 et al.), one with a 3D model (Chakraborty & Choudhury 2009) and one (Morgenstern et al. 2016) uses both 2D and 3D schemes.

Another fundamental aspect concerning the geometry of an FEM model is the distance of the bottom and side boundaries from the study domain because, as well known, an inappropriate distance can cause unrealistic boundary effects on the results. On the other hand, too far distance can lead to a model that is unnecessarily large with oversized analysis times and costs. There is no unique solution to this problem, and it is often based on operator experience and common sense. In the case of tailings dams, the analysis generally refers to the study of a large embankment consisting of a valley bank characterized by a considerable slope. Various authors found different solutions to model the geometry of the structure. Figure 4.2 shows the geometries of the models created by the authors of the analyzed papers. In some cases, the geometry represented in Fig. 4.2 is simplified compared to that of the original paper, as the purpose of this analysis is to examine the dimensions given to the model with respect to the dimensions of the dam.

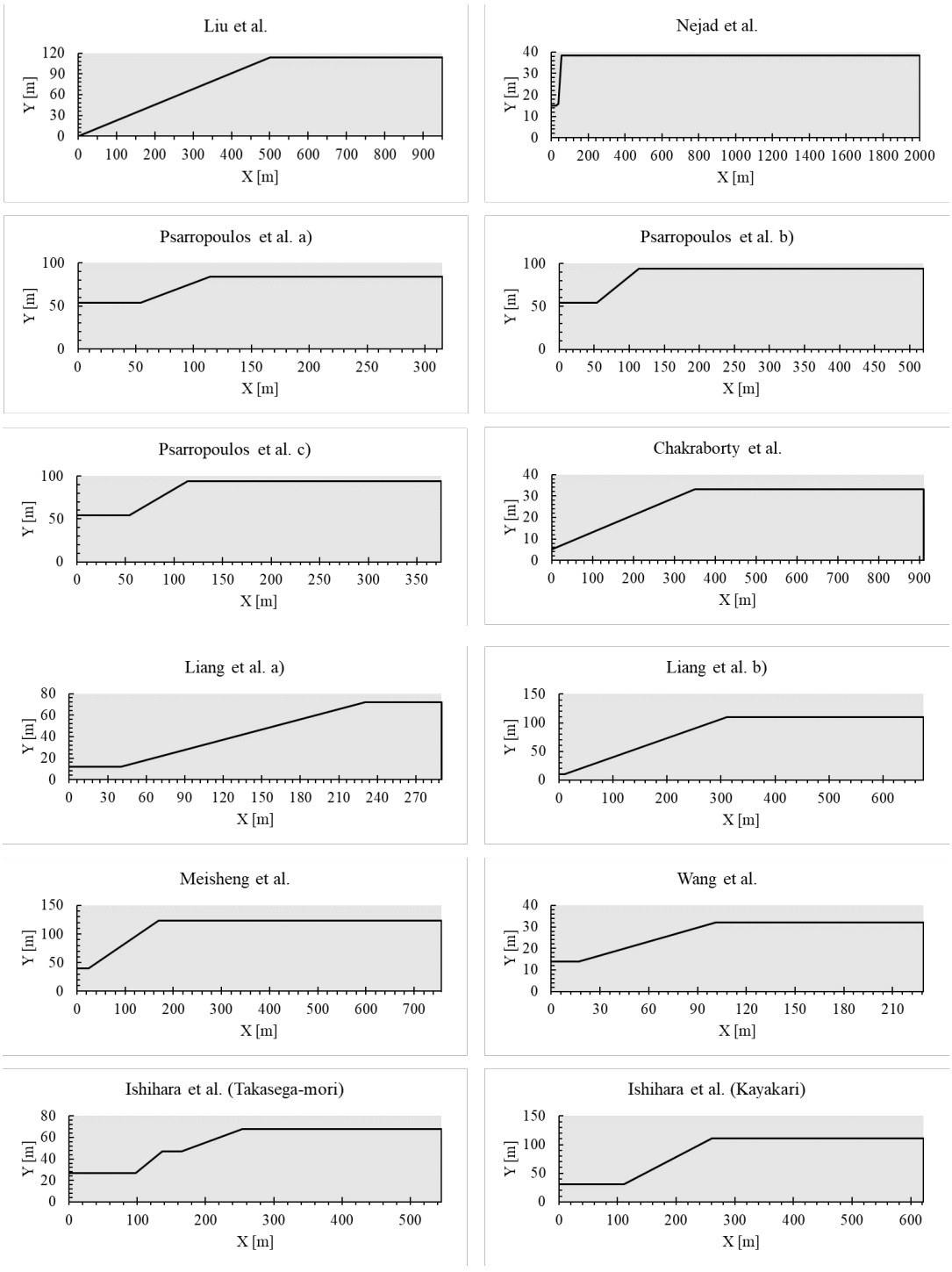
Liu et al.
Y [m]
X [m]
Nejad et al.
Y [m]
X [m]
Psarropoulos et al. a)
Y [m]
X [m]
Psarropoulos et al. b)
Y [m]
X [m]
Psarropoulos et al. c)
Y [m]
X [m]
Chakraborty et al.
Y [m]
X [m]
Liang et al. a)
Y [m]
X [m]
Liang et al. b)
Y [m]
X [m]
Meisheng et al.
Y [m]
X [m]
Wang et al.
Y [m]
X [m]
Ishihara et al. (Takasega-mori)
Y [m]
X [m]
Ishihara et al. (Kayakari)
Y [m]
X [m]

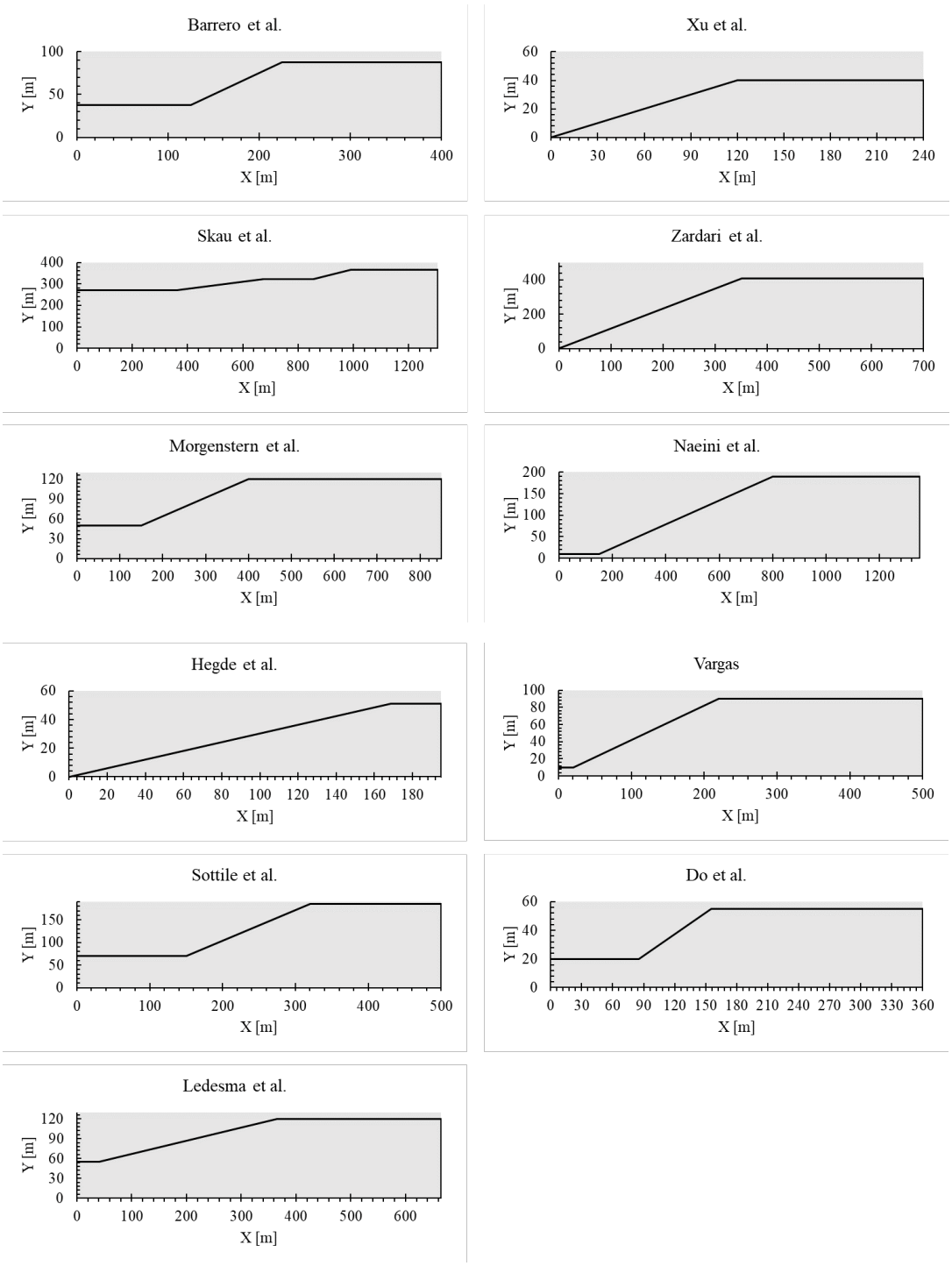

Figure 4.2: *Geometry of 2D models used in analyzed articles.*

From Figure 4.2 it is possible to observe that, in most cases, in the horizontal direction, the dimension of the model is approximately double compared to the extension of the dam (Liu et al. 2007; Psarropoulos & Tsompanakis a. and c.; Liang & Elias 2010 b.; Nejad et al. (n. d.); Chakraborty & Choudhury 2011; Wang et al. 2011; Skau et al. 2013; Ishihara et al. 2015 (Takasega-mori and Kayakari); Barrero et al. 2015; Xu et al. 2015; Morgenstern et al. 2016; Zardari et al. 2017; Naeini & Akhtarpour 2018; Vargas 2019; Sottile et al. 2020; Do et al. 2021; Ledesma et al. 2022). In some cases, (Psarropoulos & Tsompanakis 2008 b.; Chakraborty & Choudhury 2011; Meisheng & Laigui 2011) the

horizontal dimension of the model is much greater than the extent of the slope while in two cases (Liang & Elias 2010 a.; Hegde & Das 2019) the vertical and horizontal dimensions are comparable. The vertical extension of the model essentially depends on the stratigraphic conditions of the site.

Mesh and elements

Once the geometry has been defined, the model is discretized with a mesh that is characterized by the shape, dimension, and number of nodes of the elements that compose it. In the case of 2D modeling of tailings dams, triangular or quadrangular elements are generally used with a denser structure (smaller element sizes) in the areas of greatest interest and coarser in the distant areas. In most cases, the triangular elements are characterized by six or fifteen nodes, while the quadrangular ones have eight or nine nodes. Of 20 papers that deal with 2D models, six of them (Vick 1990; Nejad et al. (n. d.); Liang & Elias 2010; Chakraborty & Choudhury 2011; Wang et al. 2011; Ishihara et al. 2015; Barrero et al. 2015; Vargas 2019) utilize quadrangular elements; two (Psarropoulos & Tsompanakis 2008; Hegde & Das 2019) six-noded triangular elements, four (Liang & Elias 2010; Zardari et al. 2017; Do et al. 2021; Ledesma et al. 2022) fifteen-noded triangular elements; one (Machaček et al. 2018) six-noded triangular elements; and one (Naeini & Akhtarpour 2018) triangular and quadrangular elements. For the remaining articles the definition of the elements is not clear.

Boundary conditions

A fundamental aspect for the correct functioning of a numerical model is the appropriate attribution of the boundary conditions. Models of any dimension (1D, 2D and 3D) must be fixed in space in order to guarantee equilibrium and be able to solve the global stiffness equation on which the finite element analyses are based (Lees 2013). Usually, the base constraints of the model prevent displacements in all directions or only in the vertical direction, while those on the sides allow only vertical translation. In the case of earthquake simulations, these constraints must somehow be able to absorb the seismic waves without reflecting them into the model, generating a stress-strain state that does not exist in real conditions. Most of the articles analyzed (Psarropoulos & Tsompanakis 2008; Chakraborty & Choudhury 2011; Zardari et al. 2017) present constraints that prevent displacements in vertical and horizontal directions at the base of the model, while absorbing transmission boundaries are utilized on the sides. Naeini & Akhtarpour (2018), Hegde & Das (2019) and Do (2021) assign skates in the horizontal direction with no absorbing transmission boundaries. In the model studied by Machaček (2018) vertical displacements at the base nodes and horizontal displacements on the edges of the model are prevented during the construction simulation phases of the sctructure. Prior to the dynamic analysis the lateral boundary conditions are replaced with horizontal forces equivalent to the constraint reactions. For the remaining articles, the definition of boundary conditions is not clear.

Initial conditions

Obviously, the conditions of a geotechnical structure at a given time analyzed using a numerical model are affected by processes of various kinds which, in some cases, have occurred over hundreds if not thousands of years. These processes and conditions must somehow be recreated before carrying out the analysis, in order to reproduce the settings of the site as realistically as possible. One aspect being almost always present in tailings dams is that these structures are built in successive phases during which, to say it simply, a layer of material is placed on top of the previous one. As the stress state of the structure before the analysis is greatly affected by this feature, it would be desirable to reproduce the construction in phases also in the numerical model. Another common aspect of the modeling of tailings dams is the initial position of the water table and filtration motions, which are usually imposed following considerations based on the hydrogeological conditions of the site. In some studies (Psarropoulos & Tsompanakis 2008; Barrero et al. 2015; Morgenstern et al. 2016; Zardari et al. 2017; Sottile et al. 2020; Do et al. 2021; Ledesma et al. 2022), the construction of the dam is modeled in stages. In general, the phreatic surface is raised together with the elevation of the structure. In the studies presented by Nejad (2010), Liang & Elias (2010), Chakraborty & Choudhury (2011), Meisheng & Laigui (2011), Wang (2011), Skau (2013), Ishihara (2014), Xu (2016), Naeini & Akhtarpour (2018), Hegde & Das (2019), and Vargas (2019), a static analysis of the structure is carried out at its ultimate configuration. For the remaining articles the definition of initial conditions is not clear.

Load definition

In the numerical analyses of tailings dams, the applied loads, which induce the instability, are generally either external static loads, which can be placed in specific areas of the structure or changes (generally sudden) of pore pressures, or seismic actions. In some cases, the analysis can be limited to the study of the stability of the structure under the action of gravity. The numerical stability analyses are often conducted by reducing the shear strength parameters of materials until the structure collapses and the coefficient necessary to reduce the strength parameters represents the safety factor FS (Duncan 1996). This method is commonly referred to as shear strength reduction (SSR). In Liu (2007), the reaction of the Baizhishan tailing dam subject to the scaled Tangshan earthquake is studied. Psarropoulos & Tsompanakis (2008) analyze three types of conventional tailings dams in static conditions with the shear strength reduction method and in seismic conditions referring to the 1995 Shinkobe, Kobe, Japan, and the 1995 Aegion, Greece earthquake records. Nejad (2010), Liang & Elias (2010), and Chakraborty & Choudhury (2011) perform the analysis with a non-specified natural scaled earthquake records. Meisheng & Laigui (2011) and Wang both analyze the static stability of Chinese tailings with the shear strength reduction method. Skau (2013) examines the static stability and the deformations of the Żelazny most tailings dams located in South-West Poland. Ishihara (2014) performs a back analysis of the Kayakari and Takasega-mori tailings dam in Japan after the 2011 earthquake. Also, Barrero (2015) performs a seismic analysis on a non-specified tailings dam with the 2010 Darfield, New Zealand record. Xu (2015) analyzes the stability of the Lingshan tailings dam in China subjected to the Tangshan earthquake. Morgenstern (2016) performs a back analysis of the Fundão Tailings Dam (Brazil) that failed on November 5, 2015. Zardari (2017) studies

the stability of the Aitik tailings dam in Sweden subjected to a 3.6 local magnitude earthquake that occurred in 2010 outside Skelleftea, in northern Sweden, and to a 5.8 magnitude earthquake that occurred in 2011 in Virginia, eastern United States. Machaček (2018), Naeini & Akhtarpour (2018), Hegde & Das (2019) and Vargas (2019) perform seismic analysis with natural scaled signals. Sottile (2020) evaluates the liquefaction potential due to undrained lateral spreading, while Do (2022) investigates the effects of pond filling rates on pore water pressure. Ledesma (2022) analyzes the failure of Fundão tailings dam due to flow liquefaction.

Constitutive models

Constitutive models link strains to stresses through mathematical equations. It is not meaningful to model the behavior of tailings dam materials by means of elastic constitutive models, due to their high non-linearity. Elastic-plastic models (for example the Mohr-Coulomb model) can be appropriately used to perform gravitational analyses aimed to determine the initial conditions. More sophisticated models (such as hypoplastic or elasto-plastic models) are generally used for analyses under seismic conditions. Most of the works analyzed (Psarropoulos & Tsompanakis 2008; Chakraborty & Choudhury et al. 2011; Nejad et al. (n. d.); Liang & Elias 2010; Chakraborty & Choudhury 2011; Meisheng & Laigui 2011; Wang et al. 2011; Barrero et al. 2015; Morgenstern et al. 2016; Zardari et al. 2017; Naeini & Akhtarpour 2018; Hegde & Das 2019; Sottile et al. 2020; Do et al. 2021) utilize the Mohr-Coulomb model for materials that do not reach the liquefaction condition. For liquefiable material, the Finn-Byrne (Nejad et al. (n. d.); Chakraborty & Choudhury 2011; Meisheng & Laigui 2011; Wang et al. 2011) and UBCSAND (Zardari et al. 2017; Do et al. 2021) models are the most used; this is probably because these models are implemented in most commonly commercial software and because they require fewer input parameters compared to other models. More sophisticated constitutive models to simulate liquefaction are: Sanisand that has been used by Barrero (2015) to model a not specified tailings dam under seismic conditions; Norsand proposed by Morgenstern (2016); a modified Pastor-Zienkiewicz model that has been used by Ledesma (2022) to back-analyze the Fundão disaster; and the hypoplastic model that has been used by Machaček et al. (2018) to analyze the behavior of sand dumps in seismic conditions. With some exceptions (Ishihara et al. 2015, Zardari et al. 2017, Machaček et al. 2018; Naeini & Akhtarpour 2018; Ledesma et al. 2022), in many of the articles analyzed, information on the constitutive models, the parameters used, and their determination and calibration, are not clearly stated or not stated at all.

Bibliography

Barrero, A. R., Taiebat, M., & Lizcano, A. (2015). Application of an advanced constitutive model in nonlinear dynamic analysis of tailings dam. In 68th Canadian Geotechnical Conference (pp. 20-23).

Chakraborty, D., & Choudhury, D. (2009). Investigation of the behavior of tailings earthen dam under seismic conditions. American Journal of Engineering and Applied Sciences, 2(3), 559-564.

Chakraborty, D., & Choudhury, D. (2011). Seismic behavior of tailings dam using flac3d. In Geo-Frontiers 2011: Advances in Geotechnical Engineering (pp. 3138-3147).

Do, T. M., Laue, J., Mattsson, H., & Jia, Q. (2021). Numerical analysis of an upstream tailings dam subjected to pond filling rates. Applied Sciences, 11(13), 6044.

Duncan, J. M. (1996). State of the art: limit equilibrium and finite-element analysis of slopes. Journal of Geotechnical engineering, 122(7), 577-596.

Geppetti, A., Facciorusso, J., & Madiai, C. (2022). Tailings Dams Numerical Models: A Review. Proceedings of the 7th World Congress on Civil, Structural, and Environmental Engineering (CSEE'22), 22(241)

Hegde, A., & Das, T. (2019). Finite element-based probabilistic stability analysis of rock-fill tailing dam considering regional seismicity. Innovative Infrastructure Solutions, 4, 1-14.

Ishihara, K., Ueno, K., Yamada, S., Yasuda, S., & Yoneoka, T. (2015). Breach of a tailings dam in the 2011 earthquake in Japan. Soil Dynamics and Earthquake Engineering, 68, 3-22.

James, M., & Aubertin, M. (2017). Comparison of numerical and analytical liquefaction analyses of tailings. Geotechnical and Geological Engineering, 35(1), 277-291.

Ledesma, O., Sfriso, A., & Manzanal, D. (2022). Procedure for assessing the liquefaction vulnerability of tailings dams. Computers and Geotechnics, 144, 104632.

Lees, A. (2016). Geotechnical finite element analysis: a practical guide. ICE publishing.

Liang, J. Z., & Elias, D. (2010, November). Seismic evaluation of tailings storage facility. In Proceedings of the Australian Earthquake Engineering Society 2010 Conference, Perth, Western Australia.

Liu, H. X., Li, N., Liao, X., Wu, C. S., & Pan, X. D. (2007). Effective stress analysis method of seismic response for high tailings dam. Journal of Central South University of Technology, 14(1), 129-134.

Machaček, J., Triantafyllidis, T., & Staubach, P. (2018). Fully coupled simulation of an opencast mine subjected to earthquake loading. Soil Dynamics and Earthquake Engineering, 115, 853-867.

Meisheng, F., & Laigui, W. (2011, April). A tailings dam dynamic stability study based on numerical simulation. In 2011 International Conference on Consumer Electronics, Communications and Networks (CECNet) (pp. 1002-1005). IEEE.

Morgenstern, N. R., Vick, S. G., Viotti, C. B., & Watts, B. D. (2016). Fundão tailings dam review panel report on the immediate causes of the failure of the Fundão dam. Cleary Gottlieb Steen & Hamilton LLP, New York.

Naeini, M., & Akhtarpour, A. (2018). Numerical analysis of seismic stability of a high centerline tailings dam. Soil Dynamics and Earthquake Engineering, 107, 179-194.

Nejad, B. G., Taiebat, H., Dillon, M., & Seddon, K. (n. d.). Numerical Modelling of Seismic Liquefaction for Bobadil Tailings Dam.

Psarropoulos, P. N., & Tsompanakis, Y. (2008). Stability of tailings dams under static and seismic loading. Canadian Geotechnical Journal, 45(5), 663-675.

Skau, K., Andresen, L., Jostad, P., Fornes, P., Grimstad, G., & Page, A. (2013). Stability and deformations of Zelazny Most dam–One of the World's largest deponies for copper tailings. Fjellsprengningsdagen, Bergmekanikkdagen, Geoteknikkdagen.

Sottile, M. G., Cueto, I. A., & Sfriso, A. O. (2020). A simplified procedure to numerically evaluate triggering of static liquefaction in upstream-raised tailings storage facilities.

Świdziński, W. (2016). Modelling of post-flotation tailings liquefaction induced by paraseismic events. Archives of Hydro-Engineering and Environmental Mechanics, 63(2-3), 215-233.

Vargas, C. O. (2019, November). Analysis and Seismic Design of Tailings Dams and Liquefaction Assessment. In American Conference on Soil Mechanics and Geotechnical Engineering (Vol. 7, p. 392).

Vick, S. G. (1990). Planning, design, and analysis of tailings dams. BiTech Publishers Ltd.

Wang, T., Zhou, Y., Lv, Q., Zhu, Y., & Jiang, C. (2011). A safety assessment of the new Xiangyun phosphogypsum tailings pond. Minerals Engineering, 24(10), 1084-1090.

Xu, B., & Wang, Y. (2015). Stability analysis of the Lingshan gold mine tailings dam under conditions of a raised dam height. Bulletin of Engineering Geology and the Environment, 74, 151-161.

Yang, J., Hu, J., Wu, Y., & Zhang, B. (2022). Numerical Simulation of Seepage and Stability of Tailing Dams: A Case Study in Ledong, China. Sustainability, 14(19), 12393.

Zardari, M. A., Mattsson, H., Knutsson, S., Khalid, M. S., Ask, M. V., & Lund, B. (2017). Numerical analyses of earthquake induced liquefaction and deformation behaviour of an upstream tailings dam. Advances in Materials Science and Engineering, 2017, 1-12.

Zdravković, L. (1999). Finite element analysis in geotechnical engineering: theory. Thomas Telford.

5. Case study overview

As mentioned in the previous chapters, the tailings dam analyzed in this thesis is located in southern Tuscany (Italy) in the National Park of the Metalliferous Hills. The first evidence of mining activities in this area is represented by a jasper pit dating back to 5000 years ago (Storia - Parco Nazionale delle Colline Metallifere 2022). An ancient Etruscan settlement was found near the mine and the related tailings dams investigated for the purpose of this PhD thesis; the inhabitants exploited the subsoil resources mainly in search of metals such as: iron, copper, lead, and silver (Camporeale 2005). In the thirteenth century, one of the most important cities of this area was Massa Marittima, where one of the first mining codes, "Ordinamenta super arte rameriae et argenteriae civitatis Massae", was drafted. A strong boost to mining activity in these territories occurred in the 1800s following mineralogical and geological studies. An early example is Porte's manuscript (1833) which urges politicians and thinkers of that time to resume mining activities in the region. A few years later, Haupt (1847) wrote that "Tuscany offers material to supply the mining industry probably for many centuries, that such industry may become much more important than what it has been so far, that Tuscany is comparable to the most renowned European mining countries, and worthy of being called properly land of mines; and that therefore this industry must be considered as a natural industry in Tuscany, capable of gaining considerable economic and national importance"[1].

The construction of the mine, whose wastes went to form the tailings dam under examination, began in 1846 with the excavation of various wells, tunnels, and shafts necessary to reach the veins from which copper, zinc, lead, and iron ore were extracted (Capperi & Nannoni 1997). Various companies took ownership of the mine, which developed rapidly to the point where it was necessary to create special drains to lower the groundwater level. In 1859, the mine reached a length of 3559 m, and the water coming from the drainage was collected to be reused in the processing of materials. In the early 1900s, the plant was equipped with state-of-the-art machinery for that time for crushing and classifying the extracted material. In 1950 the construction of a new treatment plant began which, with reference to what has been detailed in Chapter 2, can be called mill, began operating in 1953. In the new mill, the material was crushed and subjected to flotation and decantation processes (Fig. 5.1).

[1] Translated from Haupt (1847)

Figure 5.1: *View of the 1953 mill from Basin No.1.*

Over the years, with the progress of extraction technology, the materials in the landfills have been repeatedly subjected to separation processes, allowing the extraction of valuable material that otherwise would have remained among the waste (Capperi & Nannoni 1997). In 1980 the new mill was definitively closed for economic reasons. In 1985 the personnel working in the mine were sent to other sites owned by the company and the mine closed permanently. The total area of the plant has an extension of about 30 hectares. A schematic site plan of the area and a related cross section are depicted in Figures 5.2 and 5.3 respectively.

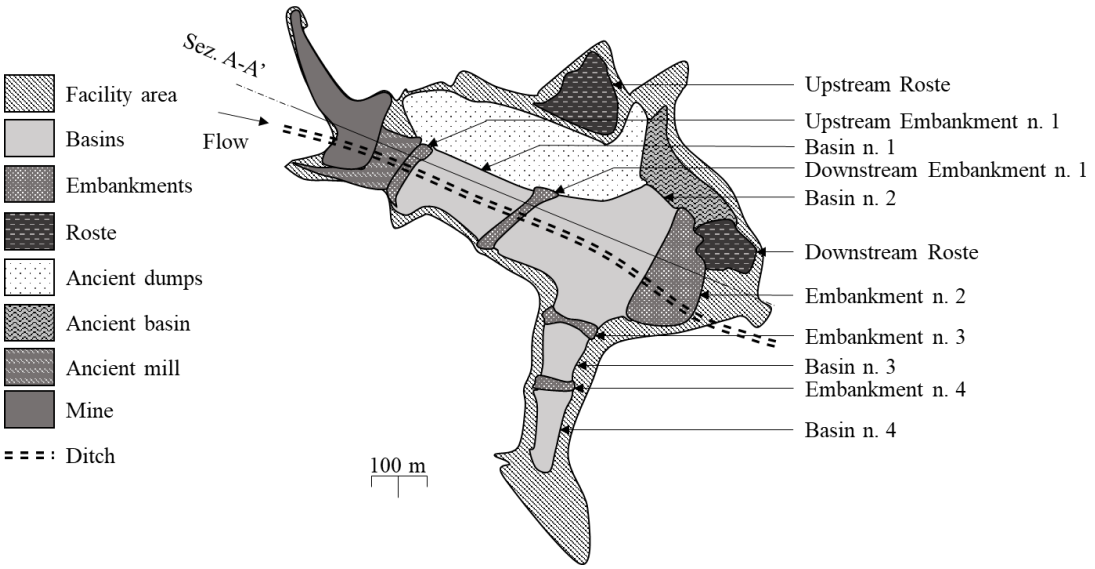

Figure 5.2: *Site plan of the area.*

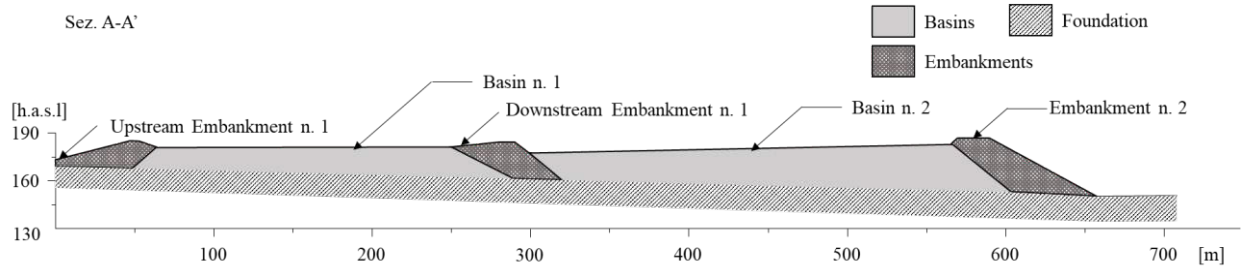

Figure 5.3: *Cross section A-A'.*

The area is partly occupied by different sectors: Roste, ancient basins, and ancient dumps. These areas were used as landfill during operations prior to 1957. There are no specific testimonies of these sectors with the exception of the so-called Roste, which take their name from a technique of "roasting" the material. In fact, the extracted material was transported and accumulated in special areas and roasted in the open air. Subsequently, water was flowed onto the mounds which, through a leaching process, was enriched with copper and iron sulphates. The "enriched" water was then placed in special furnaces, which, through an electrochemical process, made it possible to obtain pure copper. The Roste are therefore the resulting material left over from this particular copper extraction process and still characterize the territories of the National Park of the Metalliferous Hills (Figure 5.4).

Figure 5.4: *Roste area (Gruppo di lavoro Regione Toscana (n.d.).*

The first tailings pond and associated embankments were built in 1957 (Basin No. 1 Fig. 5.1, 5.2 and 5.3). Basin No. 1 covers an area of approximately 25.000 m^2 and contains approximately 300.000 m^3 of tailings. Subsequently, settling basin No. 2, which is the largest of the whole plant with a surface area of approximately 55.000 m^2 and a volume of approximately 600.000 m^3, was built (Fig. 5.5 b). Basin No. 2 is contained downstream by embankment No. 2, which is the largest structure of the whole facility. This embankment was built using the upstream method and has a height of approximately 36.5 m above ground level and a length of about 67 m (Fig. 5.3 and Fig. 5.5 a).

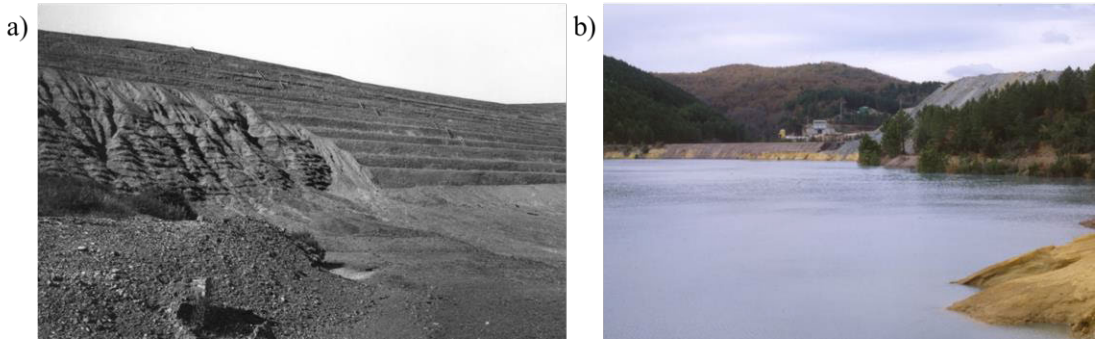

Figure 5.5: *Historical images of: a) Embankment No. 2, b) Basin No. 2.*

Both basins 1 and 2 extend along a valley in which a ditch flows, which has been suitably filled. The order from upstream to downstream of these structures is: Upstream Embankment No. 1, Basin No. 1, Downstream Embankment No. 1, Basin No. 2; Embankment no. 2 (Fig. 5.3). Basins 3 and 4 (Figure 5.2.) were built on the hydraulic right of the ditch in the 1980s and contain a volume of residues of 55.000 m^3 and 30.000 m^3, respectively. In the context of this work, the seismic behavior of the basin and embankment number 2 was analyzed. They are the most important from a dimensional and structural point of view and their collapse could cause the greatest damage to the surrounding territories. The distance of approximately 300 m between downstream banks 1 and 2 was considered sufficient to avoid interaction effects between the two structures and therefore to focus attention on bank 2.

5.1. Geological and geomorphological framework

The site of interest is located within the Metalliferous Hills which are a stretch of the "Paleo-Apennine" chain generated between the upper Eocene-lower Miocene (Figure 5.6).

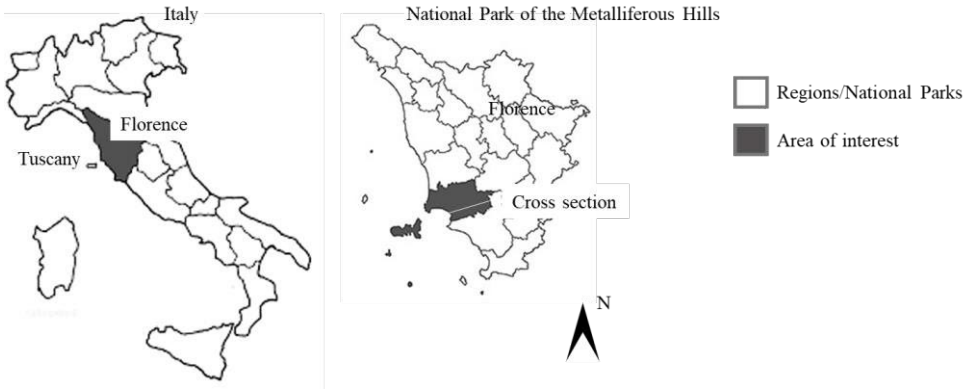

Figure 5.6: *Localization of the National Park of the Metalliferous Hills.*

Two distinct geological complexes outcrop in the examined area. The basement is the so-called "Tuscan Series" and consists of Triassic phyllite, evaporites, and cavernous limestone. It is widely overlaid by the "Sub-Ligurian" and "Ligurian" Units, which are composed of clay schists and marly limestones (Figure 5.7) (Capperi & Nannoni 1997). The geological setting results from the hydrothermal mineralization that characterized southern Tuscany in the Miocene-Pliocene due to events of magmatism,

metamorphism, and extensional tectonics (Tanelli 1983; Cuteri & Mascaro 1995). The area is characterized by extension faults that follow the direction of the Apennine chain and dip towards the east with a slope of about 45°. As for the mineralogical aspect, there are two distinct areas. A cupriferous one, originating from a deep granitic pluton represented by manganese-bearing, and characterized by hedenbergite skarn, diopside, quartz, epidote, and calcite, where the metallic minerals originate from prevalent oxides and pyrite, and a chalcopyrite together with bismuthinite and native bismuth with arsenopyrite, galena, sphalerite, all in a chlorite-quartz gangue from a later genesis. The other area is characterized by lead, zinc, and copper, typical of silicification and pyritization phenomena of scaly clays (Capperi & Nannoni 1997). In correspondence with the major impluvia there are more recent deposits, such as alluvial, eluvial-colluvial, and slope deposits.

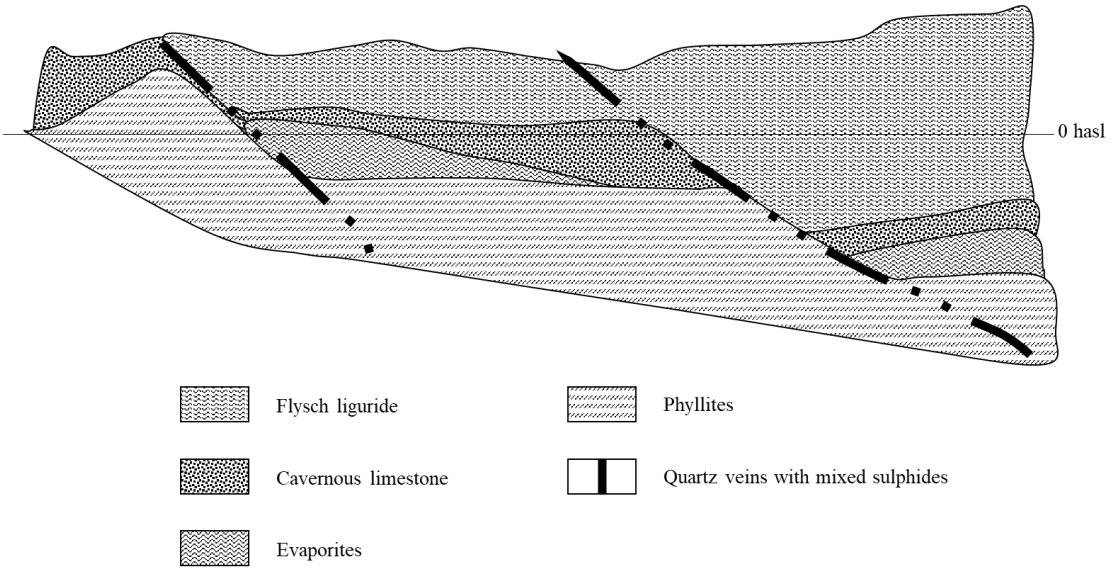

Figure 5.7: *Geological section. (reworked from Nannoni & Capperi 1983).*

Due mostly to surface outflows and, to a lesser extent, to gravitational reasons, the lower and middle parts of the hillsides and the valley, which are close to the tailing ponds, are characterized by a moderate morphological fragility with superficial or cortical susceptibility to instability. The average altitude of these territories is between 150-250 m asl with peaks of 300 m asl. The average slope of the hills on the right side of the ditch is about 32% while on the left side it is about 21%. The asymmetry of the slopes can be attributed to geological reasons: the right side contains mainly dip-slope layers with slope inclination between 15° and 50°, while on the left there are common anti dip-slope layers with inclination between 15° and 30°.

5.2. Hydrological and hydrogeological framework

The area is characterized by a developed hydrographic network of the sub-dendritic type. The structural conditions of the substrate give a preferential direction to the ditch that passes under the tailings dams. The slopes substantially condition the minor hydrography, which is straight and parallel on the right side, while it is more centripetal on the left (Fig. 5.2). The rainwater flows into the ditch after streaming on the slopes, which are mainly covered with vegetation. The ditch has a length of about 3 km and is part of the Ombrone River basin; in the area of interest, it drains the runoff water from the slopes and part of the basin seepage. Precipitation determines the presence of water in the ditch. The valley is characterized by a sub-stratum consisting of argillites and siltstones on which layers of alluvial material formed by crushed rock transported by hydrographic networks are locally present. Altered argillites and siltstones ranging in color from hazelnut-ochre to gray with interspersed sandy silt or gravelly sandy layers make up the surface part of the sub-stratum. The levels of the piezometers installed in the settling basins suggest the constant presence water table over the area.

5.3. Seismogenic and seismic framework

From the seismogenic zoning map reported in Gasperini (2004) it is possible to observe that the reference tailings storage facility is located a few kilometers from the zone called 921 (Figure 5.8).

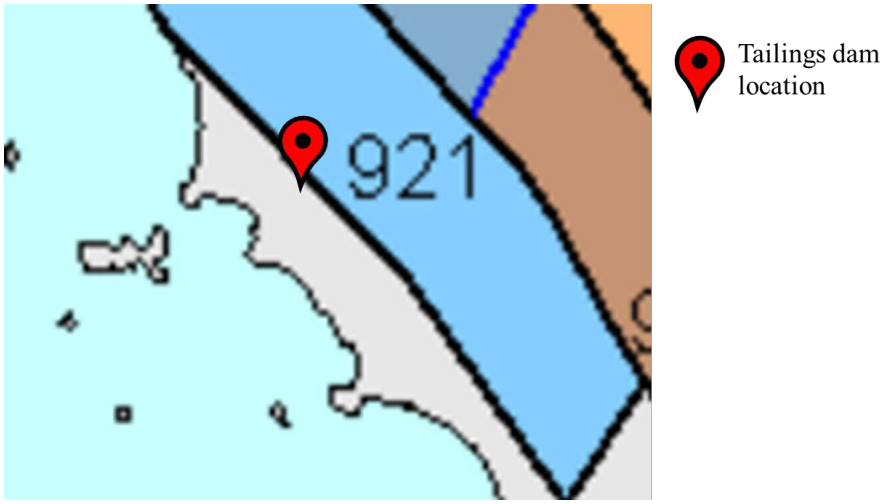

Figure 5.8: *Tailings dam ubication with respect to seismogenic zone 921. (reworked from Gasperini et al. 2004).*

This area is characterized by high heat flux and widespread moderate energy seismicity with few events of higher magnitude. An "effective" depth, that is the depth band to which the greatest number of earthquakes is released, of 1-5 km has been attributed to this zone. The observation of a combination of focal mechanisms with geological data at various scales allowed to attribute to the 921 zone an expected prevailing faulting mechanism of normal type. The maximum value of the moment magnitude attributed to zone 921 is M_{wmax}=6.14 (Gruppo di Lavoro MPS, 2004).

The tailings dam under study is located at a distance of about 105 km from the composite seismogenic source called Mugello-Citta' di Castello-Leonessa, which is located on the Apennine ridges and characterized by a maximum magnitude M_w=6.9. More or less at the same distance are the individual seismogenic sources Northern Apennines Arc and Monterchi characterized by maximum magnitudes of 8.1 and 5.8 respectively (Figure 5.3.2). To the north, near to the Thyrrhenian coast, at a distance of about 57 km there is the composite seismogenic source called the Livorno hills characterized by a maximum magnitude of 6.2. In the same area there is the individual seismogenic source of Orciano Pisano characterized by a maximum magnitude of 5.7 (Figure 5.9).

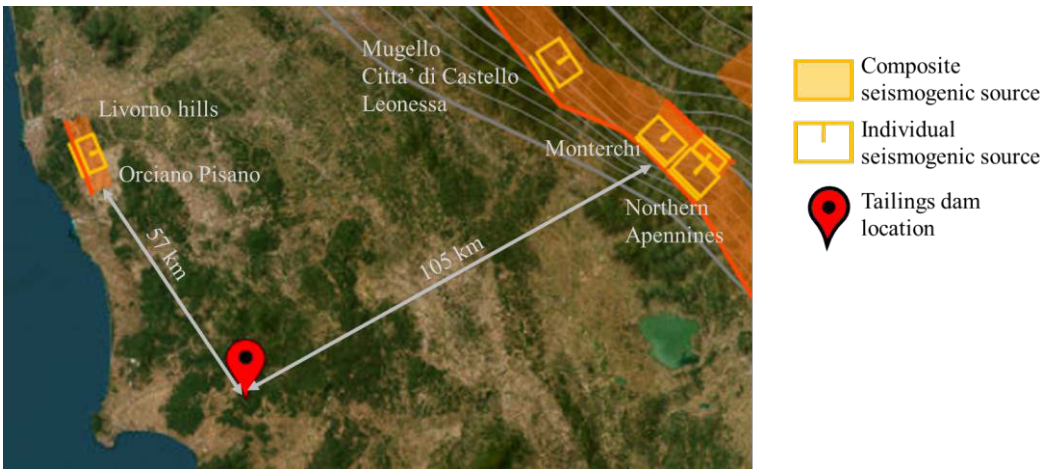

Figure 5.9: *Individuation and distances of seismogenic sources. (reworked from DISS Working Group 2021).*

From the seismic hazard maps produced by the Gruppo di Lavoro MPS (2004), the value a_g of the site reference peak ground acceleration on flat type A ground, for a return period of 2475 years, ranges between 0.125 and 0.150 g (Figure 5.10). According to the Italian building code (NTC2018), type A ground includes rock or rock-like formations are characterized by a S-wave propagation velocity greater than 800 m/s, possibly including at most 3 m of weaker material at the surface.

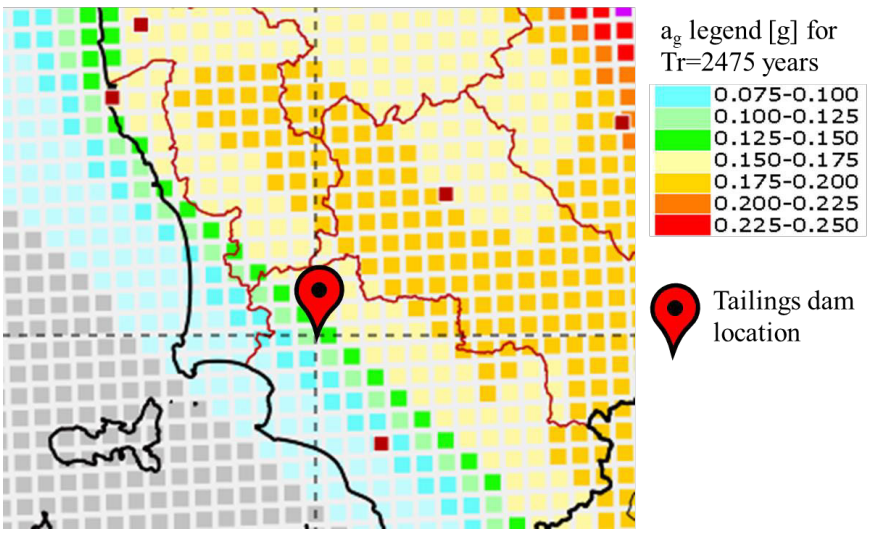

Figure 5.10: *Seismic hazard at the tailings dam. (reworked from Gruppo di Lavoro MPS 2004).*

5.4. Geotechnical model

The geotechnical model of the structure was developed on the basis of the results of the laboratory tests presented in chapter 3 and through the analysis of data from previous exploration and investigation campaigns, which are presented below. The numerical analyses focused on the embankment and on basin No. 2 (Figs. 5.2, 5.3 and 5.5) as they are the most important structures of the entire facility, the collapse of which would have a devastating impact on the surrounding territories. The analysis of data from previous survey campaigns focused on documents and reports of field and laboratory tests conducted in these areas. In particular, reference was made to four survey campaigns performed in 2007, 2010, 2015, and 2018, in which various field and laboratory tests were carried out on the structures of interest (Fig. 5.11).

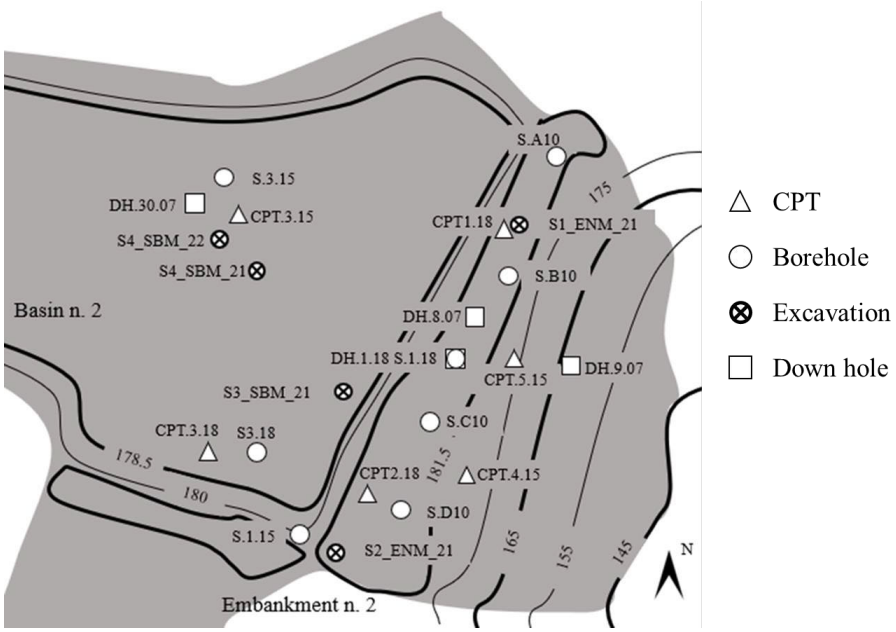

Figure 5.11: *Surveys overview.*

Regarding the investigations performed on the embankment in 2007, two downhole tests were carried out, DH.8.07 of 29 m depth and DH.9.07 of 15 m depth, while a 23 m deep downhole test, DH.30.07, was performed within the basin. In 2010, four boreholes (SA.10, SB.10, SC.10 and SCD.10) were completed in the embankment from which 16 samples were taken and where numerous Standard Penetration Tests (SPT) tests were carried out. In 2015, one borehole (S.1.15) and two Piezocone Penetration Tests (CPTu) tests (CPT.4.15 and CPT.5.15) were carried out on the embankment, and one borehole (S.3.15) from which 8 samples were collected, and one CPT test (CPT.3.15) were performed within the basin. In 2018, a borehole (S.1.18) was carried out from which 6 samples were collected, 9 SPT tests were performed, and a downhole test was accomplished on the embankment, while a survey was carried out in the basin, from which 5 samples were collected, and in which 7 SPT tests were

performed. Moreover, two CPTu tests were also performed within the basin. The list of the above mentioned investigations is summarized in Tables 5.1, 5.2, and 5.3.

Table 5.1: S*ite tests overview.*

Basin						
Year	Survey code	Borehole	No. of samples	No. SPT	CPTu	Down Hole
2007	DH.30.07					X
2015	S.3.15	X	8			
2015	CPT.3.15				X	
2018	S.3.18	X	5	7		
2018	CPT.1.18				X	
2018	CPT.2.18				X	
Embankment						
Year	Survey code	Borehole	No. of samples	No. SPT	CPTu	Down Hole
2007	DH.8.07					X
2007	DH.9.07					X
2010	SA.10	X	4	9		
2010	SB.10	X	4	8		
2010	SC.10	X	4	11		
2010	SD.10	X	4	7		
2015	S.1.15	X				
2015	CPT.4.15				X	
2015	CPT.5.15				X	
2018	S.1.18	X	6	9		
2018	DH.1.18					X

Summing up, a total of 6 boreholes were performed on the embankment from which 22 samples were collected and in which 44 SPT tests were performed. Only 2 boreholes were performed within the basin from which 13 samples were taken and in which 7 SPT tests were performed.

5.4.1. Analysis of laboratory tests on collected samples

The types of laboratory tests performed on the samples collected from the basin boreholes are shown in Table 5.2, while those performed on the samples collected from the embankment boreholes are shown in Table 5.3.

Table 5.2: *Laboratory tests performed on the samples collected from the basin boreholes.*

Year	Borehole code	Sample code	Depth [m]	Grain size analysis	Atterberg limits	Direct shear test
2015	S.3.15	S.3.15_C1	3.0-4.0	X	X	X
2015	S.3.15	S.3.15_C2	6.0-7.0	X	X	X
2015	S.3.15	S.3.15_C3	24.5-25.0	X	X	X
2015	S.3.15	S.3.15_C4	2.7-4.3	X	X	
2015	S.3.15	S.3.15_C5	5.7-7.3	X	X	
2015	S.3.15	S.3.15_C6	9.0-9.5	X	X	
2015	S.3.15	S.3.15_C7	12.0-12.5	X	X	
2015	S.3.15	S.3.15_C8	15.0-15.5	X	X	
2015	S.3.15	S.3.15_C9	18.0-18.5	X	X	
2015	S.3.15	S.3.15_C10	21.0-21.5	X	X	
2015	S.3.15	S.3.15_C11	24.5-24.7	X	X	
2018	S.3.18	S.3.18_C1	5.0-5.5	X	X	X
2018	S.3.18	S.3.18_C2	14.0-14.5	X	X	
2018	S.3.18	S.3.18_C3	18.0-18.5	X	X	
2018	S.3.18	S.3.18_C4	21.0-21.5	X	X	
2018	S.3.18	S.3.18_C5	24.0-24.5	X	X	

As regards the samples extracted from the boreholes drilled within the basin, direct shear tests were performed in some cases, in addition to the classification tests.

Table 5.3: *Laboratory tests performed on the samples collected from the embankment boreholes.*

Year	Borehole code	Sample code	Depth [m]	Grain size Analysis	Atterberg limits
2010	SA.10	SA.10_C1	4.2-4.5	X	X
2010	SA.10	SA.10_C2	10.0-10.4	X	
2010	SA.10	SA.10_C3	17.5-17.8	X	X
2010	SA.10	SA.10_C4	21.5-21.8	X	X
2010	SB.10	SB.10_C1	8.2-8.5	X	
2010	SB.10	SB.10_C4	12.2-12.6	X	X
2010	SB.10	SB.10_C2	16.3-16.6	X	X
2010	SB.10	SB.10_C3	22.0-22.3	X	X
2010	SC.10	SC.10_C2	13.5-13.9	X	X
2010	SC.10	SC.10_C3	18.3-18.6	X	X

Year	Borehole code	Sample code	Depth [m]	Grain size Analysis	Atterberg limits
2010	SC.10	SC.10_C4	23.5-24.0	X	X
2010	SC.10	SC.10_C1	28.2-28.5	X	X
2010	SD.10	SD.10_C1	6.2-6.5	X	X
2010	SD.10	SD.10_C2	11.5-11.8	X	X
2010	SD.10	SD.10_C3	17.7-18.1	X	X
2010	SD.10	SD.10_C4	23.2-23.5	X	X
2018	S.1.18	S.1.18_C1	4.6-5.0	X	X
2018	S.1.18	S.1.18_C2	11.0-11.5	X	X
2018	S.1.18	S.1.18_C3	17.5-18.0	X	X
2018	S.1.18	S.1.18_C4	23.5-24.0	X	X
2018	S.1.18	S.1.18_C5	33.7-34.0		
2018	S.1.18	S.1.18_C6	39.0-39.4		

For the materials extracted from the boreholes drilled on the embankment, it was only possible to carry out classification tests (as described in Chapter 3), as the presence of large diameter fractions does not allow for other types of tests with standard size instrumentation.

Table 5.4 summarizes the results obtained from the laboratory tests carried out on the samples collected from the basin boreholes.

Table 5.4: *Results of laboratory test results performed on the samples collected from the basin boreholes.*

S. code	Depth [m]	Gravel [%]	Sand [%]	Silt [%]	Clay [%]	FC [%]	w_L [%]	w_P [%]	IP [%]	γ_v [kN/m³]	γ_d [kN/m³]	γ_{sat} [kN/m³]	γ_s [kN/m³]	c' [kPa]	φ [°]
S.3.15_C1	3-4	0.1	13.8	67.3	18.8	86.1	40.8	23.8	17	17.69	13.36	18.54	28.28	7	27
S.3.15_C2	6-7	0.1	70.9	21.5	7.5	29	28.1	19.2	8.9	19.83	16.11	20.1	27.16	4	29
S.3.15_C3	24.5-25	0	4.1	67.7	28.2	95.9	37.1	22.3	14.8	18.68	13.74	18.68	27.46	6	23
S.3.15_C4	2.7-4.3	0	19.9	59.3	20.8	80.1	31.8	25.5	6.3				27.51		
S.3.15_C5	5.7-7.3	0	49.9	40.3	9.8	50.1							27.52		
S.3.15_C6	9-9.5	1.5	69.8	21.9	6.8	28.7							26.31		
S.3.15_C7	12-12.5	0	71.2	22.9	5.9	28.8							26.41		
S.3.15_C8	15-15.5	0	67.1	21.1	11.8	32.9							26.1		
S.3.15_C9	18-18.5	0	71.2	22.9	5.9	28.8	32.3	25.8	6.5				26.47		
S.3.15_C10	21-21.5	0.1	61.4	32.3	6.2	38.5							26.54		
S.3.15_C11	24.5-24.7	0	3.2	69.5	27.3	96.8	37	23.2	13.7				27.27		
S.3.18_C1	5-5.5	0	35.14	57.98	6.88	64.86	28	21	7	18.17	14.03	18.72	26.43	8.52	28.9
S.3.18_C2	14-14.5	0	45.9	48.69	5.41	54.1	23	17	6	17.92	14.8	19.2	26.4		
S.3.18_C3	18-18.5	27.36	58.39	13.15	1.11	14.26	30	22	8	19.51	17.5	20.9	26.5		
S.3.18_C4	21-21.5	56.23	24.32	16.03	3.42	19.45	29	21	8	19.76	17.49	20.91	26.57		
S.3.18_C5	24-24.5	28.76	39.75	25.01	6.48	31.49	29	20	9	19.93	17.49	20.9	26.53		

Analyzing the results obtained from the grain size analyses of the samples taken from the S.3.15 borehole, it is possible to note an absence of the gravel fraction along the entire depth. As regards the fine fractions, the fines content (FC) is between 30% and 50% for almost all samples (in good agreement with what is determined in Chapter 3, paragraph 3.1.2), with the exception of samples S.3.15_C1, S.3.15_C3, S. 3.15_C4, and S. 3.15_C11. Samples S.3.15_C1 and S.3.15_C4 were collected at approximately the same depth (4-4.5 m), at which a lens of material with a higher presence of clay was found. As for samples S.3.15_C3 and S.3.15_C11, these were collected at a depth of 24.5-25 m, i.e., where the level of the natural ground prior to the construction of the tailings dam abuts. All the samples of this borehole, except those just mentioned, have very low or even undeterminable plasticity indices (PI). The gravel fraction of the samples collected from the S.3.18 survey is negligible except for samples S.3.18_C3, S.3.18_C4 and S.3.18_C5, in which percentages of gravel were determined to be between 27 and 56. This borehole was drilled in basin No. 2 near embankment No. 3; therefore, it is possible that from a depth of about 18 m the borehole intercepted the embankment material. Also, for these samples, the determined plasticity index (PI) is very low, denoting the non-plastic character of these materials.

For all materials attributable to tailings, the specific gravity G_s value is between 2.7 and 2.8, which is comparable with what is set out in Chapter 3, paragraph 3.1.3. The direct shear tests were performed on samples S.3.15_C1, S.3.15_C2, and S.3.18_C1 collected at depths ranging from 3 to 6 m, giving values of the effective friction angle and the cohesion that were comparable to each other. Samples S.3.15_C1, S.3.15_C2, S.3.15_C4, S.3.15_C6, S.3.15_C7, S.3.15_C8, S.3.15_C9, S.3.15_C10, S.3.18_C1, S.3.18_C2, C1_GRN_SBM_21, C2_GRN_SBM_21, and C3_GRN_SBM_21 (the last 3 described in chapter 3) were assigned to basin material (SBM) as described in Chapter 3. The grain size distribution and the Casagrande chart of the samples assigned to basin material (SBM) are presented in Figure 5.12 and 5.13, respectively.

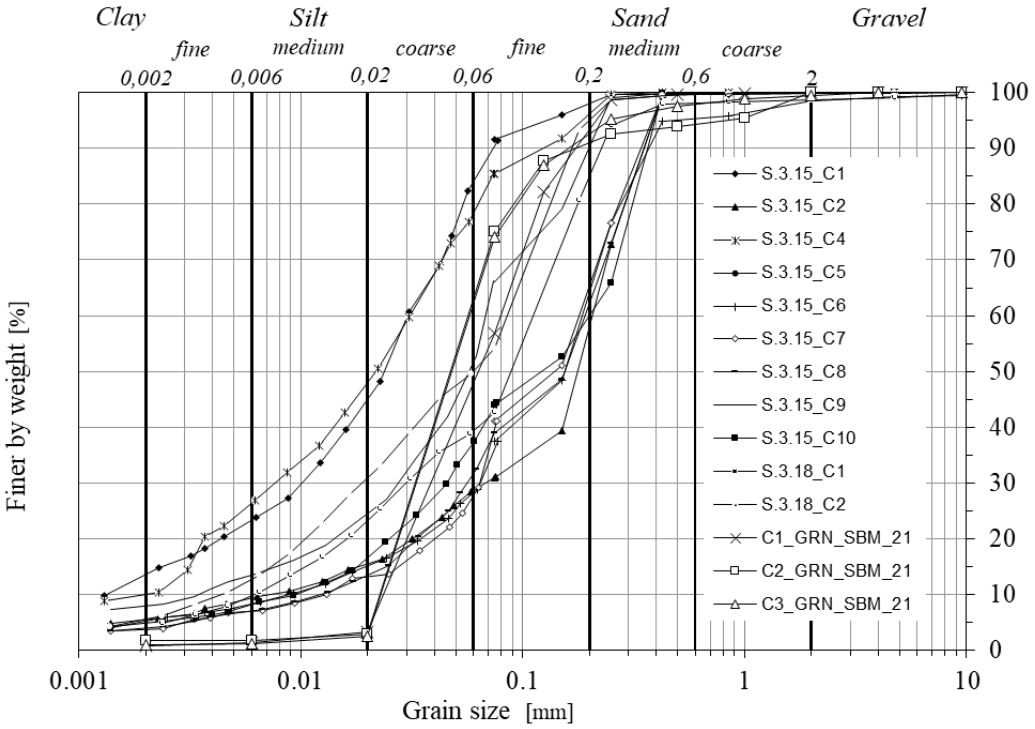

Figure 5.12: *Grain size distribution curves of samples extracted from basin material (SBM).*

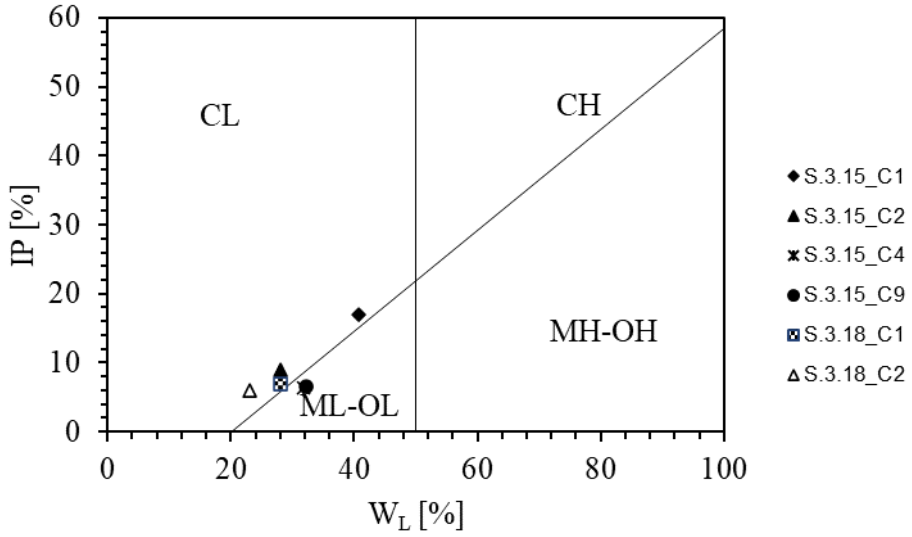

Figure 5.13: *Casagrande chart of samples extracted from basin material (SBM).*

From the grain size distribution curves in Figure 5.12 it is possible to note that the basin materials range from medium-fine sands to silts of all sizes with small percentages of clay. From the Casagrande plasticity chart (Fig. 5.13) it is possible to observe that for few samples it has been possible to obtain the Atterberg limits and that they are located on the border between inorganic silts (ML) and inorganic clays (CL). The definition of inorganic silts (ML) also includes the so-called "rock flours",

a definition attributable to tailings. Table 5.5 summarizes the results obtained from the laboratory tests carried out on the samples collected from the embankment boreholes.

Table 5.5: *Results of laboratory tests performed on the samples collected from the embankment boreholes.*

Sample code	Gravel [%]	Sand [%]	Silt [%]	Clay [%]	FC [%]	w_L [%]	w_P [%]	IP [%]	γ_v [kN/m^3]	γ_d [kN/m^3]	γ_{sat} [kN/m^3]	γ_s [kN/m^3]
SA.10_C1	24	31	45		45	26	19	7				
SA.10_C2	51	35	14		14							
SA.10_C3	31	44	25		25							
SA.10_C4	4	5	91		91	43	21	22				
SB.10_C1	46	41	13		13							
SB.10_C4	22	44	34		34							
SB.10_C2		78	22		22							
SB.10_C3	4	20	76		76							
SC.10_C2	6	49	45		45							
SC.10_C3		4	96		96	22	21	1				
SC.10_C4		35	65		65							
SC.10_C1	4	57	39		39							
SD.10_C1	43	23	34		34	38	22	16				
SD.10_C2	3	54	43		43							
SD.10_C3		46	54		54							
SD.10_C4		86	14		14	20	18	2				
S.1.18_C1	28.4	46.66	21.98	2.96	24.94				19.18	17.75	21.04	26.47
S.1.18_C2	0.11	81.58	15.8	2.51	18.31				18.71	17.05	20.59	26.39
S.1.18_C3	1.21	56.12	38.52	4.15	42.67				18.03	15.81	19.82	26.37
S.1.18_C4	0.22	85.31	12.86	1.61	14.47				18.81	16.29	20.12	26.43
S.1.18_C5												
S.1.18_C6												

From the analysis of Table 5.5 it is possible to deduce that the samples from the embankment have a non-negligible portion of coarse fraction. It is also possible to observe that the plasticity index, when determinable, is very low, denoting a non-plastic character also of these materials, with the exception of sample SA.10_C4, which was collected at a depth where natural soil is present. Samples SA.10_C1, SA.10_C2, SA.10_C3, SB.10_C1, SB.10_C4, SD.10_C1, S.1.18_C1, C1_GRN_ENM_21, C2_GRN_ENM_21, and C2_GRN_ENM_21 (the last 3 described in chapter 3) were assigned to the embankment material (ENM) as described in Chapter 3. The Grain size distribution and the Casagrande chart of the samples assigned to the embankment material (ENM) are represented in Figures 5.14 and 5.15, respectively.

From the analysis of the grain size distribution curves in Figure 5.14 it is possible to observe a more heterometric trend of these materials compared to the tailings. Also in this case, the only two samples on which it was possible to determine the Atterberg limits lie approximately on the line between inorganic silts (ML) and inorganic clays (CL) of the Casagrande chart (Figure 5.15).

With reference to what is explained in Chapter 3, the grain size distribution curves and Atterberg limits obtained from the samples assigned to the foundation materials (FNM) are shown in Figures 5.16 and 5.17, respectively. Figure 5.16 points out a more uniform grain size distribution and a higher fines content for the foundation soils compared to embankment materials and tailings. Figure 5.17 shows slightly higher plasticity values for the foundation soils than for the embankment materials and tailings.

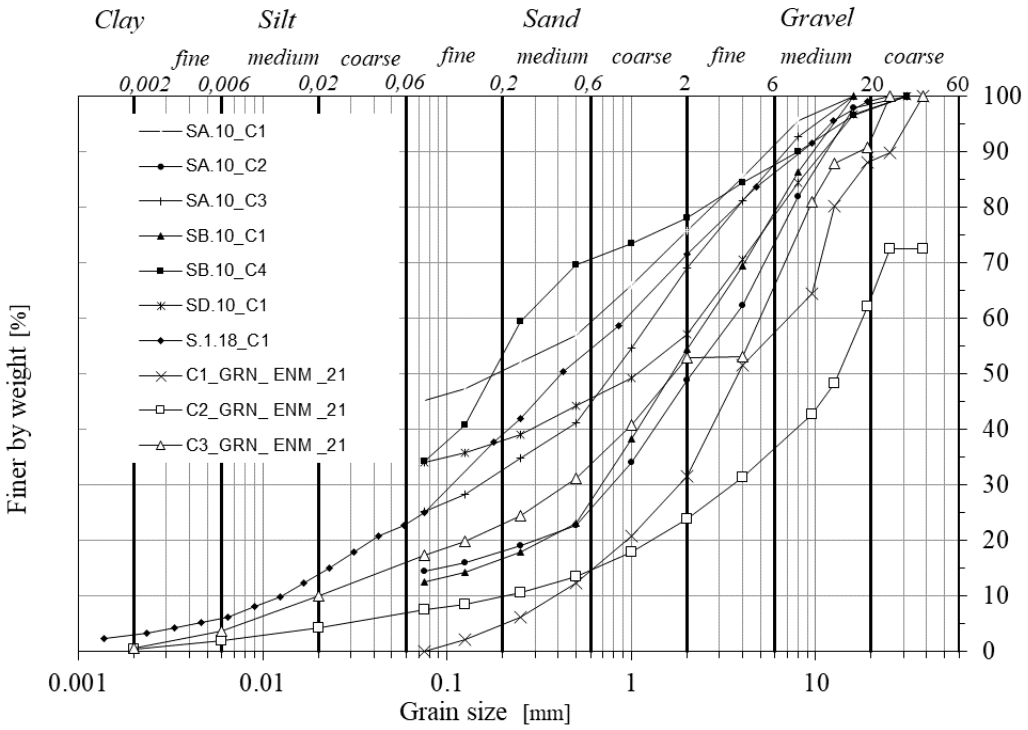

Figure 5.14: *Grain size distribution curves of samples extracted from embankment material (ENM).*

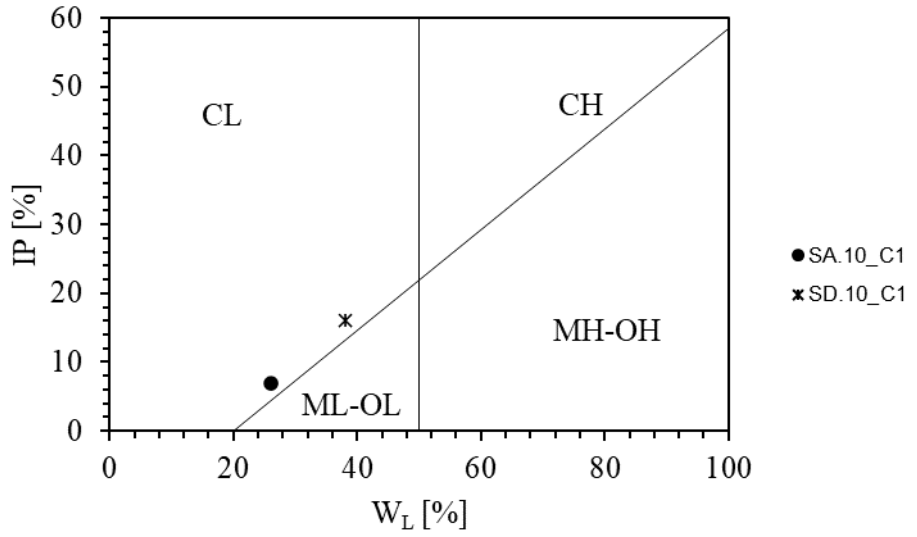

Figure 5.15: *Casagrande chart of samples extracted from embankment material (ENM).*

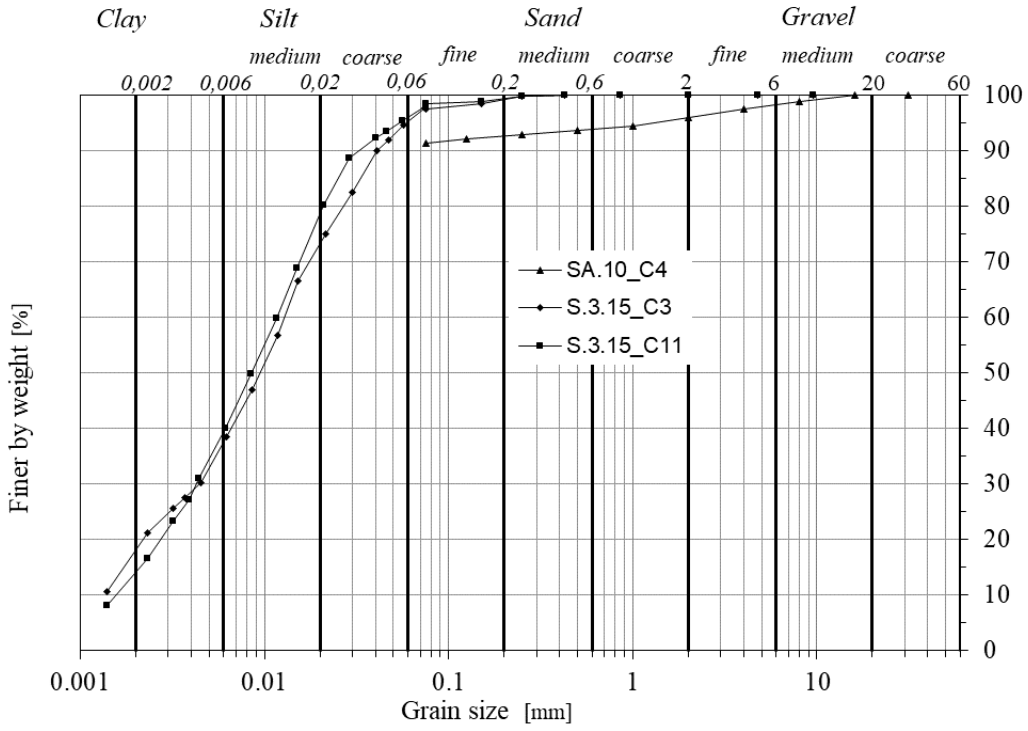

Figure 5.16: *Grain size distribution curves of samples assigned to foundation materials (FNM).*

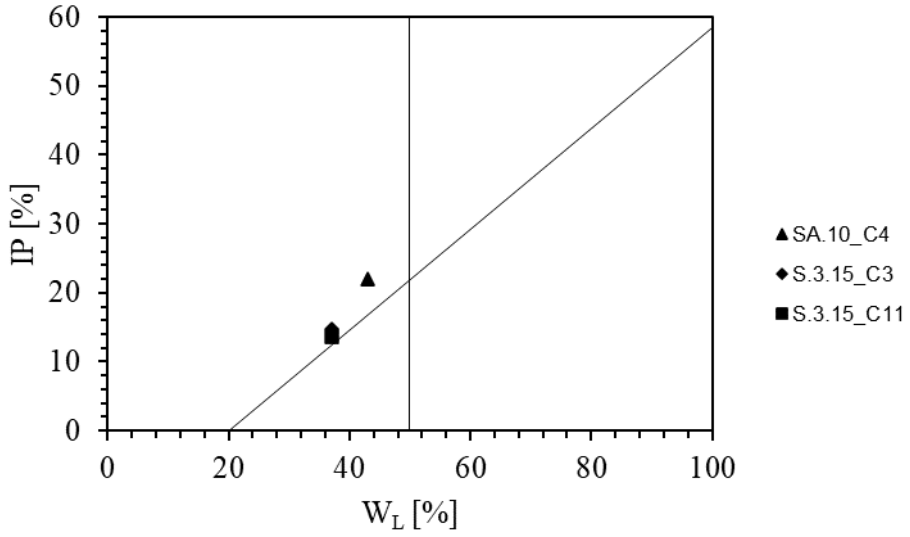

Figure 5.17: *Casagrande chart of samples assigned to foundation materials (FNM).*

5.4.2. Standard Penetration Tests (SPT) analysis

Standard Penetration Tests (SPT), although influenced by many uncertainties, have been extensively studied and used for many decades, and allow the estimation of geotechnical parameters that can be compared with those obtained by other tests. The parameters that have been estimated are the relative density D_R and the effective friction angle φ' through different correlations. The relative density was evaluated with the relationship proposed by Gibbs & Holtz (1957):

$$D_R = 1.5\left(\frac{N_{SPT}}{F}\right)^{0.222} - 0.6 \tag{5.1}$$

where:

$$F = 0.65\left(\frac{\sigma'_{v0}}{p_a}\right)^2 + 16.8\left(\frac{\sigma'_{v0}}{p_a}\right) + 14 \tag{5.2}$$

where σ'_{v0} is the vertical effective stress and, p_a is the atmospheric pressure assumed to be 100 kPa and N_{SPT} is the measured blow-count in Standard Penetration Test. Another correlation used for estimating relative density is the one proposed by Meyerhof (1957):

$$D_R = 0.21\sqrt{\frac{N_{SPT}}{\frac{\sigma'_{v0}}{p_a} + 0.7}} \tag{5.3}$$

The relative density was also evaluated through the Skempton (1986) relation:

$$D_R = \sqrt{\frac{C_N N_{SPT}}{60}} \tag{5.4}$$

where:

$$C_N = \frac{2}{1 + \frac{\sigma'_{v0}}{p_a}} \tag{5.5}$$

for fine sands and tailings:

$$C_N = \frac{3}{2 + \frac{\sigma'_{v0}}{p_a}} \tag{5.6}$$

for coarse sands (embankment). Furthermore, relative density was also evaluated through the correlation proposed by Yoshida & Kokusho (1988):

$$D_R = 0.25 N_{SPT}^{0.46} \left(100 \frac{\sigma'_{v0}}{p_a}\right)^{-0.12} \tag{5.7}$$

and with the relation proposed by Mujtaba (2018):

$$D_R = 1.96 N_{60} - 19.2 \left(\frac{p_a}{\sigma'_{v0}}\right)^{0.23} + 29.2 \tag{5.8}$$

where:

$$N_{60} = \frac{E_m C_B C_S C_R N}{0.6} \tag{5.9}$$

Therein E_m=0.5 is the hammer efficiency value suggested by Kibria & Masood (1998), C_B=1 is the diameter correction, C_S=1 is the sampler correction, C_R=0.75 is the rod correction and is the N average number of blows. The effective friction angle was estimated through the correlation proposed by Schmertmann & Smith (1977):

$$\varphi' = 31.5 + 0.11 D_R \tag{5.10}$$

for medium sand and well-graded fine sand (tailings) and:

$$\varphi' = 38 + 0.08 D_R \tag{5.11}$$

for gravel and for sand and slightly silty gravel (embankment).

To characterize the basin materials, there are only 7 SPT tests that were performed in S.3.18 borehole. The results obtained through the above correlations from these SPT tests are shown in table 5.6.

Table 5.6: Relative density D_R and effective friction angle φ' derived from *SPT performed in basin boreholes*

Year	Survey code	SPT code	Depth [m]	No. of shots	D_R [%] Gibbs (1957)	D_R [%] Meyerhof (1957)	D_R [%] Skempton (1986)	D_R [%] Yoshida (1988)	D_R [%] Mujtaba (2018)	D_R [%] average	φ [°] Schmertmann (1977)
2018	S.3.18	S.3.18_SPT1	3-3.45	3-5-6	66	61	48	46	14	47	37
2018	S.3.18	S.3.18_SPT2	6-6.45	8-7-8	65	59	48	49	20	48	37
2018	S.3.18	S.3.18_SPT3	9-9.45	7-6-6	52	47	38	42	20	40	36
2018	S.3.18	S.3.18_SPT4	12-12.45	8-7-7	50	45	38	44	22	40	36
2018	S.3.18	S.3.18_SPT5	14.5-14.95	4-6-8	46	42	35	43	21	38	36
2018	S.3.18	S.3.18_SPT6	17.5-17.95	25-26-27	78	76	64	77	47	68	39
2018	S.3.18	S.3.18_SPT7	21.5-21.95	27-26-24	70	68	57	73	47	63	38

From Table 5.6 it is possible to deduce that the average estimated relative density ranges from 29% to 64% while the friction angle is around 42 degrees. The effective vertical stress was determined by considering the average value of the specific unit weight obtained from the laboratory tests. From Table 5.6 it is possible to note that the various correlations for relative density give different results; therefore, the average value of the relative density found with the various correlations was used to estimate the friction angle. In paragraph 3.3.3, based on the own monotonic triaxial tests, the critical state stress ratio M_{CS} was determined with a value of 1.459. The friction angle can be found through the relationship:

$$\varphi' = \sin^{-1}\frac{3M_{CS}}{(6+M_{CS})} \tag{5.12}$$

From the previous equation, a value of the friction angle of 36 degrees is determined, which is in good agreement with what is determined from the correlations in Table 5.6.

Regarding the embankment, SPT tests were carried out in all surveys carried out in 2010 and in a 2018 survey. The values of relative density and effective friction angle determined from the correlations based on these SPT data are summarized in Table 5.7.

Table 5.7: *Relative density D_R and effective friction angle φ' derived from SPT performed in embankment boreholes.*

Year	Survey code	SPT code	Depth [m]	No. of shots	D_R [%] Gibbs (1957)	D_R [%] Meyerhof (1957)	D_R [%] Skempton, (1986)	D_R [%] Yoshida (1988)	D_R [%] Mujtaba (2018)	D_R [%] average	φ' [°] Schmertmann (1977)
2010	SA.10	SA.10_SPT1	4.6-5.5	10-9-9	73	69	55	55	21	55	42
2010	SA.10	SA.10_SPT2	6.6-7.05	14-9-7	65	60	49	50	21	49	42
2010	SA.10	SA.10_SPT3	8.45-8.9	6-3-3	37	34	29	31	16	29	40
2010	SA.10	SA.10_SPT4	11.1-11.5	14-13-13	68	64	56	59	29	55	42
2010	SA.10	SA.10_SPT5	13.5-13.95	12-10-10	57	52	47	51	26	47	42
2010	SA.10	SA.10_SPT6	15-15.45	17-12-10	57	52	48	53	28	47	42
2010	SA.10	SA.10_SPT7	17-17.45	21-11-12	55	51	47	53	29	47	42
2010	SA.10	SA.10_SPT8	19.5-19.95	12-8-10	46	43	40	46	26	40	41
2010	SA.10	SA.10_SPT9	21-21.45	10-12-13	53	49	46	54	31	46	42
2010	SB.10	SB.10_SPT1	5-5.45	5-4-5	54	49	39	40	15	39	41
2010	SB.10	SB.10_SPT2	7-7.45	9-5-5	52	46	39	40	17	39	41
2010	SB.10	SB.10_SPT3	12.6-13.5	9-11-11	61	56	50	54	27	49	42
2010	SB.10	SB.10_SPT4	14.8-15.25	12-10-7	51	46	42	47	24	42	41
2010	SB.10	SB.10_SPT5	17-17.45	14-13-14	60	55	51	57	31	51	42
2010	SB.10	SB.10_SPT6	20-20.45	11-12-13	54	50	47	54	30	47	42
2010	SB.10	SB.10_SPT7	22.3-22.75	19-22-21	65	62	59	68	42	59	43
2010	SB.10	SB.10_SPT8	24.5-24.95	15-27-25	68	66	63	74	48	64	43
2010	SC.10	SC.10_SPT1	4.4-4.85	4-3-3	46	41	32	33	13	33	41
2010	SC.10	SC.10_SPT2	5.9-6.35	4-4-5	52	46	38	39	16	38	41
2010	SC.10	SC.10_SPT3	7.3-7.75	3-4-9	58	52	44	45	19	44	41
2010	SC.10	SC.10_SPT4	9.6-10.05	6-6-6	51	46	40	42	20	40	41
2010	SC.10	SC.10_SPT5	11-11.45	9-12-14	69	64	56	59	29	55	42

Year	Survey code	SPT code	Depth [m]	No. of shots	D_R [%] Gibbs (1957)	D_R [%] Meyerhof (1957)	D_R [%] Skempton, (1986)	D_R [%] Yoshida (1988)	D_R [%] Mujtaba (2018)	D_R [%] average	φ' [°] Schmertmann (1977)
2010	SC.10	SC.10_SPT6	13-13.45	10-10-10	58	53	47	51	26	47	42
2010	SC.10	SC.10_SPT7	14.9-15.35	10-10-12	57	52	48	53	28	48	42
2010	SC.10	SC.10_SPT8	17.35-17.8	7-11-12	55	50	47	53	29	47	42
2010	SC.10	SC.10_SPT9	20-20.45	13-18-13	59	55	52	60	34	52	42
2010	SC.10	SC.10_SPT10	24-24.45	7-6-6	33	32	30	38	23	31	40
2010	SC.10	SC.10_SPT11	26.4-26.85	15-19-18	57	54	52	62	39	53	42
2010	SD.10	SD.10_SPT1	7.7-8.15	21-8-10	65	60	51	52	23	50	42
2010	SD.10	SD.10_SPT2	9-9.45	7-10-10	65	60	52	53	25	51	42
2010	SD.10	SD.10_SPT3	11-11.45	10-10-11	63	58	51	53	26	50	42
2010	SD.10	SD.10_SPT4	13-13.45	9-12-10	60	55	50	53	27	49	42
2010	SD.10	SD.10_SPT5	14.9-15.35	8-7-7	46	42	38	43	23	38	41
2010	SD.10	SD.10_SPT6	17.2-17.65	19-20-22	72	68	63	70	40	63	43
2010	SD.10	SD.10_SPT7	20-20.45	16-13-17	58	54	51	59	33	51	42
2018	S.1.18	S.1.18_SPT1	3-3.45	7-29-26				97	41	69	46
2018	S.1.18	S.1.18_SPT2	9-9.45	9-6-6	52	47	40	42	20	40	41
2018	S.1.18	S.1.18_SPT3	12-12.45	6-4-6	42	38	34	38	19	34	41
2018	S.1.18	S.1.18_SPT4	15-15.45	8-10-10	55	50	45	50	26	45	42
2018	S.1.18	S.1.18_SPT5	18-18.45	16-14-14	59	55	51	58	32	51	42
2018	S.1.18	S.1.18_SPT6	21-21.45	13-12-12	52	48	45	53	30	45	42
2018	S.1.18	S.1.18_SPT7	24-24.45	8-8-8	39	37	35	43	25	36	41
2018	S.1.18	S.1.18_SPT8	27-27.45	6-8-7	35	34	33	41	25	34	41
2018	S.1.18	S.1.18_SPT9	30-30.45	66-7-5	28	29	28	37	24	29	40

From Table 5.7 it is possible to deduce that the average estimated relative density ranges from 29% to 64% while the friction angle is around 42 degrees.

5.4.3. Piezocone Penetration Tests (CPTu) analysis

Using the tip resistance q_c, the lateral friction resistance f_s and the pore pressure u measured in Piezocone Penetration Tests (CPTu), it is possible to carry out a stratigraphic recognition of the deposit as well as allowing the estimation of the relative density and the friction angle, among others. There are numerous empirical relationships that relate the quantities measured by the CPTu test to the stratigraphy. In the present work reference has been made to what was proposed by Robertson (2010) based on the definition of the Soil Behaviour Type index, *Ic*, defined as:

$$I_c = [(3.47 - \log Q_{tn})^2 + (\log F_r + 1.22)^2]^{0.5} \tag{5.13}$$

where:

$$Q_{tn} = \left[\frac{(q_t - \sigma'_{v0})}{p_a}\right]\left(\frac{p_a}{\sigma'_{v0}}\right)^n \tag{5.14}$$

$$F_r = \left[\left(\frac{f_s}{q_t - \sigma'_{v0}}\right)\right]100\% \tag{5.15}$$

In the previous equations $q_t = q_c + u_2(1 - a)$ is the corrected cone resistance, with a being the tip net area ratio n being an exponent *Ic*:

$$n = 0.381(I_c) + 0.05\left(\frac{\sigma'_{v0}}{p_a}\right) - 0.15 \tag{5.16}$$

Therefore Q_{tn} is determined by iterations.

On the basis of the I_c value, a soil typology was assigned to a layer. Furthermore, the relative density of the coarse-grained soils was then estimated through the Baldi (1986) correlation:

$$D_R = \frac{1}{C_2} \ln \left[\frac{q_t}{C_0 (\sigma'_{v0})^{C_1}} \right] \tag{5.17}$$

where C_0=157, C_1=0.55 and C_2=2.41 are the suggested empirical constants. The friction angle was estimated through (Robertson et al. 1983):

$$\varphi' = \tan^{-1} \left[0.1 + 0.38 \log \frac{q_t}{\sigma'_{v0}} \right] \tag{5.18}$$

while the small-strain shear stiffness was evaluated through (Robertson et al. 1992):

$$G_{max} = 0.0188 (10^{0.55\, I_c + 1.68})(q_t - \sigma'_{v0}) \tag{5.19}$$

Permeability was finally estimated through the relation proposed by Robertson (2010):

$$k = 10^{(0.952 - 3.04 I_c)} \tag{5.20}$$

if $1<I_c<3.27$ and:

$$k = 10^{(-4.52 - 1.37 I_c)} \tag{5.21}$$

if $3.27<I_c<4$.

Figures 5.18, 5.19 and 5.20 show the results of the analysis carried out on the CPTu tests performed either within the settling basin or on the embankment.

From the analysis of CPTu.3.15 and CPTu.3.18 it is possible to deduce that the basin materials are rather homogeneous and attributable to sands and silts with an average relative density of about 37% and an average friction angle of 36 degrees. It seems that the CPTu.3.15 reaches the natural clay layer at a depth of 18 m.

From the analysis of Figure 5.17 it is possible to observe that the embankment is also composed of materials attributable to sands and silts with an average relative density of 36% and an average friction angle of 35 degrees. CPTu2.18 seems to intercept the natural clay soil at a depth of 23 m.

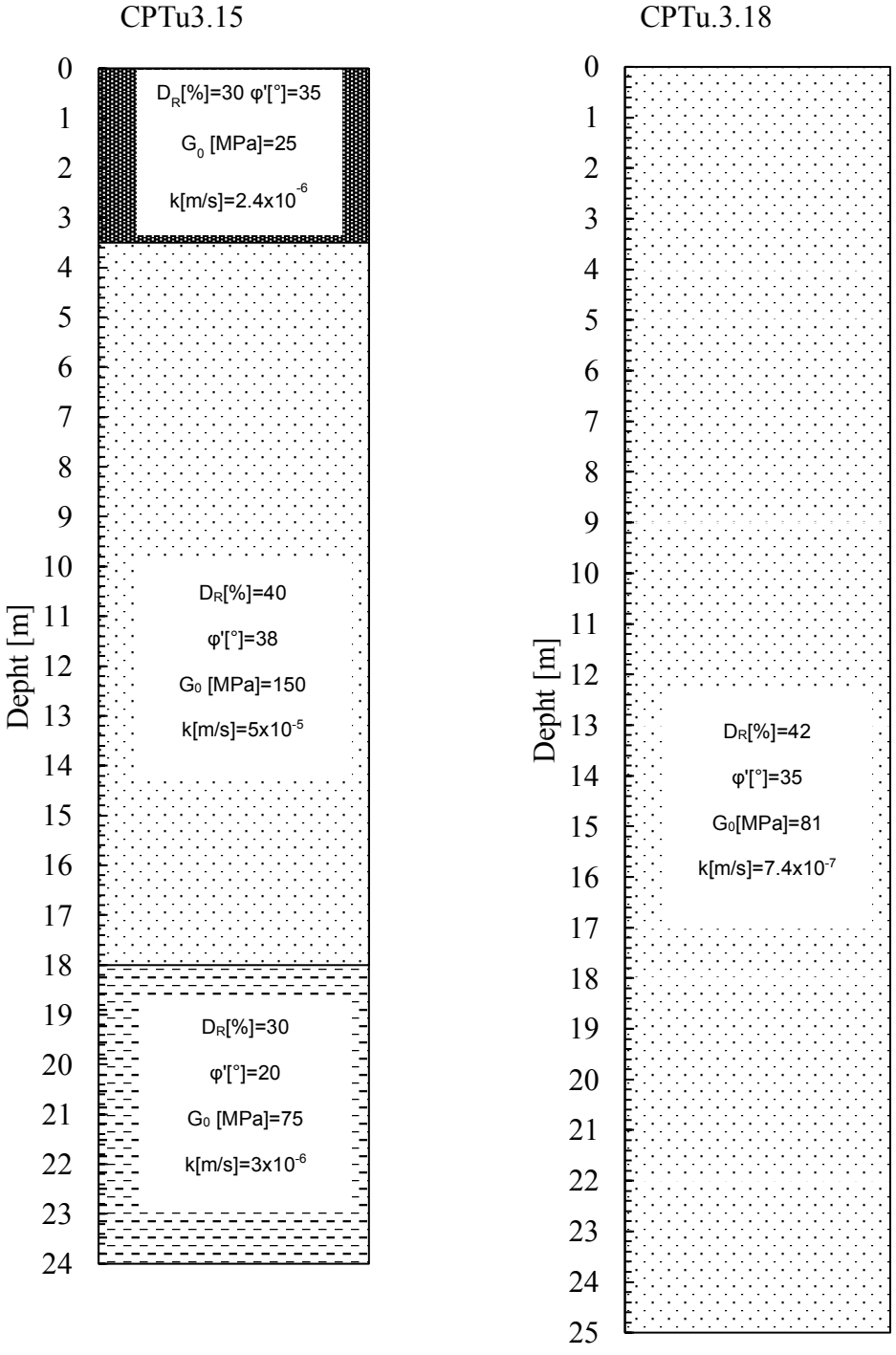

Figure 5.18: *Results from analysis of CPTu.3.15 and CPTu.3.18 performed within the basin.*

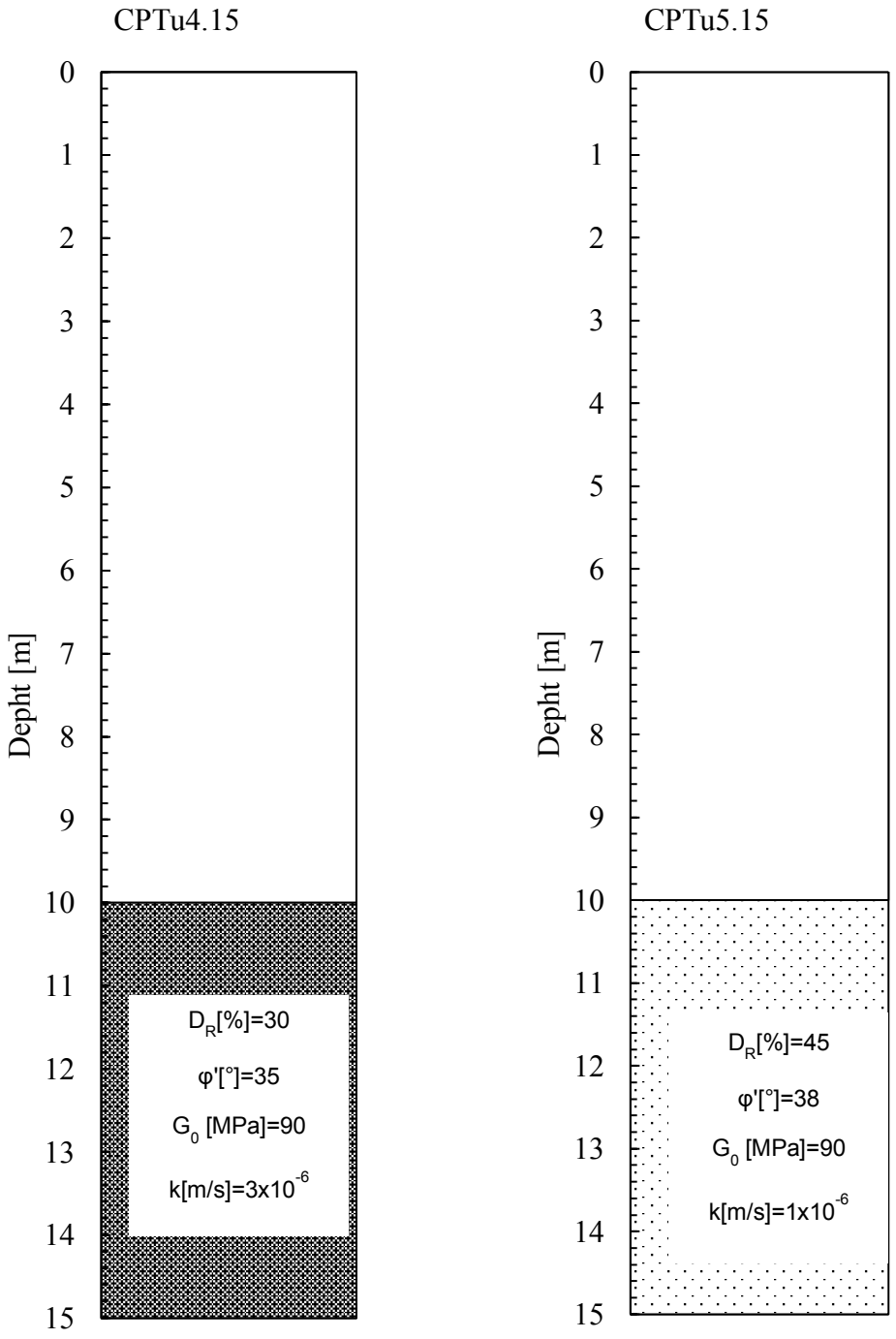

Figure 5.19: *Results from elaborations of CPTu.4.15 and CPTu.5.15 performed on the embankment*

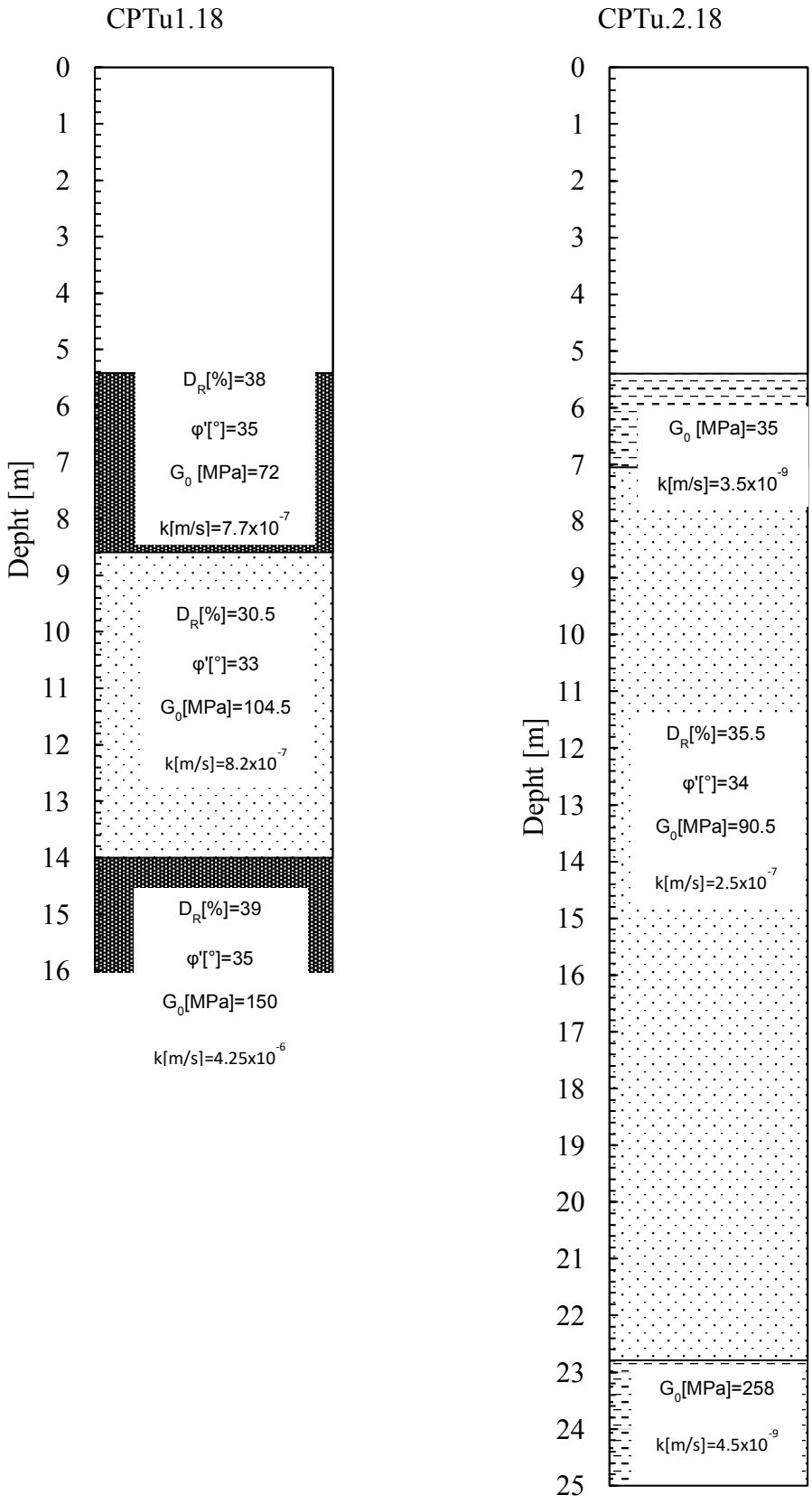

Figure 5.20: *Results from elaborations of CPTu.1.18 and CPTu.2.18 performed on the embankment.*

5.4.4. Down hole tests analysis

Four down hole tests have been conducted on the structure: three on the embankment and one in the basin. Vertical soil profiles were available only for down holes DH.9.07 and DH.1.18. In Figure 5.21 the position (projected) of the analyzed down hole tests is shown on the investigation section, along with averaged values of the shear wave velocity for certain soil layers.

None of the analyzed down hole tests reaches the seismic bedrock (soil unit characterized by a S-wave propagation velocity greater than 800 m/s), so it was determined through the analysis of a refraction seismic survey. The results show that the seismic bedrock is encountered at a depth of about 40 to 45 m.

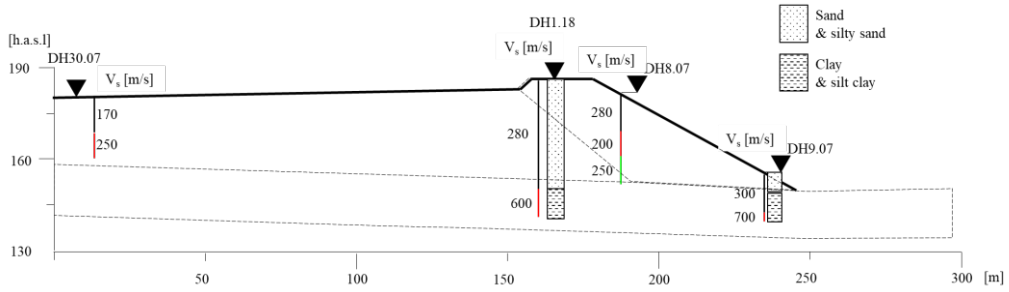

Figure 5.21: Location of d*own hole profiles on structure cross section and averaged values of shear wave velocity for certain soil layers.*

5.4.5. Geotechnical model

Based on the analysis of the data from the laboratory and field tests made it possible to build the geotechnical model of the structure was built.

Basin material (SBM)

Figure 5.22 shows the lithologic descriptions of the settling basin material as a function of depth obtained both from the samples tested in the laboratory and from the CPTu analysis.

The description of the materials shown in Figure 5.22 confirms that the settling basin is homogeneous and mainly composed of silty and sandy soils with slight differences in the percentages of the two fractions.

Figure 5.23 a shows the values of relative density D_R determined through laboratory, SPT and CPTu tests conducted on the basin area. From this presentation one can deduce that D_R is approximately constant with depth with an average value of about 40%. However, the upper 7 m show more scatter of the relative densities, with values lying between 20 and 50%. Figure 5.23 b shows the values of the friction angle obtained with the same previous mentioned tests from which it is possible to deduce that it does also not undergo substantial variations with an average value of 37 degrees. The only exception is the depth between 3 m and 7 m, where the friction angle varies between 29 and 48 degrees.

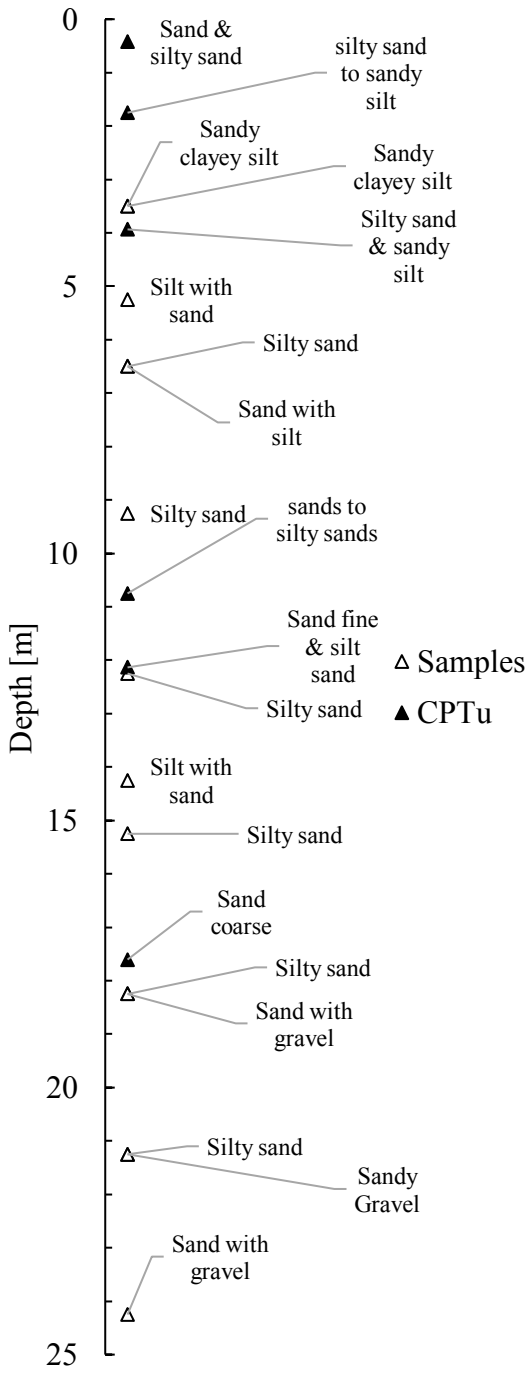

Figure 5.22: *Soil description of the specimens from laboratory or CPTu tests on basin material (SBM).*

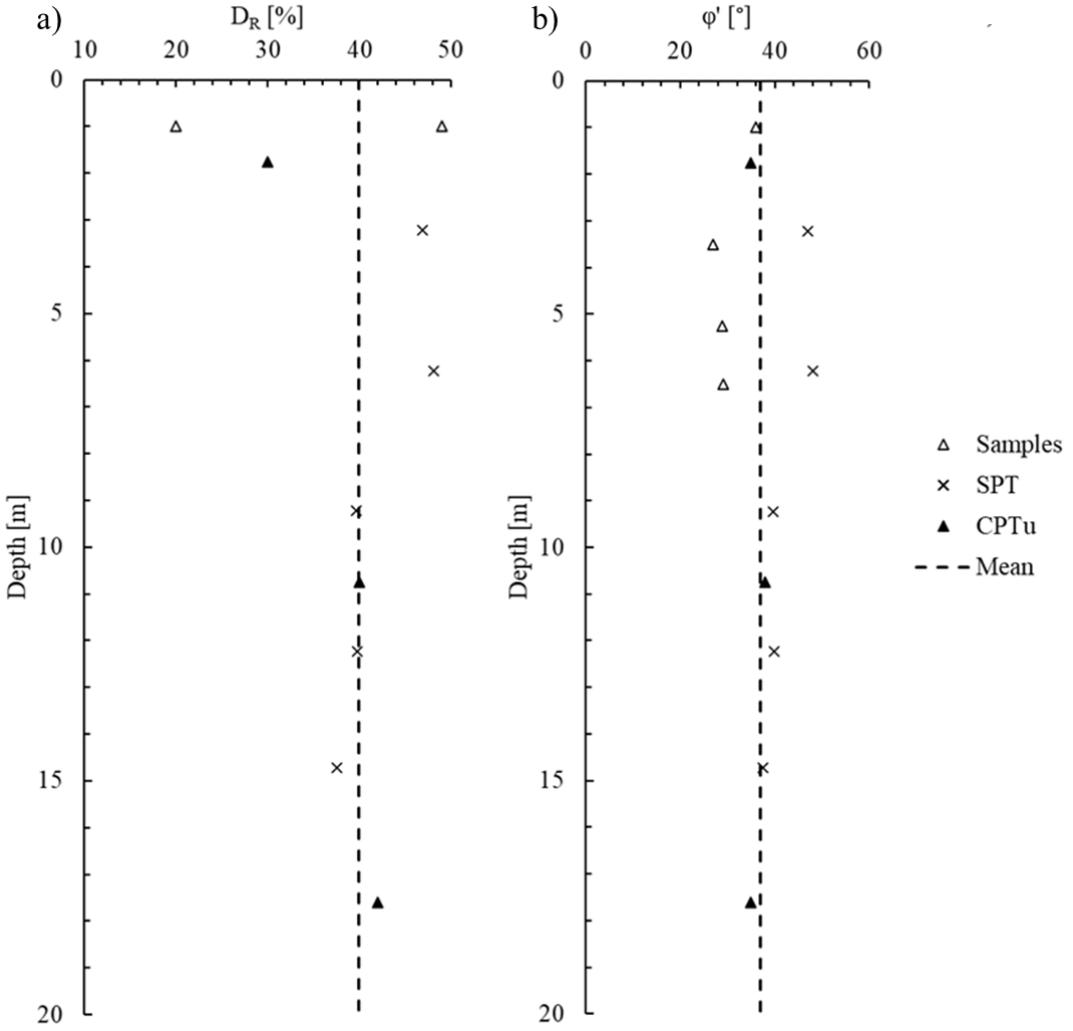

Figure 5.23: *a) Soil relative density b) friction angle determined from laboratory SPT and CPTu test data for the basin material (SBM).*

Embankment material (ENM)

Figure 5.24 shows the lithologic descriptions of the embankment material as a function of depth obtained both from the samples tested in the laboratory and from the CPTu data analysis.

Also, in this case the embankment appears to be rather homogeneous consisting of materials attributable to sands and silts, with also the presence of gravels.

For the reasons previously explained, the granulometric characteristics of the embankment material do not allow laboratory tests to be performed (at least with standard equipment). Therefore, the relative density and the friction angle shown in Figure 5.25 a and 5.25 b respectively were estimated through the results of SPT and CPTu tests. Also in this case the obtained values of both the relative density and the friction angle are rather uniform, although they are a little more dispersed than for the

basin material. In particular, average values of 45% for the relative density and 41 degrees for the friction angle are obtained.

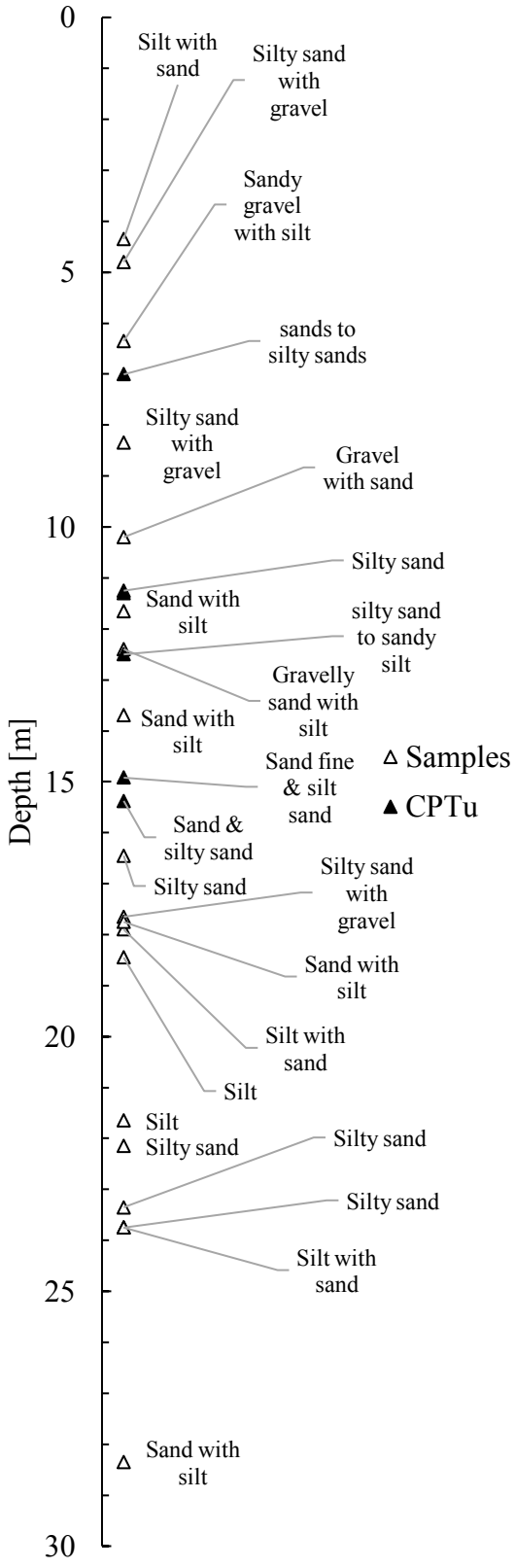

Figure 5.24: *Soil description of the specimens or from CPTu tests on embankment material (ENM).*

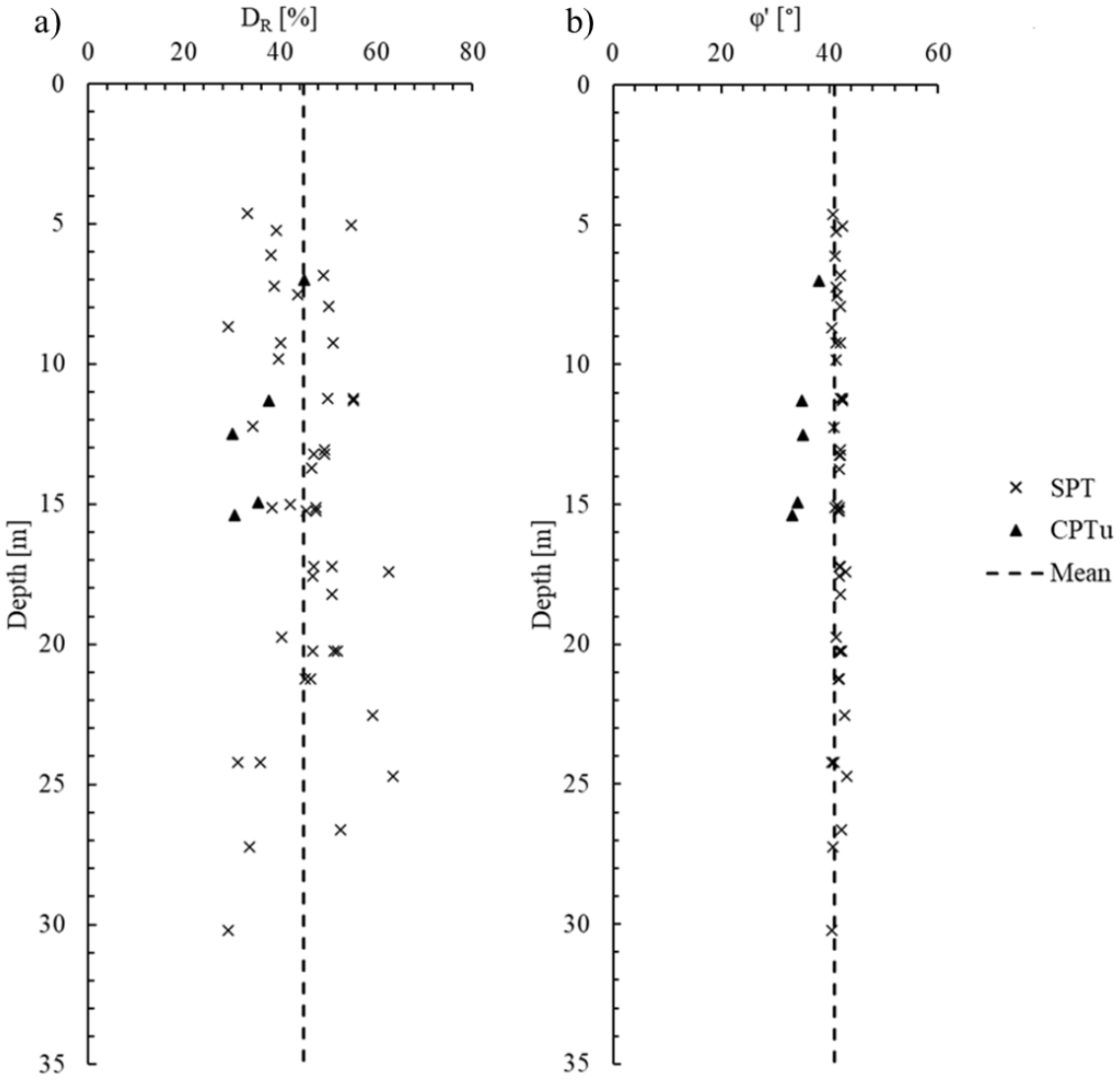

Figure 5.25: *a) Soil relative density b) friction angle determined from SPT and CPTu test for the embankment material (ENM).*

Foundation soil (FNM)

For the foundation soil less information is available than for the other two geotechnical units, and in particular the three samples SA.10_C4, S.3.15_C3 and S.3.15_C11 and the last meters of the CPTu.2.18 test. From the description of these materials, it is possible to deduce that they consist of a significant fraction of clay. Three direct shear tests were performed on sample S3.15_C3 from which the values of cohesion and effective friction angle were obtained, which are 6 kPa and 23 degrees respectively. From test CPTu.2.18 it is possible to deduce that the initial shear stiffness modulus of this material is 258 MPa.

Finally Figure 5.26 shows the position (projected) of both the soil vertical profiles and CPTu tests on the section under analysis while Figure 5.27 shows the section of the geotechnical model obtained.

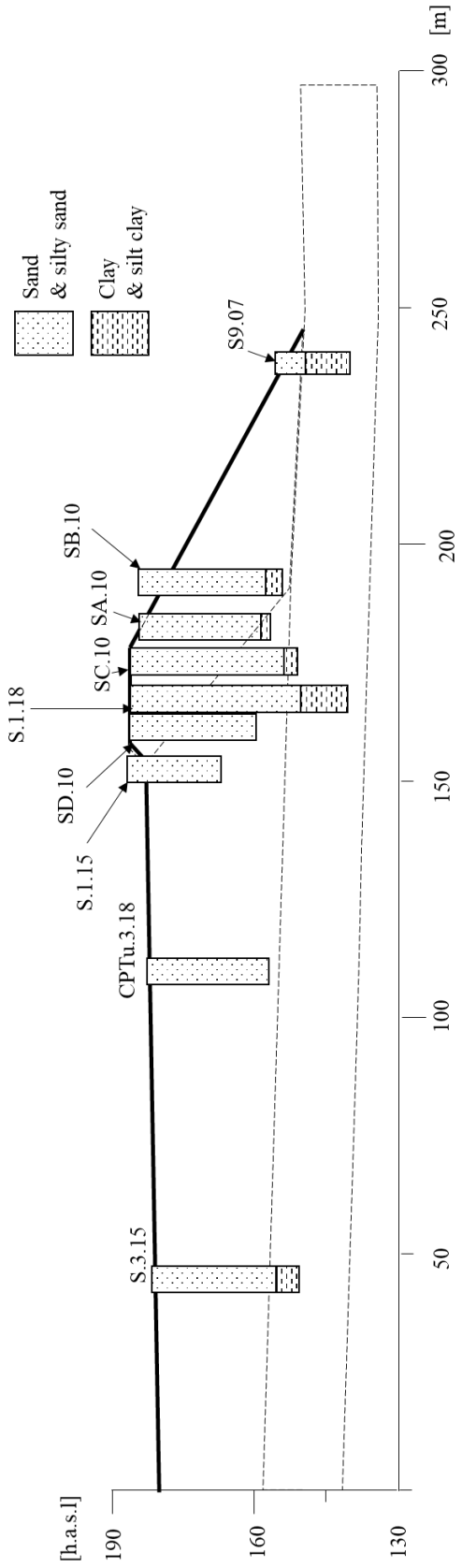

Figure 5.26: *Projection of vertical soil profiles and CPTu tests on cross section.*

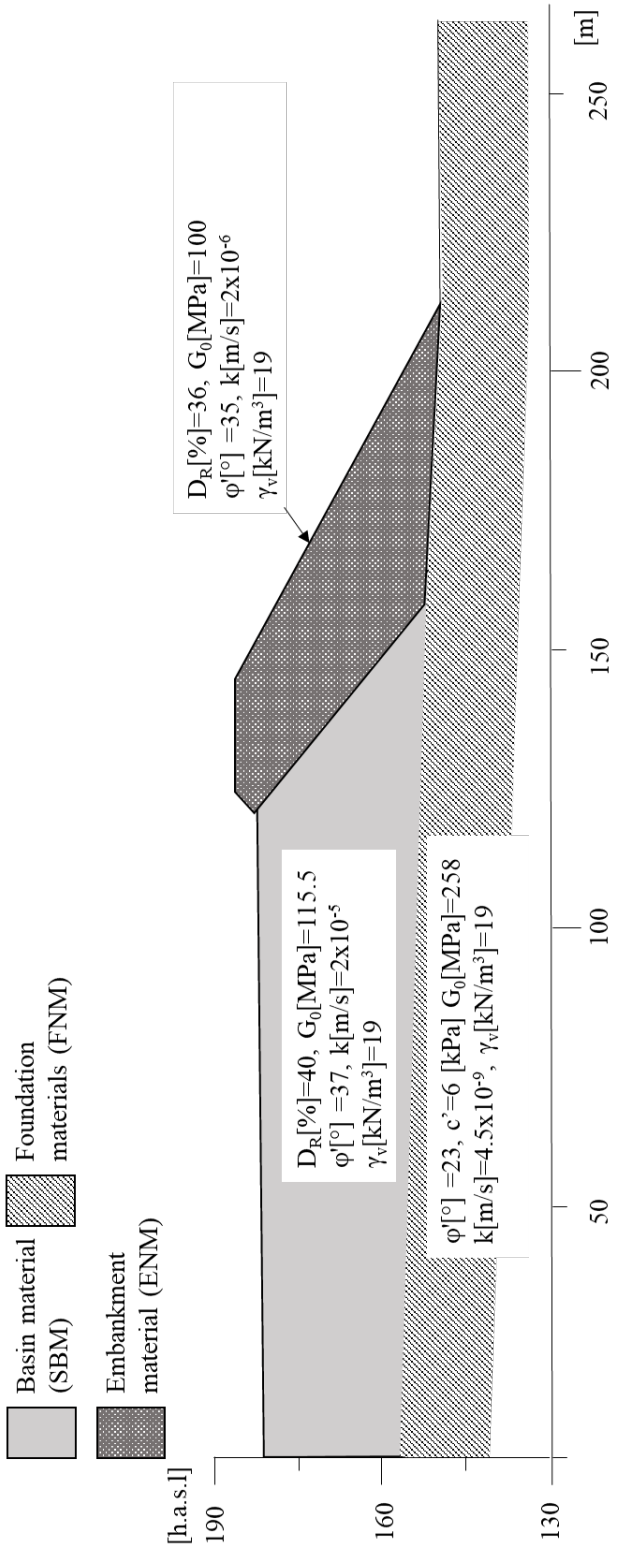

Figure 5.27: *Cross section of geotechnical model.*

Bibliography

Baldi, G. (1986). Interpretation of CPT's and CPTU's. Proc. 4th Int. Geotech. Semin., Singapore, 1, 3-10.

Camporeale, G. (2005). Massa Marittima (GR): gli scavi dell'Accesa: campagna 2005. Massa Marittima (GR): gli scavi dell'Accesa: campagna 2005, 429-432.

Capperi, M., & Nannoni, R. (1997). La miniera di Fenice Capanne (Grosseto). Rivista mineralogica italiana. (1), 63-82.

Cuteri, F., & Mascaro I. (1995). Colline Metallifere Inventario del Patrimonio Minerario e Mineralogico. Dipartimento Ambiente. Regione Toscana.

DISS Working Group (2021). Database of Individual Seismogenic Sources (DISS), Version 3.3.0: A compilation of potential sources for earthquakes larger than M 5.5 in Italy and surrounding areas. Istituto Nazionale di Geofisica e Vulcanologia (INGV). https://doi.org/10.13127/diss3.3.0

DM 17 gennaio 2018. Norme tecniche per le costruzioni. G.U. n.42 del 20 febbraio 2018.

Gasperini, P., Stucchi, M., & Vannucci, G (2004). Zonazione sismogenetica ZS9– App. 2 al Rapporto Conclusivo. Rapporto Conclusivo per il Dipartimento della Protezione Civile. INGV.

Gibbs, H. J., & Holtz, W. G. (1957). "Research on Determining the Density of Sands by Spoon Penetration Testing." Proc. 4th Int'l Conference on Soil Mechanics and Foundation Engineering, London, England, Vol. 1, 35-39.

Gruppo di Lavoro MPS (2004). Redazione della mappa di pericolosità sismica prevista dall'Ordinanza PCM 3274 del 20 marzo 2003. Rapporto Conclusivo per il Dipartimento della Protezione Civile. INGV, Milano-Roma. http://zonesismiche.mi.ingv.it.

Gruppo di lavoro Regione Toscana (n.d.). Ambito 16 colline metallifere. Scheda d'ambito, Regione Toscana.

Haupt, T. (1847). Delle miniere e della loro industria in Toscana. Tip. Le Monnier.

Kibria, S., & Masood, T. (1998). SPT, relative density and PHI relationships for indus sands at chashma. In Proceeding of VII national conference of Pakistan national society for soil mechanics and foundation engineering (pp. 169-188).

Meletti, C. (2007). Proseguimento della assistenza al DPC per il completamento e la gestione della mappa di pericolosità sismica prevista dall'Ordinanza PCM 3274 e progettazione di ulteriori sviluppi. Progetto S1.

Meyerhof, G.G. (1957). Discussion on Research on determining the density of sands by penetration testing. Proc. 4th Int. Conf. on Soil Mech. and Found. Engrg., Vol. 1: 110.

Mujtaba, H., Farooq, K., Sivakugan, N., & Das, B. M. (2018). Evaluation of relative density and friction angle based on SPT-N values. KSCE Journal of Civil Engineering, 22, 572-581.

Nannoni, R., & Capperi, M. (1983). La miniera di «Fenice-Capanne». Minerali e genesi del giacimento.

Porte, L. (1833). Ragionamento intorno alla riattivazione che si propone d'intraprendere di alcune miniere in Toscana. Pezzati.

Robertson, P. K. (2010, May). Estimating in-situ soil permeability from CPT & CPTu. In Memorias del 2nd International Symposium on Cone Penetration Testing, California State Polytechnic University Pomona, CA. http://www. cpt10. com/PDF_Files/2-51Robehc. pdf.

Robertson, P. K. (2010, May). Soil behaviour type from the CPT: an update. In 2nd International symposium on cone penetration testing (Vol. 2, No. 56, p. 8). Huntington Beach: Cone Penetration Testing Organizing Committee.

Robertson, P. K., & Campanella, R. G. (1983). Interpretation of cone penetration tests. Part II: Clay. Canadian geotechnical journal, 20(4), 734-745.

Robertson, P. K., Woeller, D. J., & Finn, W. D. L. (1992). Seismic cone penetration test for evaluating liquefaction potential under cyclic loading. Canadian Geotechnical Journal, 29(4), 686-695.

Schmertmann, J. H., & Smith, T. V. (1977). A summary of SPT energy calibration services performed for the Florida DOT under service contract 99700-7150-010 (Vol. 73). Final Research Report 245.

Storia - Parco Nazionale delle Colline Metallifere. (2022, April 6). Parco Nazionale Delle Colline Metallifere. https://parcocollinemetallifere.it/storia-e-cultura/

Tanelli, G. (1983). Mineralizzazioni metallifere e minerogenesi della Toscana. Memorie della Società Geologica Italiana, 25, 91-109.

Yoshida, Y., & Kokusho, K. (1988). A proposal on application of penetration tests on gravelly soils. Denryoku Chuo Kenkyusho Hokoku, 1-4.

6. Constitutive models

Given the fundamental role that soil constitutive models play in numerical analyses, this chapter is dedicated to the description of the models used, the tests undertaken to define the input parameters and the appropriate calibration procedures. As explained in Chapter 5, the geotechnical model includes 3 geotechnical units. The behavior of the geotechnical units called embankment (ENM) and foundation (FNM) materials has been described by means of the constitutive models PM4Sand (Boulanger & Ziotopoulou 2017) and Pressure Independent Multi yield (PIMY), respectively. The geotechnical unit called basin materials (SBM) includes all the materials within the tailings pond. These soils have characteristics attributable to sands and silts. Their behavior has been extensively investigated through field and laboratory tests (Chapters 3 and 5) and has been described by means of two different constitutive models as well: SANISAND (Dafalias & Manzari 2004) and Pressure Dependent Multi Yield (PDMY) (Elgamal et al. 2003, Yang et al. 2003, Yang et al. 2004, Khosravifar 2012, Khosravifar et al. 2018). The attribution of these two constitutive models to reproduce the behavior of soils in seismic liquefaction conditions has allowed, through the comparison of the results, to point out similarities and differences between the two models, and to obtain a more complete and diversified information on the behavior of the structure.

6.1. Brief description of the utilized constitutive models

In this section a brief description of the theory for each constitutive model utilized in the numerical analysis is given. The purpose of this introduction to the different models is mostly to recall the equations involving the material constants used in this PhD thesis for numerical modelling. More details on the constitutive models can be found in the respective bibliographic references. These models were chosen because they are very advanced and considered suitable to describe well the behavior in dynamic conditions of the various materials of the structure. As described in Chapter 4, many works dealing with seismic behavior of TSFs use rather simple constitutive models such as the Mohr-Coulomb model. The OpenSees software returns results using the typical structural science sign conventions of positive for tension and negative for compression. In this work the results are presented according to the typical geotechnical conventions (positive for compression and negative for traction).

6.1.1. SANISAND (Dafalias & Manzari 2004 version)

SANISAND is an acronym of Simple ANIsotropic SAND constitutive models. These constitutive models are framed within the critical state theory of bounding plastic surfaces (Taiebat & Dafalias 2008). Referring to an axisymmetric triaxial space formulation, elastic strain increments are defined as:

$$d\varepsilon_q^e = \frac{dq}{3G} \tag{6.1}$$

$$d\varepsilon_v^e = \frac{dp'}{K} \tag{6.2}$$

where $\varepsilon_q = \frac{2}{3}(\varepsilon_1 - \varepsilon_2)$ is the deviatoric strain, $\varepsilon_v = (\varepsilon_1 + 2\varepsilon_2)$ is the volumetric strain, $q = \sigma_1' - \sigma_3'$ is the deviatoric stress, $p' = \frac{1}{3}(\sigma_1' + 2\sigma_3')$ is the mean effective stress (Roscoe convention), G is the shear incremental modulus and K is the bulk incremental modulus. The superscript e indicates elastic deformation. The elastic shear modulus can be determined by the relationship (Richart et al. 1970, Li & Dafalias 2000):

$$G = G_0 p_a \frac{(2.97 - e)^2}{1 + e}\left(\frac{p'}{p_a}\right)^{\frac{1}{2}} \tag{6.3}$$

where G_0 is a constant, e is the current void ratio, p' is the current mean effective stress and p_a is the atmospheric pressure.

The bulk modulus is defined as:

$$K = \frac{2(1+\nu)}{3(1-2\nu)}G \tag{6.4}$$

where ν is the Poisson's ratio.

Deviatoric and volumetric plastic strain increments are respectively:

$$d\varepsilon_q^p = \frac{d\eta}{H} \tag{6.5}$$

$$d\varepsilon_v^p = \mathrm{d}\left|d\varepsilon_q^p\right| \tag{6.6}$$

where $\eta = \frac{q}{p'}$ is the stress ratio, H is the plastic hardening modulus, d differential symbol and d dilatancy symbol. The apex p stands for plastic deformations. The yield function is defined as:

$$f = |\eta - \alpha| - m = 0 \tag{6.7}$$

In the q-p' space, this equation represents the Drucker-Prager criterion that generate in the origin. α is the slope of the bisector of the Drucker-Prager cone. For a given p_c', the value of the distance between the two lines is $2mp_r'$.

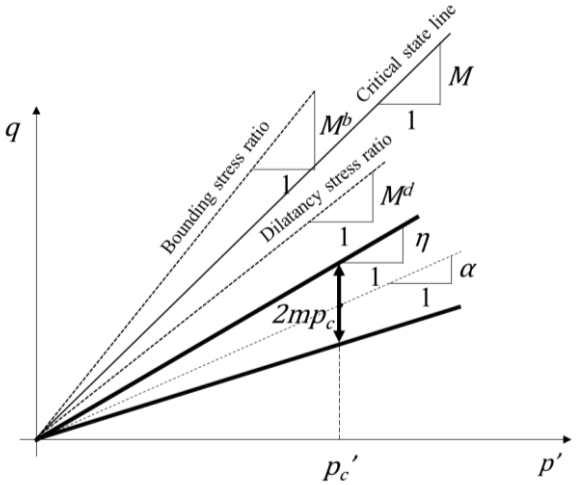

Figure 6.1: *Representation of yield, dilatancy and boundary surfaces in q-p' space (Reworked from Dafalias & Manzari 2004).*

If the current η lies within the two lines, only elastic strains occur; otherwise, if η reaches the upper line and $d\eta$>0 or if η reaches the lower line and $d\eta$<0, plastic strains develop. To ensure that η remains on the yield surface, that means that f=0 is fulfilled, α changes orientation m remains constant in the model. There is no isotropic hardening, only kinematic in order to ensure kinematic hardening. The stress ratio η can increase until it reaches the bounding stress ratio M^b. The plastic hardening modulus H is related to M^b by the following equation:

$$H = h(M^b - \eta) \tag{6.8}$$

where:

$$h = \frac{b_0}{|\eta - \eta_{in}|} \tag{6.9}$$

and:

$$b_0 = G_0 h_0 (1 - c_h e) \left(\frac{p'}{p_a}\right)^{-\frac{1}{2}} \tag{6.10}$$

where h_0 and c_h are scalar parameters and η_{in} is the initial value of the stress ratio. The model also incorporates the concept of the dilatancy stress ratio M^d (Rowe 1962) or equivalently phase transformation angle (Ishihara et al. 1975). The dilatancy d is proportional to the "distance" between the current stress ratio and the dilatancy stress ratio M^d:

$$d = A_d (M^d - \eta) \tag{6.11}$$

where A_d is a function of the state.

If η<M^d, then d>0 and the behavior is contractive, while if η>M^d, then d<0 and the behavior is dilative. As stated before, when η reaches the lower straight line ($\eta = \alpha - m$) the increment of stress ratio is negative $d\eta$<0, and so the plastic deformations will be in the reverse sense. Therefore, during extension (where $d\eta$<0), the plastic hardening modulus becomes:

$$H = h(M_e^b + \eta) \tag{6.12}$$

and:

$$d = A_d (M_e^d + \eta) \tag{6.13}$$

where M_e^b and M_e^d are the bounding stress ratio and the dilatancy stress ratio in extension, respectively. Therefore, the "distance" between the current stress ratio, the bounding stress ratio, and the dilatancy stress ratio is measured. The critical state line in the void ratio - mean effective stress space is expressed as (Li & Wang 1998):

$$e_c = e_0 - \lambda_c \left(\frac{p'_c}{p_a}\right)^{\xi} \tag{6.14}$$

where e_0 is the void ratio for $p'_c = 0$ and λ_c and ξ are constants. To prevent the volumetric deformations from tending to infinity and allow the softening behavior to be expressed, the bounding stress ratio and the dilatancy stress ratio tend to the critical state line as the material tends to the critical state. This trend was achieved through the state parameter $\Psi = e - e_c$ introduced by Been and Jefferies (1985) which defines the "distance" between the current void ratio and the critical one at the same mean effective stress.. M^b and M^d are related to the state parameter via the following expressions:

$$M^b = M - k^b\Psi \tag{6.15}$$
$$M^d = M - k^d\Psi \tag{6.16}$$

From the previous equations it is possible to deduce that as the material tends to the critical state, Ψ decreases making M^b and M^d tend to M. If the state of the soil is denser than critical, the dilatancy stress ratio must be lower than the critical stress ratio that must be lower than the bounding stress ratio $M^d<M<M^b$, while if the state is looser than critical, the order must be $M^b<M<M^d$.

In order to correctly simulate pore-water pressure build-up in saturated soils during cyclic loading, a fabric-dilatancy internal variable z has been introduced. Its evolution is described by:

$$dz = -c_z\langle -d\varepsilon_v^p\rangle(sz_{max} + z) \tag{6.17}$$

where z_{max} is the maximum value that z can reach and c_z is a constant that controls the evolution of z. The A_d parameter introduced in the dilatancy equation is expressed as a function of z:

$$A_d = A_0(1 + \langle sz\rangle) \tag{6.18}$$

where A_0 is in the presence of A_d. For a generic x variable, the Macauley brackets $\langle x\rangle$ work as if $x>0$ than $\langle x\rangle = x$ while if $x\leq 0$ than $\langle x\rangle = 0$. Moreover, $s = 1$ if $\eta = \alpha + m$, while $s = -1$ if $\eta = \alpha - m$.

If loading starts at $\eta = 0$ (for example after isotropic consolidation) and $z = 0$ the equation becomes: $A_d = A_0(1 + 0) = A_0$. If the volumetric plastic strain is positive $d\varepsilon_v^p > 0$, the behavior is contractive, $dz = -c_z\langle -\left(d\varepsilon_v^p > 0\right)\rangle(sz_{max} + z) = -c_z 0(sz_{max} + z) = 0$. When $\eta > M^d$ dilatancy takes a negative value $d = A_d(M^d - \eta)<0$ and, consequently, also the volumetric plastic strain becomes negative, $\langle -d\varepsilon_v^p\rangle = 1$ and $dz = -c_z(sz_{max} + z)$. and negative z develops. So, since z is negative if $\eta = \alpha + m$ than $s = 1$ and so $A_d = A_0(1 + 0) = A_0$. At this point, when the load increment reverses $d\eta<0$ and the stress ratio reaches the lower yield function line, $\eta = \alpha - m$, and so $s = -1$. Because z is also negative, for previous considerations, $A_d = A_0(1 + z)$. Since the load is reversed, $d = A_d(M_e^d + \eta)$ and so $d = A_0(1 + z)(M_e^d + \eta)$. Considering the total volume strain increment as $d\varepsilon_v = d\varepsilon_v^e + d\varepsilon_v^p = 0$, it is possible to obtain $d\varepsilon_v^e = -d\varepsilon_v^p$, and from equation (7.2) the mean effective stress increment is $dp' = -d\varepsilon_v^p K$ but $d\varepsilon_v^p = d\left|\frac{d\eta}{H}\right|$, and so:

$$dp' = -d\left|\frac{d\eta}{H}\right| K \tag{6.19}$$

From the previous equation it is possible to deduce that a dilatancy increase leads to a decrease in mean effective stress. The description of the model in the triaxial stress space follows from Dafalias & Manzari (2004) to introduce the reader to the concepts in a "simpler" manner, but the model is formulated in a generalized stress space. In the general multiaxial stress space the elastic relations are:

$$d\boldsymbol{e}^e = \frac{d\boldsymbol{s}}{2G} \tag{6.20}$$

$$d\varepsilon_v^e = \frac{dp'}{K} \tag{6.21}$$

where $\boldsymbol{e}^e$ is the deviatoric elastic strain tensor and $\boldsymbol{s} = \boldsymbol{\sigma} - p'\boldsymbol{I}$ is the deviatoric stress tensor (where $\boldsymbol{\sigma}$ and $\boldsymbol{I}$ are the total stress tensor and the identity tensor, respectively).

The increments of plastic deformations are:

$$d\boldsymbol{e}^p = \langle L \rangle \boldsymbol{R}' \tag{6.22}$$

$$d\varepsilon_v^P = \langle L \rangle D \tag{6.23}$$

where L is the loading index, $\boldsymbol{R}'$ and D are, respectively, the deviatoric and the volumetric component of $\boldsymbol{R} = \boldsymbol{R}' + \frac{1}{3}D\boldsymbol{I}$ that represents the direction of the plastic strain increment $d\boldsymbol{\varepsilon}^p = \langle L \rangle \boldsymbol{R}$. The yield function generalized to the multiaxial stress space is:

$$f = [(\boldsymbol{s} - p'\boldsymbol{\alpha}) : (\boldsymbol{s} - p'\boldsymbol{\alpha})]^{\frac{1}{2}} - \sqrt{\frac{2}{3}}p'm = 0 \tag{6.24}$$

where $\boldsymbol{\alpha}$ is the back stress-ratio tensor, generalizing α of the triaxial space, and $(\boldsymbol{s} - p'\boldsymbol{\alpha}) : (\boldsymbol{s} - p'\boldsymbol{\alpha}) = tr[(\boldsymbol{s} - p'\boldsymbol{\alpha})(\boldsymbol{s} - p'\boldsymbol{\alpha})]$. The deviatoric stress-ratio tensor (recalling η in the triaxial formulation) can be introduced as:

$$\boldsymbol{r} = \frac{\boldsymbol{s}}{p'} \tag{6.25}$$

Considering the stress-ratio space, where the three axes are $\boldsymbol{r_1} = \frac{\boldsymbol{s_1}}{p'}$, $\boldsymbol{r_2} = \frac{\boldsymbol{s_2}}{p'}$ and $\boldsymbol{r_3} = \frac{\boldsymbol{s_3}}{p'}$, the yield surface represents the Drucker-Prager cone (Fig. 6.2). The trace of the cone on a π plane represents a circle with center $\boldsymbol{\alpha}$ and radius $\sqrt{\frac{2}{3}}m$. In the multiaxial generalization M, M^b and M^d represent the critical, bounding and dilatancy surface, respectively. Furthermore, α^c, α^b and α^d are also introduced, being the corresponding critical, bounding and dilatancy back stress ratios.

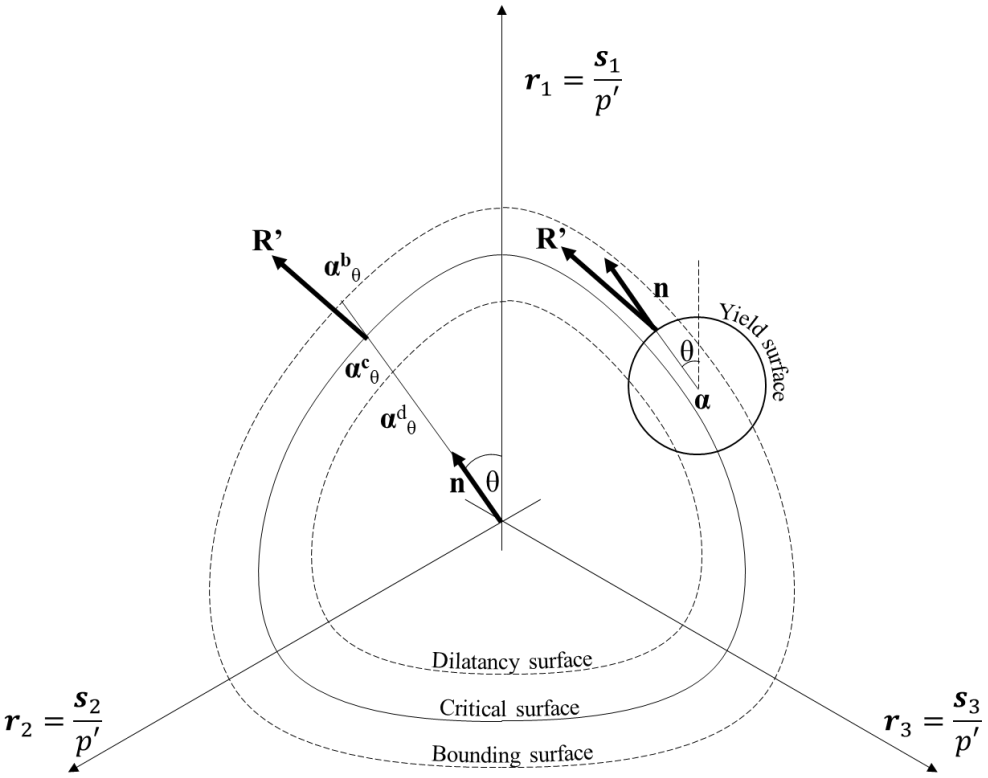

Figure 6.2: *Representation of yield, dilatancy and boundary surfaces in stress ratio space (Reworked from Dafalias & Manzari 2004).*

In the multiaxial generalization the "distance" from the current state to the various surfaces is defined as $\alpha^c - \boldsymbol{\alpha}$, $\alpha^b - \boldsymbol{\alpha}$ and $\alpha^d - \boldsymbol{\alpha}$. The potential function for a given $\boldsymbol{r}$ is:

$$\frac{\partial f}{\partial \boldsymbol{\sigma}} = \boldsymbol{n} - \frac{1}{3}(\boldsymbol{n}:\boldsymbol{r})\boldsymbol{I} \tag{6.26}$$

where:

$$\boldsymbol{n} = \frac{\boldsymbol{r} - \boldsymbol{\alpha}}{\sqrt{\frac{2}{3}m}} \tag{6.27}$$

In general, $\boldsymbol{R}$ is different from $\frac{\partial f}{\partial \boldsymbol{\sigma}}$ and so a non-associated flow rule is defined. The Lode angle θ is such that:

$$\cos 3\theta = \sqrt{6}tr\boldsymbol{n}^3 \tag{6.28}$$

It varies from 0 to $\frac{\pi}{3}$ and can be represented by the angle included between $\boldsymbol{r_1} = \frac{\boldsymbol{s_1}}{p'}$ and $\boldsymbol{r} - \boldsymbol{\alpha}$. The critical, dilatancy and bounding surfaces depend on θ and on a parameter c, which represents the ratio between a quantity in extension Q_e and in compression Q_c. The quantity Q_θ, which can be M, M^b and M^d or, equivalently, α^c, α^b and α^d, is given by:

$$Q_\theta = g(\theta, c)Q_c \tag{6.29}$$

where:

$$g(\theta, c) = \frac{2c}{(1+c) - (1-c)\cos 3\theta} \tag{6.30}$$

The image back-stress ratio tensors (intersection between the line from the origin, parallel to $\boldsymbol{n}$, and the critical, bounding and dilatancy surfaces, respectively) are defined as:

$$\boldsymbol{\alpha}_\theta^c = \sqrt{\frac{2}{3}\alpha_\theta^c \boldsymbol{n}};\ \boldsymbol{\alpha}_\theta^b = \sqrt{\frac{2}{3}\alpha_\theta^b \boldsymbol{n}};\ \boldsymbol{\alpha}_\theta^d = \sqrt{\frac{2}{3}\alpha_\theta^d \boldsymbol{n}} \tag{6.31}$$

where:

$$\alpha_\theta^c = g(\theta, c)M - m;\ \alpha_\theta^b = g(\theta, c)Me^{(\mp n^b \Psi)} - m;\ \alpha_\theta^d = g(\theta, c)Me^{(\mp n^d \Psi)} - m \tag{6.32}$$

The loading index L is expressed as:

$$L = \frac{1}{K_p}\frac{\partial f}{\partial \boldsymbol{\sigma}} : d\boldsymbol{\sigma} = \frac{1}{K_p} p\boldsymbol{n} : d\boldsymbol{r} = \frac{1}{K_p}[\boldsymbol{n} : d\boldsymbol{s} - \boldsymbol{n} : \boldsymbol{r} dp] = \frac{2G\boldsymbol{n} : d\boldsymbol{e} - \boldsymbol{n} : \boldsymbol{r} d\varepsilon_v}{K_p + 2G(B - Ctr\boldsymbol{n}^3) - KD\boldsymbol{n} : \boldsymbol{r}} \tag{6.33}$$

where $B = 1 + \frac{3}{2}\frac{1-c}{c} g \cos 3\theta$, $C = 3\sqrt{\frac{3}{2}}\frac{1-c}{c} g$, and $K_p = \left(\frac{2}{3}\right) ph\left(\boldsymbol{\alpha}_\theta^b - \boldsymbol{\alpha}\right) : \boldsymbol{n}$ is a hardening parameter with $h = \frac{b_0}{(\boldsymbol{\alpha} - \boldsymbol{\alpha}_{in}) : \boldsymbol{n}}$. In the previous equation, $\boldsymbol{\alpha}_{in}$ is the initial value of $\boldsymbol{\alpha}$ at the beginning of a new loading process and is updated when the denominator of the equation becomes negative.

The stress increment can then be expressed as:

$$d\boldsymbol{\sigma} = 2Gd\boldsymbol{e} + Kd\varepsilon_v \boldsymbol{I} - \langle L \rangle \left\{ 2G\left[B\boldsymbol{n} - C\left(\boldsymbol{n}^2 - \frac{1}{3}\boldsymbol{I}\right)\right] + KD\boldsymbol{I} \right\} \tag{6.34}$$

6.1.2. Pressure Dependent Multi Yield (PDMY) and Pressure Independent Multi Yield (PIMY) models

Pressure Dependent Multi Yield (PDMY) and Pressure Independent Multi Yield (PIMY) are elastic-plastic models that differ essentially because the first is sensitive to confinement pressure while the second is not. Recalling the deviatoric stress tensor $\boldsymbol{s}$**,** the second deviatoric stress invariant J_2 can be defined as:

$$J_2 = \frac{1}{2}[\boldsymbol{s} : \boldsymbol{s} - tr(\boldsymbol{s})^2] = \frac{1}{2}[\boldsymbol{s} : \boldsymbol{s}] \tag{6.35}$$

The yield surface is obtained setting equal the second deviatoric stress invariant to the constant $\frac{1}{3}(M^2 p'^2)$:

$$J_2 = \frac{M^2 p'^2}{3} \rightarrow \frac{3}{2}[\boldsymbol{s} : \boldsymbol{s}] - M^2 p'^2 = 0 \tag{6.36}$$

Introducing the tensor $\boldsymbol{\alpha}$ that defines the center of the yield surface that has a conical Drucker-Prager shape (for PIMY the cone degenerates to a von Mises cylinder), the following formulation for the yield function with formulation is obtained (Figure 6.3):

$$f = \frac{3}{2}[\boldsymbol{s} - (p' + p'_{res})\boldsymbol{\alpha}]:[\boldsymbol{s} - (p' + p'_{res})\boldsymbol{\alpha}] - M^2 p'^2 = 0 \tag{6.37}$$

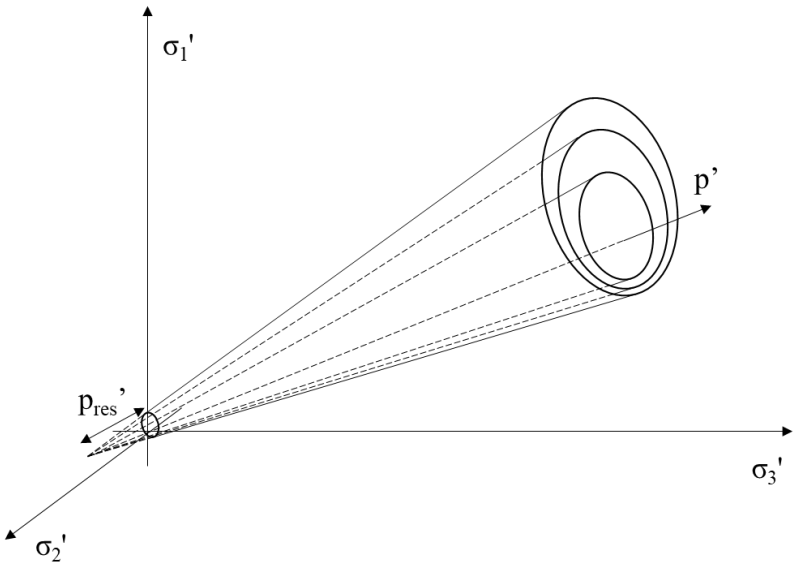

Figure 6.3: *Yield surfaces in principal stress space (Reworked from Yang et al. 2003).*

Therein p'_{res} is a small positive constant and M is the yield surface size. These concepts are based on Prevost's (1985) framework of multi-surface plasticity in which an increasing number of similar surfaces define hardening and the outermost major one defines failure. The size of the failure yield surface is related to the friction angle through:

$$M_f = \frac{6\sin\varphi'}{(3 - \sin\varphi')} \tag{6.38}$$

The shear modulus is defined as:

$$G = G_r \left[\frac{(p' + p'_{res})}{(p'_r + p'_{res})}\right]^n \tag{6.39}$$

where G_r is the small-strain octahedral shear modulus at p'_r and n is a material parameter. The bulk modulus is defined the same as in SANISAND model (equation 7.4) but is named by the letter *B*. For PDMY the flow rule is non-associative while for PIMY it is associative. The outer normal to the yield surface is defined as:

$$\boldsymbol{Q} = \boldsymbol{Q}' + Q''\boldsymbol{I} \tag{6.40}$$

where $\boldsymbol{Q}'$ is the deviatoric component of the outer normal to the yield surface and $\boldsymbol{Q}''$ is the volumetric component of the outer normal to the yield surface. The kinematic hardening rule proposed by Prevost (1985) is used:

$$p' d\boldsymbol{\alpha} = \frac{H'}{\boldsymbol{Q}':\boldsymbol{\mu}} \langle L \rangle \boldsymbol{\mu} \tag{6.41}$$

where $\boldsymbol{\mu}$ is a deviatoric tensor that defines the direction of translation, H' is the plastic modulus, and $L = \frac{1}{H'}\boldsymbol{Q}:d\boldsymbol{\sigma}$ is the plastic loading function. The direction of the plastic deformations is:

$$\boldsymbol{P} = \boldsymbol{P'} + P''\boldsymbol{I} \tag{6.42}$$

where $\boldsymbol{P'}$ is the deviatoric component of the plastic deformations and $\boldsymbol{P''}$ is the volumetric component of the plastic deformations. In these models the dilation or contraction behavior refers to the stress state of the material with respect to the phase transformation surface introduced by Ishihara et al. (1975), defined as the stress ratio:

$$\eta = \sqrt{\frac{2}{3}[\boldsymbol{s}:\boldsymbol{s}]}(p' + p'_{res}) \tag{6.43}$$

η_{PT} is the stress ratio at which phase transformation occurs. The behavior of the soil varies depending on the position of η with respect to η_{PT} and on $d\eta$. Contraction occurs if $\eta<\eta_{PT}$ or if $\eta>\eta_{PT}$ and $d\eta<0$. In these conditions the volumetric component of the plastic deformations is defined as:

$$P'' = \left[1 - \frac{sign(d\eta)}{\eta_{PT}}\right](c_1 + c_2\varepsilon_c) \tag{6.44}$$

where c_1 and c_2 are material constants and ε_c is a non-negative scalar. Dilation occurs when $\eta>\eta_{PT}$ and $d\eta>0$ and the volumetric component of the plastic deformations becomes:

$$P'' = \left(1 - \frac{\eta}{\eta_{PT}}\right) d_1(\gamma_d)^{d_2} \tag{6.45}$$

where d_1 and d_2 are material constants and γ_d is the octahedral shear deformation defined as:

$$\gamma_d = \frac{2}{3}\sqrt{(\varepsilon_{11} - \varepsilon_{22})^2 + (\varepsilon_{22} - \varepsilon_{33})^2 + (\varepsilon_{11} - \varepsilon_{33})^2 + 6\varepsilon_{12}^2 + 6\varepsilon_{13}^2 + 6\varepsilon_{23}^2} \tag{6.46}$$

The model is not formulated state dependent but when the failure surface is approached, then the volume remains constant ($P'' = 0$).

6.1.3. PM4Sand

In the introduction of the publication by Boulanger & Ziotopoulou (2017) describing PM4Sand the authors specify that the model has been developed applying modifications to SANISAND (Dafalias & Manzari 2004) with the aim of pursuing two main objectives: to be able to approximate the empirical correlations used in engineering practice and to be calibrated with a reasonable effort. The relationships and equations of the model are presented in plane stresses and the effective stress tensor is presented as:

$$\boldsymbol{\sigma}' = \begin{pmatrix} \sigma'_{11} & \sigma'_{12} \\ \sigma'_{12} & \sigma'_{22} \end{pmatrix} \tag{6.47}$$

The mean effective stress is:

$$p' = \frac{\sigma'_{11} + \sigma'_{22}}{2} \tag{6.48}$$

The deviatoric stress and stress-ratio tensor are defined as:

$$\boldsymbol{s} = \boldsymbol{\sigma}' - p'\boldsymbol{I} = \begin{pmatrix} \sigma'_{11} - p' & \sigma'_{12} \\ \sigma'_{12} & \sigma'_{22} - p' \end{pmatrix} \tag{6.49}$$

$$\boldsymbol{r} = \frac{\boldsymbol{\sigma}' - p'\boldsymbol{I}}{p'} = \begin{pmatrix} \dfrac{\sigma'_{11} - p'}{p'} & \dfrac{\sigma'_{12}}{p'} \\ \dfrac{\sigma'_{12}}{p'} & \dfrac{\sigma'_{22} - p'}{p'} \end{pmatrix} \tag{6.50}$$

Since $\sigma'_{11} - p' = \sigma'_{11} - \frac{\sigma'_{11}}{2} - \frac{\sigma'_{22}}{2} = \frac{\sigma'_{11}}{2} - \frac{\sigma'_{22}}{2}$ and $-(\sigma'_{22} - p') = -\sigma'_{22} + \frac{\sigma'_{11}}{2} + \frac{\sigma'_{22}}{2} = \frac{\sigma'_{11}}{2} - \frac{\sigma'_{22}}{2}$ or $s_{11} = -s_{22}$ the trace of $\boldsymbol{s}$ is 0. The same is true for $\boldsymbol{r}$. In plane the volumetric strain becomes:

$$\varepsilon_v = \varepsilon_{11} + \varepsilon_{12} \tag{6.51}$$

while the deviatoric strain tensor is defined as:

$$\boldsymbol{e} = \boldsymbol{\varepsilon} - \frac{\varepsilon_v}{3}\boldsymbol{I} = \begin{pmatrix} \varepsilon_{11} - \dfrac{\varepsilon_v}{3} & \varepsilon_{12} \\ \varepsilon_{12} & \varepsilon_{22} - \dfrac{\varepsilon_v}{3} \end{pmatrix} \tag{6.52}$$

where $\boldsymbol{\varepsilon}$ is the strain tensor. The elastic deviatoric and volumetric strain increments are defined as in Dafalias & Manzari (2004) in multiaxial stress space recalling the different formulation of stresses and strains. The bulk modulus is the same as the one reported in Dafalias & Manzari (2004). The elastic shear modulus is defined as:

$$G = G_0 p_a \left(\frac{p}{p_a}\right)^{\frac{1}{2}} C_{SR} \left(\frac{1 + \frac{z_{cum}}{z_{max}}}{1 + \frac{z_{cum}}{z_{max}} C_{GD}}\right) \tag{6.53}$$

where C_{SR} is a factor that accounts for stress ratio effects and is expressed as:

$$C_{SR} = 1 - C_{SR,o}\left(\frac{M}{M^b}\right)^{m_{SR}} \tag{6.54}$$

and C_{GD} is a shear modulus degradation factor. z_{cum} and z_{max} are factors described below. M is the critical state stress ratio in plane stress that can be determined with the help of Figure 6.4.

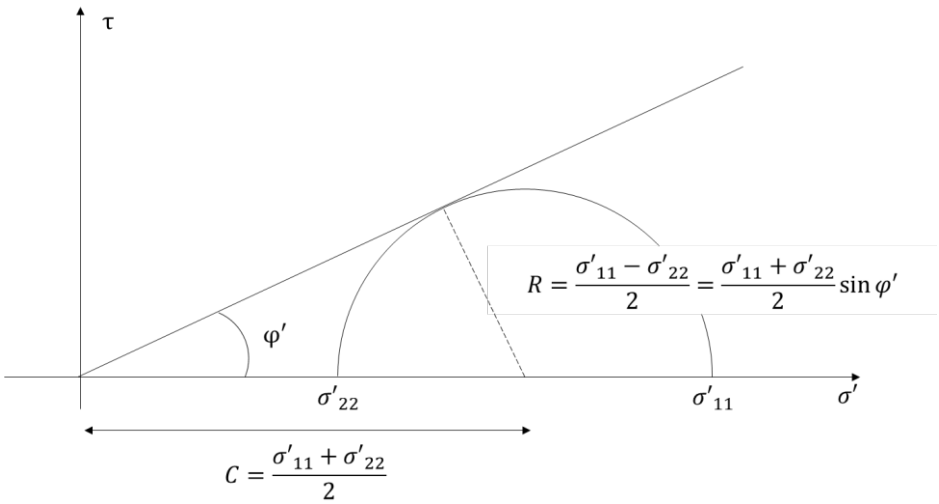

Figure 6.4: *Radius definition in Mohr circle.*

$$M = \frac{q}{p'} = 2\frac{(\sigma'_{11} - \sigma'_{22})}{(\sigma'_{11} + \sigma'_{22})} = 2\frac{\sigma'_{22}\left(\frac{1+\sin\varphi'}{1-\sin\varphi'} - 1\right)}{\sigma'_{22}\left(\frac{1+\sin\varphi'}{1-\sin\varphi'} + 1\right)} = \\ = 2\frac{(1+\sin\varphi' - 1 + \sin\varphi')}{(1+\sin\varphi' + 1 - \sin\varphi')} = 2\frac{2\sin\varphi'}{2} = 2\sin\varphi' \tag{6.55}$$

Following Dafalias & Manzari (2004), M^b is the stress ratio at the bounding surface with the difference that here it does not depend on the Lode angle (the friction angle is the same in compression and extension) and is expressed as:

$$M^b = Me^{(-n^b\xi_R)} \tag{6.56}$$

where e is the Euler number, n^b is material constant, and $\xi_R = D_{R,cs} - D_R$ is the difference between critical state relative density and current relative density, where:

$$D_{R,cs} = \frac{R}{Q - \ln\left(100\frac{p'}{p_a}\right)} \tag{6.57}$$

In the previous equation, Q is about 10 and R is about 1 for quarzitic sands (Bolton 1986).

The dilatancy surface is defined as:

$$M^d = Me^{(n^d\xi_R)} \tag{6.58}$$

where n^d is a material constant. As for SANISAND during shearing M^b and M^d approach the stress ratio of the the critical state surface M. The yield surface formulation is analogous to the Dafalias & Manzari (2004) one and it does not depend on Lode angle:

$$f = [(\boldsymbol{s} - p'\boldsymbol{\alpha}) : (\boldsymbol{s} - p'\boldsymbol{\alpha})]^{\frac{1}{2}} - \sqrt{\frac{1}{2}}p'm = 0 \tag{6.60}$$

The bounding and dilatancy back-stress ratio are defined respectively as:

$$\boldsymbol{\alpha}^b = \sqrt{\frac{1}{2}}[M^b - m]\boldsymbol{n} \tag{6.61}$$

$$\boldsymbol{\alpha}^d = \sqrt{\frac{1}{2}}[M^b - m]\boldsymbol{n} \tag{6.62}$$

where $\boldsymbol{n}$ is the normal to the yield surface. Reversal in loading direction occurs when:

$$(\boldsymbol{\alpha} - \boldsymbol{\alpha}_{in}):\boldsymbol{n} < 0 \tag{6.63}$$

where $\boldsymbol{\alpha}_{in}$ is the initial back-stress ratio. The volumetric and deviatoric strain increments are formulated as in Dafalias & Manzari (2004), but not being dependent on the Lode angle $\boldsymbol{R}' = \boldsymbol{n}$.

The hardening coefficient is:

$$z = \frac{2}{3}\frac{K_p}{p'(\boldsymbol{\alpha}^b - \boldsymbol{\alpha}):\boldsymbol{n}} \tag{6.64}$$

where K_p is the plastic modulus:

$$K_p = Gh_0 \frac{[(\boldsymbol{\alpha}^b - \boldsymbol{\alpha}):\boldsymbol{n}]^{0.5}}{\left[\left[e^{(\boldsymbol{\alpha}-\boldsymbol{\alpha}_{in}^{app}):\boldsymbol{n}}\right] - 1\right] + C_{\gamma 1}} \\ C_{rev}\frac{C_{k\alpha}}{1 + C_{Kp}\left(\frac{z_{peack}}{z_{max}}\right)\langle(\boldsymbol{\alpha}^b - \boldsymbol{\alpha}):\boldsymbol{n}\rangle\sqrt{1 - C_{zpk2}}} \tag{6.65}$$

In the previous equation, e is the Euler number, h_0 is a scalar parameter and $C_{\gamma 1}$ is a constant to avoid dividing by 0. The factor C_{rev} considers the effects of loading cycles:

$$C_{rev} = \frac{(\boldsymbol{\alpha} - \boldsymbol{\alpha}_{in}^{app}):\boldsymbol{n}}{(\boldsymbol{\alpha} - \boldsymbol{\alpha}_{in}^{true}):\boldsymbol{n}} \tag{6.66}$$

If $(\boldsymbol{\alpha} - \boldsymbol{\alpha}_{in}^{p}):\boldsymbol{n} \leq 0$ otherwise C_{rev}=1. $\boldsymbol{\alpha}_{in}^{app}$ and $\boldsymbol{\alpha}_{in}^{true}$ are back-stress tensors that are used to avoid over-stiffening of the stress-strain path and $C_{k\alpha}$, C_{Kp}, C_{zpk2} are parameters that depend on fabric-dilatancy variables and on mean effective stresses. Dilatancy D that relates plastic volumetric strain increments to plastic deviatoric strain increments has been improved to represent better the relationship between cyclic stress ratio versus the number of uniform loading cycles to failure. The fabric-dilatancy tensor is modified with respect to the one proposed by Dafalias & Manzari (2004) and is expressed as:

$$d\boldsymbol{z} = -\frac{c_z}{1 + \langle\frac{z_{cum}}{2z_{max}} - 1\rangle}\frac{\langle -d\varepsilon_v^p\rangle}{D}(z_{max}\boldsymbol{n} + \boldsymbol{z}) \tag{6.67}$$

where z_{cum} is the absolute cumulative value of $\boldsymbol{z}$ increments, z_{max} is the maximum value that $\boldsymbol{z}$ can attain and z_{peak} is the greatest past peak value of $\boldsymbol{z}$ during loading history.

6.2. Material constants of constitutive models

The material constants required by the different constitutive models used have been determined by different methods for two reasons. On the one hand, each model requires procedures that are better suited to its formulation and on the other hand different models have been used for different materials for which a different degree of knowledge, in terms of geotechnical data, is available. The SANISAND and PDMY constitutive models assumed for the basin materials (SBM) require the definition of several material constants each that have been determined through element test simulations, iterative procedures and literature data. The input data required by PM4Sand and PIMY used to model the embankment (ENM) and foundation (FNM) materials, respectively, are relatively fewer and have been determined mainly on the basis of information obtained from field tests. Since the definition of some parameters of SANISAND and PDMY models was obtained through element tests in which the constants were determined with iterative procedures, by comparing the real laboratory test results with the simulation ones, the next paragraph is dedicated to this issue.

6.2.1. Single element test simulation

The single element test simulated essentially consists in recreating a specific laboratory test through a numerical simulation in which the sample is modeled through one element with one Gauss point. In the present PhD thesis, Cyclic Triaxial and Direct Simple Shear (DSS) tests were simulated by using the software Opensees (Mazzoni et al. 2006). The specimens of the real tests have a cylindrical shape with a height twice the diameter (h ≈ 10 cm and d ≈ 5 cm). The simulations were performed with an hexahedral element (3D) for the triaxial test simulations and with a quad element (2D) for the direct simple shear (DSS) simulations. In the Opensees library, they are called SSPbrickUP Element and SSPquadUP Element, respectively. These elements were developed for the dynamic analysis of saturated porous materials through a mixed formulation of pressure and displacements based on Biot's (Biot 1955) theory then further explored by Zienkiewicz et al (1984). The SSPbrickUP Element is composed of eight nodes with four degrees of freedom each, three displacements in space and one degree contemplating pore pressure while the SSPquadUP Element is composed of four nodes with three degrees of freedom each, two displacements in the plane and one for pore pressure. Mixed formulations of saturated soils must ensure the stability of the pore pressure field tending to the incompressible-impermeable limit. Stability can be guaranteed through the achievement of the *inf-sup*, or Babusˇka-Brezzi condition (Fortin & Brezzi 1991; Wriggers 2008). However, this condition cannot be achieved with elements such as SSPbrickUP and SSPquadUP in which displacements and pressures have the same degree of interpolation. To overcome this drawback, a stabilization parameter α has been introduced. Stabilization is realized by adding the product of α with the divergence of the time derivative of the system's equation of

motion to the combined equation of motion of the fluid and mixture (McGann et al. 2012). The parameter α can be determined through the equation:

$$\alpha = \frac{h^2}{4K_s + \frac{4}{3}G_s} \tag{6.68}$$

where h is the element size, K_s and G_s are the bulk and shear modulus of the solid phase. As previously mentioned, since there is no cylindrical element in Opensees, the specimen must be schematized as a prism for the triaxial test. In particular, a quarter of the area of the square of the base for the entire height of the prism was modeled (Figure 6.5).

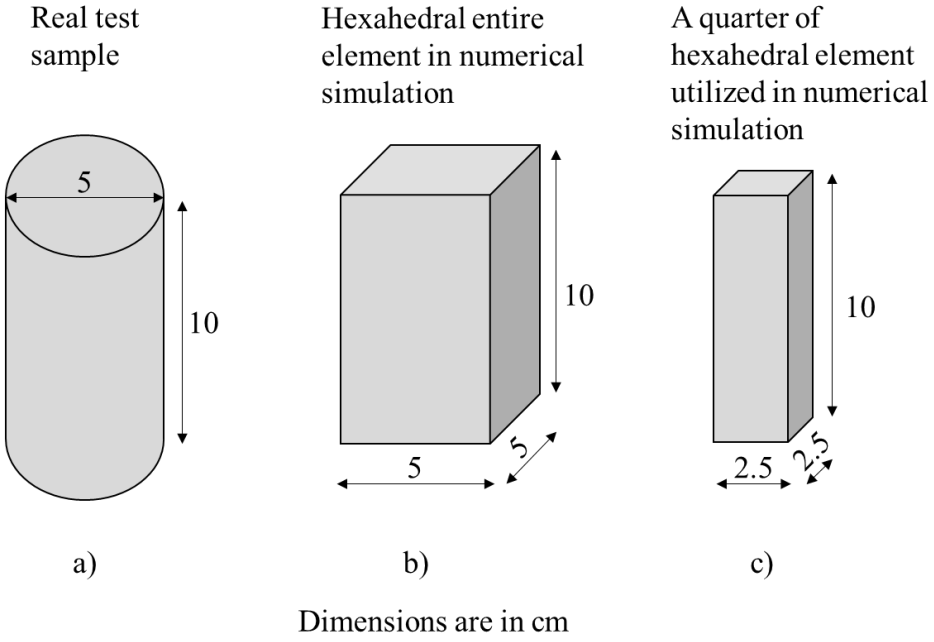

Figure 6.1: *Single element test schematization a) real triaxial test specimen, b) Hexahedral element representing entire specimen, c) a quarter of hexahedral element utilized in test simulation.*

Following the proportions of the real specimens used in triaxial tests, the side of the base of the element used in the simulations is much smaller than the height of the prism. This is difficult to reconcile with the fact that in finite element analyzes for computational reasons it is preferable to use elements that are as regular as possible (Rice 1985). A similar issue concerns the SSPquadUP Element where the vertical cross section of the specimen is schematized with a square instead of a rectangle. By comparing cyclic triaxial test simulations performed with prismatic and cubic elements, Geppetti et al. (2023) have found that the results were different and more precise for the cubic element during the consolidation phase during which the deviatoric stress was not maintained equal to 0 for prismatic element the, while in the two-dimensional case the results were quite similar between a square and a rectangular element (Figure 6.6).

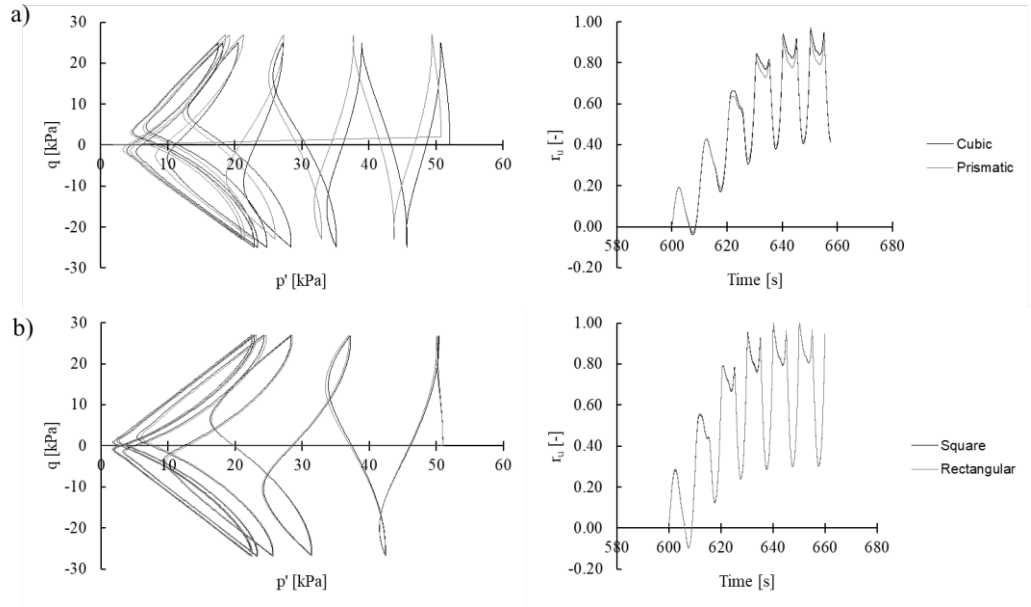

Figure 6.2: *Comparison between stress paths and excess pore water pressure ratio r_u trends from SANISAND model: a) in the three-dimensional case between cube and prism, b) in the two-dimensional case between square and rectangle.*

On the basis of these results, the element test simulations were carried out with cubic and square elements. Referring to the three-dimensional configuration represented in Figure 6.7 a, the translation of node 4 of the SSPbrickUP Element must be completely prevented (for symmetry reasons).

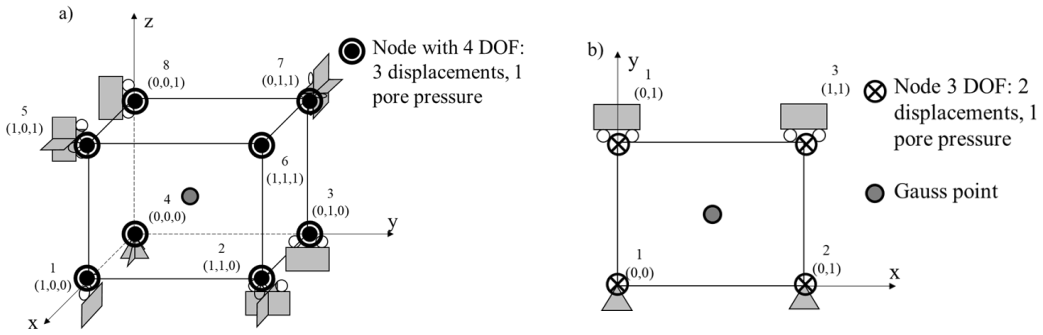

Figure 6.7: *Elements restraint used in element test simulations a) SSPbrickUP b) SSPquadUP.*

Table 6.1: *SSPbrickUP restraints used in element test simulations.*

Node number	DOF 1: x displacement	DOF 2: y displacement	DOF 3: z displacement	DOF 4: Drainage
1	Free	Fixed	Fixed	Consolidation open/Loading closed
2	Free	Free	Fixed	Consolidation open/Loading closed
3	Fixed	Free	Fixed	Consolidation open/Loading closed
4	Fixed	Fixed	Fixed	Consolidation open/Load closed
5	Free	Fixed	Free	Consolidation open/Loading closed
6	Free	Free	Free	Consolidation open/Loading closed
7	Fixed	Free	Free	Consolidation open/Loading closed
8	Fixed	Fixed	Free	Consolidation open/Loading closed

Table 6-1: *SSPquadUP restrain ts used in element test simulations.*

Node number	DOF 1: x displacement	DOF 2: y displacement	DOF 4: Drainage
1	Fixed	Fixed	Consolidation open/Load closed
2	Free	Free	Consolidation open/Load closed
3	Free	Fixed	Consolidation open/Load closed
4	Free	Fixed	Consolidation open/Load closed

Looking at Figure 6.7 a and Table 6.1 it can be noted that nodes 2 and 3 are allowed to translate in the x and y direction respectively while node 1 is prevented from vertical translation. This configuration simulates the condition of the specimen base in contact with the pedestal of the triaxial cell. As far as the upper base of the element is concerned, nodes 5 and 7 are prevented from translation in the y and x directions, respectively, while node 8 can only translate vertically (again for symmetry reasons) and node 6 can move in all directions. This configuration of the top base nodes represents the condition of a quarter of the top of the specimen in the real laboratory test.

Looking at Figure 6.7 b and Table 6.2 which refers to the two-dimensional case, it can be noted that nodes 3 and 4 are completely blocked while nodes 1 and 2 can translate along the x axis. This configuration simulates the condition of the middle section of a DSS specimen.

It is worth noting that during a real triaxial test the stresses are applied to the specimen as pressures transferred by the cell water σ_c and the piston σ_a whereas in the numerical simulation with OpenSees the loads are applied to the nodes (particularity of

OpenSees). So, the experimental pressures must be multiplied by the area of influence and applied as forces on the nodes in the numerical model (Figure 6.8).

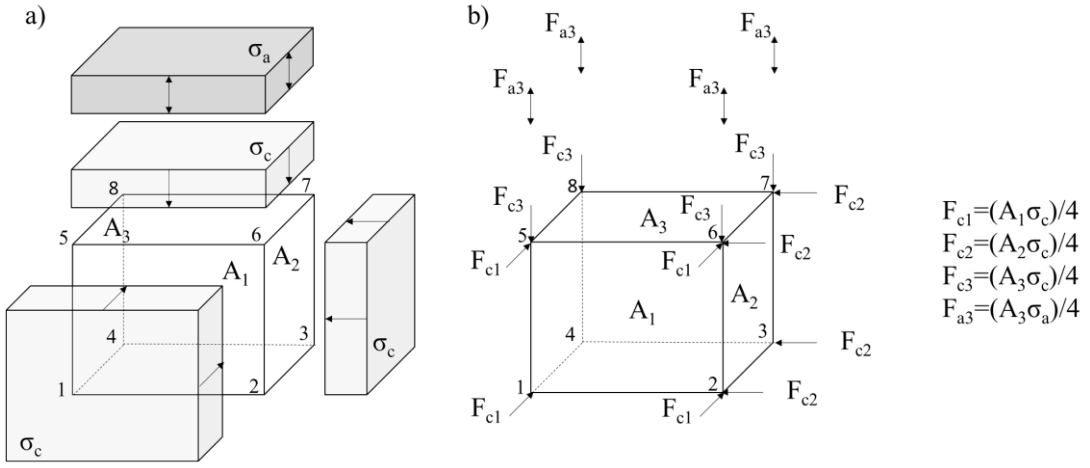

Figure 6.3: *Load schematization on SSPbrickUP a) Pressure loads b) node forces.*

The simulations consist of two steps: first an isotropic consolidation phase, in which the sample reaches the initial mean effective stress, and second a deviatoric load phase. During consolidation the drainage is allowed while during load application it is prevented. The simulations of the undrained cyclic tests performed are stress controlled and a sinusoidalcyclic load is applied to describe the cyclic loading. The simulation is not dynamic but static with harmonic loading.

6.2.2. Determination of the SANISAND material constants

SANISAND requires the determination of 15 material constants used in the model equations (Table 6.3).

Table 6.3. *SANISAND model parameters*

Field of application	Parameters	Description
Elasticity	G_0 [-]	Shear modulus for small deformations
	ν [-]	Poisson's ratio
Critical state	M_c [-]	Stress ratio in compression
	c [-]	Ratio of the critical stress ratio in extension and in compression
	λ_c [-]	Constant
	e_0 [-]	Void ratio
	ξ [-]	Constant
Yield surface	m [-]	Yield function parameter
Plastic modulus	h_0 [-]	Plastic modulus

Field of application	Parameters	Description
	c_h [-]	Yield function parameter
	n^b [-]	Yield function parameter
Dilatancy	A_0 [-]	Dilatancy parameter
	n^d [-]	Yield function parameter
Fabric-dilatancy tensor	z_{max} [-]	Fabric-dilatancy
	c_z [-]	Fabric-dilatancy

Dafalias & Manzari (2004) subdivide the various constants according to the category of the membership function. The so-called elastic constants are the shear modulus for small deformations G_0 and the Poisson's ratio ν. The parameters that define the critical state are: the critical stress ratio M, the ratio of the critical stress ratio in extension and in compression $c = \frac{M_e}{M_c}$, the void ratio e_0 and the constants λ_c and ξ. The yield function requires only the definition of the parameter m, while for the plastic modulus it is necessary to define the scalar parameters h_0 and c_h and the constant n^b. Dilatancy requires the parameter A_0 that is related to fabric-dilatancy and n^d. Finally, the fabric-dilatancy tensor needs the definition of the maximum value z_{max} of the internal variable z, and of the quantity c_z that controls the evolution of z.

The value of the shear modulus for small deformations G_0 was determined through the procedure proposed by Taiebat & Dafalias (2010) fitting triaxial monotonic tests results through the equations:

$$d\varepsilon_q^e = \frac{dq}{3G} \text{ and } G = G_0 p_a \frac{(2.97-e)^2}{1+e}\left(\frac{p\prime}{p_a}\right)^{\frac{1}{2}} \tag{6.69}$$

and replacing G:

$$\varepsilon_q^e = \frac{100q(1+e)}{\left[3G_0(2.97-e)^2(p_a p')^{\frac{1}{2}}\right]} \tag{6.70}$$

with ε_q^e expressed in [%].

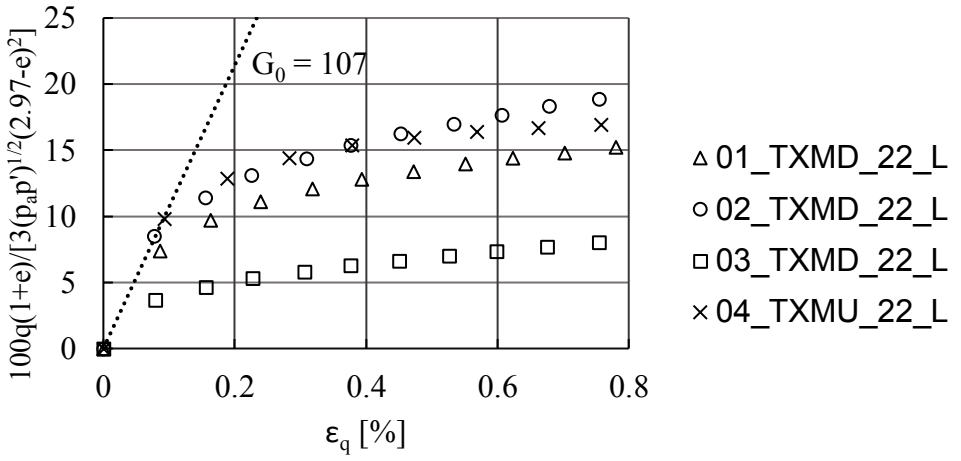

Figure 6.9: *Determination of G_0 of from monotonic triaxial tests.*

From Figure 6.9 it is possible to deduce that the value of G_0 obtained from the drained and undrained monotonic triaxial tests presented in Chapter 3 is G_0=107. It should be noted that according to the formulation presented G_0 is dimensionless.

The value of 0.05 represents the Poisson's ratio. This value is unrealistic for granular materials, as also pointed out by Wichtmann et al. (2019); however, it is used by numerous authors (Dafalias & Manzari 2004; Taiebat & Dafalias 2008; Petalas et al. 2020; Yang et al. 2022) because it allows for an adequate calibration.

The critical state stress ratio $M_c = 1.46$ was defined in Chapter 3 as the slope of the line interpolating the critical state points in the q-p' plane. This parameter was determined from the monotonic triaxial compression tests. The critical state stress ratio for triaxial extension tests can be estimated through the relationship:

$$M_e = \frac{6 \sin \varphi'}{3 + \sin \varphi'} \tag{6.71}$$

Knowing the critical state stress ratio in extension, it is possible to determine the ratio of the critical state stress ratio in extension and in compression that is $c = \frac{M_e}{M_c}$=0.7.

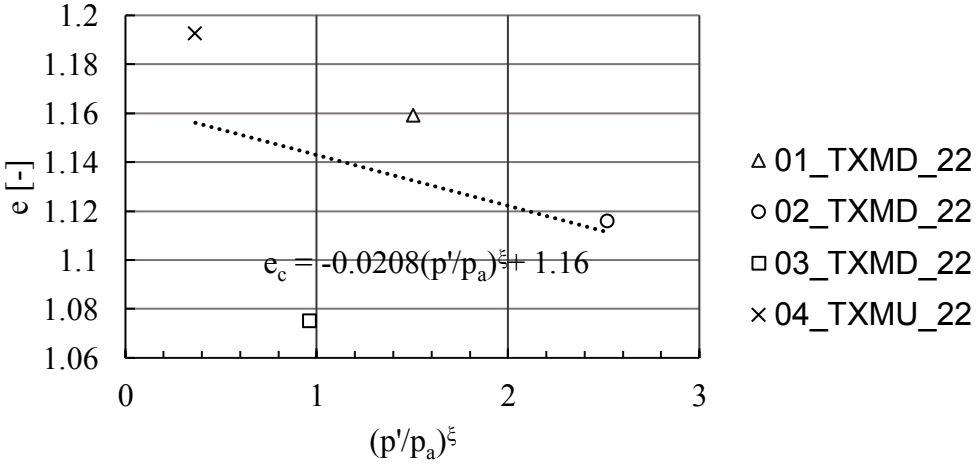

Figure 6.4: *Determination of critical state parameters from monotonic triaxial tests.*

The critical state parameters λ_c=0.0208, e_0=1.16 and ξ=0.7 were determined as proposed by Taiebat & Dafalias (2010) by interpolating the failure data of the monotonic triaxial tests in the e- $\left(\frac{p\prime}{p_a}\right)^{\xi}$ plane (Figure 6.10). The value of m was set equal to $\frac{M_c}{100}$=0.01 as suggested by Dafalias & Manzari (2004). Finally, the parameters h_0=60, c_h=0.91, n^b=1.2, A_0=0.5, n^d=3, z_{max}=12 and c_z=900 were found through an iterative procedure by comparing the results obtained by the simulations to the ones obtained from laboratory tests in the CSR-N chart (Figure 6.11).

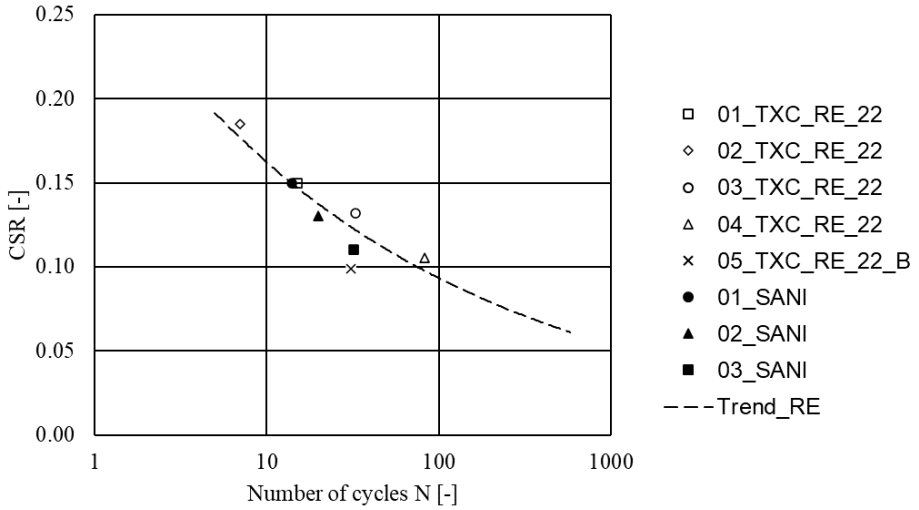

Figure 6.5: *Comparison of cyclic Stress Ratio (CSR) vs. number of cycles at failure from simulations (filled symbols) and from laboratory tests (empty symbols) for SANISAND.*

The plot in Figure 6.10 is restricted to the results obtained on reconstituted samples (Chapter 3) because also the CSL parameters were obtained from monotonic triaxial tests performed on reconstituted samples. In fact, much more tests were performed on this type of samples because a very small number of undisturbed samples taken by the freezing technique was available.

To validate the calibrated parameters, the results of simulation 01_SANI were compared with the results obtained from triaxial test 01_TXC_RE (Figure 6.12).

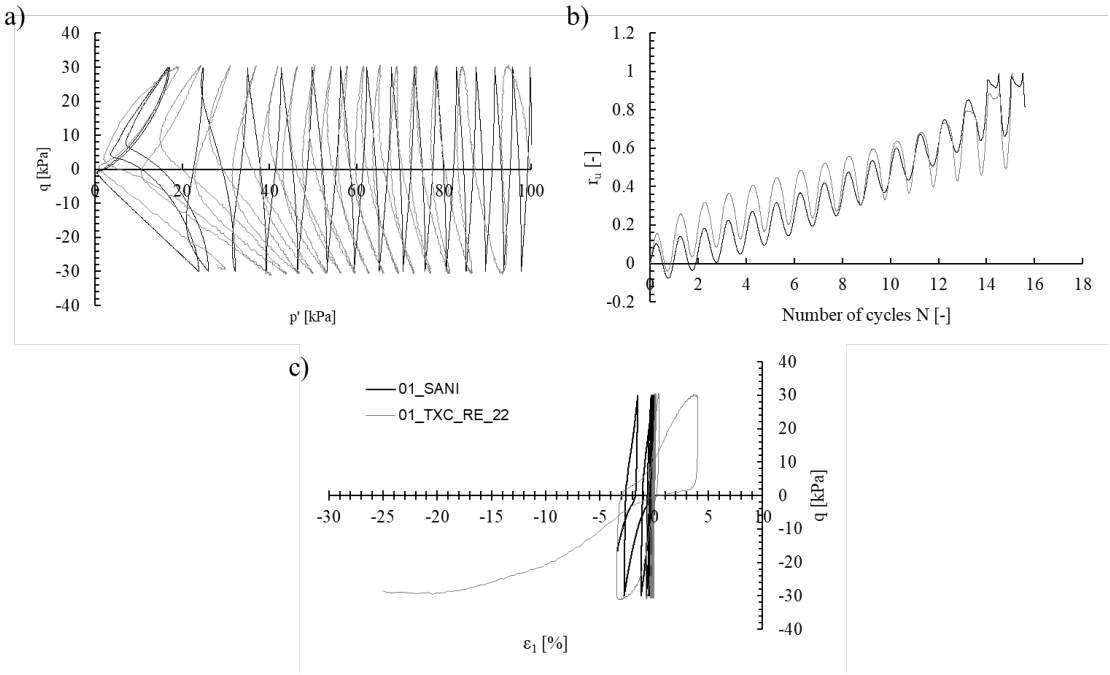

Figure 6.12: *Comparison between simulation 01_SANI and test 01_TXC_RE_22 in terms of: a) effective stress paths, b) pore water pressure ratio vs. number of cycles, c) deviatoric stress vs. axial strain.*

From the analysis of Figure 6.12 it is possible to deduce that SANISAND simulates well the trends of the experimental test in terms of effective stress path and pore water pressure ratio while there are larger differences between the simulation and the experiment in the diagram showing the axial deformations as a function of the deviatoric stress, in particular in the final phase of the test. As stated by the authors of the model parameters that mostly influence the cyclic behavior are z_{max} and c_z.

6.2.3. Determination of the PDMY material constants

The Pressure Dependent Multi Yield (PDMY) constitutive model requires the definition of 16 material constants (Table 6.4).

Table 6.4. *PDMY model parameters*

Variable	Description
G_r [MPa]	Small-strain octahedral shear modulus
B_r [MPa]	Bulk modulus
ϕ [°]	Friction angle
$\gamma_{max,r}$ [-]	Maximum octahedral shear strain
p'_r [kPa]	Reference effective confining pressure
d [-]	Pressure dependency coefficient
ϕ_{PT} [°]	Phase transformation angle
NYS [-]	Number of yield surfaces

Variable	Description
c_1 [-]	Contracting coefficient 1
c_2 [-]	Contracting coefficient 2
c_3 [-]	Contracting coefficient 3
d_1 [-]	Dilatant coefficient 1
d_2 [-]	Dilatant coefficient 2
d_3 [-]	Dilatant coefficient 3
l_1 [-]	Liquefaction coefficient 1
l_2 [-]	Liquefaction coefficient 2

The first two parameters required are the small-strain octahedral shear modulus G_r and the bulk modulus B. As suggested by Khosravifar (2012) G_r was determined from G_0=115.5 [MPa] (of course it differs from the SANISAND one) that was estimated through field tests (Chapter 5) as:

$$G_r = \frac{3}{\sqrt{6}} G_0 = 141 \text{ [MPa]} \tag{6.72}$$

Setting the Poisson's ratio equal to 0.5 (saturated soil under undrained conditions), the bulk modulus can be obtained as:

$$B = G \frac{2(1+\nu)}{3(1-\nu)} = 283 \text{ [MPa]} \tag{6.73}$$

The third parameter to be defined is the friction angle that is set equal to 36° based on the results of the monotonic triaxial tests (Chapter 3). The maximum octahedral shear strain $\gamma_{max,r}$, the reference effective confining pressure p'_r and the pressure dependency coefficient d are set equal to 0.1, 100 [kPa] and 0.5 respectively as suggested by Khosravifar (2012). A reasonable choice for the phase transformation angle is to assume it 5 degrees lower than the friction angle (Khosravifar 2012). The parameter NYS that defines the number of yield surfaces (as defined in Figure 6.3) is set equal to 20. The remaining 8 parameters to be defined are: c_1, c_2 and c_3, which are related to the contracting behavior of the material, d_1, d_2 and d_3 which are related to the dilatant behavior, and l_1 and l_2 that influence the liquefaction potential. More specifically, c_1 controls the plastic volumetric strains rate, or the pore pressure rate, c_2 considers the material damage, c_3 considers the overburden stresses, d_1 is related to the dilatation rate, d_2 to the fabric damage and d_3 enables the overburden effect, so is set to 0 in this study. Finally, the liquefaction-induced plastic shear strain is controlled by $l_1$and l_2. The above mentioned parameters were determined with an iterative procedure like that used for SANISAND. Figure 6.13 shows the comparison between simulated and experimental results in the CSR-N chart.

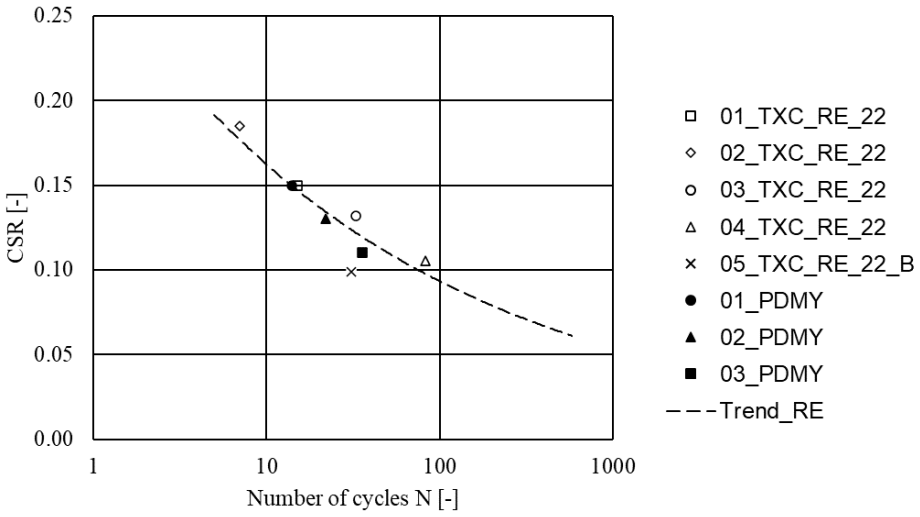

Figure 6.13: *Comparison of cyclic Stress Ratio (CSR) vs. number of cycles at failure from simulations (filled symbols) and from laboratory tests (empty symbols) for PDMY.*

As done for SANISAND, validation of the calibrated parameters was obtained through the comparison of the results from simulation 01_PDMY with those from triaxial test 01_TXC_RE (Fig. 6.14).

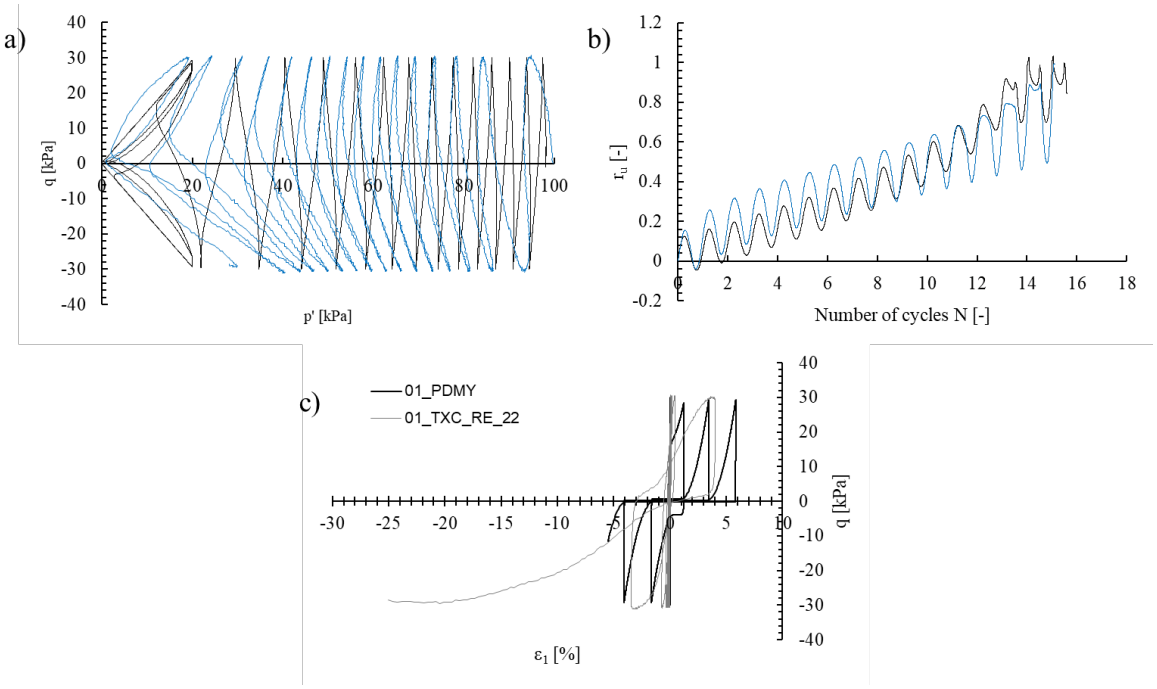

Figure 6.6: *Comparison between simulation 01_PDMY and test 01_TXC_RE_22 in terms of: a) effective stress paths, b) pore water pressure ratio vs. number of cycles, c) deviatoric stress vs. axial strain.*

A comparison of Figure 6.14 and Figure 6.12 shows that PDMY even better simulates the behavior of the soil in terms of effective stress paths and stress-strain relationship (reproducing also the symmetric increase in compression and extension) while SANISAND better simulates the trend of the pore pressure build-up. SaniSand and

PDMY tend to underestimate the excess pore water pressure accumulation during the first cycles, and that is why in p'-q less relaxation of p' can be observed during the first cycles. PDMY tends to overestimate the PWP accumulation at the end of the cycles

6.2.4. Determination of the PIMY material constants

The Pressure Independent Multi Yield (PIMY) model requires the definition of "only" 7 material constants, many of which (G_r, B, $\gamma_{max,r}$, p'_r, NYS and d) are the same as in PDMY. The small-strain octahedral shear modulus and the bulk modulus are determined according to the same procedure as used for PDMY. For the foundation material (FNM), based on the value G_0=258 [MPa] from field tests (see Chapter 5), G_r is obtained from:

$$G_r = \frac{3}{\sqrt{6}} G_0 = 315 \text{ [MPa]} \tag{6.74}$$

and, setting the Poisson's ratio equal to 0.5, the bulk modulus is:

$$B = G \frac{2(1+\nu)}{3(1-\upsilon)} = 630 \text{ [MPa]} \tag{6.75}$$

To the parameters $\gamma_{max,r}$, p'_r, NYS and d, the same values as assumed for the PDMY model are assigned. The last parameter to be determined for PIMY model is the apparent cohesion at zero confinement pressure. Due to the lack of information to determine this parameter, it was decided to assign it a value of 37 [kPa] as suggested by Mazzoni et al. (2006) for medium clays.

6.2.5. PM4Sand material constants definition

As mentioned in paragraph (6.1.3) on the model description, one of the reasons why the authors developed PM4Sand is to offer a tool that can be calibrated without excessive effort. This purpose has been achieved by the need of determining only 3 of the 24 material constants of the model. These parameters defined as 'primary', are the apparent relative density D_R, the shear modulus coefficient G_0, and the contraction rate parameter h_0. Since PM4Sand is utilized to model the embankment material (ENM), values of 36% to the relative density and 100 MPa to the shear modulus were assumed (with the concepts explained in Chapter 5). The contraction rate parameter h_0 must be determined after the relative density and the shear modulus. The procedure used is the one suggested by Boulanger & Ziotopoulou (2017) and consists in calibrating h_0 for specific values of cyclic resistance ratio (CRR). CRR for a 7.5 magnitude earthquake and an overburden stress of 1 atm is determined through the liquefaction triggering correlation of Idriss & Boulanger (2008):

$$CRR_{M=7.5,\sigma=1\,[atm]} = e^{\left[\frac{(N_1)_{60cs}}{14.1}+\left(\frac{(N_1)_{60cs}}{126}\right)^2-\left(\frac{(N_1)_{60cs}}{23.6}\right)^3+\left(\frac{(N_1)_{60cs}}{25.4}\right)^4-2.8\right]} \tag{6.76}$$

where e is the Euler number and $(N_1)_{60cs}$ is the corrected SPT penetration resistance for equivalent clean sand:

$$(N_1)_{60cs} = (N_1)_{60} + \Delta(N_1)_{60cs} \tag{6.77}$$

The fines content correction $\Delta(N_1)_{60cs}$ is given by:

$$\Delta(N_1)_{60cs} = e^{\left(1.63+\frac{9.7}{FC+0.01}-\left(\frac{15.7}{FC+0.01}\right)^2\right)} \cong 2 \quad (6.78)$$

where FC is the mean value of the fines contents. In this work, a value of FC=6.88 [%] was found for the embankment material as reported in Chapter 3.

$(N_1)_{60}$ is the corrected SPT penetration resistance defined as:

$$(N_1)_{60} = C_N C_E C_R C_B C_S N_{SPT} \quad (6.79)$$

where C_E is the hammer energy percentage, C_R is the rod correction parameter, C_B accounts for the borehole diameter and C_S is a correction factor for split samplers. All these factors are set equal to unity in this work (due to available equipment data). C_N is an overburden correction factor given by:

$$C_N = \left(\frac{p_a}{\sigma'_v}\right)^m \leq 1.7 \quad (6.80)$$

$$m = 0.784 - 0.0768\sqrt{(N_1)_{60cs}} \quad (6.81)$$

So m, C_N and $(N_1)_{60}$ must be determined through an iterative procedure. The trend of $(N_1)_{60}$ found when processing the results of the SPT tests performed on the embankment is rather constant with depth. Therefore, it is possible to attribute a value of 12 to this quantity, equal to the average of the measurements. From the knowledge of $(N_1)_{60}$ and $\Delta(N_1)_{60cs}$, it is possible to obtain $(N_1)_{60cs}$ which is equal to 14. The corresponding value of CRR is equal to 0.147. Being CRR evaluated for a 7.5 magnitude earthquake, this must be assumed equivalent to a peak shear strain of 3% in a DSS test with 15 uniform cycles. Therefore, h_0 has to be calibrated with an iterative procedure in order to obtain a strain of 3% in 15 uniform cycles in a DSS test to which a CRR of 0.147 is imposed. This condition was obtained by attributing a value of 0.60 to h_0 as shown in Figure 6.15.

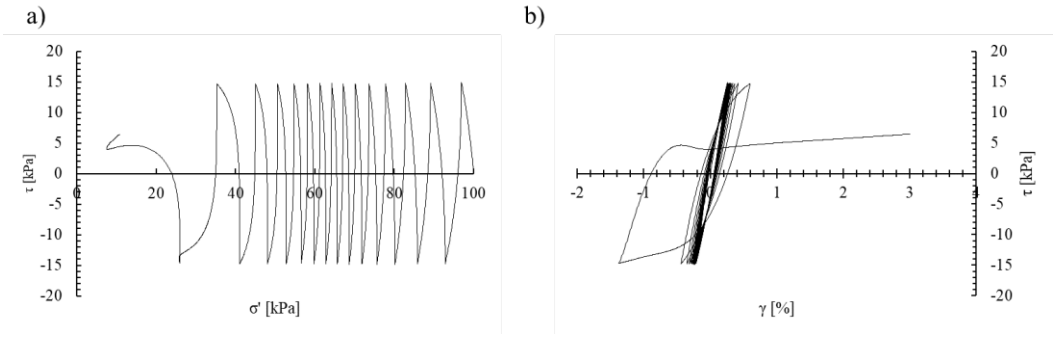

Figure 6.15: *DSS test simulation to calibrate h_0 a) stress path, b) shear stress vs. shear strain.*

Obviously, each of the constitutive models used has its own qualities and critical issues. Describing complex phenomena such as the dynamic behavior of granular materials in undrained conditions with mathematical models is certainly a challenge that is not easy to solve. Certainly one of the major critical issues of these models is their intrinsic complexity and the need for the user to define numerous input constants that often have no physical basis but are mathematical expedients. The PM4Sand model, which tries to circumvent these problems by offering the user the possibility of determining only 3 constants that are fairly easy to calibrate, however presents other

stability problems. The calibrated values of the model constants used are summarized in the Table 6.5.

Table 6.5: *Constitutive model input parameters.*

SANISAND		PDMY		PIMY		PM4Sand	
G_0 [-]	107	G_r [MPa]	141	G_r [MPa]	315	D_R [%]	36
ν [-]	0.05	B_r [MPa]	283	B_r [MPa]	630	G_0 [MPa]	100
M_c [-]	1.46	ϕ [°]	36	$\gamma_{max,r}$ [-]	0.1	h_{p0} [-]	0.6
c [-]	0.7	$\gamma_{max,r}$ [-]	0.1	p'_r [kPa]	100	h_0 [-]	2
λ_c [-]	0.0208	p'_r [kPa]	100	d [-]	0.5	e_{max} [-]	0.8
e_0 [-]	1.16	d [-]	0.5	NYS [-]	20	e_{min} [-]	0.5
ξ [-]	0.7	ϕ_{PT} [°]	31	c [kPa]	37	n^d [-]	0.1
m [-]	0.01	NYS [-]	20			n^b [-]	0.5
h_0 [-]	60	c_1 [-]	0.06			A_{d0} [-]	1
c_h [-]	0.91	c_2 [-]	6			z_{max} [-]	1
n^b [-]	1.2	c_3 [-]	0.019			c_z [-]	250
A_0 [-]	0.5	d_1 [-]	0.15			c_e [-]	1
n^d [-]	3	d_2 [-]	3			ϕ_{cv} [°]	33
z_{max} [-]	12	d_3 [-]	0			C_{GD} [-]	2
c_z [-]	900	l_1 [-]	1			C_{DR} [-]	1
		l_2 [-]	0			C_{kaf} [-]	1
						Q [-]	10
						R [-]	1.5
						m [-]	0.01
						$F_{sed,min}$ [-]	1
						$p'_{sed,o}$ [-]	1

Bibliography

Been, K., & Jefferies, M. G. (1985). A state parameter for sands. Géotechnique, 35(2), 99-112.

Biot, M. A. (1955). Theory of elasticity and consolidation for a porous anisotropic solid. Journal of Applied Physics, 26(2), 182-185.

Bolton, M. D. (1986). The strength and dilatancy of sands. Géotechnique, 36(1), 65-78.

Boulanger, R. W., & Ziotopoulou, K. (2017). PM4Sand (version 3.1): A sand plasticity model for earthquake engineering applications. Rep. No. UCD/CGM-17/01. Davis, CA: Center for Geotechnical Modeling, Dept. of Civil and Environmental Engineering, Univ. of California.

Dafalias, Y. F., & Manzari, M. T. (2004). Simple plasticity sand model accounting for fabric change effects. Journal of Engineering Mechanics, 130(6), 622-634.

Elgamal, A., Yang, Z., Parra, E., & Ragheb, A. (2003). Modeling of cyclic mobility in saturated cohesionless soils. International Journal of Plasticity, 19(6), 883-905.

Fortin, M., & Brezzi, F. (1991). Mixed and hybrid finite element methods (Vol. 2). New York: Springer-Verlag.

Geppetti, A., Facciorusso, J., Ciardi, G., Prada-Sarmiento, L. F., & Madiai, C. (2023). Calibration of Constitutive Models for Tailings Material with OpenSees. In Proceedings of the 2022 Eurasian OpenSees Days (pp. 182-191). Cham: Springer Nature Switzerland.

Idriss, I. M., & Boulanger, R. W. (2010). SPT-based liquefaction triggering procedures. Rep. UCD/CGM-10, 2, 4-13.

Ishihara, K., Tatsuoka, F., & Yasuda, S. (1975). Undrained deformation and liquefaction of sand under cyclic stresses. Soils and Foundations, 15(1), 29-44.

Khosravifar, A. (2012). Analysis and design for inelastic structural response of extended pile shaft foundations in laterally spreading ground during earthquakes. University of California, Davis.

Khosravifar, A., Elgamal, A., Lu, J., & Li, J. (2018). A 3D model for earthquake-induced liquefaction triggering and post-liquefaction response. Soil Dynamics and Earthquake Engineering, 110, 43-52.

Li, X. S., & Dafalias, Y. F. (2000). Dilatancy for cohesionless soils. Géotechnique, 50(4), 449-460.

Li, X. S., & Wang, Y. (1998). Linear representation of steady-state line for sand. Journal of Geotechnical and Geoenvironmental Engineering, 124(12), 1215-1217.

Mazzoni, S., McKenna, F., Scott, M. H., & Fenves, G. L. (2006). OpenSees command language manual. Pacific Earthquake Engineering Research (PEER) Center, 264(1), 137-158.

McGann, C. R., Arduino, P., & Mackenzie-Helnwein, P. (2012). Stabilized single-point 4-node quadrilateral element for dynamic analysis of fluid saturated porous media. Acta Geotechnica, 7, 297-311.

Petalas, A. L., Dafalias, Y. F., & Papadimitriou, A. G. (2020). SANISAND-F: Sand constitutive model with evolving fabric anisotropy. International Journal of Solids and Structures, 188, 12-31.

Prevost, J. H. (1985). A simple plasticity theory for frictional cohesionless soils. International Journal of Soil Dynamics and Earthquake Engineering, 4(1), 9-17.

Rice, J. R. (1985). The Aspect Ratio Significant for Finite Element Problems.

Richart, F. E., Hall, J. R., & Woods, R. D. (1970). Vibrations of soils and foundations.

Rowe, P. W. (1962). The stress-dilatancy relation for static equilibrium of an assembly of particles in contact. Proceedings of the Royal Society of London. Series A. Mathematical and Physical Sciences, 269(1339), 500-527.

Taiebat, M., & Dafalias, Y. F. (2008). SANISAND: Simple anisotropic sand plasticity model. International Journal for Numerical and Analytical Methods in Geomechanics, 32(8), 915-948.

Taiebat, M., Jeremić, B., Dafalias, Y. F., Kaynia, A. M., & Cheng, Z. (2010). Propagation of seismic waves through liquefied soils. Soil Dynamics and Earthquake Engineering, 30(4), 236-257.

Wichtmann, T., Fuentes, W., & Triantafyllidis, T. (2019). Inspection of three sophisticated constitutive models based on monotonic and cyclic tests on fine sand: Hypoplasticity vs. Sanisand vs. ISA. Soil Dynamics and Earthquake Engineering, 124, 172-183.

Wriggers, P. (2008). Nonlinear finite element methods. Springer Science & Business Media.

Yang, M., Taiebat, M., & Dafalias, Y. F. (2022). SANISAND-MSf: a sand plasticity model with memory surface and semifluidised state. Géotechnique, 72(3), 227-246.

Yang, Z., Elgamal, A., & Parra, E. (2003). Computational model for cyclic mobility and associated shear deformation. Journal of Geotechnical and Geoenvironmental Engineering, 129(12), 1119-1127.

Yang, Z., Elgamal, A., Adalier, K., & Sharp, M. K. (2004). Earth dam on liquefiable foundation and remediation: numerical simulation of centrifuge experiments. Journal of Engineering Mechanics, 130(10), 1168-1176.

Zienkiewicz, O. C., & Shiomi, T. (1984). Dynamic behaviour of saturated porous media; the generalized Biot formulation and its numerical solution. International Journal for Numerical and Analytical Methods in Geomechanics, 8(1), 71-96.

7. Numerical modeling of the case study

As stated in the previous chapters, the main purpose of this PhD thesis is to study the behavior of a Tailings Storage Facility (TSF) subjected to seismic loads. In Chapter 4, which presented an analysis of the main literature cases dealing with the numerical analysis of tailings storage facilities, it was shown that finite element analysis is one of the most suitable methods for obtaining comprehensive information on the behavior of these structures, as it provides the evolution of the stress and strain field, as well as the distribution of pore water pressures during shaking. Although not without limitations and characterized by numerous uncertainties, finite element analysis is a suitable tool for predicting the behavior, and thus the related effects, of a given structure under particular loads and specific boundary conditions. This chapter initially presents the procedures, constraints, and limitations of the creation of the numerical model for the boundary value problem using the software OpenSees. Then, the results obtained from the simulations are presented and discussed. Concerning the creation of the model, the global geometry and the various structures that compose it are defined, and details are given on how the mesh was built and the elements chosen. Then, the initial conditions and the procedures used to define the initial state are described and the choices regarding the boundary conditions attributed to the system are presented and justified. Finally, the procedures used to define the seismic input are described. As mentioned in Chapter 5, where the reference tailings storage facility is described, the analyses focus on the structures called Basin No. 2 and Embankment No. 2, as they are the most important ones in terms of size and effects on the surrounding area following a possible failure event.

7.1. Geometry definition

The geometry of the model was defined based on several considerations. For the reasons already explained in Chapter 4, i.e., that one-dimensional modeling is unable to capture the non-negligible multi-dimensional effects present in tailings dams and, on the other hand, three-dimensional models, although more representative of the real situation, require information that was not available, the analyses were performed on a two-dimensional plane-strain model. The longitudinal extension of the computational domain was assumed based on the evaluations reported in Chapter 4, in which the geometries analyzed in 22 scientific articles were compared, and from which it resulted that, in the majority of cases, the width of the model was approximately double with respect to the horizontal projection of the dam bank. This proportion seemed the best compromise in terms of computational effort and minimizing boundary effects. In the case study, a longitudinal extension of 274 m was attributed to the domain, which is approximately 4 times longer than the horizontal projection of the dam bank (approximately 67 m). Although this choice involves a higher computational cost, it ensures lower boundary effects on the behaviour of the structure, especially in terms of possible spurious waves associated to seismic motion. In the vertical direction, the domain size is essentially imposed by the stratigraphic configuration. Specifically, as explained in Chapter 5, since the seismic bedrock has

been identified at a depth that is approximately 48 m below the ground level of the basin, the lower boundary of the domain was placed in this depth. The geometries of the different components of the system, which are the foundation, the basin, and the dam, have been chosen on the basis of the geotechnical model defined in Chapter 5. The final geometry configuration of the numerical model is presented in Figure 7.1. The aspect of the model dimensions has been further explored in paragraph 7.4.

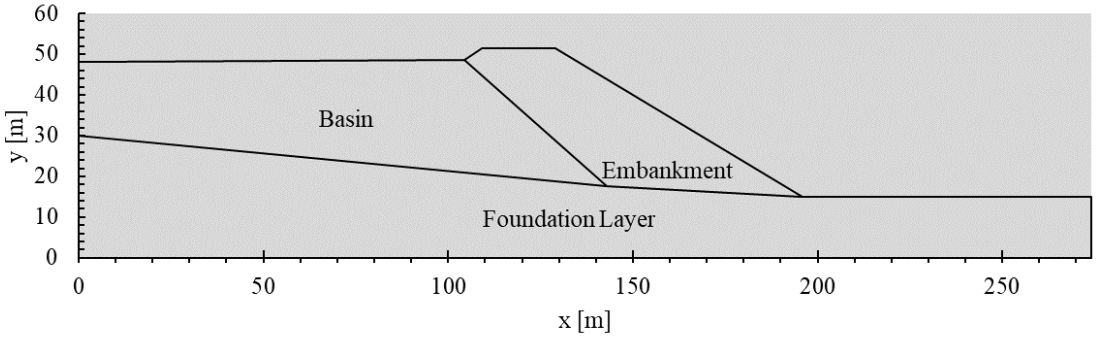

Figure 7.1: *Geometry of the numerical model.*

7.2. Element definition and mesh discretization

Analyses were performed with OpenSees software (Mazzoni et al. 2006), and a nine-node element, which in the program library is termed Nine Four Node Quad u-p Element, was used to discretize the domain. This plane-strain element is formed by four nodes (called 'pore pressure nodes') at vertices, which have three degrees of freedom each, i.e. the displacements in the two plane directions and the pore pressure, and five further nodes (called 'internal nodes') on the edges or in the center, which have only two degrees of freedom each, i.e. the displacement in the two plane directions (Figure 7.2).

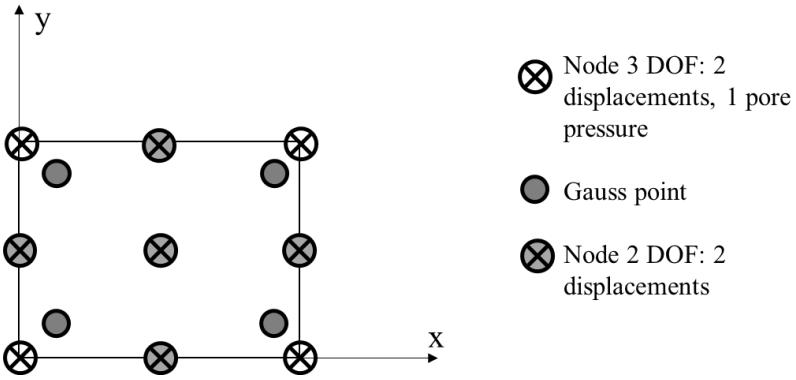

Figure 7.2: *Nine Four Node Quad u-p Element representation.*

The maximum side length of the elements to conduct wave propagation analyses was determined through the known relationship:

$$\Delta h = \frac{V_s}{kf} \qquad 7.1$$

where V_s is the minimum value of the shear wave velocity, k is a reduction coefficient, and f is the maximum significant frequency of the seismic input signal. Considering a shear wave velocity of 250 m/s, a frequency of 10 Hz and a reduction coefficient value of 8, Eq. (7.1) results in Δh results 3.125 m. It was therefore decided to discretize the mesh with quadrangular elements with regular sides (at least where possible) of 3 m. OpenSees has neither pre nor post-processors; therefore, AUTOMESH-2D/3D (Ma et al. 2011) software was used to create the mesh. Although this generator was designed for simulations in the field of metallic materials, being open source, its ability to create meshes with quadrangular elements was used. However, because this software is able to create only quadrangular elements with four nodes, it was necessary to add five specific internal nodes to each element, through a dedicated algorithm especially developed, of the Nine Four Node Quad u-p Element. The model for the case study was ultimately discretized using a mesh composed of 1278 elements with 1386 pore pressure nodes and 2687 internal nodes. The geometry of the discretized model and of 5 control points on which acceleration time histories were registered are shown in Figure 7.3. These nodes were chosen on the basis of expert judgment as they were considered particularly representative of the dynamic response of the system.

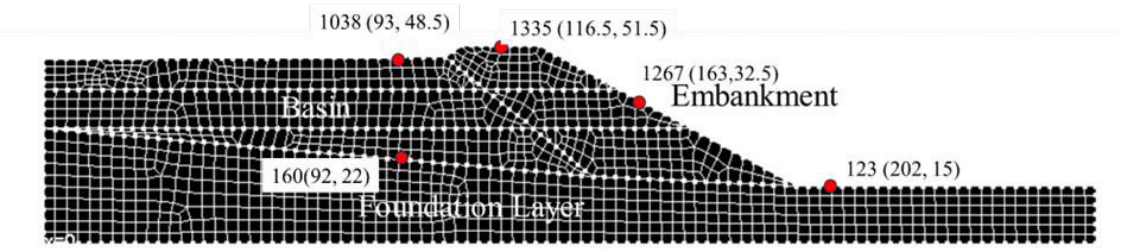

Figure 7.3: *Mesh discretization with AUTOMESH-2D/3D.*

From Figure 7.3 it is possible to notice that two horizontal lines are placed within the basin and the dam areas. These lines represent the boundaries used for the simulation of the construction phases of the structure, as will be explained in detail in the paragraph dedicated to the definition of the initial conditions of the model. To validate the size of the mesh, a gravitational analysis of the model was carried out with elements characterized by decreasing sizes: 25, 20, 10, 5 and 3 m (Figure 7.4).

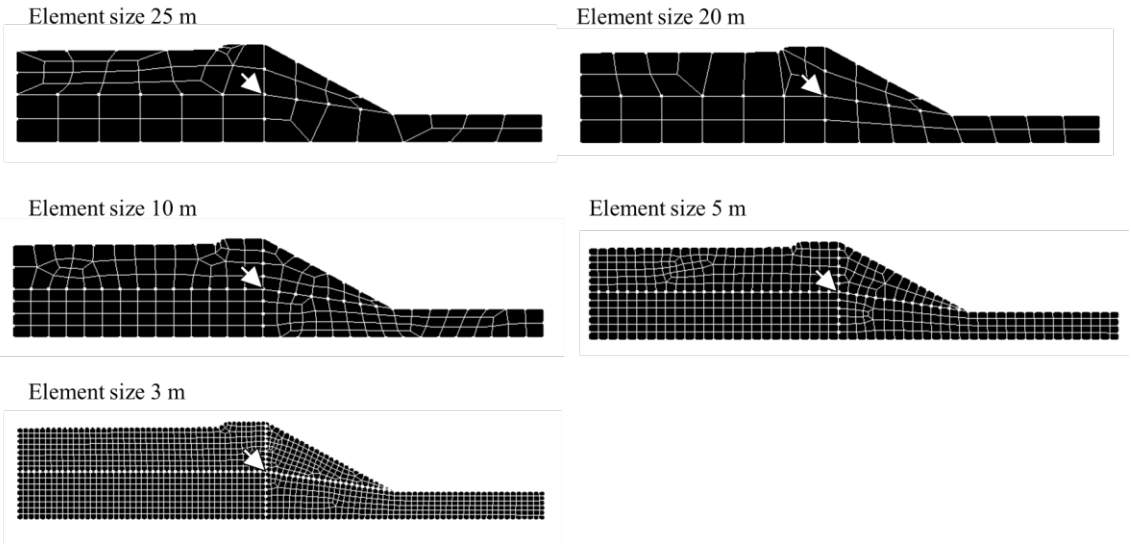

Figure 7.4: *Models with elements of different sizes for validating mesh discretization. The white arrow indicates the node on which the displacements were evaluated.*

At the end of the gravity analysis, the horizontal and vertical displacements of a node located under the crest of the dam were evaluated (coordinates x=129 m, y=25 m, white arrow in Figure 7.4) as shown in Figure 7.5.

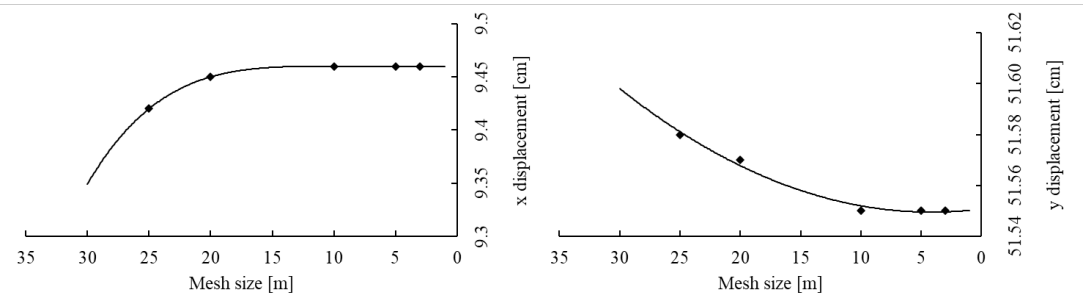

Figure 7.5: *Horizontal and vertical displacements determined at the point indicated by the white arrow in Figure 7.4 for models with different mesh discretizations.*

From Figure 7.5 it is possible to notice that both the displacements in the horizontal and vertical directions tend to an asymptotic value as the mesh gets denser and that the use of elements with a size of approximately 3 m gives sufficiently precise results.

7.3. Materials and constitutive models

Due to the importance that the choice of an adequate constitutive model plays in geotechnical numerical analyses, Chapter 6 was dedicated to this topic, where a brief description of the theory behind each model was given and the procedures utilized for material parameter calibration were presented. Among the constitutive models presented in Chapter 6, Pressure Independent Multi Yield (PIMY) and PM4Sand were assigned to the foundation and embankment sectors, respectively. Multiple analyses were conducted, attributing to the basin sector two different constitutive models, SANISAND and Pressure Dependent Multi Yield (PDMY). This made it possible to compare the results obtained with the two models, understanding the strengths and

weaknesses of each. The input parameters defined for the different constitutive models in Chapter 6 are summarized in Table 7.1.

Table 7.1: *Constitutive model input parameters.*

SANISAND (basin)		PDMY (basin)		PIMY (foundation)		PM4Sand (embankment)	
G_0 [-]	107	G_r [MPa]	141	G_r [MPa]	315	D_R [%]	36
ν [-]	0.05	B_r [MPa]	283	B_r [MPa]	630	G_0 [MPa]	100
M_c [-]	1.46	ϕ [°]	36	$\gamma_{max,r}$ [-]	0.1	h_{p0} [-]	0.6
c [-]	0.7	$\gamma_{max,r}$ [-]	0.1	p'_r [kPa]	100	h_0 [-]	2
λ_c [-]	0.0208	p'_r [kPa]	100	d [-]	0.5	e_{max} [-]	0.8
e_0 [-]	1.16	d [-]	0.5	NYS [-]	20	e_{min} [-]	0.5
ξ [-]	0.7	ϕ_{PT} [°]	31	c [kPa]	37	n^d [-]	0.1
m [-]	0.01	NYS [-]	20			n^b [-]	0.5
h_0 [-]	60	c_1 [-]	0.06			A_{d0} [-]	1
c_h [-]	0.91	c_2 [-]	6			z_{max} [-]	1
n^b [-]	1.2	c_3 [-]	0.019			c_z [-]	250
A_0 [-]	0.5	d_1 [-]	0.15			c_e [-]	1
n^d [-]	3	d_2 [-]	3			ϕ_{cv} [°]	33
z_{max} [-]	12	d_3 [-]	0			C_{GD} [-]	2
c_z [-]	900	l_1 [-]	1			C_{DR} [-]	1
		l_2 [-]	0			C_{kaf} [-]	1
						Q [-]	10
						R [-]	1.5
						m [-]	0.01
						$F_{sed,min}$ [-]	1
						$p'_{sed,o}$ [-]	1

7.4. Boundary conditions

The subsoil volume below the foundation layer (seismic bedrock) is modeled as an elastic half-space. In this way, the downward-traveling stress waves that reach the bottom boundary will be reflected only partially: part of their energy will be subtracted from the numerical domain simulating the actual radiation damping. In order to assume an input seismic motion represented by plane S-waves propagating in the vertical direction, only horizontal displacements are allowed at the base nodes. The base nodes are "linked" to each other with respect to the horizontal translation, through the OpenSees command equalDOF. In addition, to simulate the elastic seismic bedrock, the leftmost base node (coordinates 0, 0) is connected to a Lysmer-Kuhlemeyer (1969) dashpot. This dashpot is a viscous damper characterized by a viscosity coefficient c given by the product between the shear wave velocity and density of the bedrock. To obtain an equivalent load, the coefficient c must be multiplied by the base area of the

model. The actual free field conditions on the sides of the model are simulated by attributing to the elements positioned at the lateral boundaries of the model a 'thickness' five orders of magnitude greater than that of the other, regular elements, as proposed by McGann-Arduino (2011) (Figure 7.6 b). The thickness is a property of the Nine Four Node Quad u-p Element, which can be defined by the user during the construction of the model. The attribution of an increased thickness involves a proportional increase in the mass of these elements, whose nodes are linked together through the equalDOF command. This free-field simulation method is the best one as demonstrated in Gorini (2023) and as proposed by several authors (Forcellini & Tarantino 2013; Masoudi & Vadeghani 2018; Hwang 2023). In this way it is as if at the ends of the domain there were massive columns of soil that prevent the seismic action from reflecting on the edges and creating additional loads that do not exist in physical reality. It is worth noting that, in order to adequately size the Lysmer-Kuhlemeyer dashpot when multiplying the coefficient c by the base area of the model, it is necessary to take into account the increased thickness of the edge elements. Figure 7.6 a schematizes the domain with the boundary conditions just described.

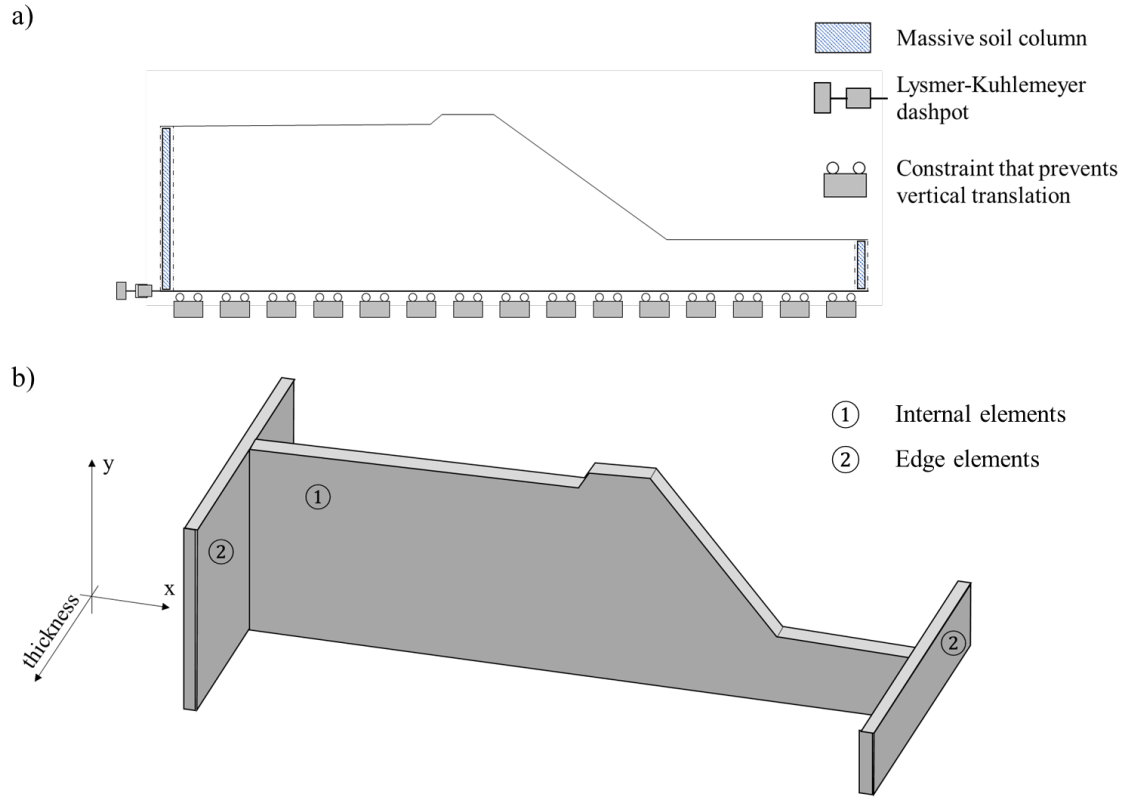

Figure 7.6: *Domain boundary conditions a) boundary conditions, b) elements thickness.*

To validate the dimensions and boundary conditions attributed to the model, a comparison was made between the results obtained with the model just described, called Short model, and a model characterized by larger dimensions (which should better simulate free field conditions but which has a significantly higher computational cost), called Long model, in terms of acceleration response recorded at node 903 as shown in Figure 7.7. The seismic input with which the analysis was conducted is the S1 signal as described in paragraph 7.6.

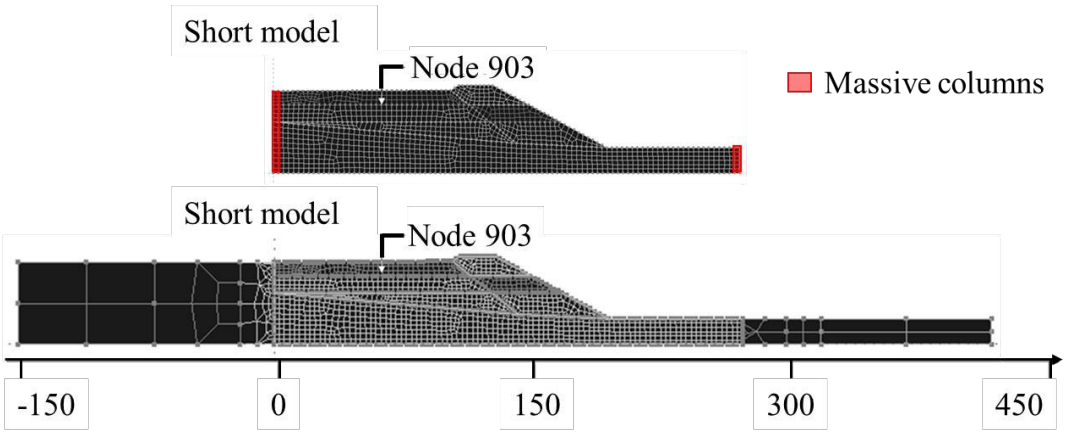

Figure 7.7: *Models used to validate dimensions and boundary conditions.*

Figure 7.8 shows the acceleration time histories and Fourier amplitude spectrum obtained with the two models at node 903.

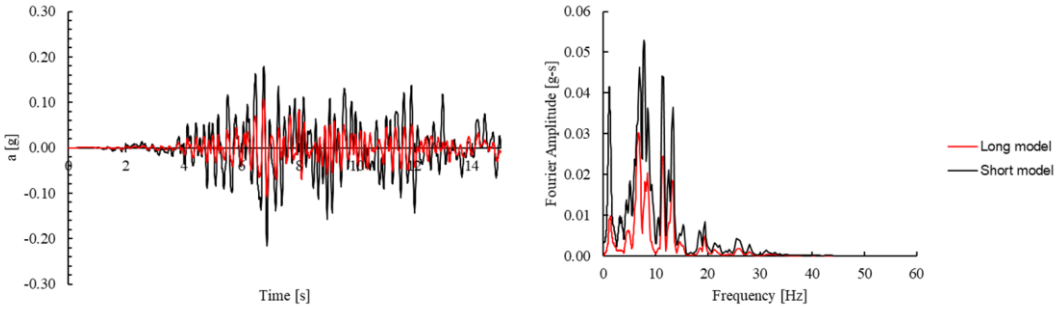

Figure 7.8: *Acceleration time histories of node 903 obtained with Short and Long model.*

From the examination of Figure 7.8 it is possible to observe that even if the amplitudes of the long model are smaller than those of the short model the general shape is quite similar, and it was considered the most appropriate solution in terms of computational costs.

7.5. Initial conditions

As mentioned in Chapter 4, numerical analyses of geotechnical structures are, in a sense, snapshots of time with respect to the history of the examined soil volume. It is therefore important to try to recreate as realistically as possible the stress deposition or loading history experienced by the structure up to the time instance considered in the analysis. In the present case, it would be crucial to represent the construction of both the embankment and the basin over time. Since it was not possible to model the actual construction of the structure, which was probably raised almost continuously over time, it was considered, on the basis of analyses carried out on historical documents and photos, that it was sufficiently accurate to simulate the construction of the system in three successive phases. The first step consisted in carrying out an initial

gravitational analysis following the construction of the starter dike (about 15m high) and the complete filling of the settling basin upstream of it. The next stage was to perform a second gravity analysis following the construction of the embankment over the starter dike and after the basin was completely filled, just prior to the construction of the end portion of the embankment. The last step consisted of a gravity analysis carried out once construction was completed, with the structure in its current configuration. Figure 7.9 represents the sequence of the construction and analysis phases.

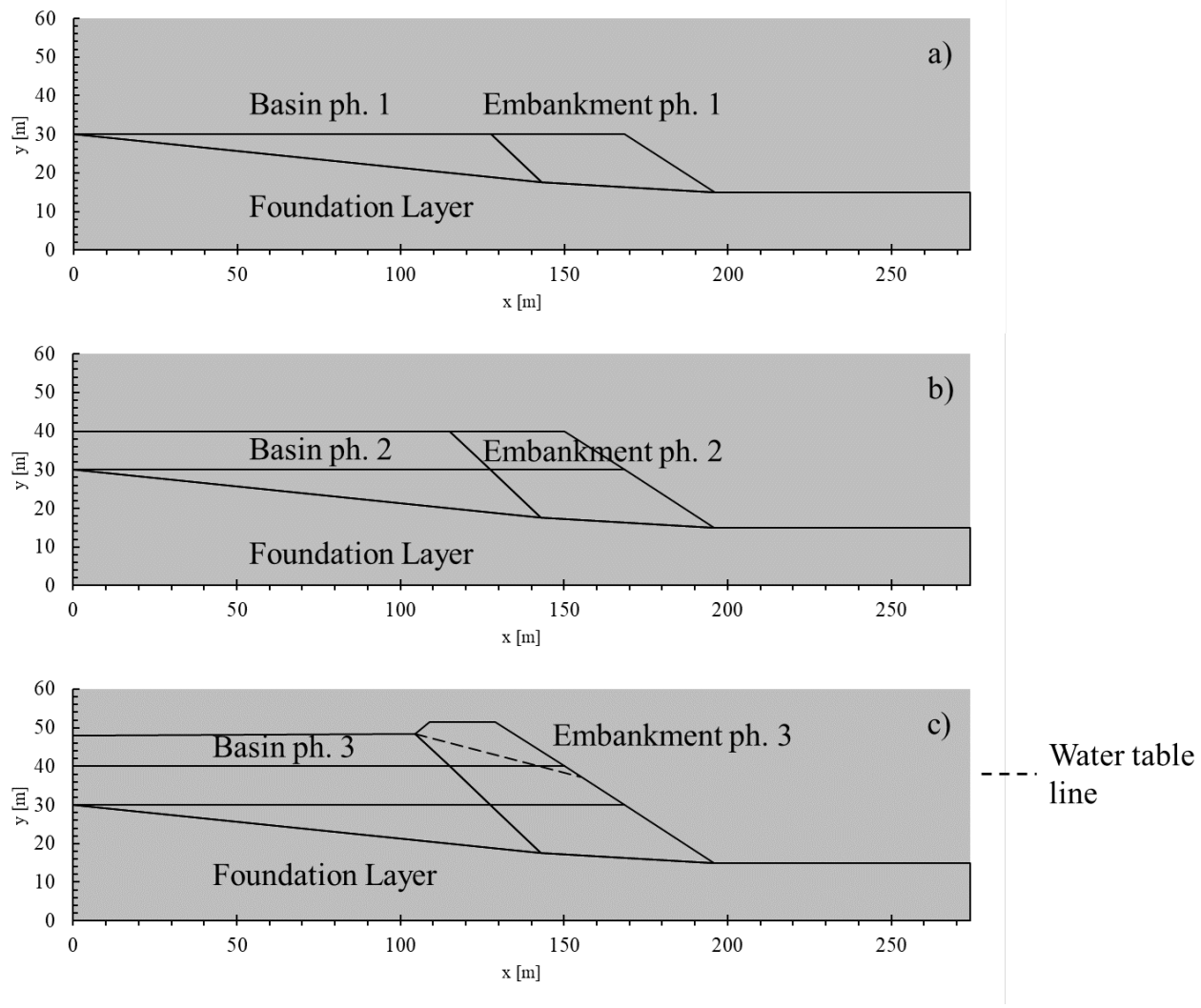

Figure 7.9: *Tailings dam construction stages simulation: a) phase 1- construction of the starter dike, b) phase 2 - construction of the second embankment portion, c) phase 3 - current configuration.*

During the "construction" phases, the groundwater level was maintained at the top of the basin and the embankment in order to guarantee a consolidation process in saturated conditions. In the current configuration (Figure 7.9 c), the groundwater level was assumed to be at the top of the tailings level in the basin. This condition is certainly realistic generally rainier winter months and also often occurs in the warmer seasons. Within the embankment, the groundwater level was assumed linearly decreasing with an inclination of 1/5. This trend of the water table is suggested by Vick (1990) for

tailings dams built with the upstream method in which the ratio of the projected distance between the foot of the dam and the innermost part of the top and the height is approximately 3.

As explained in Chapter 5, from the combination of the information obtained from laboratory and field tests carried out for this work and obtained from previous processing, it was possible to conclude that for the settling basin the relative density is approximately homogeneous for the entire volume of interest and equal to 40%. This information was translated into the input parameters required by the different constitutive models used.

The OpenSees software does not allow to activate some elements of the model in successive phases like other software; therefore, it was necessary to define the elements and the nodes of the various phases following each gravitational analysis. In order to avoid problems of congruence between the nodes and to carry out the seismic analyses in the current configuration of the structure, the InitialStateAnalysis command of OpenSees was used (McGann et al. n.d). This command, specifically developed to determine the initial state in geotechnical problems, allows the establishment of a soil stress and strain state following a gravitational load without the associated nodal displacements. In Figures 7.10 and 7.11 the average $\sigma'_m = \frac{\sigma'_v+\sigma'_h}{2}$ and the vertical σ'_v effective stress fields of the 3 phases are reported, using the geotechnical convention for stresses (compression is positive). In order not to burden the discussion, the results reported in Figures 7.10 and 7.11 refer only to the analyses carried out by attributing the SANISAND constitutive model to the settling basin material (SBM); the same procedure was also applied in the case where the PDMY constitutive model was used for SBM, obtaining very similar results.

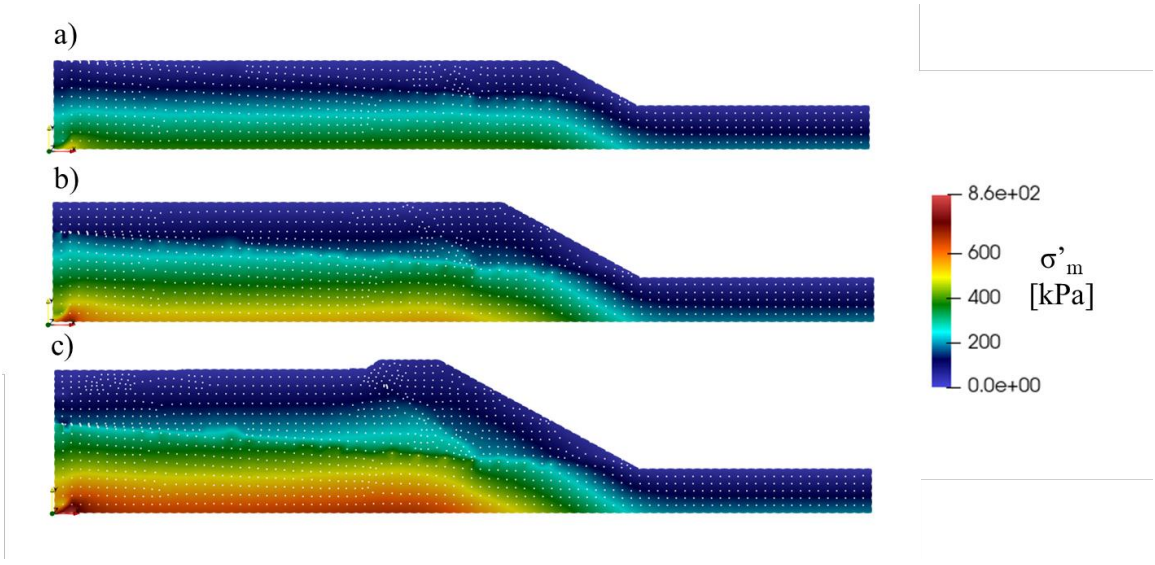

Figure 7.10: *Mean effective stress field obtained using the SANISAND model for the settling basin material (SBM): a) phase 1 - construction of starter dike, b) phase 2 - construction of the second embankment portion, c) phase 3 - current configuration.*

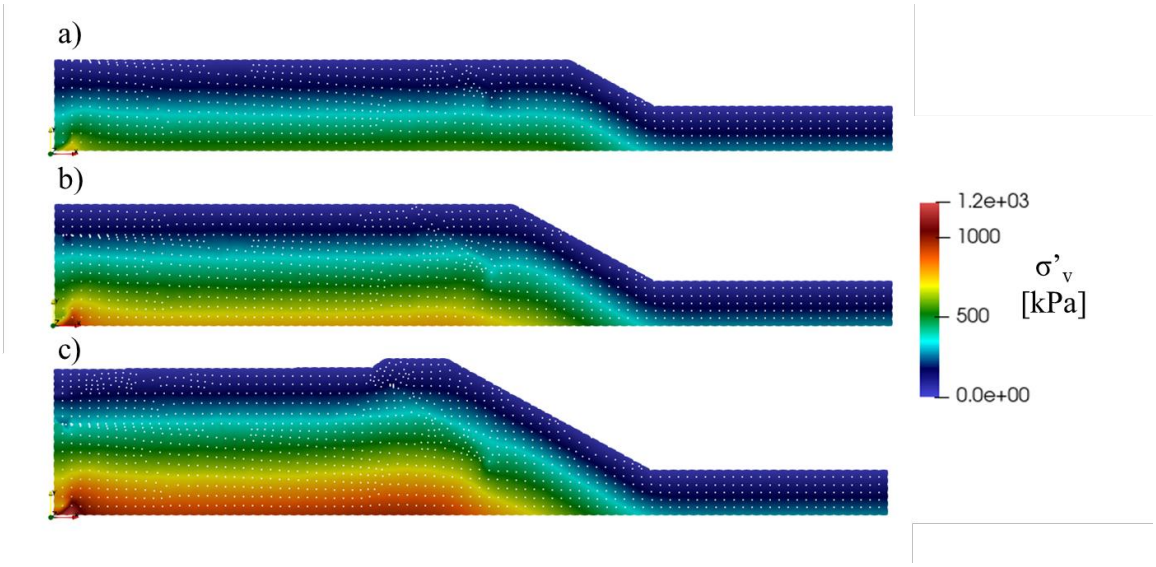

Figure 7.11: *Vertical effective stress field obtained with the SANISAND model for the settling basin material (SBM): a) phase 1 - construction of starter dike, b) phase 2 - construction of the second embankment portion, c) phase 3 - current configuration.*

The results from the simulations performed by OpenSees were graphically processed with the software Paraview (Henderson 2007). In addition to the analysis of the stress and strain field, this procedure made it possible to inspect the spatial distribution of the memory parameters of the various constitutive models before carrying out seismic analyses.

7.6. Ground motion definition

The definition of the seismic motion was done using a tool made available by the Tuscan region and called SCALCONA (Lai et al. 2017). SCALCONA software requires as input the definition of the site geographical coordinates and the return period of the expected event at the site, giving back a set of seven signals (as prescribed by the regulations) that are recorded on outcropping-rock, i.e. soils of Class A (V_S = 800 m/s) according to the Italian Technical Standards 2018 (NTC2018) (Consiglio Superiore dei Lavori Pubblici 2018), and are spectrum-compatible on average as required from the aforementioned standard. The return period was determined with reference to the Italian Technical Standards 2018 (NTC2018) and its explanatory attachment (Consiglio Superiore dei Lavori Pubblici 2019).

The formulation of the return period is given in paragraph 3.2.1 of the NTC2018:

$$T_R = -\frac{C_U V_N}{\ln\left(1 - P_{V_R}\right)} \tag{7.2}$$

where C_U is the usage coefficient of the structure defined in paragraph 2.4.3 of the NTC2018. It is related to the usage class that is defined with reference to the consequences of potential operational interruption or collapse. In the specific case, class IV was chosen since it includes structures such as dams, albeit of the water retention type; the corresponding usage coefficient C_U is equal to 2. V_N is the nominal

life of the structure which is equal to 100 years for constructions with high performance levels (Table 2.4.I NTC2018). Italian regulations are based on the concept of "limit states" related to the performance level of the structure. In the specific case, reference has been made to the 'collapse' limit state, to which corresponds a seismic action with a probability of exceedance $P_{V_R} = 5\%$ during the nominal life of the structure (Table 3.2.I of the NTC2018). By inserting these data in equation 7.2, a return period $T_R = 3900$ years was obtained. However, based on the suggestion given in Chapter C3.2.1 of the NTC2018 explanatory attachment (Consiglio Superiore dei Lavori Pubblici 2019) and the requirement of paragraph C7.7.2 of the Italian standards for embankments and dams 2014 (Consiglio Superiore dei Lavori Pubblici 2014) a return period of the seismic action $T_R = 2475$ years was assumed. Through the geographical coordinates of the site and the return period it was possible to retrieve the input signals using the SCALCONA software. Table 7.2 shows some information regarding the seismic signals derived from SCALCONA, while Figures 7.12, 7.13 and 7.14 show the corresponding accelerograms, velocity time histories and Fourier amplitude spectrum respectively. The elastic response spectra compared to the site target spectrum is shown in Figure 7.15.

Table 7.2: *Main information on the seismic signals derived from SCALCONA for a return period of 2475 years.*

Signal	Magnitude [Mw]	Epic. Distance [km]	Scaling Factor [-]	Source database	Accelerogram name
S1	6.2	29.9	1.33	ESM	EU.HRZ..HNE.D.19790524.172317.C.ACC.ASC
S2	5.74	12.57	1.53	NGA-West2	RSN146_COYOTELK_G01320.AT2
S3	6.93	83.53	1.07	NGA-West2	RSN804_LOMAP_SSF205.AT2
S4	6.69	38.07	0.86	NGA-West2	RSN1091_NORTHR_VAS000.AT2
S5	6.6	31	0.54	KiK-net	SMNH100010061330.EW2
S6	6.6	62	1.83	KiK-net	SAGH050503201053.NS2
S7	5.2	11.8	2.79	ESM	IT.AQP..HNN.D.20090409.005259.C.ACC.ASC

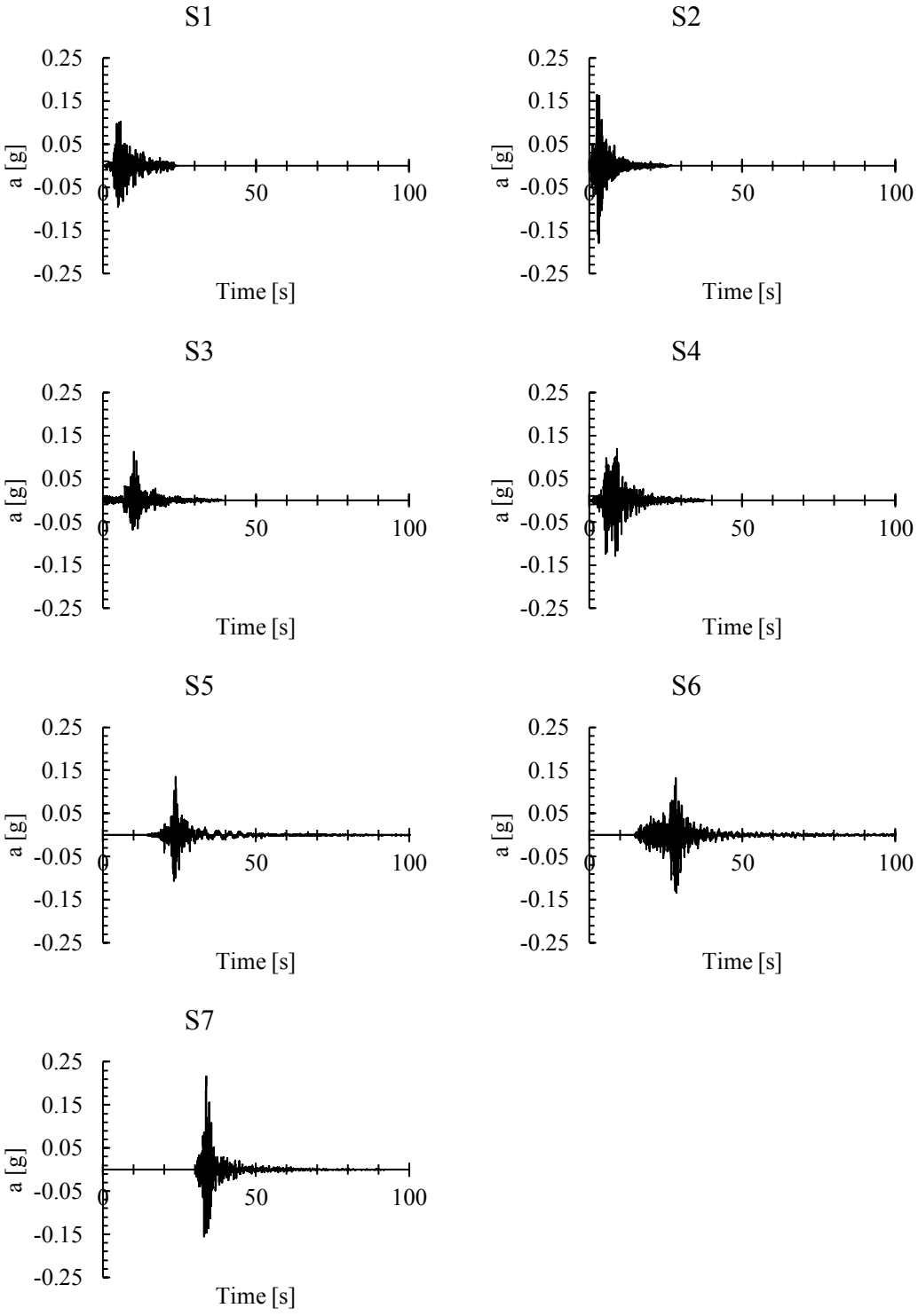

Figure 7.12: *Accelerograms provided by SCALCONA of the seven input signals.*

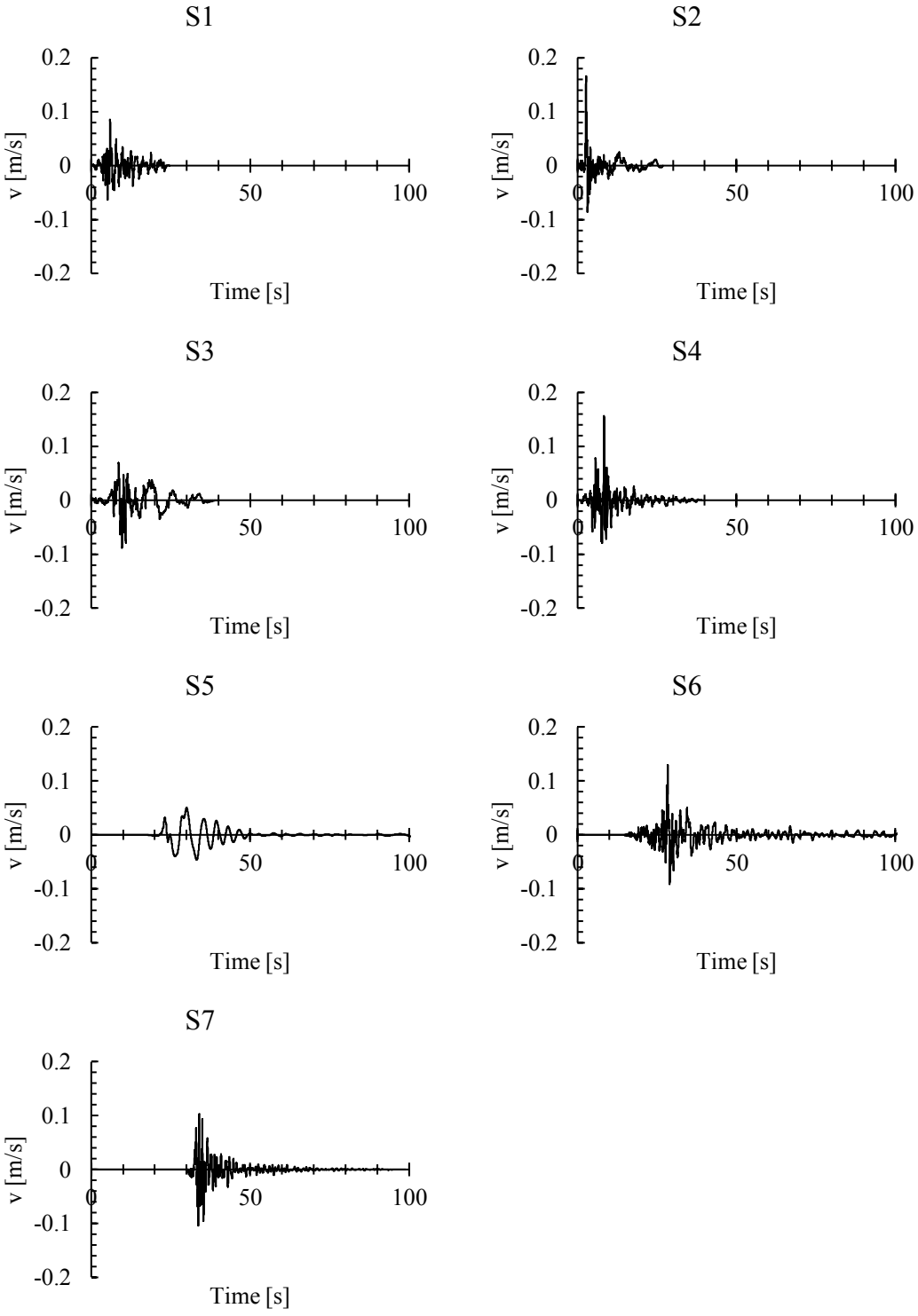

Figure 7.13: *Velocity time histories provided by SCALCONA of the seven input signals.*

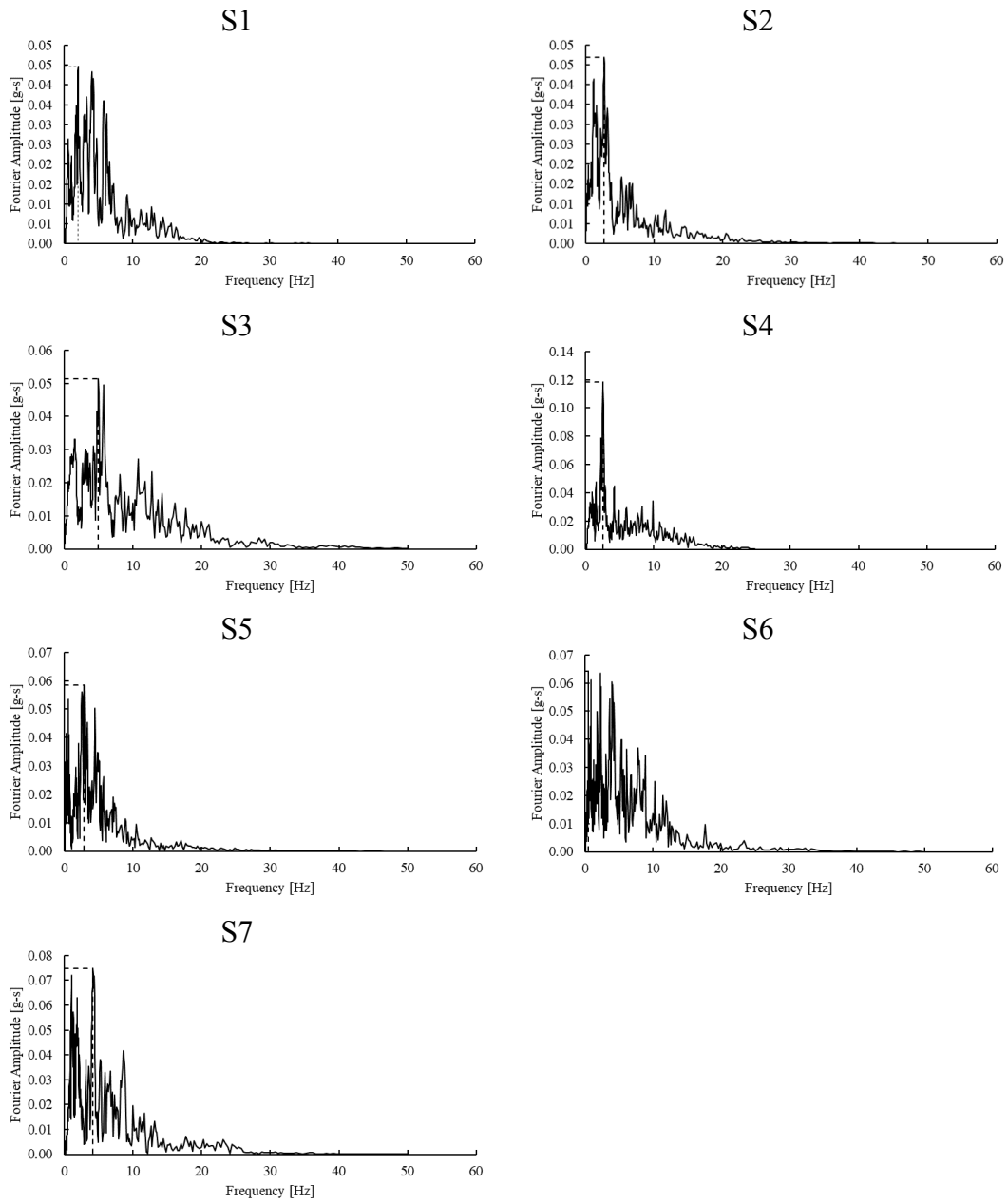

Figure 7.14: *Fourier amplitude spectrum time histories provided by SCALCONA of the seven input signals.*

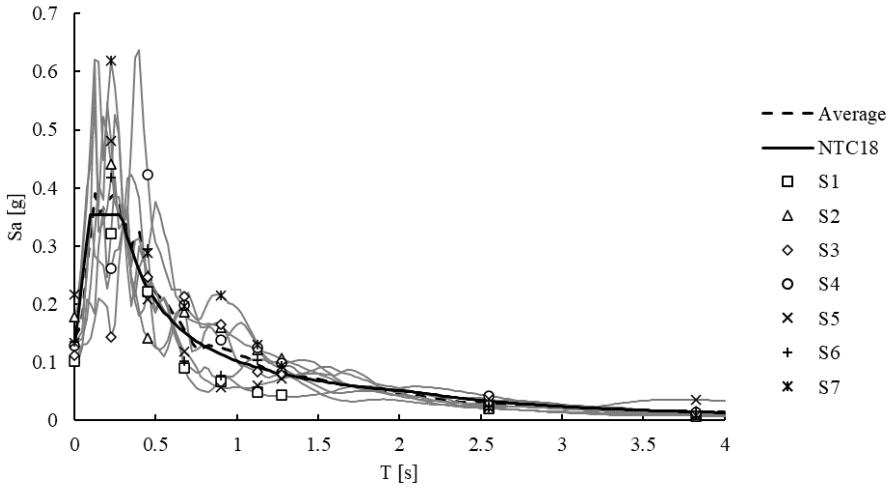

Figure 7.15: E*lastic response spectra of the seven input signals, average spectrum and site target spectrum as defined by NTC18 for 2475-year return period.*

Table 7.3 shows the values of the peak velocities, predominant frequencies obtained considering the maximum value of the Fourier amplitude in relation to the spectrum and the peak spectral acceleration shown in Figures 7.13, 7.14 and 7.15 respectively. From Table 7.3 it is possible to deduce that the predominant frequencies are quite different from each other with a minimum of 0.49 Hz for the S6 signal and a maximum of 4.96 Hz for the S2 signal.

Table 7.3: *Predominant frequencies Peak velocities of the seven signals.*

Signal	Peak velocity [m/s]	Predominant frequency [Hz]	Peak spectral acceleration [g]
S1	0.09	2.03	0.42
S2	0.17	4.96	0.54
S3	0.09	2.70	0.37
S4	0.16	2.55	0.64
S5	0.05	2.89	0.55
S6	0.13	0.49	0.61
S7	0.10	4.16	0.62

Since OpenSees requires the input motion to be assigned in terms of velocities, velocity time histories have been assigned at the basis of the numerical model has described in the previous paragraphs.

The Peak velocities (Table 7.3) range between a minimum of 0.05 m/s (S5) and a maximum of 0.17 m/s (S2). From the observation of the time histories, it is possible to deduce that signal number 2 has a markedly impulsive character while the others show several more evenly distributed peaks over time, with signals 4 and 6 containing a peak being much higher than the average approximately halfway through the shaking.

7.7. Seismic analysis results

In this section of the thesis, the results obtained from the numerical analyses carried out on the investigated tailings dam under seismic conditions are presented and discussed. The analyzes were carried out by imposing at the basis of the model the seven seismic inputs presented in the previous chapter in terms of velocity time histories, and by attributing once the SANISAND constitutive model and once the PDMY model to the material called settling basin materials (SBM) (see Chapter 6 and paragraph 7.3). Therefore, a total of 14 numerical models were analyzed. The hardware used to perform the analyses is characterised by fairly common components and each analysis lasted approximately 24 hours. The results from the analyses are presented in the following in terms of displacements (vertical upwards and horizontal left positive), shear strains and of the decay of the effective stresses caused by the increase of the pore water pressure that can be calculated by the formulation proposed by Machaček et al. (2018):

$$\zeta = -\frac{\sigma'_{ii}(t^{dyn}) - \sigma'_{ii}(t^0)}{\sigma'_{ii}(t^0)} \tag{7.3}$$

where $\sigma'_{ii}(t^{dyn}) = \sigma'_{xx}(t^{dyn}) + \sigma'_{yy}(t^{dyn})$ is the trace of the effective stress tensor at a certain time during the shaking and $\sigma'_{ii}(t^0) = \sigma'_{xx}(t^0) + \sigma'_{yy}(t^0)$ is the trace of the effective stress tensor at the beginning of the earthquake. ζ is 0 at the beginning of the earthquake ($\sigma'_{ii}(t^{dyn}) = \sigma'_{ii}(t^0)$). If, during the seismic event, the effective stresses decrease, ζ increases. If the latter reaches unity, there is a total loss of effective stresses and thus of the frictional component of the strength., i.e. soil liquefies and behaves like a fluid.

7.7.1. Results attributing SANISAND constitutive model to the settling basin material

Figures 7.16 to 7.22 show the results of the numerical analysis for the various seismic inputs attributing the SANISAND constitutive model to the settling basin material (SBM), the PIMY model to the foundation material (FNM) and the PM4Sand model to the embankment material (ENM). In the upper left corner of each Figure, the time elapsed since the start of application of the earthquake motion is indicated, corresponding to the time in which in considerable portions of the domain ζ=0 was reached. These times were chosen by evaluating all the time instants during the earthquake and considering the most critical ones on the basis of a qualitative evaluation (which was always rather straight forward). Section a) of each Figure shows the color map of the spatial distribution of ζ over the numerical domain with reference to the indicated time. Section b) of each Figure shows the color map of the shear strain γ of the numerical domain. Section c) of each Figure shows the displacements at the indicated time. The displacements of the nodes are magnified by 10 times for better legibility of the drawing. The values of y and x shown on the figure indicate the maximum vertical and horizontal displacement, respectively, of the external node of

the embankment crest. Finally, sections d) and e) of each Figure show color maps of the horizontal and vertical components of the displacements respectively.

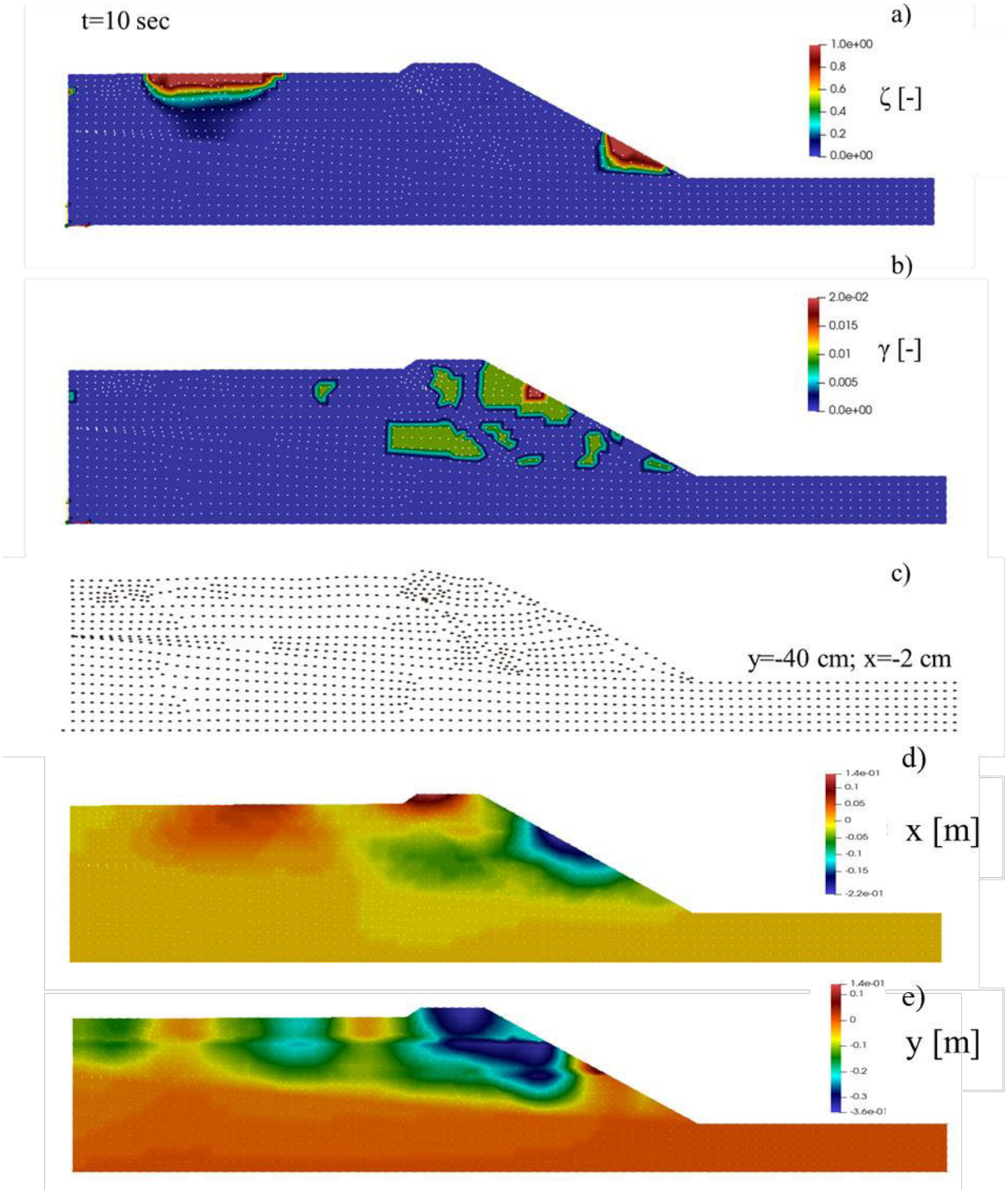

Figure 7.16: *Results from numerical analysis with signal S1 after 10 seconds from beginning of seismic event: a) decay of the effective stresses ζ, b) shear strain γ, c)*

displacements (the displacements shown in the figure are amplified 10 times), d) horizontal components of displacements, e) vertical components of displacements.

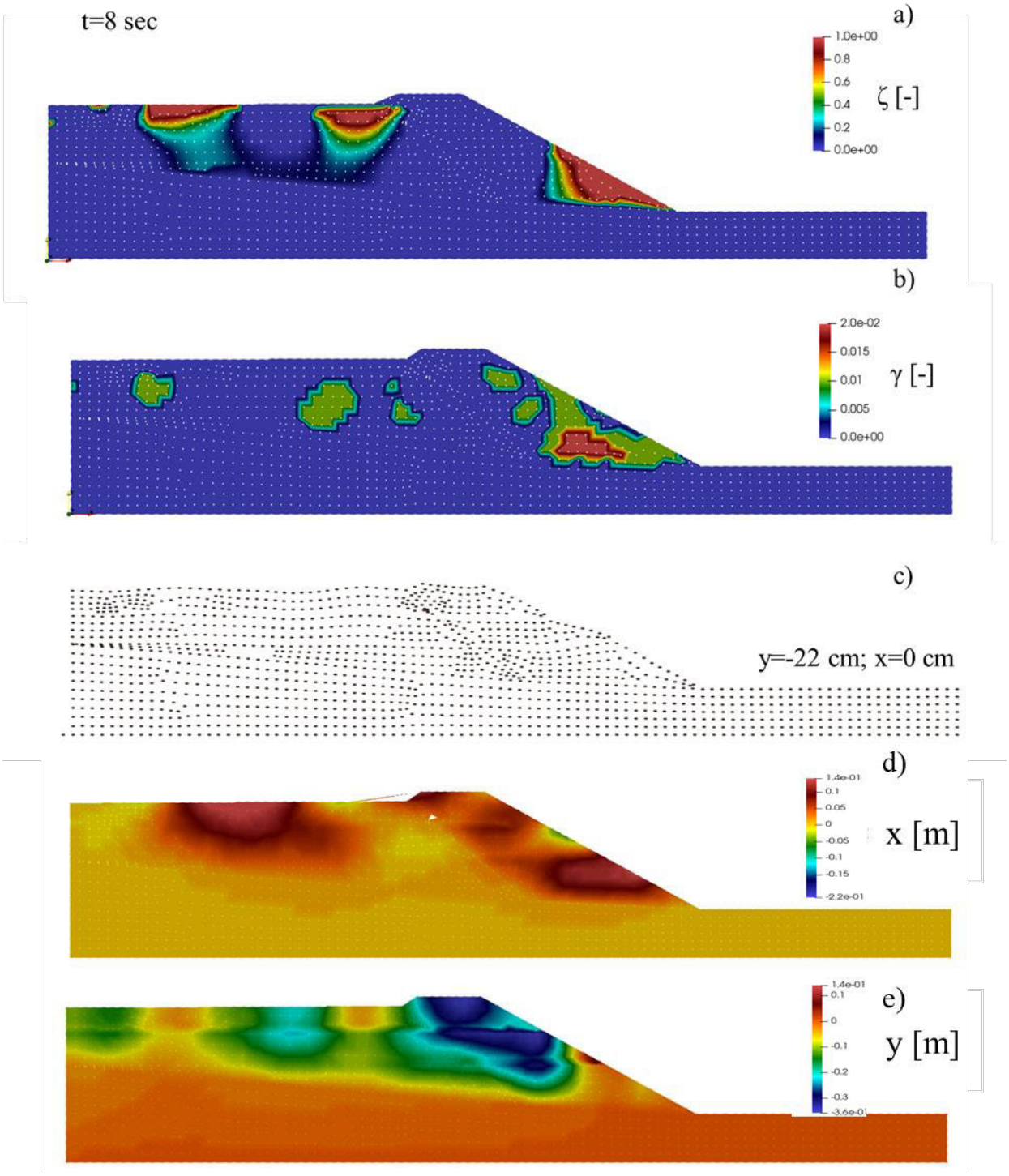

Figure 7.17: *Results from numerical analysis of signal S2 after 8 seconds from beginning of seismic event: a) decay of the effective stresses ζ, b) shear strain γ, c)*

displacements (the displacements shown in the figure are amplified 10 times), d) horizontal components of displacements, e) vertical components of displacements.

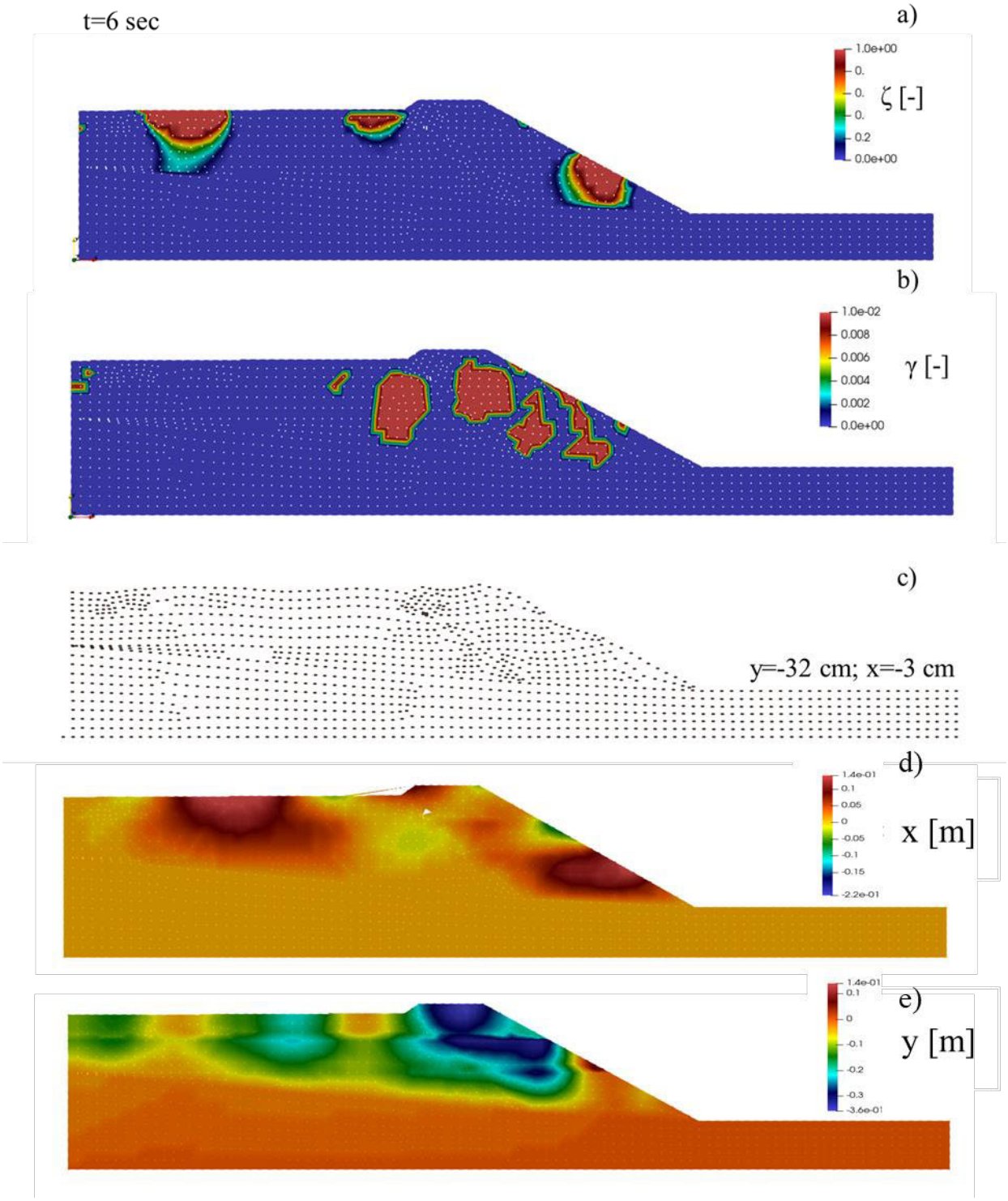

Figure 7.18: *Results from numerical analysis of signal S3 after 6 seconds from beginning of seismic event: a) decay of the effective stresses ζ, b) shear strain γ, c) displacements (the displacements shown in the figure are amplified 10 times), d) horizontal components of displacements, e) vertical components of displacements.*

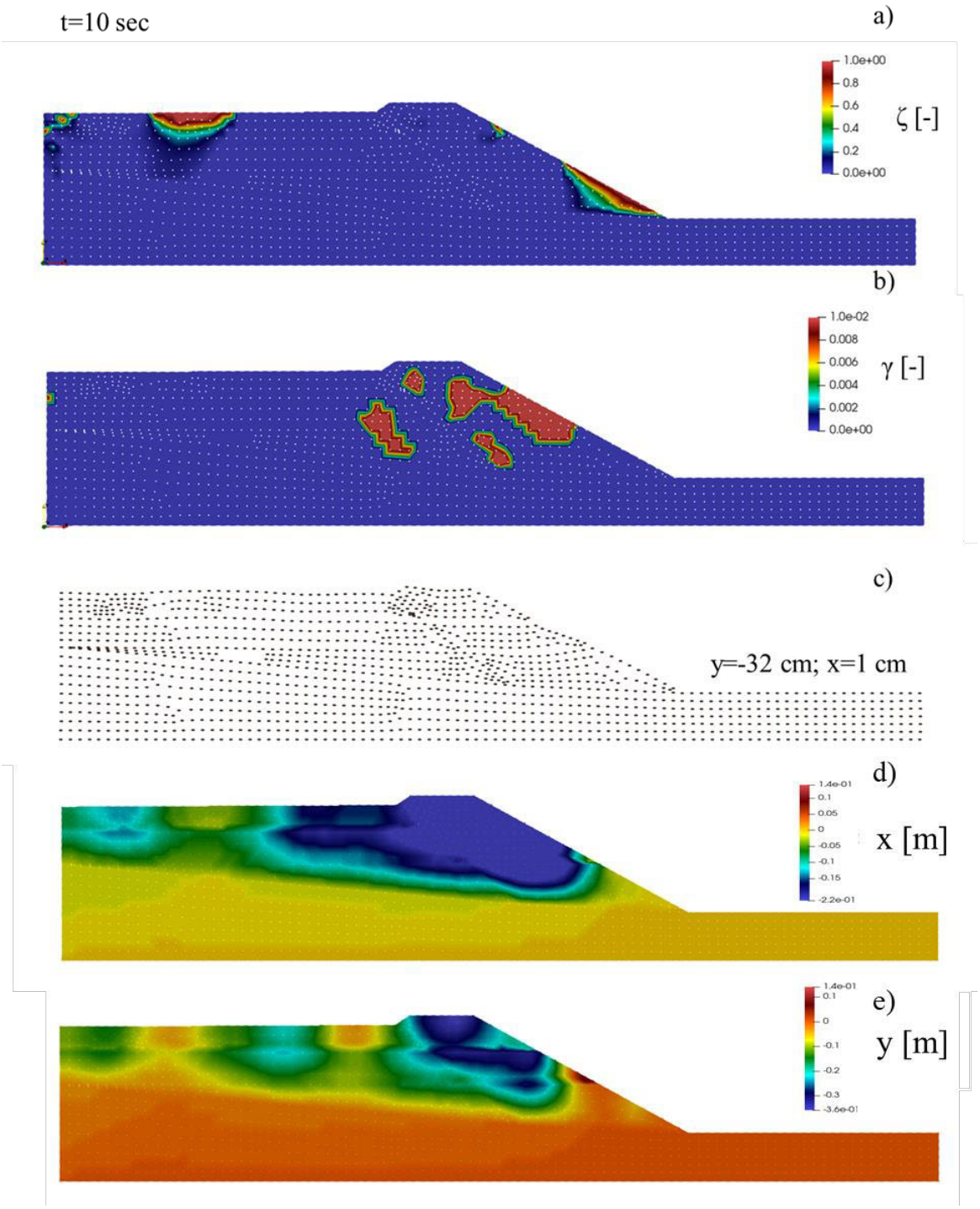

Figure 7.19: *Results from numerical analysis of signal S4 after 10 seconds from beginning of seismic event: a) decay of the effective stresses ζ, b) shear strain γ, c) displacements (the displacements shown in the figure are amplified 10 times), d) horizontal components of displacements, e) vertical components of displacements.*

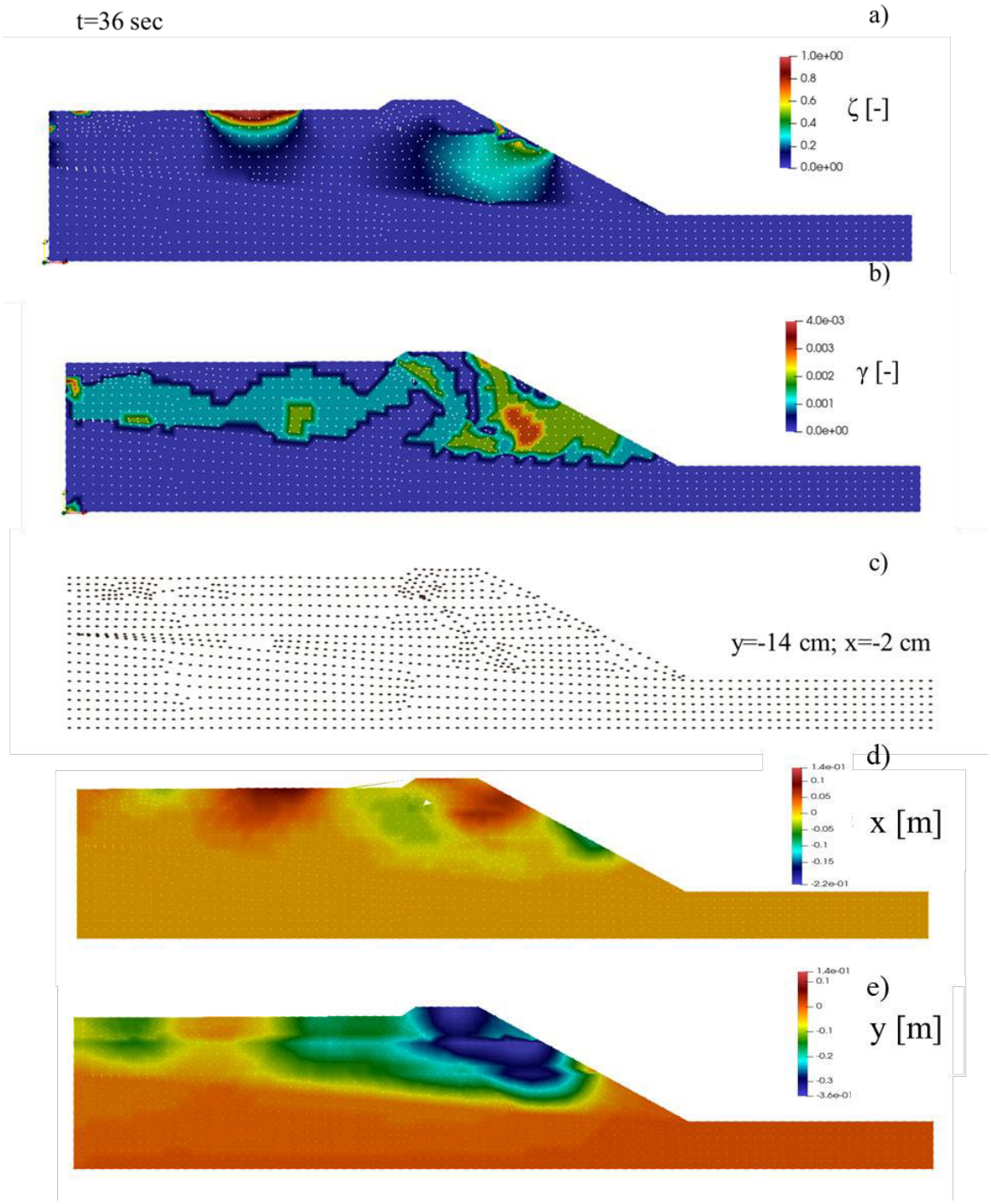

Figure 7.20: *Results from numerical analysis of signal S5 after 36 seconds from beginning of seismic event: a) decay of the effective stresses ζ, b) shear strain γ, c) displacements (the displacements shown in the figure are amplified 10 times), d) horizontal components of displacements, e) vertical components of displacements.*

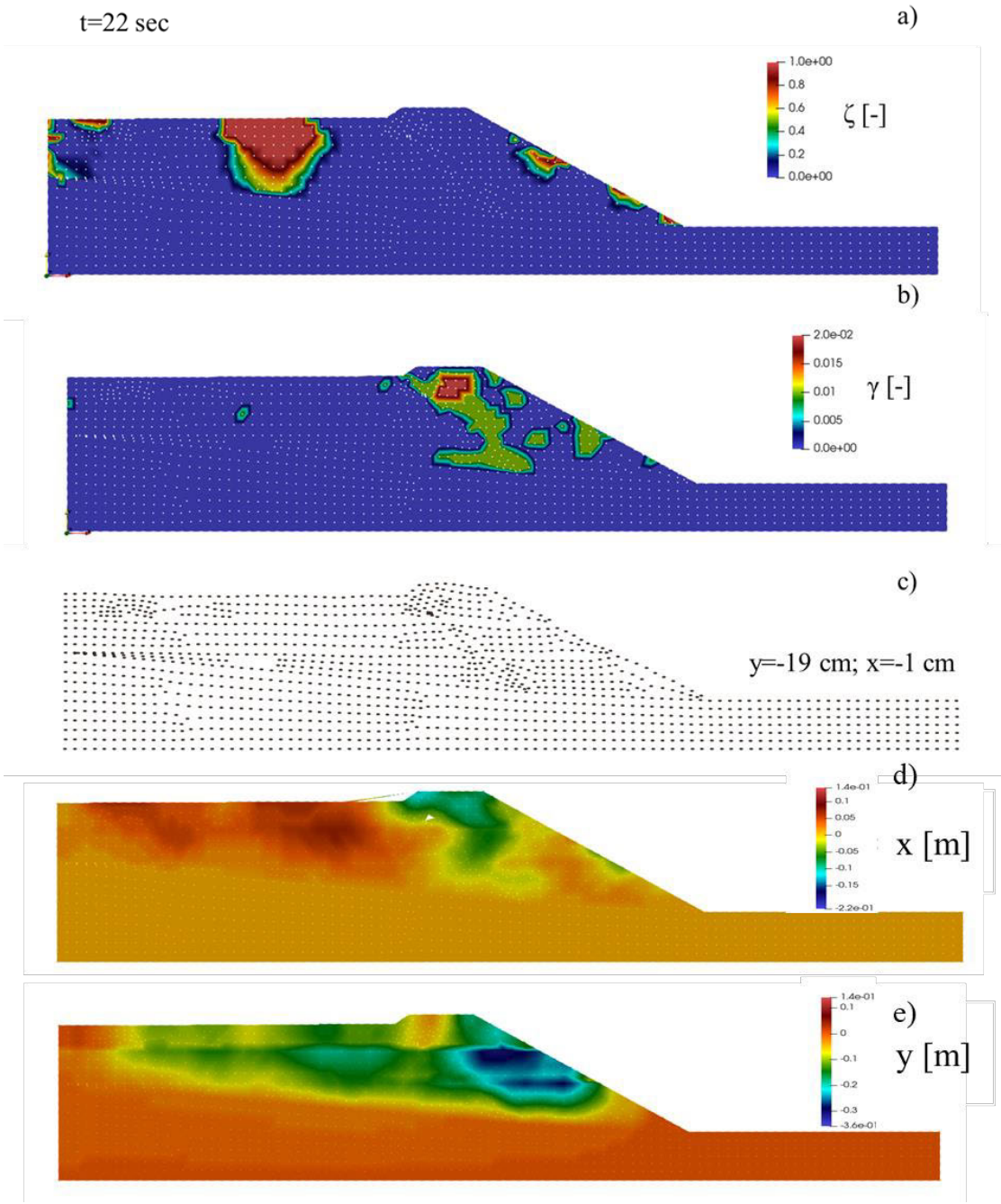

Figure 7.21: *Results from numerical analysis of signal S6 after 22 seconds from beginning of seismic event: a) decay of the effective stresses ζ, b) shear strain γ, c) displacements (the displacements shown in the figure are amplified 10 times), d) horizontal components of displacements, e) vertical components of displacements.*

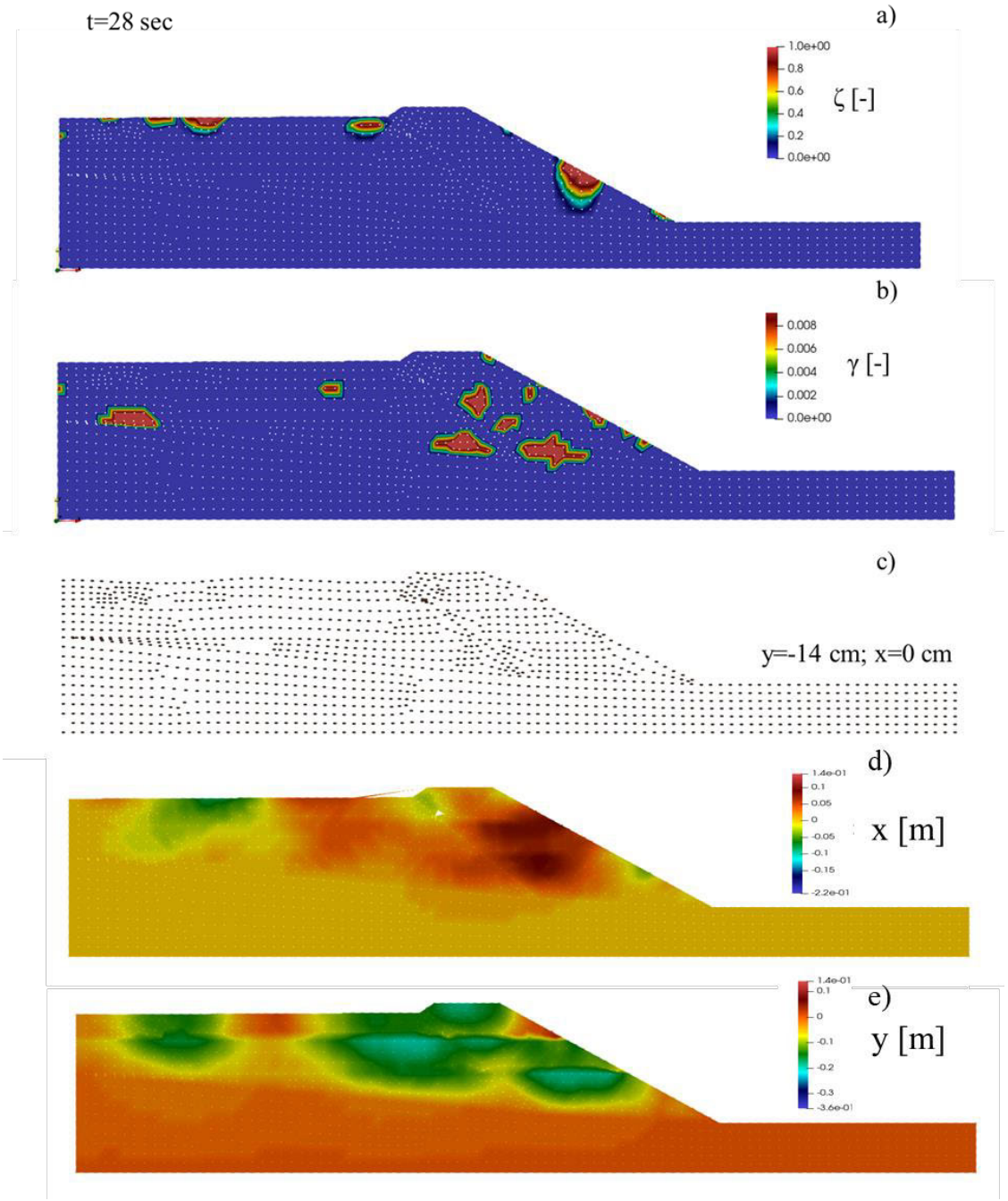

Figure 7.22: *Results from numerical analysis of signal S7 after 28 seconds from beginning of seismic event: a) decay of the effective stresses ζ, b) shear strain γ, c) displacements (the displacements shown in the figure are amplified 10 times), d) horizontal components of displacements, e) vertical components of displacements.*

Looking at section a) of Figures 7.16 to 7.22, it can be seen that the parameter ζ locally reaches the unity value (corresponding to a complete drop in the effective stresses) with all the used seismic input signals. In all cases, the areas most affected by the decay of the effective stresses are the surface areas of the settling basin and the areas adjacent to the foot of the embankment. In case the basin area remains (as the current condition) forbidden from any activity, the decay of the effective stresses calculated for this area does not involve major problems in terms of territorial safety. However, if the area was to be exploited in some way, it will be necessary to foresee countermeasures to mitigate these phenomena. On the contrary, a failure of the embankment can have devastating consequences for the downstream territories. In particular, in Figure 7.16 a) it is possible to observe that 10 seconds after the application of signal S1, ζ reaches a unit value in a cross-sectional area of about 126 m^2 at about 36 m from the crest in the basin and in an area of about 100 m^2 close to the embankment foot. The situation is worse with the application of the S2 signal, which causes a complete decay of the effective stresses, 8 seconds after the start of the seismic event (Figure 7.17 a), in two areas of about 160 m^2 (one close to the crest of the bank) and in a large portion at the foot of the bank (440 m^2). A similar condition is recorded 6 seconds after the application of the S3 signal (Figure 7.18 a) but, with smaller decay areas. The situation that occurs 10 seconds after the application of signal S4 (Figure 7.19 a) is very similar to that encountered for signal S1 (Figure 7.16 a). In the case of the application of the S5 signal (Figure 7.20 a) the total loss of the effective stresses occurs only in the basin area, while in the embankment ζ reaches the value of 0.6 on the slope surface near the seepage line. In the case of the application of the signal S6 (Figure 7.21 a), the effective stresses in the basin fall to zero in a band which is located about 25 m upstream of the embankment. Finally, in the case of the application of the S7 signal (Figure 7.20 a), after 28 seconds from the start of the earthquake, three small areas of degradation of the effective stresses are generated in the basin and a slightly larger one at the foot of the embankment.

The results obtained in terms of effective stress decay inside the tailing basin are qualitatively comparable with those presented by Meisheng & Laigui, (2011) that analyzed the behavior during an earthquake of a tailings dam located in the Hebei province (China) with geotechnical characteristics similar to those of the tailing dam analyzed in the present study. The dimensions of the structure presented by Meisheng & Laigui, (2011) are greater than those of the TSF under examination with a height of the dam of about 80 m and a horizontal projection of about 160 m, however, the slope of the banks is comparable to about 1/2. Seismic inputs are not clearly defined so it was not possible to compare this aspect. Similar results are also presented by Zardari

et al. (2017) who studied the seismic behavior of the Aitik tailings dam built with the upstream method in Sweden. Also, in this case the dimensions of the Aitik dam are much greater with a height of about 75 m and a horizontal projection of the bank of about 300 m. Since Sweden is a low seismicity country, the analyzes were conducted with reference to a Swedish earthquake of magnitude 3.6 called the normal case and with reference to an earthquake that occurred in the United States of magnitude 5.8 called the extreme case. The results in terms of liquefaction are reported with reference only to the extreme case which is comparable to the S7 signal used in these analyses.

Regarding shear strain, the greatest values ($\gamma \approx 2x10^{-2}$) were recorded 10, 8 and 22 seconds after the application of signals S1, S2 and S6 (Figures 7.16 b, 7.17 b and 7.21 b). In all three cases, the areas with the greatest shear strains are concentrated at different depths of the embankment body. The maximum shear strains reached as a result of applying signals S3, S4 and S7 are smaller, taking values of $\gamma \approx 1x10^{-2}$ (Figures 7.18 b, 7.19 b and 7.22 b). The results in terms of magnitude and spatial distribution of the shear strains are qualitatively comparable to those proposed in the work by Barrero et al. (2015) in which a tailings dam with similar dimensions to the examined one was modeled with SANISAND. In this case the earthquake considered has a magnitude of 7 and a peak ground acceleration of 0.26 [g]. Similar results are also reported by Nejad et al. (n.d.) where the upstream tailing dam Bobadil in Tasmania with dimensions quite similar to the present case is analyzed. From the little information available it would seem that the seismic signal used for the analysis is comparable with the seven signals presented in the previous paragraph. Table 7.4 summarizes the maximum vertical and horizontal displacements of the far-right node on the crest of the bank. This node was chosen because from the analysis of the deformation fields it appears to be the one that undergoes the greatest displacements and because it can be considered very representative of the deformation situation of the structure.

Table 7.4: *Vertical and horizontal displacement of the upper node of the crest.*

Signal	Vertical displacement y [cm]	Horizontal displacement x [cm]
S1	-40	-2
S2	-22	0
S3	-32	-3
S4	-32	1
S5	-14	-2
S6	-19	-1
S7	-14	0

From the analysis of Table 7.4 it is possible to deduce that the component with the greatest displacements is the vertical one, ranging from a minimum of 14 cm (signals S5 and S7) to a maximum of 40 cm (signal S1). The maximum settlement does not correspond to the signal with the maximum peak velocity (S2) and this is probably because not only the maximum peak plays a role with respect to the response of the system but also the duration and the frequency content. The displacements in the horizontal component, on the other hand, are minor and in some cases even null (signals S2 and S7), and reach a maximum of 2 cm (signals S2 and S7). The vertical

displacements are always downwards, as indicated by the negative values. From the observation of section c) of Figures from 7.16 to 7.22 it is possible to deduce that the movement of the system is concentrated in the slope area with the greatest displacements in the crest. In some cases (signals S1, S2 and S3) a bulging in the area close to the foot of the slope is more accentuated (Figures 7.16, 7.17 and 7.18 c). Comparable results in terms of displacements are reported in the works by Nejad et al. (n.d.), Chakraborty & Choudhury (2011), Barrero et al. (2015), Ishihara et al. (2015) and Vargas (2019). In five nodes of the model, two on the dam bank (nodes 123 and 1267), one on the dam crest (node 1335) and two in the basin (nodes 160 and 1038) acceleration time histories were recorded. The presentation of the records in Figure 7.12 is restricted to signals S5 and S6 that are quite different in terms of signal shape and frequency content so that they can be considered representative of different seismic loading conditions.

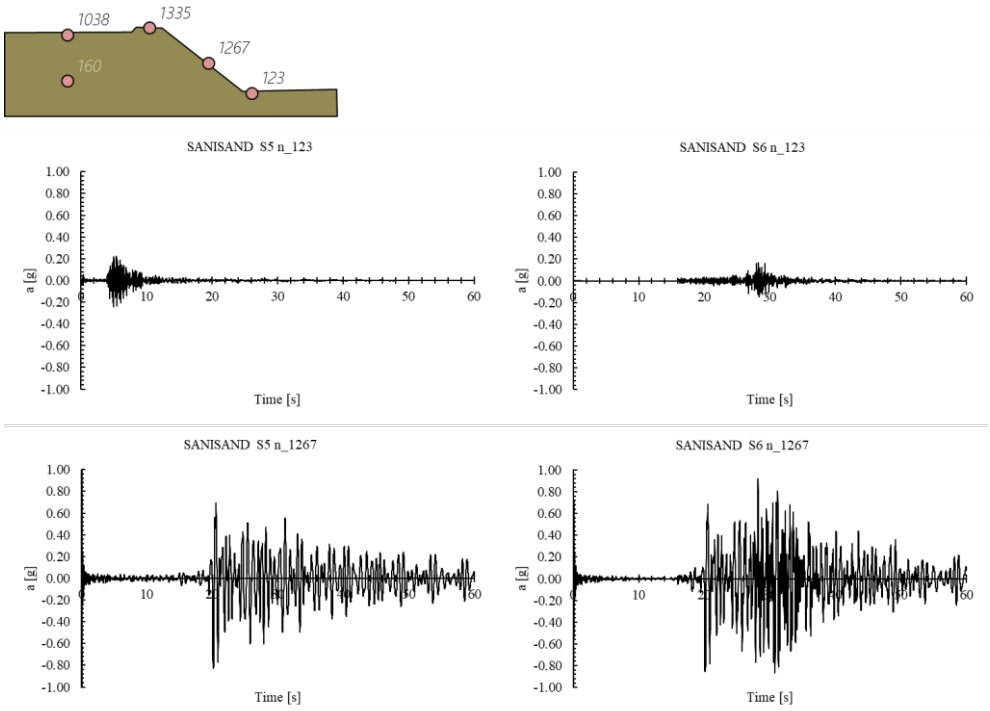

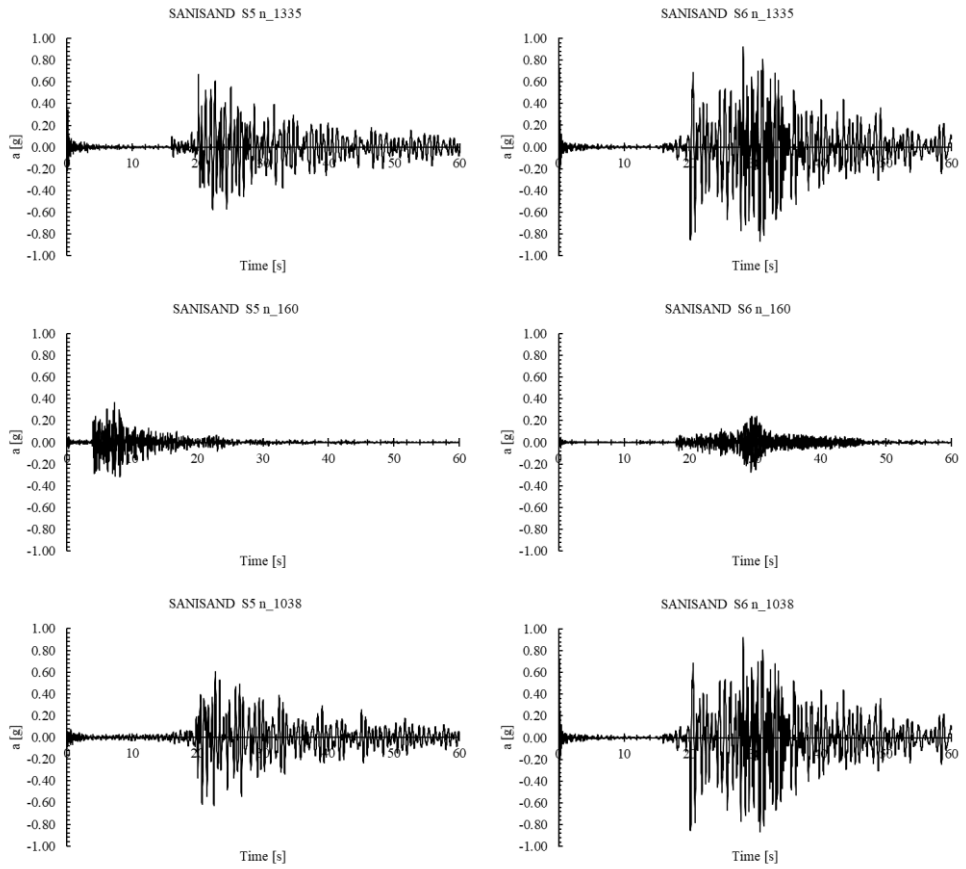

Figure 7.23: *S5 and S6 acceleration time histories for SANISAND model*

From the analysis of the signals, it can be deduced that the recordings at nodes 123 and 160 positioned at lower altitudes compared to the foundation ground do not undergo considerable amplification compared to the input signals while the signals recorded at nodes 1267, 1335 and 1038 are affected by considerable amplification effects. These results differ from those found in the work presented by Ishihara et al. (2015) and in which two tailings dams in Japan were studied. Therein the nodes located at higher altitudes showed a deamplification effect compared to those at the foot of the slope.

7.7.2. Results attributing PDMY constitutive model to the settling basin material

Figures 7.24 to 730 present the results of the numerical analysis attributing the various seismic inputs and attributing the Pressure Dependent Multi Yield (PDMY) constitutive model to the settling basin material (SBM), the PIMY model to the foundation material (FNM) and the PM4Sand model to the embankment material (ENM). The results are presented in the same way as in the previous paragraph, i.e. in terms of stress decay ζ, shear strain γ and displacements.

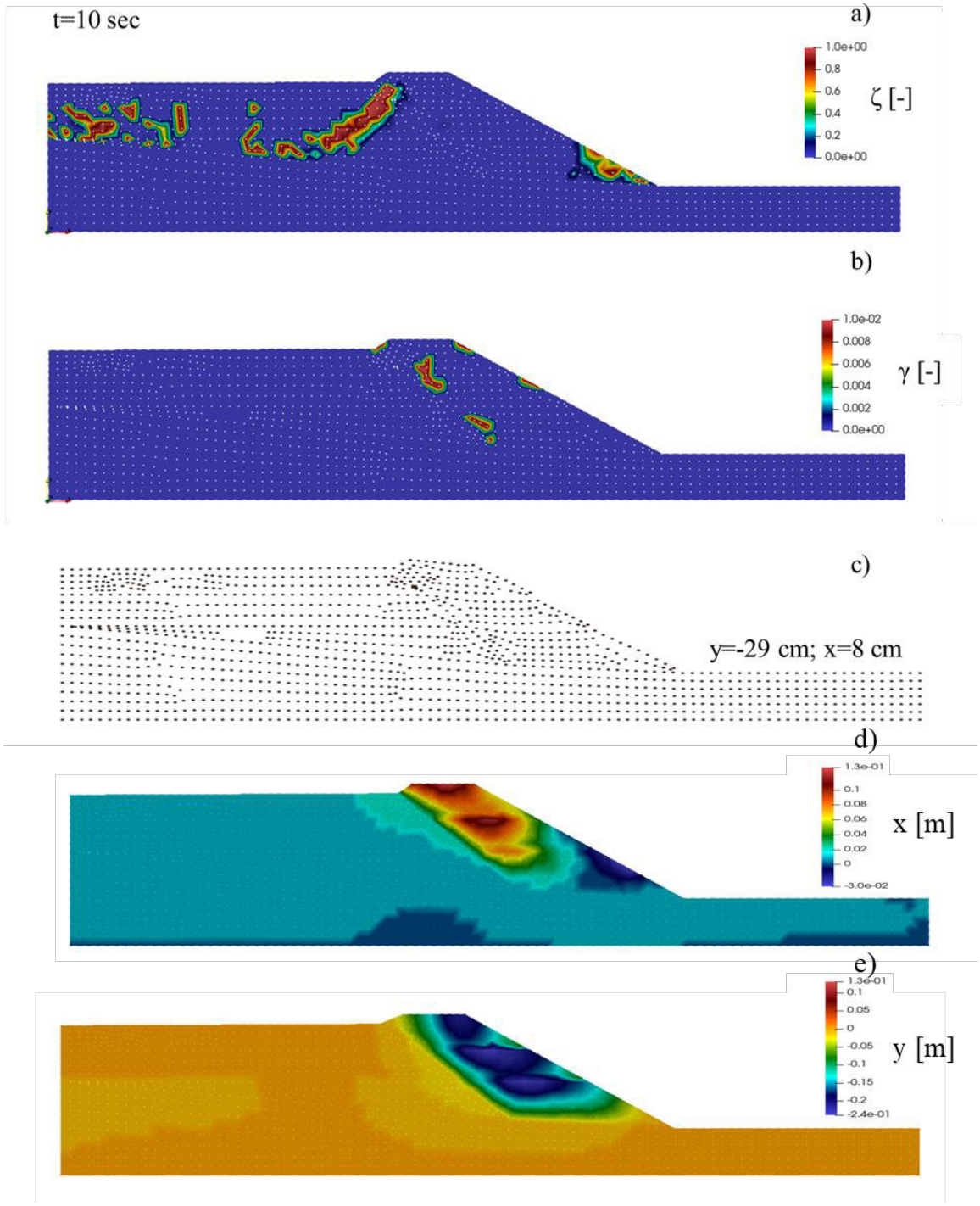

Figure 7.24: *Results from numerical analysis of signal S1 after 10 seconds from beginning of seismic event: a) decay of the effective stresses ζ, b) shear strain γ, c) displacements (the displacements shown in the figure are amplified 10 times), d) horizontal components of displacements, e) vertical components of displacements.*

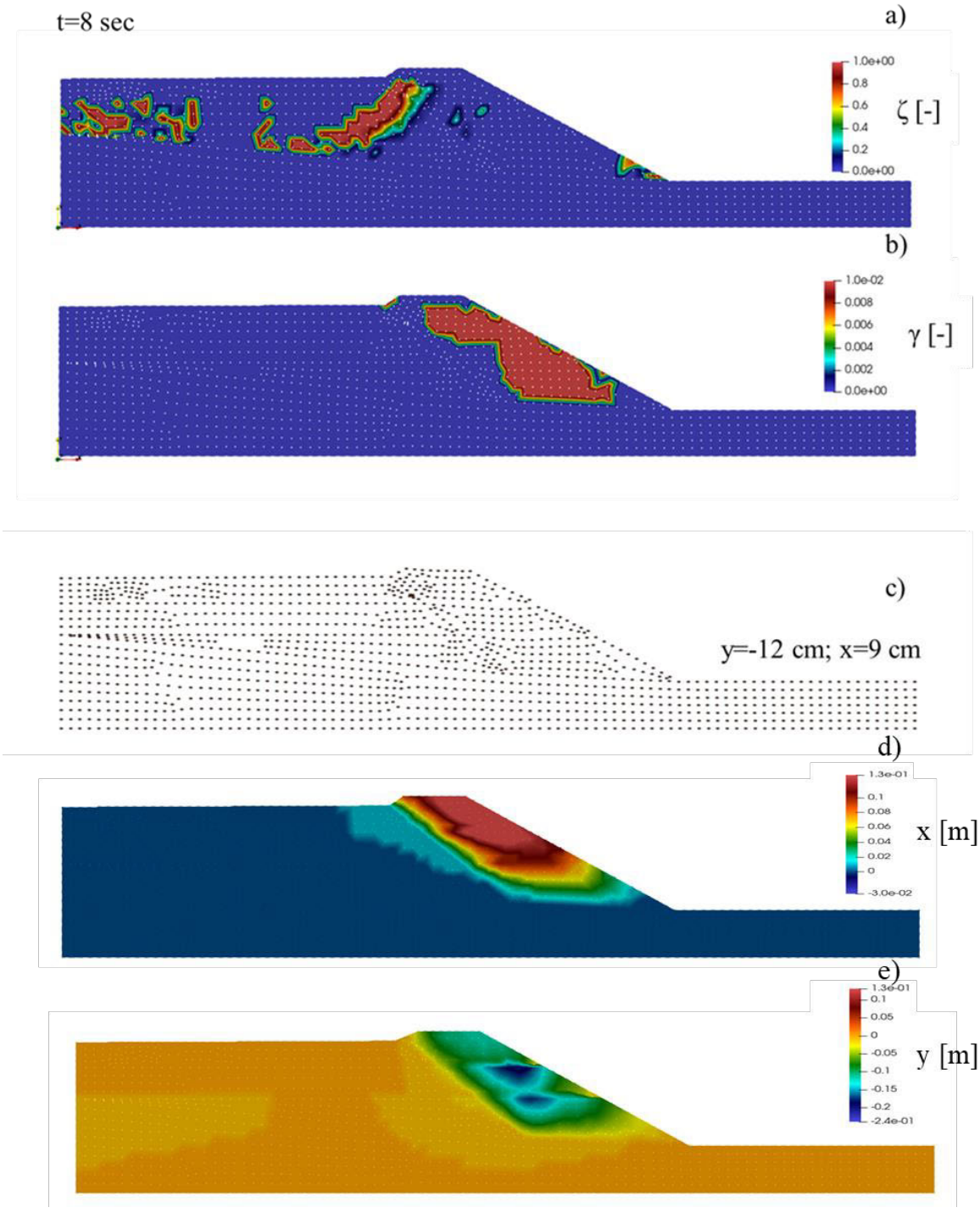

Figure 7.25: *Results from numerical analysis of signal S2 after 8 seconds from beginning of seismic event: a) decay of the effective stresses ζ, b) shear strain γ, c) displacements (the displacements shown in the figure are amplified 10 times), d) horizontal components of displacements, e) vertical components of displacements.*

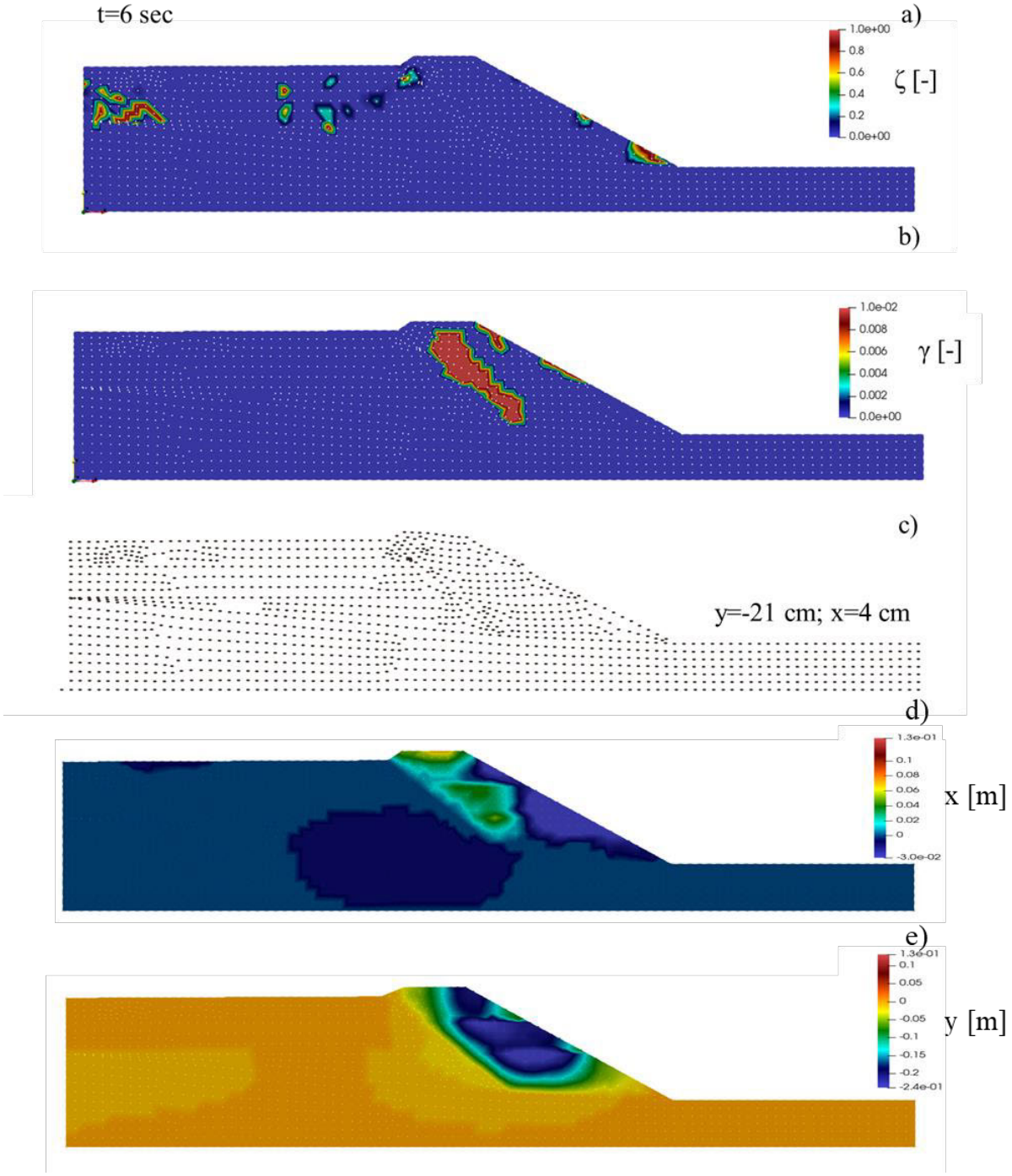

Figure 7.26: *Results from numerical analysis of signal S3 after 6 seconds from beginning of seismic event: a) decay of the effective stresses ζ, b) shear strain γ, c) displacements (the displacements shown in the figure are amplified 10 times), d) horizontal components of displacements, e) vertical components of displacements.*

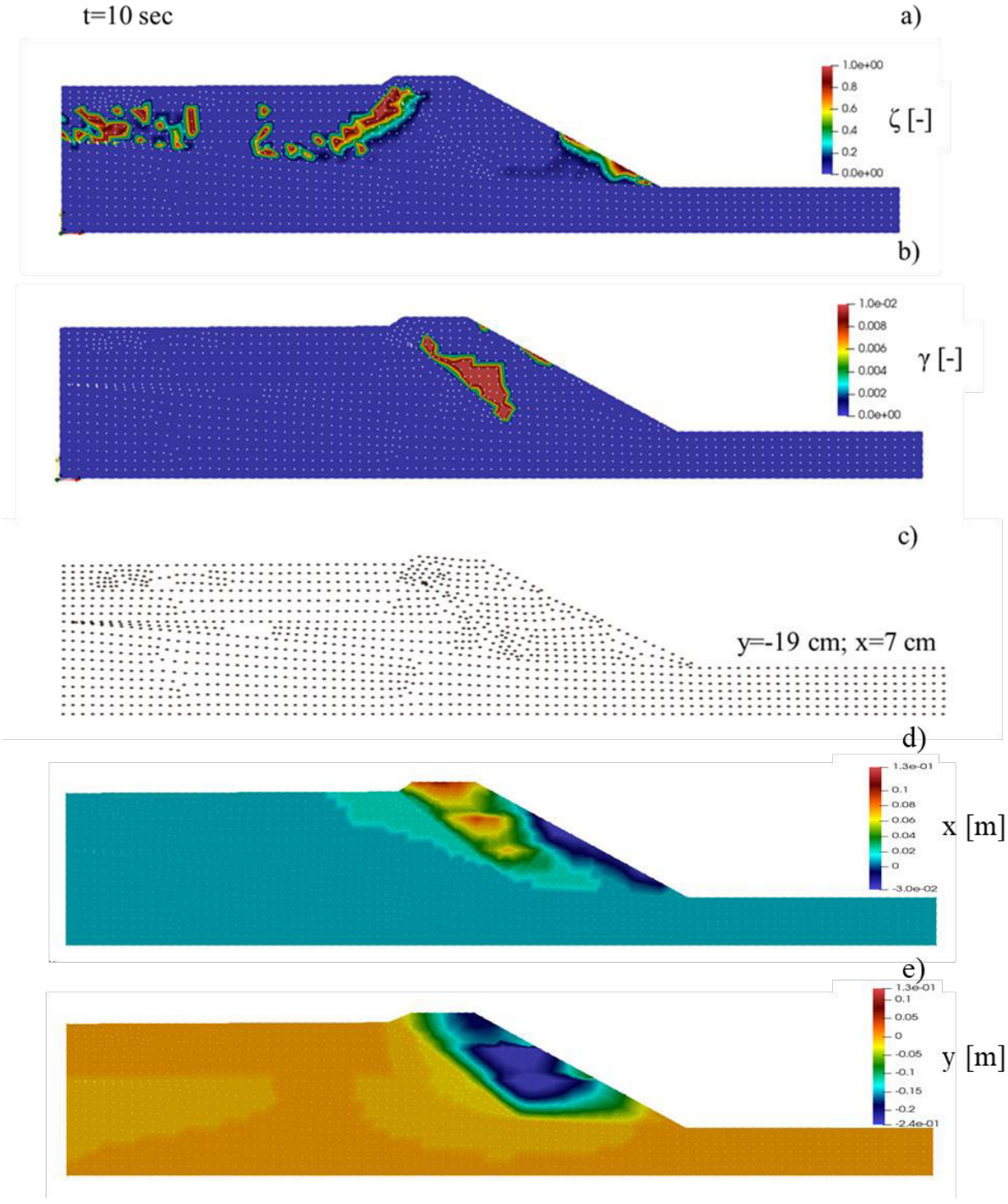

Figure 7.27: *Results from numerical analysis of signal S4 after 10 seconds from beginning of seismic event: a) decay of the effective stresses ζ, b) shear strain γ, c) displacements (the displacements shown in the figure are amplified 10 times), d) horizontal components of displacements, e) vertical components of displacements.*

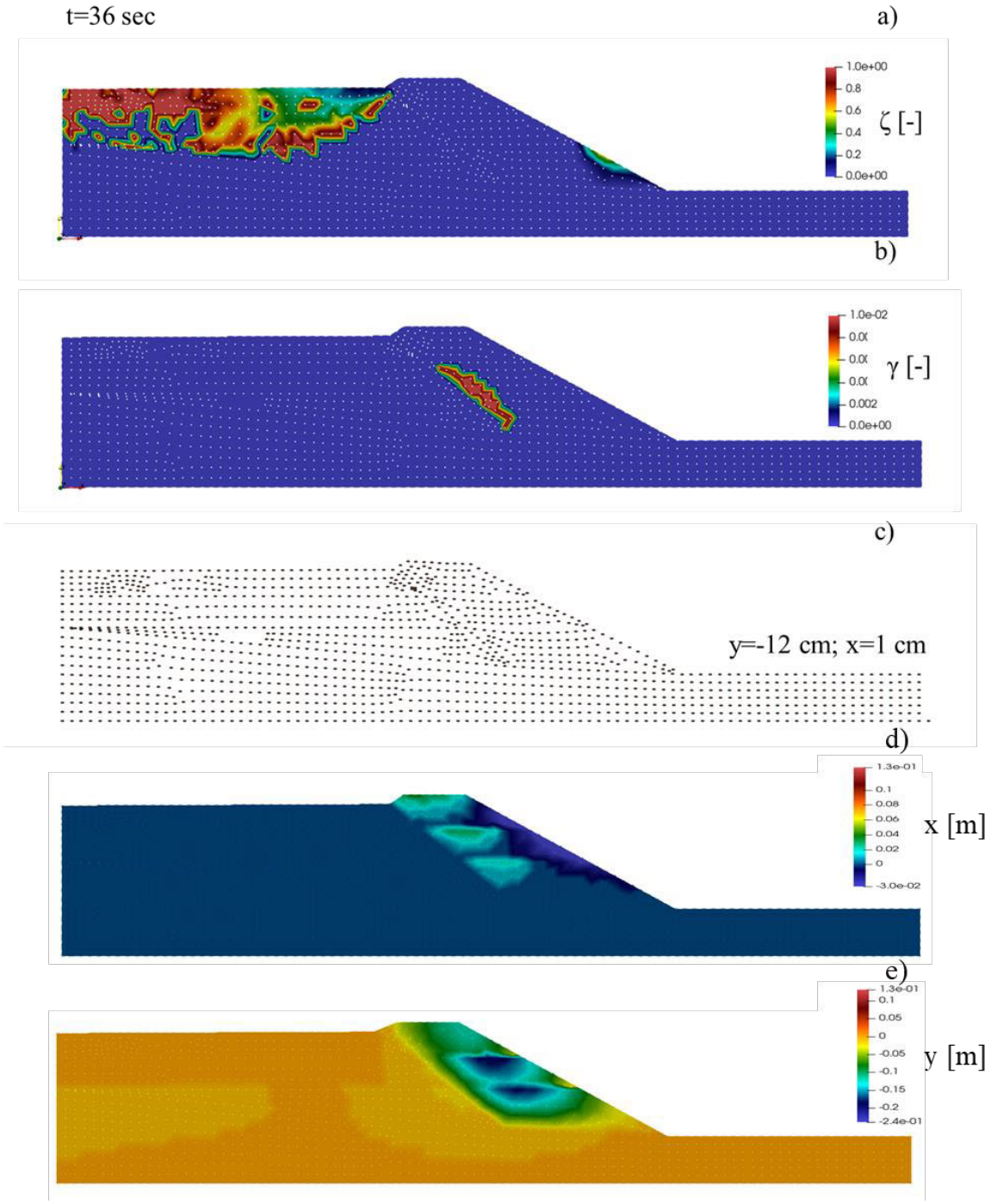

Figure 7.28: *Results from numerical analysis of signal S5 after 36 seconds from beginning of seismic event: a) decay of the effective stresses ζ, b) shear strain γ, c) displacements (the displacements shown in the figure are amplified 10 times), d) horizontal components of displacements, e) vertical components of displacements.*

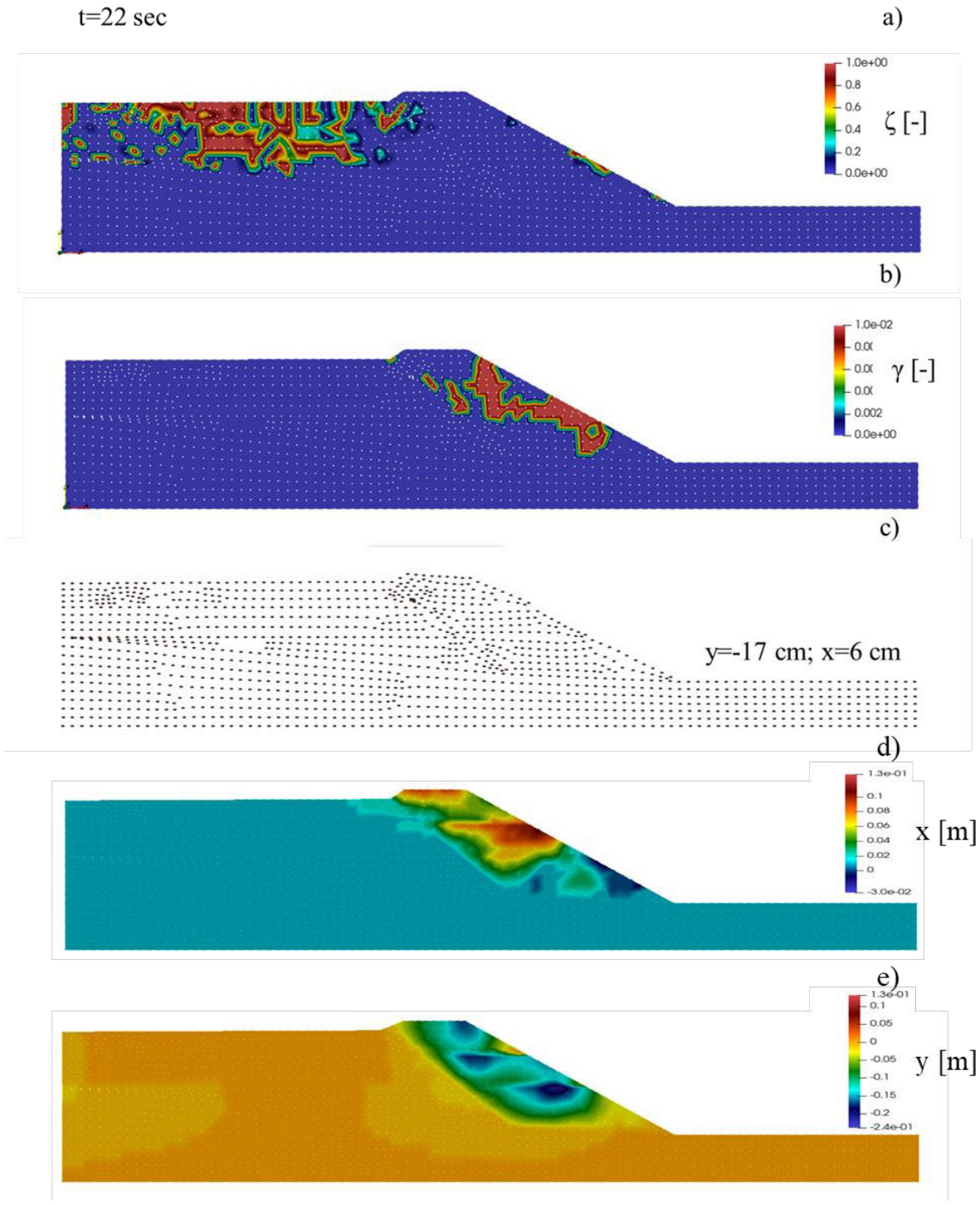

Figure 7.29: *Results from numerical analysis of signal S6 after 22 seconds from beginning of seismic event: a) decay of the effective stresses ζ, b) shear strain γ, c) displacements (the displacements shown in the figure are amplified 10 times), d) horizontal components of displacements, e) vertical components of displacements.*

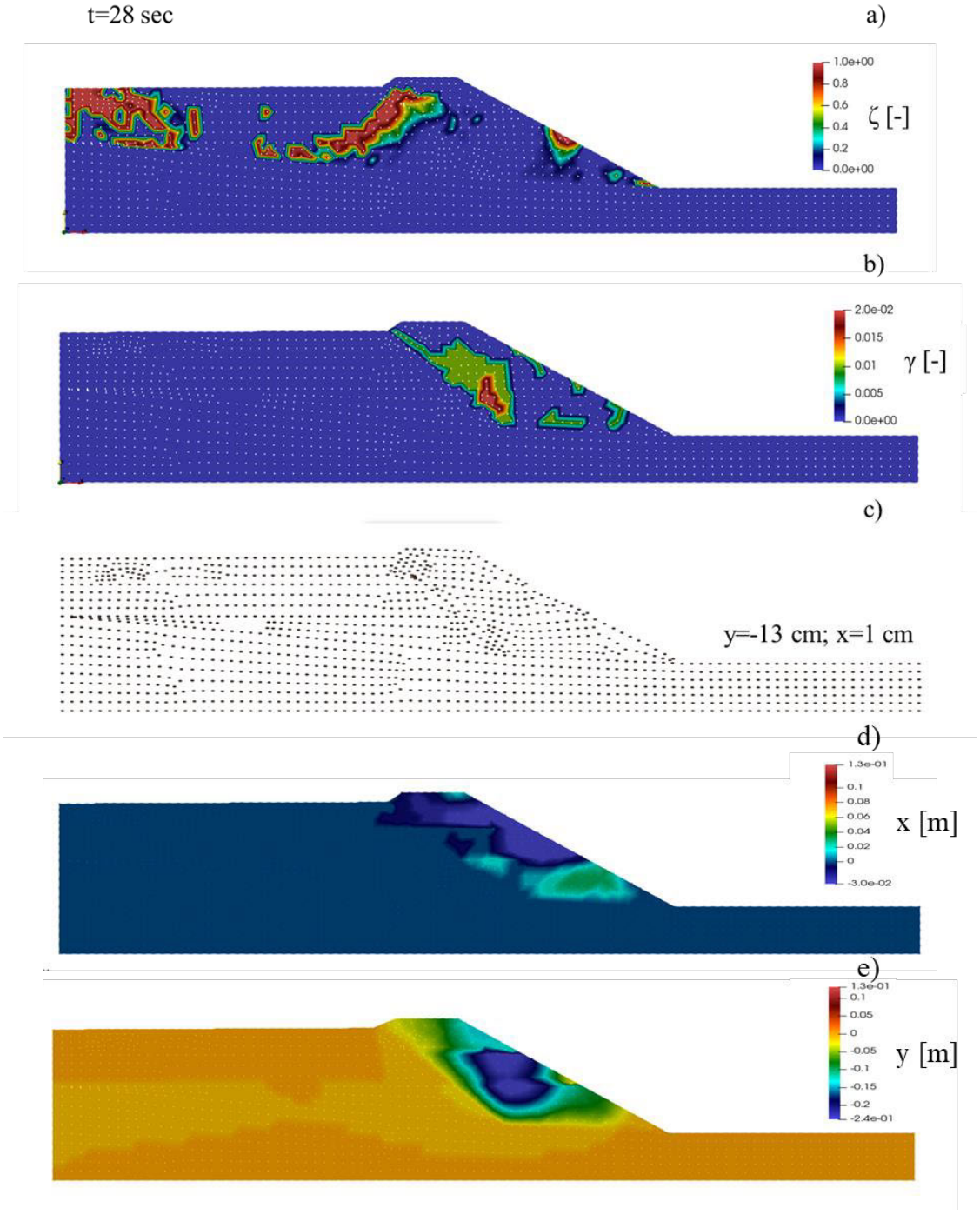

Figure 7.30: *Results from numerical analysis of signal S7 after 28 seconds from beginning of seismic event: a) decay of the effective stresses ζ, b) shear strain γ, c) displacements (the displacements shown in the figure are amplified 10 times), d) horizontal components of displacements, e) vertical components of displacements.*

From the observation of section a) of Figures 7.24 to 7.30 it is possible to deduce that the complete reduction of the effective stresses to 0 (ζ=1) occurs to a greater extent in the tailing dam basin and in a smaller extent on the embankment comparable to the results obtained by Liu et al. (2007). In particular, it is possible to observe that the results obtained from signals S1, S2, S4 and S7 (Figures 7.24, 7.25, 7.7.3.4 and 7.30 a) after 10, 8, 10 and 28 seconds respectively from the onset of the earthquake are similar with a rather large zone of zero effective stresses in the basin and a small area near the foot of the embankment. Similar results are also obtained with signals S5 and S6 (Figures 7.28 and 7.29 a) in which the basin area is mainly involved. The results obtained from signal S3 (Figure 7.26 a) are different from the others with much smaller decay areas in the basin, while that at the foot of the embankment. For all signals the shear strains are concentrated in the embankment area. The S7 signal (Figure 7.30 b) causes the greatest shear strain ($\gamma \approx 2x10^{-2}$ [-]) while for the other signals the maximum shear strain reached is around $\gamma \approx 1x10^{-2}$ [-]. Noteworthy is the extension of the shear deformation caused by signal S2 (Figure 7.25 b) which almost entirely involves the area occupied by the embankment (≈540 m^2). Table 7.5 summarizes the maximum vertical and horizontal displacements of the far-right node on the crest of the bank.

Table 7.5: *Vertical and horizontal displacement of the upper right node of the crest.*

Signal	Vertical displacement y [cm]	Horizontal displacement x [cm]
S1	-29	8
S2	-12	9
S3	-21	4
S4	-19	7
S5	-12	1
S6	-17	6
S7	-13	1

From the analysis of Table 7.5 it is possible to note that in the vertical direction the displacements are directed downwards with a minimum settlement of 12 cm (signals S2 and S5) and a maximum settlement of 29 cm (signal S1). The horizontal component of the displacements is smaller than the vertical one with a minimum of 1 cm (signals S5 and S7) and a maximum of 9 cm (signal S2). The general movement of the slope mass is downwards and outwards.

Also with PDMY the acceleration time histories have been recorded at the same nodes for the same seismic signals (Figure 7.31).

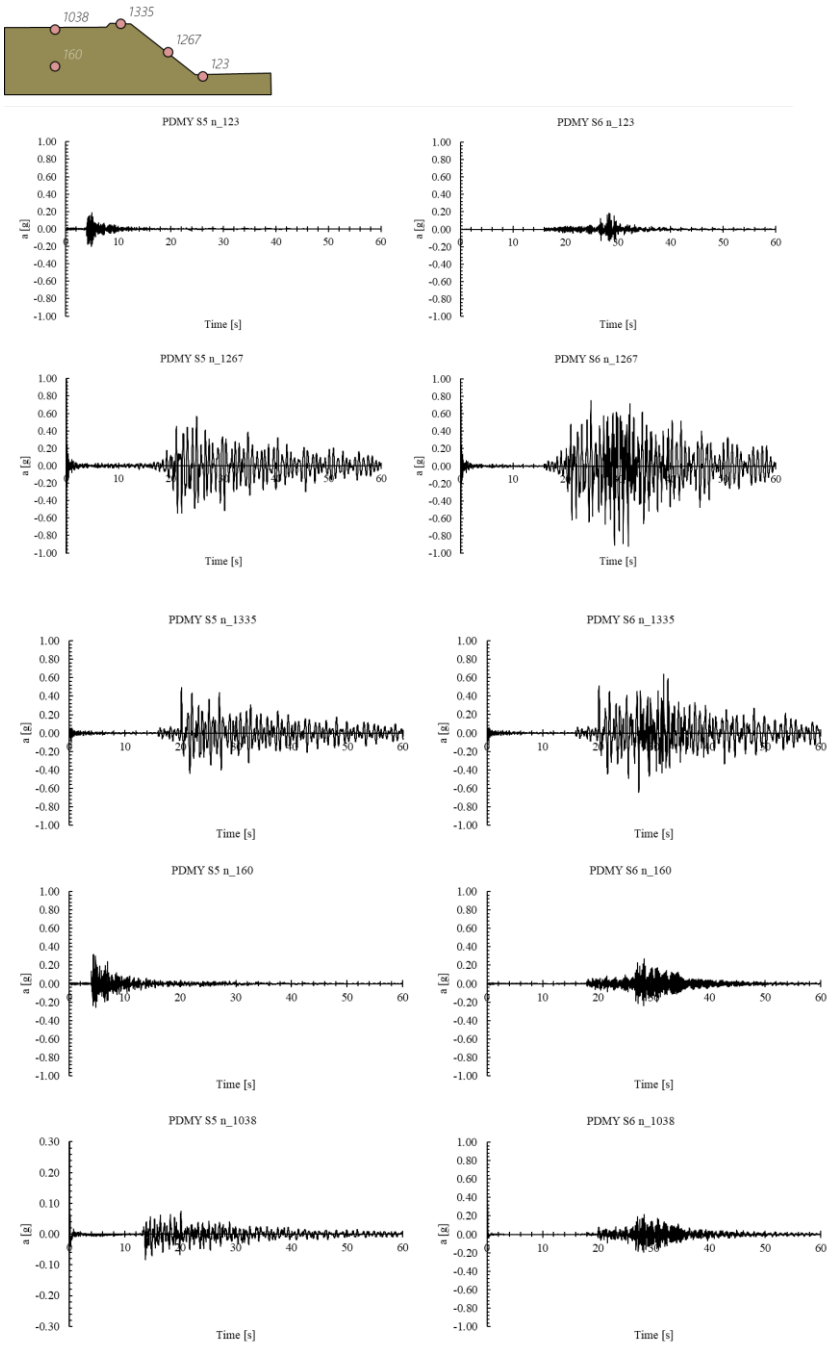

Figure 7.31: *S5 and S6 acceleration time histories for PDMY model*

The results obtained are comparable to the ones obtained with the SANISAND model.

7.7.3. Comparison between the results obtained with the two constitutive models

The results obtained attributing the two different constitutive models (SANISAND and PDMY) to the settling basin material have been compared in terms of the parameters discussed in the two previous sections. As regards the decay of the effective stresses, indicated through the magnitude of the ζ parameter (Figures 7.16-7.30 a), it can be noted that the results are very similar on the embankment area for the various signals and with both models assumed for the settling basin material. In all cases, the embankment material was modeled with the PM4Sand constitutive model; therefore, it is plausible that the results on this area are similar. The complete decay of the effective stress (ζ=1) is concentrated in most cases in superficial areas close to the foot of the slope. Exceptions to this trend are the results obtained with signals S5, S6 and S7 model (Figures 7.20, 7.21 and 7.22 a) in which these phenomena appear at higher altitudes. A possible explanation of the localization of the effective stress decay at the surface close to the foot of the dam is the way the groundwater plane has been assumed, which leads to an accentuation of interstitial pressures due to seepage and hydrostatic pressure already before the earthquake. As far as the basin area is concerned, instead, the results obtained with the two constitutive models are quite different. As described in detail in Paragraph 7.7.1, in the case where the SANISAND constitutive model has been assumed for the tailings materials, the areas with zero effective stress have different extensions and are concentrated near the superficial part of the pond (Figure 7.16-7.22 a). Instead, in the simulations with the PDMY model, ζ =1 occurs in an area close to the border between the embankment and the basin with an elongated shape in counter-slope with respect to the slope of the embankment. In addition, other small areas that are distributed in depth of the basin reach zero effective stress (Figures 7.24-7.30 a). This could be due to the fact that the basin area under the embankment has undergone some kind of compaction due to the load of the dam and is therefore less prone to trigger liquefaction phenomena. Table 7.5 shows the ratio of the area in which the effective stresses reduced to zero with respect to the total area of the dam and the basin as a percentage.

Table 7.5: Ratio between the e*ffective stresses reduced to zero area respect to the total area of the dam (ENM) and the basin (SBM).*

SANISAND		PDMY	
S1	[%]	S1	[%]
ENM	7	ENM	6
SBM	4	SBM	8
S2	[%]	S2	[%]
ENM	24	ENM	24
SBM	15	SBM	15
S3	[%]	S3	[%]
ENM	22	ENM	4
SBM	14	SBM	3
S4	[%]	S4	[%]
ENM	7	ENM	6
SBM	4	SBM	10
S5	[%]	S5	[%]

SANISAND		PDMY	
ENM	0	ENM	4
SBM	4	SBM	51
S6	[%]	S6	[%]
ENM	6	ENM	2
SBM	4	SBM	55
S7	[%]	S7	[%]
ENM	6	ENM	6
SBM	3	SBM	14

Concerning the results in terms of shear deformations, in the case of the use of the PDMY model, the maximum values, which lie around $\gamma \approx 1x10^{-2}$ [-], are mainly concentrated in the embankment, particularly close to the boundary between the embankment and the basin. In the case of the SANISAND model, maximum shear strains are also mainly recorded in the embankment area but, in some cases, significant average shear strains also involve the basin area. Finally, as regards the nodal displacements, by comparing Tables 7.4 and 7.5 in which the vertical and horizontal components of the displacement of the extreme right node of the embankment crest are reported, it is possible to observe that in both cases the vertical component of the displacement is always directed downwards with slightly higher values in the case of SANISAND but, in any case, comparable and in the order of tens of centimeters. As regards the horizontal component, however, in the case of SANISAND the absolute values are always lower and, in some cases, they have a negative sign indicating a displacement to the right. Although one would expect an outward displacement of these nodes (as is typical of landslides), the absolute value of this displacement is practically negligible with a maximum of only 3 cm. In the case of PDMY, on the other hand, the horizontal component of the displacements is always directed outwards with a maximum value of 9 cm. The observation of the deformed configurations of the structure (Figures 7.16-7.22 c) indicates that the main movements occur on the slope with cases in which they are more concentrated on the crest and cases in which they are instead more present in the center.

Altogether, the differences in the results, which have been found mainly in the basin area using the two constitutive models, demonstrate the great level of uncertainty that affects the numerical analysis. However, the repeated occurrence of complete effective stress decay (especially on the embankment), the level of shear strain occurring in the boundary between the basin and the embankment, and the deformations of the structure indicate the high probability of failure of the analyzed system subject to an earthquake with the characteristics than those used in the simulations. Sensitivity analysis for each constitutive model could help in choosing the most appropriate model. However, FEM analyses with advanced constitutive models allow to obtain very important information on the seismic behavior of the structure compared to simpler methodologies such as LEM.

Bibliography

ASCE 95, 859–877 (1969).

Barrero, A. R., Taiebat, M., & Lizcano, A. (2015). Application of an advanced constitutive model in nonlinear dynamic analysis of tailings dam. In 68th Canadian Geotechnical Conference (pp. 20-23).

Chakraborty, D., & Choudhury, D. (2011). Seismic behavior of tailings dam using flac3d. In Geo-Frontiers 2011: Advances in Geotechnical Engineering (pp. 3138-3147).

Consiglio Superiore dei Lavori Pubblici (2014). DM 26 giugno 2014. Norme tecniche per la progettazione e la costruzione degli sbarramenti di ritenuta (dighe e traverse). Gazzetta ufficiale n. 156 dell'8 luglio 2014.

Consiglio Superiore dei Lavori Pubblici (2018). DM 17 gennaio 2018. Norme tecniche per le costruzioni. G.U. n.42 del 20 febbraio 2018

Consiglio Superiore dei Lavori Pubblici (2019). Circolare 21 Gennaio 2019, n. 7 C.S.LL.PP. "Istruzioni per l'applicazione dell'«Aggiornamento delle "Norme tecniche per le costruzioni"» di cui al decreto ministeriale 17 gennaio 2018.". Gazzetta Ufficiale n. 35 del 11 febbraio 2019 (Suppl. Ordinario n. 5).

Forcellini, D., & Tarantino, A. M. (2013). Countermeasures assessment of liquefaction-induced lateral deformation in a slope ground system. Journal of Engineering, 2013, 1-9.

Gorini, D. N (2023, February 7-10). Coupled modelling of soil-structure domains. Soil-structure interaction in OpenSeesstrategies, applications and perspectives (Presentation). Winter school, 7-10 February 2023.

Henderson, A.: ParaView Guide, A Parallel Visualization Application. Kitware Inc. (2007).

Hwang, Y. W., & Rathje, E. M. (2023). Insights into seismic slope deformation patterns using finite element analysis. Soil Dynamics and Earthquake Engineering, 164, 107660.

Ishihara, K., Ueno, K., Yamada, S., Yasuda, S., & Yoneoka, T. (2015). Breach of a tailings dam in the 2011 earthquake in Japan. Soil Dynamics and Earthquake Engineering, 68, 3-22.

Lai, C. G., Zuccolo E (2017). Prosecuzione delle attività di definizione di input sismici sismocompatibili e spettrocompatibili per i comuni della regione Toscana. Scientific Report

Liu, H. X., Li, N., Liao, X., Wu, C. S., & Pan, X. D. (2007). Effective stress analysis method of seismic response for high tailings dam. Journal of Central South University of Technology, 14(1), 129-134.

Lysmer, J., & Kuhlemeyer, R. L. (1969). Finite dynamic model for infinite media. Journal of the engineering mechanics division, 95(4), 859-877.

Ma, X.W., Zhao, G.Q., Sun, L.: AUTOMESH-2D/3D: robust automatic mesh generator for metal forming simulation. Mater. Res. Innovations 15(s1), s482–s486 (2011)

Machaček, J., Triantafyllidis, T., & Staubach, P. (2018). Fully coupled simulation of an opencast mine subjected to earthquake loading. Soil Dynamics and Earthquake Engineering, 115, 853-867.

Masoudi, M., & Vadeghani, A. G. (2018 November). Earthquake response of slopes under massive loads. 9-th International conference on Seismology & Earthquake Engineering. International Institute of Earthquake Engineering and Seismology (IIEES).

Mazzoni, S., McKenna, F., Scott, M. H., & Fenves, G. L. (2006). OpenSees command language manual. Pacific Earthquake Engineering Research (PEER) Center, 264(1), 137-158.

McGann, C., Arduino, P., & Mackenzie-Helnwein, P. (n.d.-b). Initial state analysis wrapper. https://opensees.berkeley.edu.https://opensees.berkeley.edu/wiki/index.php/InitialStateAnalysisWrapper

McGann, C., Arduino, P.: Dynamic 2D Effective Stress Analysis of Slope. OpenSees user manual (2011).

Meisheng, F., & Laigui, W. (2011, April). A tailings dam dynamic stability study based on numerical simulation. In 2011 International Conference on Consumer Electronics, Communications and Networks (CECNet) (pp. 1002-1005). IEEE.

Nejad, B. G., Taiebat, H., Dillon, M., & Seddon, K. (n. d.). Numerical Modelling of Seismic Liquefaction for Bobadil Tailings Dam.

Vargas, C. O. (2019, November). Analysis and Seismic Design of Tailings Dams and Liquefaction Assessment. In American Conference on Soil Mechanics and Geotechnical Engineering (Vol. 7, p. 392).

Vick, S. G. (1990). Planning, design, and analysis of tailings dams. BiTech Publishers Ltd.

Zardari, M. A., Mattsson, H., Knutsson, S., Khalid, M. S., Ask, M. V., & Lund, B. (2017). Numerical analyses of earthquake induced liquefaction and deformation behaviour of an upstream tailings dam. Advances in Materials Science and Engineering, 2017, 1-12.

8. Concluding remarks

In this doctoral thesis, the behavior of tailings dams under seismic loading conditions has been investigated. The study of this complex and highly relevant topic has been tackled on different levels in terms of scale and detail. The thesis first introduces the more general aspects of these types of structures by defining the peculiarities that characterize them, and the aspects that distinguish them from other types of engineering structures. A non-negligible aspect of these structures is their susceptibility to failure that, considering the frequency of failure events in the past, should be evaluated with great care, especially under seismic loading conditions. Over time, many different causes of failure of these structures have been documented. A cataloguing of these failures has been provided by ICOLD (ICOLD, U. 2001) and can be summarized as: slope instability (SI), seepage (SE), Tailings storage facilities and failure mechanisms foundation (FN), overtopping (OT), structural (ST), earthquake (EQ), mine subsidence (MS), erosion (ER), unknown (U). An in-depth treatment of this topic is provided in Chapter 2.

By cross-referencing the data collected from databases of various sources (ICOLD, WISE, World mine tailings failures-from 1915, and CSP2 Rico et al. 2008; Azam & Li 2010; Lyu et al. 2019; Clarkson & Williams 2021; Piciullo 2022; Stark 2022), it was possible to determine that in as many as 33 cases the causes of failure were classified as unknown. Through an in-depth literature research, it was possible to find a possible explanation for the failure in 11 cases that were classified as unknown (Table 2.2). However, further research would be necessary to better specify the dynamics of the identified accidents and possibly define the reason for the failure of the 22 remaining cases. Failure cases due to seismic liquefaction have been noticed since the recording of such events started (Chapter 2); however, it would be very useful to increase knowledge on the mechanisms of these collapses by means of a back analyses with numerical methods of these known events, which may also serve for the validation of the analyses. An analysis carried out on 24 numerical studies on tailings storage facilities (TSF) concluded that: the longitudinal dimension attributed to the model in most cases is double compared to the horizontal projection of the embankment; that the most-used elements are of the triangular type that in less than half of the studies, the phased construction of the structure is simulated; and that in most cases, the constitutive models used are rather simple and calibrated through literature information rather than on experimental tests conducted on materials collected from the TSF under examination.

A tailings dam located in the National Park of the Metalliferous Hills in southern Tuscany (Italy) has been extensively examined. To the authors knowledge the present work is the only one that addresses the topic of the behavior of a tailings dam subjected to seismic actions for a tailings storage facility located in southern Europe. This is an aspect that certainly contributes in an innovative way to research on the topic. The system consists of three main units with different types of soils, which have been defined as settling basin materials (SBM), embankment materials (ENM), and foundation materials (FNM) (Figure 5.26). Numerous laboratory tests, such as:

classification tests, electron scanning microscope, chemical investigations, and monotonic and cyclic triaxial tests were performed to characterize the embankment and settling basin materials. An innovative method to collect undisturbed samples by freezing with liquid nitrogen has been proposed. The methodology made it possible to collect high quality undisturbed samples at depths not exceeding 1 m from ground level, and the sampling of the specimens was rather complicated and not always successful. It would therefore be desirable to proceed with the development of this technique, perhaps coupling it with soundings, in order to collect samples from greater depths and to study in more detail any changes or processes (e.g. volume change) undergone by the samples during freezing and thawing phases. The mechanical characterization of the basin material was based on the results obtained from four monotonic and cyclic triaxial tests (Chapter 3). Although the results obtained from these tests proved to be of fundamental importance for the definition of resistance parameters and dynamic characteristics of the material, it would be necessary to increase the number of experiments to confirm the results obtained and to investigate the effective homogeneity of the soil in the volume of the basin. It would also be useful to take undisturbed samples from the embankment in order to carry out mechanical characterization tests with devices that allow for tests on soils with large particle size fractions. Another aspect that should be investigated is the behavior of unsaturated or partially saturated material above the water table. The geotechnical model was built by combining the information obtained through the own experimental tests with those collected through an in-depth study of the documentation deriving from numerous investigations carried out on the structure since 2007. However, to improve the knowledge of the stratigraphy and materials, it would be necessary to carry out further investigations. In particular, it would be necessary to drill further boreholes of at least 50 m depth, especially in the basin area equipped for down hole tests. From the boreholes it would be desirable to collect undisturbed samples at different depths (by coupling the freezing method proposed in Chapter 3 to the boreholes), in order to directly verify the homogeneity of the mechanical characteristics of the basin materials. The boreholes should be extended to a depth of at least 50 m for two reasons: first, to be able to collect samples of the foundation material of which little information is currently available, and second, to try to reach the seismic bedrock through down hole tests. As previously mentioned, in order to more accurately characterize the structure, it would also be of great importance to be able to perform laboratory tests on the materials that constitute the embankment, whose mechanical characteristics have been estimated through documented of field tests (SPT, CPTu and Down Hole).

Four different constitutive models were used to describe the mechanical behaviour of the different materials in the numerical analyses. To the soils belonging to the so-called foundation layer (FNM), the constitutive model Pressure Independent Multi Yield (PIMY) was attributed, while the PM4Sand model was used for the embankment materials (ENM),. Two different constitutive models, SANISAND and Pressure Dependent Multi Yield (PDMY), have been attributed to the materials of the settling basin (SBM). This led to a doubling of the number of analyses, but allowed us to examine the differences in the results from the two models. The input parameters were determined on the basis of the results obtained with laboratory and field tests, through values defined in the literature and with iterative procedures. The parameters were then

validated by comparing the results of element test simulations with the results of the real tests in terms of stress-strain relationships, effective stress paths and pore pressure increase (Figures 6.10 and 6.12). The evaluation was done qualitatively through the visual comparison of the graphs obtained from the simulations and the real tests, as done by numerous authors before (Elgamal et al. 2003; Yang et al. 2003; Dafalias & Manzari 2004; Taiebat et al. 2010; Boulanger & Ziotopoulou 2017; Mandokhail et al. 2017; Beaty et al. 2018; Wichtmann et al. 2019; Flora et al. 2020; Ismael 2020; Banerjee et al. 2021; Wang et al. 2022). Based on the comparison of methods proposed by various authors, in the current thesis for each model a semi-innovative and efficient calibration methodology has been developed. To the authors knowledge the literature, despite numerous works partially or completely dedicated to the calibration of constitutive models, lacks proposals for clear and defined methodologies for the calibration of the parameters. In this thesis, a complete and structured procedure is therefore provided to the scientific community to identify and validate the input parameters of the constitutive models used.

The numerical analyses were performed with the open-source software OpenSees. Also the calibration of the material constants of the constitutive models, especially as regards the iterative procedures, was conducted through element test simulations with OpenSees. Many authors carry out the calibrations with different software specifically developed for element test simulations, because the conduction of element tests with on OpenSees is quite complex. In this doctoral thesis, perform also the element tests with OpenSees, because the use of different software can lead to differences (albeit minimal) in the definition of the input parameters.

The behavior of the structure under seismic conditions was analyzed through finite element numerical analyses. The results have been reported in terms of decay of the effective stresses caused by the increase of pore water pressures during the seismic loading through a quantity termed ζ. If the value of ζ reaches unity, it means that the effective stresses have become zero with consequent complete loss of the shear resistance of the material. Furthermore, the results in terms of shear deformations and displacements of the structure have been reported. First, the results obtained the SANISAND constitutive model by assigning to the settling basin materials (SBM) are reported (Figures 7.9 to 7.15). From an examination of the results, it was possible to deduce that, with all seven seismic input signals, being typical for the region and an earthquake of 2475 years annuality, there is a complete loss of the effective stresses in rather superficial areas of the settling basin and at the foot of the embankment. The fact that the effective stress decay is concentrated in the most superficial part of the embankment foot can be explained by the fact that considerable pore pressures are already present in this area before the seismic shaking, due to the slope conformation and the groundwater level and due to relatively low confinement. As far as the basin area is concerned, the decay of the effective stresses is concentrated on the surface at a certain distance from the dam. This could be explained by the fact that the confining pressure is lower in these areas. Furthermore, as far as shear deformations are concerned, these are mostly concentrated in the embankment body with maximum values equal to $\gamma \approx 2 \times 10^{-2}$ [-]. While the trend of the displacements was that of an outward and downward slope mass movement with, the maximum displacement

values recorded at the outermost node of the dam crest were obtained for the vertical direction, reaching in one case 40 cm settlement, while the horizontal displacements were negligible. The movement encountered in the numerical simulations is qualitatively expected for a structure with the present geometric characteristics.

The results obtained by attributing the PDMY constitutive model to the materials of the settling basin (SBM) then reported afterwards. The loss of the effective stresses (ζ=1) occurred locally following the application of all the seismic signals, almost always at the foot of the embankment and including large zones of the basin. Also, in this case, the shear deformations were concentrated in the embankment with average values equal to $\gamma \approx 1x10^{-2}$ [-] and in one case $\gamma \approx 2x10^{-2}$ [-]. The results in terms of displacements do not differ significantly from those obtained with the SANISAND model, recording a maximum vertical displacement component of 29 cm and a horizontal component of 9 cm. Ultimately, comparing the results obtained by attributing the two different constitutive models, it is possible to conclude that they are comparable in terms of shear strain and displacements, but that they differ in terms of stress aspects, especially in the basin area. These differences can certainly be attributed to the use of the two different constitutive models, underlining the high degree of uncertainty present in the numerical simulations. Further research would be needed to clarify these differences, for example by carrying out a sensitivity analysis that examines how the results change by modifying some input parameters of the two constitutive models.

However, the local occurence of complete loss of effective stress (especially on the embankment), the level of shear strain occurring in the interface between the basin and the embankment, and the deformations of the structure indicate the possible of failure of the analyzed system subject to an earthquake with the characteristics used in the simulations, but these possibility should be better studied with dedicated stability analysis. Therefore, the aim of to preventing the risk of damage to the areas adjacent to the plant, it is therefore necessary to deepen the level of knowledge of the site, in order to be able to carry out increasingly refined analyses that allow the planning of adequate risk mitigation interventions.

As already mentioned, these analyses were conducted with the open-source software OpenSees. This software (like most open-source software) does not include pre-or post- processors; therefore, the generation of the model and the visualization of the results must be carried out either with specifically created tools or with expensive paid programs. As part of this doctoral thesis, programs capable of generating numerical models to be analyzed by OpenSees were developed. These tools, which need to be further developed, can be made available free-of-charge to researchers who study tailings dams. In conclusion, it is challenging to recommend one constitutive model rather than another since each is characterized by a number of strengths and weaknesses. The SANISAND version used is slightly simpler and more intuitive to calibrate than PDMY, but on the other hand it doesn't develop plastic deformation in case of isotropic loading, an aspect that is overcome by the PDMY model. However, versions of SANISAND have been developed that consider this aspect but contain additional parameters to be calibrated and therefore complicate the calibration and validation procedure. Furthermore, SANISAND has been much more used by the

scientific community and therefore there is much more respective literature than for PDMY. This is also because, at least to the author's knowledge, the PMDY model has only been implemented in Opensees while SANISAND is available in numerous commercial software. Finally, the SANISAND constitutive model is framed within the critical state theory, a fundamental characteristic for models that simulate the behavior of liquefying materials. For the reasons just described, the SANISAND model is most recommended for modeling liquefying materials subjected to monotonic and cyclic stresses.

What has been deduced from this study is that tailings dams remain geotechnical structures that are not well understood and thus need to be further studied from many points of view in order totally reliably predict their behavior, particularly under seismic conditions. As stated by Davies (2002) tailings dams are probably one of the greatest challenges that a geotechnical engineer can face in his career, given that: they are structures that bear all the difficulties associated with water retention dams; they must maintain the structural design characteristics for time periods of hundreds of years; during the period of activity they are structures that continuously change in size, often being subjected to significant extensions (the largest dam ever built is a tailings dam); construction times can vary between 50 and 100 years; the stress states are in continuous evolution; the tailings dams are highly susceptible to fragile behavior as a result of undrained loads; the tailings often contain pollutants and contaminants, and tailing storage facilities are economically disadvantageous and, therefore, seen as a burden by the owners and managers of mining concessions.

The International Council on Mining & Metals (ICMM) together with the United Nations Environment Program (UNEP) and Principles for Responsible Investment (PRI) drafted the Global Industry Standard on Tailings Management, which points out that the catastrophic consequences on populations and the environment resulting from the failure of tailings dams are no longer acceptable. For this reason, The Technical Committee TC221 Tailings and Mine Waste of the International Society for Soil Mechanics and Geotechnical Engineering (ISSMGE) is organizing numerous meetings and discussions with experts, to help all the actors involved to pursue this goal. International guidelines covering all aspects, from design to management during the operational phase up to after plant closure, with particular attention paid to numerical modeling and constitutive models adequate to represent tailings, would be desirable. In this context, with all the limitations previously mentioned, this doctoral thesis aims to be a starting contribute to pursuing these objectives of fundamental importance in this sector.

In conclusion, this work proposes a complete methodology to analyze tailings storage facilities under seismic loading conditions, that includes a thorough field investigation of the basins and the embankment, laboratory tests on undisturbed samples taken by ground freezing, the calibration and validation of sophisticated constitutive models, and their application in finite element simulations of the whole structure.

Bibliography

Azam, S., & Li, Q. (2010). Tailings dam failures: a review of the last one hundred years. Geotechnical news, 28(4), 50-54.

Banerjee, R., Chattaraj, R., Parulekar, Y. M., & Sengupta, A. (2021). Numerical prediction of undrained cyclic triaxial experiments on saturated Kasai river sand using two constitutive models of liquefaction. Bulletin of Engineering Geology and the Environment, 80, 8565-8582.

Beaty, M. H. (2018). Application of UBCSAND to the LEAP centrifuge experiments. Soil Dynamics and Earthquake Engineering, 104, 143-153.

Boulanger, R. W., & Ziotopoulou, K. (2017). PM4Sand (version 3.1): A sand plasticity model for earthquake engineering applications. Rep. No. UCD/CGM-17/01. Davis, CA: Center for Geotechnical Modeling, Dept. of Civil and Environmental Engineering, Univ. of California.

Clarkson, L., & Williams, D. (2021). An overview of conventional tailings dam geotechnical failure mechanisms. Mining, Metallurgy & Exploration, 38(3), 1305-1328.

Dafalias, Y. F., & Manzari, M. T. (2004). Simple plasticity sand model accounting for fabric change effects. Journal of Engineering Mechanics, 130(6), 622-634.

Davies, M. P. (2002). Tailings impoundment failures are geotechnical engineers listening?. GEOTECHNICAL NEWS-VANCOUVER-, 20(3), 31-36.

Elgamal, A., Yang, Z., Parra, E., & Ragheb, A. (2003). Modeling of cyclic mobility in saturated cohesionless soils. International Journal of Plasticity, 19(6), 883-905.

Flora, A., Bilotta, E., Nappa, V., Chiaradonna, A., Fasano, G., Lirer, S., Quintero, J., Millen, M.D.L., Viana da Fonseca A., Lai, C.G., Andreotti, G., Özcebe, A.G., Bozzoni, F., Zuccolo E., (2020). Deliverable D4.4 Database of calibrated numerical modelling results. Assessment and mitigation of liquefaction potential across Europe: a holistic approach to protect structures/ infrastructure for improved resilience to earthquake-induced liquefaction disasters. H2020-DRA-2015 GA no. 700748.

ICOLD, U. (2001). Tailings dams–risk of dangerous occurrences, lessons learnt from practical experiences (bulletin 121). Commission Internationale des Grands Barrages, Paris, 155.

Ismael, B. (2020). A state-dependent approach for the evaluation of post-liquefaction behaviour of sands. The University of Manchester (United Kingdom).

Lyu, Z., Chai, J., Xu, Z., Qin, Y., & Cao, J. (2019). A comprehensive review on reasons for tailings dam failures based on case history. Advances in Civil Engineering, 2019, 1-18.

Machaček, J., Triantafyllidis, T., & Staubach, P. (2018). Fully coupled simulation of an opencast mine subjected to earthquake loading. Soil Dynamics and Earthquake Engineering, 115, 853-867.

Mandokhail, S. J., Ali, N., Siddique, M., Kakar, E., Menga, A. N., & Kakar, G. (2017). 2D numerical modeling of the cyclic simple shear test using OpenSees. Journal of Applied and Emerging Sciences, 7(1), pp40-46.

McGann, C., Arduino, P.: Dynamic 2D Effective Stress Analysis of Slope. OpenSees user manual (2011).

Piciullo, L., Storrøsten, E. B., Liu, Z., Nadim, F., & Lacasse, S. (2022). A new look at the statistics of tailings dam failures. Engineering Geology, 303, 106657.

Rico, M., Benito, G., Salgueiro, A. R., Díez-Herrero, A., & Pereira, H. G. (2008). Reported tailings dam failures: a review of the European incidents in the worldwide context. Journal of Hazardous Materials, 152(2), 846-852.

Stark, T. D., Moya, L., & Lin, J. (2022). Rates and Causes of Tailings Dam Failures. Advances in Civil Engineering, 2022.

Taiebat, M., Jeremić, B., Dafalias, Y. F., Kaynia, A. M., & Cheng, Z. (2010). Propagation of seismic waves through liquefied soils. Soil Dynamics and Earthquake Engineering, 30(4), 236-257.

Tailings dam safety. WISE Uranium Project - Tailings Dam Safety. (n.d.). Retrieved March 23, 2023, from https://www.wise-uranium.org/indexm.html

TSF failures from 1915. CSP2. (n.d.). Retrieved March 23, 2023, from http://www.csp2.org/tsf-failures-from-1915

Vick, S. G. (1990). Planning, design, and analysis of tailings dams. BiTech Publishers Ltd.

Wang, H., Stuedlein, A. W., & Sinha, A. (2022, September). Framework and Demonstration of Constitutive Model Calibration for Liquefaction Simulation of Densified Sand. In Proceedings of the 4th International Conference on Performance Based Design in Earthquake Geotechnical Engineering (Beijing 2022) (pp. 1725-1736). Cham: Springer International Publishing.

Wichtmann, T., Fuentes, W., & Triantafyllidis, T. (2019). Inspection of three sophisticated constitutive models based on monotonic and cyclic tests on fine sand: Hypoplasticity vs. Sanisand vs. ISA. Soil Dynamics and Earthquake Engineering, 124, 172-183.

Wichtmann, T., Steller, K., Triantafyllidis, T., Back, M., & Dahmen, D. (2019). An experimental parametric study on the liquefaction resistance of sands in spreader dumps of lignite opencast mines. Soil Dynamics and Earthquake Engineering, 122, 290-309.

World mine tailings failures-from 1915. World Mine Tailings Failuresfrom 1915. (n.d.). Retrieved March 23, 2023, from https://worldminetailingsfailures.org/

Yang, Z., Elgamal, A., & Parra, E. (2003). Computational model for cyclic mobility and associated shear deformation. Journal of Geotechnical and Geoenvironmental Engineering, 129(12), 1119-1127.

Schriftenreihe des Instituts für Grundbau, Wasserwesen und Verkehrswesen der Ruhr-Universität Bochum

Herausgeber: H.L. Jessberger

1 (1979) **Hans Ludwig Jessberger**
Grundbau und Bodenmechanik an der Ruhr-Universität Bochum

2 (1978) **Joachim Klein**
Nichtlineares Kriechen von künstlich gefrorenem Emschermergel

3 (1979) **Heinz-Joachim Gödecke**
Die Dynamische Intensivverdichtung wenig wasserdurchlässiger Böden

4 (1979) **Poul V. Lade**
Three Dimensional Stress-Strain Behaviour and Modeling of Soils

5 (1979) **Roland Pusch**
Creep of soils

6 (1979) **Norbert Diekmann**
Zeitabhängiges, nichtlineares Spannungs-Verformungsverhalten von gefrorenem Schluff unter triaxialer Belastung

7 (1979) **Rudolf Dörr**
Zeitabhängiges Setzungsverhalten von Gründungen in Schnee, Firn und Eis der Antarktis am Beispiel der deutschen Georg-von-Neumayer- und Filchner-Station

8 (1984) **Ulrich Güttler**
Beurteilung des Steifigkeits- und Nachverdichtungsverhaltens von ungebundenen Mineralstoffen

9 (1986) **Peter Jordan**
Einfluss der Belastungsfrequenz und der partiellen Entwässerungs-möglichkeiten auf die Verflüssigung von Feinsand

10 (1986) **Eugen Makowski**
Modellierung der künstlichen Bodenvereisung im grundwasserdurchströmten Untergrund mit der Methode der finiten Elemente

11 (1986) **Reinhard A. Beine**
Verdichtungswirkung der Fallmasse auf Lastausbreitung in nichtbindigem Boden bei der Dynamischen Intensivverdichtung

12 (1986) **Wolfgang Ebel**
Einfluss des Spannungspfades auf das Spannungs-Verformungsverhalten von gefrorenem Schluff im Hinblick auf die Berechnung von Gefrierschächten

13 (1987) **Uwe Stoffers**
Berechnungen und Zentrifugen-Modellversuche zur Verformungsabhängigkeit der Ausbaubeanspruchung von Tunnelausbauten in Lockergestein

14 (1988) **Gerhard Thiel**
Steifigkeit und Dämpfung von wassergesättigtem Feinsand unter Erdbebenbelastung

15 (1991) **Mahmud Thaher**
Tragverhalten von Pfahl-Platten-Gründungen im bindigen Baugrund,
Berechnungsmodelle und Zentrifugen-Modellversuche

Schriftenreihe des Instituts für Grundbau der Ruhr-Universität Bochum

Herausgeber: H.L. Jessberger

16 (1992) **Rainer Scherbeck**
Geotechnisches Verhalten mineralischer Deponieabdichtungsschichten
bei ungleichförmiger Verformungswirkung

17 (1992) **Martin M. Bizialiele**
Torsional Cyclic Loading Response of a Single Pile in Sand

18 (1993) **Michael Kotthaus**
Zum Tragverhalten von horizontal belasteten Pfahlreihen aus langen Pfählen in Sand

19 (1993) **Ulrich Mann**
Stofftransport durch mineralische Deponieabdichtungen:
Versuchsmethodik und Berechnungsverfahren

20 (1992) **Festschrift anlässlich des 60. Geburtstages von**
Prof. Dr.-Ing. H. L. Jessberger
20 Jahre Grundbau und Bodenmechanik an der Ruhr-Universität Bochum

21 (1993) **Stephan Demmert**
Analyse des Emissionsverhaltens einer Kombinationsabdichtung im Rahmen der
Risikobetrachtung von Abfalldeponien

22 (1994) **Diethard König**
Beanspruchung von Tunnel- und Schachtausbauten in kohäsionslosem Lockergestein
unter Berücksichtigung der Verformung im Boden

23 (1995) **Thomas Neteler**
Bewertungsmodell für die nutzungsbezogene Auswahl von Verfahren zur Altlastensanierung

24 (1995) **Ralph Kockel**
Scherfestigkeit von Mischabfall im Hinblick auf die Standsicherheit von Deponien

25 (1996) **Jan Laue**
Zur Setzung von Flachfundamenten auf Sand unter wiederholten Lastereignissen

26 (1996) **Gunnar Heibrock**
Zur Rissbildung durch Austrocknung in mineralischen Abdichtungsschichten
an der Basis von Deponien

27 (1996) **Thomas Siemer**
Zentrifugen-Modellversuche zur dynamischen Wechselwirkung zwischen Bauwerken
und Baugrund infolge stoßartiger Belastung

28 (1996) **Viswanadham V. S. Bhamidipati**
Geosynthetic Reinforced Mineral Sealing Layers of Landfills

29 (1997) **Frank Trappmann**
Abschätzung von technischem Risiko und Energiebedarf bei Sanierungsmaßnahmen für Altlasten

30 (1997) **André Schürmann**
Zum Erddruck auf unverankerte flexible Verbauwände

31 (1997) **Jessberger, H. L. (Herausgeber)**
Environment Geotechnics, Report of ISSMGE Technical Committee TC 5 on Environmental Geotechnics

Schriftenreihe des Instituts für Grundbau und Bodenmechanik der Ruhr-Universität Bochum

Herausgeber: Th. Triantafyllidis

32 (2000) **Triantafyllidis, Th. (Herausgeber)**
Boden unter fast zyklischer Belastung: Erfahrung und Forschungsergebnisse (Workshop)

33 (2002) **Christof Gehle**
Bruch- und Scherverhalten von Gesteinstrennflächen mit dazwischenliegenden Materialbrücken

34 (2003) **Andrzej Niemunis**
Extended hypoplastic models for soils

35 (2004) **Christiane Hof**
Über das Verpressankertragverhalten unter kalklösendem Kohlensäureangriff

36 (2004) **René Schäfer**
Einfluss der Herstellungsmethode auf das Verformungsverhalten von Schlitzwänden in weichen bindigen Böden

37 (2005) **Henning Wolf**
Zur Scherfugenbänderung granularer Materialien unter Extensionsbeanspruchung

38 (2005) **Torsten Wichtmann**
Explicit accumulation model for non-cohesive soils under cyclic loading

39 (2008) **Christoph M. Loreck**
Die Entwicklung des Frischbetondruckes bei der Herstellung von Schlitzwänden

40 (2008) **Igor Arsic**
Über die Bettung von Rohrleitungen in Flüssigböden

41 (2009) **Anna Arwanitaki**
Über das Kontaktverhalten zwischen einer Zweiphasenschlitzwand und nichtbindigen Böden

Schriftenreihe des Lehrstuhls für Grundbau, Boden- und Felsmechanik der Ruhr-Universität Bochum

Herausgeber: T. Schanz

42 (2009) **Yvonne Lins**
Hydro-Mechanical Properties of Partially Saturated Sand

43 (2010) **Tom Schanz (Herausgeber)**
Geotechnische Herausforderungen beim Umbau des Emscher-Systems
Beiträge zum RuhrGeo Tag 2010

44 (2010) **Jamal Alabdullah**
Testing Unsaturated Soil for Plane Strain Conditions: A New Double-Wall Biaxial Device

45 (2011) **Lars Röchter**
Systeme paralleler Scherbänder unter Extension im ebenen Verformungszustand

46 (2011) **Yasir Al-Badran**
Volumetric Yielding Behavior of Unsaturated Fine-Grained Soils

47 (2011) **Usque ad finem**
Selected research papers

48 (2012) **Muhammad Ibrar Khan**
Hydraulic Conductivity of Moderate and Highly Dense Expansive Clays

49 (2014) **Long Nguyen-Tuan**
Coupled Thermo-Hydro-Mechanical Analysis: Experimental and Back Analysis

50 (2014) **Tom Schanz (Herausgeber)**
Ende des Steinkohlenbergbaus im Ruhrrevier: Realität und Perspektiven für die Geotechnik
Beiträge zum RuhrGeo Tag 2014

51 (2014) **Usque ad finem**
Selected research papers

52 (2014) **Houman Soleimani Fard**
Study on the Hydro-Mechanical Behavior of Fiber Reinforced Fine Grained Soils,
with Application to the Preservation of Historical Monuments

53 (2014) **Wiebke Baille**
Hydro-Mechanical Behaviour of Clays - Significance of Mineralogy

54 (2014) **Qasim Abdulkarem Jassim Al-Obaidi**
Hydro-Mechanical Behavior of Collapsible Soils

55 (2015) **Veselin Zarev**
Model Identification for the Adaption of Numerical Simulation Models -
Application to Mechanized Shield Tunneling

56 (2015) **Meisam Goudarzy**
Micro and Macro Mechanical Assessment of Small and Intermediate Strain
Properties of Granular Material

57 (2016) **Oliver Detert**
Analyse einer selbstregulierenden interaktiven Membrangründung für Schüttkörper auf geringtragfähigen Böden

58 (2016) **Yang Yang**
Analyses of Heat Transfer and Temperature-induced Behaviour in Geotechnics

59 (2016) **Alborz Pourzargar**
Application of suction stress concept to partially saturated compacted soils

60 (2017) **Hanna Haase**
Multiscale Analysis of Clay-Polymer Composites for Geoenvironmental Applications

61 (2017) **Kavan Khaledi**
Constitutive modeling of rock salt with application to energy storage caverns

62 (2017) **Nina Silvia Müthing**
On the consolidation behaviour of fine-grained soils under cyclic loading

63 (2017) **Elham Mahmoudi**
Probabilistic analysis of a rock salt cavern with application to energy storage systems

64 (2017) **Negar Rahemi**
Evaluation of liquefaction behavior of sandy soils using critical state soil mechanics and instability concept

65 (2018) **Chenyang Zhao**
Numerical Modeling of Mechanized Tunnel Excavation:
Effects of Sub-systems and Advanced Process Simulation

66 (2018) **Tom Schanz (Herausgeber)**
Innovationen im Spezialtiefbau und in der Umweltgeotechnik
Beiträge zum RuhrGeo Tag 2018

67 (2019) **Linzhi Lang**
Hydro-Mechanical Behaviour of Bentonite-Based Materials Used for Disposal of Radioactive Wastes

68 (2019) **Usama Al-Anbaki**
Hydraulic Interaction of Soil and Nonwoven Geotextiles under Unsaturated Conditions

69 (2019) **Abhishek Rawat**
Coupled Hydro-mechanical Behavior of a Compacted Bentonite-Sand Mixture: Experimental and Numerical Investigations

Schriftenreihe des Lehrstuhls für Bodenmechanik, Grundbau und Umweltgeotechnik der Ruhr-Universität Bochum

Herausgeber: T. Wichtmann

70 (2019) **Mahmoud Qarmout**
Tunnel face stability using Kinematical Element Method (KEM)

71 (2021) **Raoul Hölter**
Optimal Experimental Design in Geotechnical Engineering

72 (2022) **Wolfgang Lieske**
Impact of polymer constitution on the hydro-mechanical behaviour of modified bentonite for the application in geotechnical and geoenvironmental engineering

73 (2022) **Patrick Staubach**
Contributions to the numerical modelling of pile installation processes and high-cyclic loading of soils

74 (2022) **Lingyun Li**
On the hydromechanical behaviour of loess and its effect on slope stability under rainfall infiltration

75 (2022) **Debdeep Sarkar**
Influence of particle characteristics on the behaviour of granular materials under static, cyclic and dynamic loading

76 (2023) **Torsten Wichtmann (Herausgeber)**
Umbau des Emscher-Systems – Geotechnische Erfahrungen
Beiträge zum RuhrGeo Tag 2023

77 (2023) **Abbas Farhat**
Fluidization and erosion of cemented granular materials. Experimental characterization and micromechanical simulation

78 (2023) **Andrea Geppetti**
Experimental and numerical investigations on the behaviour of tailing storage facilities under seismic loading